Springer Theses
Recognizing Outstanding Ph.D. Research

Tarik Berrada

Interferometry with Interacting Bose-Einstein Condensates in a Double-Well Potential

Springer

Springer Theses

Recognizing Outstanding Ph.D. Research

Aims and Scope

The series "Springer Theses" brings together a selection of the very best Ph.D. theses from around the world and across the physical sciences. Nominated and endorsed by two recognized specialists, each published volume has been selected for its scientific excellence and the high impact of its contents for the pertinent field of research. For greater accessibility to non-specialists, the published versions include an extended introduction, as well as a foreword by the student's supervisor explaining the special relevance of the work for the field. As a whole, the series will provide a valuable resource both for newcomers to the research fields described, and for other scientists seeking detailed background information on special questions. Finally, it provides an accredited documentation of the valuable contributions made by today's younger generation of scientists.

Theses are accepted into the series by invited nomination only and must fulfill all of the following criteria

- They must be written in good English.
- The topic should fall within the confines of Chemistry, Physics, Earth Sciences, Engineering and related interdisciplinary fields such as Materials, Nanoscience, Chemical Engineering, Complex Systems and Biophysics.
- The work reported in the thesis must represent a significant scientific advance.
- If the thesis includes previously published material, permission to reproduce this must be gained from the respective copyright holder.
- They must have been examined and passed during the 12 months prior to nomination.
- Each thesis should include a foreword by the supervisor outlining the significance of its content.
- The theses should have a clearly defined structure including an introduction accessible to scientists not expert in that particular field.

More information about this series at http://www.springer.com/series/8790

Tarik Berrada

Interferometry with Interacting Bose-Einstein Condensates in a Double-Well Potential

Doctoral Thesis accepted by
Vienna University of Technology, Austria

Springer

Author
Dr. Tarik Berrada
Vienna Center for Quantum Science and Technology
Institute of Atomic and Subatomic Physics
Vienna University of Technology
Vienna
Austria

Supervisor
Prof. Jörg Schmiedmayer
Vienna Center for Quantum Science and Technology
Institute of Atomic and Subatomic Physics
Vienna University of Technology
Vienna
Austria

ISSN 2190-5053 ISSN 2190-5061 (electronic)
Springer Theses
ISBN 978-3-319-27232-0 ISBN 978-3-319-27233-7 (eBook)
DOI 10.1007/978-3-319-27233-7

Library of Congress Control Number: 2015957223

Printed on acid-free paper

This Springer imprint is published by SpringerNature
The registered company is Springer International Publishing AG Switzerland

Parts of this thesis have been published in the following journal articles:

The main results presented in this thesis have been published in:

- **Integrated Mach-Zehnder interferometer for Bose-Einstein condensates**, T. Berrada, S. van Frank, R. Bücker, T. Schumm, J.-F. Schaff, J. Schmiedmayer, **Nat. Commun. 4**, 2077 (2013)

The following publications have resulted from the work undertaken during the course of this thesis, both at the Atomic Institute of the Vienna University of Technology and at the Institut d'Optique in Palaiseau (France):

- **Two-Point Phase Correlations of a One-Dimensional Bosonic Josephson Junction**, T. Betz, S. Manz, R. Bücker, T. Berrada, C. Koller, G. Kazakov, I. Mazets, H. Stimming, A. Perrin, T. Schumm, and J. Schmiedmayer, **Phys. Rev. L 106**, 020407 (2011)
- **Twin-atom beams**, R. Bücker, J. Grond, S. Manz, T. Berrada, T. Betz, C. Koller, U. Hohenester, T. Schumm, A. Perrin, and Jörg Schmiedmayer, **Nature Physics 7**, 608-611 (2011)
- **Sub-Poissonian Fluctuations in a 1D Bose Gas: From the Quantum Quasicondensate to the Strongly Interacting Regime**, T. Jacqmin, J. Armijo, T. Berrada, K. Kheruntsyan, and I. Bouchoule, **Phys. Rev. L 106**, 230405 (2011)
- **Dynamics of parametric matter-wave amplification**, R. Bücker, U. Hohenester, T. Berrada, S. van Frank, A. Perrin, S. Manz, T. Betz, J. Grond, T. Schumm, and J. Schmiedmayer, **Phys. Rev. A 86**, 013638 (2012)
- **Momentum distribution of one-dimensional Bose gases at the quasicondensation crossover: Theoretical and experimental investigation**, T. Jacqmin, B. Fang, T. Berrada, T. Roscilde, and I. Bouchoule, **Phys. Rev. A 86** , 043626 (2012)
- **Vibrational state inversion of a Bose-Einstein condensate: optimal control and state tomography**, R. Bücker, T. Berrada, S. van Frank, J.-F. Schaff, T. Schumm, J. Schmiedmayer, G. Jäger, J. Grond, U. Hohenester, **J. Phys. B 46**, 104012 (2013)
- **Interferometry with non-classical motional states of a Bose-Eintein condensate**, S. van Frank, A. Negretti, T. Berrada, R. Bücker, S. Montangero, J.-F. Schaff, T. Schumm, T. Calarco, J. Schmiedmayer, arXiv: 1402.0377v1, accepted by Nat. Commun. (2014)

Supervisor's Foreword

In his doctoral thesis Tarik Berrada conducted a series of experiments to realize a Mach-Zehnder interferometer with trapped, interacting Bose-Einstein condensates (BEC) of Rubidium 87 atoms confined on an atom chip. The interferometer relies on the coherent manipulation of a BEC in a magnetic double-well potential and a novel matter-wave recombiner. One fundamental difference between atomic BECs and lasers fields is the presence of atomic interactions, yielding an intrinsic nonlinearity. Interactions lead to phase diffusion and limit the interrogation time of trapped BEC interferometers. On the other hand, interactions can be used to generate nonclassical (e.g., squeezed) states to improve the sensitivity of interferometric measurements beyond the standard quantum limit (SQL). Studying and exploiting the effect of interactions in the implemented trapped atom interferometer is a central physics result of this thesis. The thesis gives a brief introduction to the theoretical framework needed and a concise overview of the experimental apparatus and the key experimental techniques. The main part describes the physics experiments: the implementation of a Mach-Zehnder interferometer for trapped interacting Bose-Einstein condensates. The three main results are:

- A detailed study of the splitting process by transforming a single well into a double well allows to generate significant (>7 dB) number-squeezing. Measuring the phase uncertainty of the resulting interference Tarik Berrada was able to show that the splitting process is close to the limit allowed by the Heisenberg relations for phase-number uncertainty, a remarkable achievement for quantum superposition of external (position) states of a many-body system. The very high contrast of the resulting interference demonstrates large spin-squeezing. From this he estimated that after the splitting the BEC with N = 1200 atoms has to contain states with typically 100 entangled atoms across the two trapped clouds in the double well. Such spin squeezed states can in future experiments potentially yield a sensitivity improvement beyond the SQL.

- By developing a recombiner for the two split clouds, Tarik Berrada was able to implement a Mach-Zehnder interferometer (MZI) for trapped BECs on the atom chip that can be read out by counting atoms on the final double well. He thereby investigated both a standard recombiner based on the Josephson coupling in a double well when the barrier is lowered, and a new "sudden" recombiner, which resulted in higher contrast of the final read-out pattern.
- Combining both, Tarik Berrada was able to perform the first direct experimental demonstration of the link between number fluctuations and interaction-induced phase diffusion, and show how the use of a nonclassical, number-squeezed state can help extending the interrogation time of a matter-wave interferometer. The experiments described in this chapter constitute an important step toward the use of BECs for matter-wave interferometry and contributes to the understanding of interacting many-body quantum systems including the generation, manipulation, and detection of nonclassical atomic states.

Vienna
November 2015

Prof. Jörg Schmiedmayer

Abstract

Mach-Zehnder interferometry with interacting Bose-Einstein condensates in a double-well potential

Particle-wave duality has enabled the construction of interferometers for massive particles such as electrons, neutrons, atoms, or molecules. Implementing atom interferometry has required the development of analogues to the optical beam-splitters, phase shifters, or recombiners to enable the coherent, i.e., phase-preserving manipulation of quantum superpositions. While initially demonstrating the wave nature of particles, atom interferometers have evolved into some of the most advanced devices for precision measurement, both for technological applications and tests of the fundamental laws of nature. Bose-Einstein condensates (BEC) of ultracold atoms are particular matter waves: they exhibit a collective many-body wave function and macroscopic coherence properties. As such, they have often been considered as an analogue to optical laser fields and it is natural to wonder whether BECs can provide to atom interferometry a similar boost as the laser brought to optical interferometry.

One fundamental difference between atomic BECs and lasers fields is the presence of atomic interactions, yielding an intrinsic nonlinearity. On one hand, interactions can lead to effects destroying the phase coherence and limiting the interrogation time of trapped BEC interferometers. On the other hand, they can be used to generate nonclassical (e.g., squeezed) states to improve the sensitivity of interferometric measurements beyond the standard quantum limit (SQL).

In this thesis, we present the realization of a full Mach-Zehnder interferometric sequence with trapped, interacting BECs confined on an atom chip. Our interferometer relies on the coherent manipulation of a BEC in a magnetic double-well potential. For this purpose, we developed a novel type of matter-wave recombiner, an element which so far was missing in BEC atom optics.

We have been able to exploit interactions to generate a squeezed atomic state with reduced atom number fluctuations that could potentially yield a sensitivity improvement beyond the SQL. We used this state to study the interaction-induced diffusion of the quantum phase. For the first time we directly evidenced the link between fundamental atom number uncertainty and phase diffusion, and

demonstrated extended coherence times by use of a nonclassical state. This constitutes an important step toward the use of BECs for quantum-enhanced matter-wave interferometry and contributes to the understanding of interacting many-body quantum systems. It opens new possibilities for the generation, manipulation, and detection of nonclassical atomic states, and calls for further studies of the role of interactions as a resource for matter-wave interferometry.

Preface

"Weil hab i erst des nötige Quantum do drin
dann merk i net was für a Trottl i bin"
Gerhard Bronner and Helmut Qualtinger,
"Krügerl vor'm G'sicht", 1960.

An interferometer is a device that makes use of the effect of wave interference. Optical interferometers rely on the interference of light waves. Since the middle of the nineteenth century, interferometry has become a key technique in physics, bringing new insight into the nature of light and the laws of nature. The celebrated interferometry experiment conducted by A. Michelson and E. Morley in 1887 is generally considered to have ruled out the theory of aether and indirectly contributed to the founding of special relativity. The development of lasers since the early 1960s has renewed the field of optics and considerably enhanced the power of interferometers by providing a bright, directed, and coherent source of light for interferometry. Today, optical interferometers range among the most sensitive measurement devices, both for fundamental (gravitational wave detection, astrophysics, …) and technical (inertial sensing for navigation of planes, satellites, …) applications.

Particle-wave duality, stated at the beginning of the twentieth century, enables the construction of interferometers for matter waves. Since the first observations demonstrating the wave nature of massive particles, ground-breaking interferometry experiments with electrons, neutrons, atoms, or molecules have allowed studying quantum phenomena, investigating the properties of matter, testing the fundamental laws of physics, and performing precision measurements [1].

Over the last decades, in particular with the progress of laser cooling and frequency combs, atom interferometers have evolved into devices at the leading edge of precision measurements. Long-lived coherent superpositions of internal atomic states have been used in atomic clocks to measure time with unprecedented accuracy, providing the definition of the second since 1967. Interferometers using quantum superposition of atomic motional states can also measure accelerations and

rotations to high precision. It has been argued that due to the high rest mass of atoms, compared to the energy of an optical photon, atom interferometers could yield a considerable gain in sensitivity to inertial forces.

Bose-Einstein condensates (BEC) are particular matter waves. Since the first realization of a BEC in an atomic vapor in 1995 [2], ultracold gases of bosons have been intensively studied as a unique example of a well-controllable system with enhanced quantum properties. In this context, matter-wave interferometry with BECs has proven to be a powerful tool to explore the rich physics of these many-body quantum systems. In particular, it is a unique probe to access the quantum phase of the condensate wavefunction and study its macroscopic coherence, i.e., the existence of a well-defined condensate phase in space and time.

Because of this macroscopic coherence, beautifully demonstrated by the first interference experiments from 1997 on [3], BECs have often been compared to atom lasers [4]. Indeed, like lasers, BEC are characterized by the macroscopic occupation of a single spatial mode. For this reason, it is natural to wonder whether BECs can provide to atom interferometry a similar boost as the laser brought to optical interferometry.

Because BECs are extremely sensitive probes of their environment, they are also fragile. In fact, only the development of ultrahigh vacuum techniques as well as "contract-free" methods to manipulate and trap atoms with optical and magnetic fields at the microscopic level has enabled the experimental realization of BECs. Developing techniques to preserve the phase coherence of atomic quantum superpositions is a challenging requirement for BEC interferometry.

One fundamental difference between atomic BECs and laser fields rises from the presence of interactions. Atom–atom interactions drive the physics of confined BECs, leading to a rich quantum phase diagram. In the context of atom interferometry, the impact of interactions is ambivalent. On the one hand, interactions are responsible for intrinsic phase diffusion effects which ultimately limit the coherence time of BEC interferometers. On the other hand, they can be exploited to generate nonclassical correlations between atoms and produce entangled states. Atomic squeezed states are an example of such nonseparable states, and have been shown to potentially reduce the effect of interaction-induced phase diffusion or improve the sensitivity of interferometric measurements beyond the sensitivity limit for uncorrelated particles, the standard quantum limit (SQL). For these reasons, studying the effect of atomic interactions is crucial to perform precise interferometric measurement with trapped BEC as well as to understand the physics of complex many-body quantum systems.

Condensates in a double-well potential implement the textbook case of a two-mode BEC. At the same time, they provide a prototypical configuration for matter-wave interferometry, reminiscent of Young's double-slit experiment. For these reasons, they have stimulated great theoretical interest [5]. It was recognized very early that a BEC in a double well implements a cold atom analogue of a superconducting Josephson junction, where the Cooper pairs are replaced by neutral atoms and the thin insulating layer by a potential barrier, justifying the name of "bosonic Josephson junction" (BJJ). A tunable BJJ offers a conceptually simple

playground to investigate the interplay of tunnel coupling and atomic interactions in BECs, yielding a rich variety of dynamical regimes. Most importantly, tuning the parameters of a BJJ also offers a handle to engineer the many-body state of the BEC.

In this thesis, we present the implementation of a Mach-Zehnder interferometer for BECs on an atom chip setup, and its use for the study of interactions in our trapped, interacting BECs.

Since the first demonstration of the phase-preserving splitting of a BEC in 1998 [6], various techniques have been developed to build atom-optics analogues to beam splitters, phase shifters, or recombiners. Our scheme relies on the coherent manipulation of a condensate in a tunable double-well potential. The splitting was implemented by smoothly deforming the potential from a single to a double well. An adjustable phase shift was applied by imposing an energy difference between the two wells. In order to close the interferometric sequence, we developed two novel phase-sensitive recombiners for trapped BECs, the first one relying on controlled tunneling through the BJJ, the second on a fast manipulation of the confining potential.

Taking advantage of interactions during the splitting, we were able to produce and characterize a nonclassical "squeezed" atomic state featuring reduced number fluctuations with respect to a coherent state. We showed that the state produced in the interferometer could potentially yield a significant metrology gain beyond the SQL.

We used this state to study interaction-induced phase diffusion in our interferometer. For the first time, we could unambiguously evidence the link between fundamental atom number uncertainty and the rate of diffusion of the quantum phase, and demonstrated a coherence time extended by more than a factor of two by use of a nonclassical state.

This work constitutes an important step toward the use of BECs for quantum-enhanced matter-wave interferometry and contributes to the understanding of interactions in BECs. It opens new possibilities for the generation, manipulation, and detection of nonclassical quantum states, and calls for further studies of the role of interactions as a resource for matter-wave interferometry.

The manuscript is structured as follows:

- In Chap. 1, the theoretical framework which forms the basis for the results of this thesis is introduced. It comprises mainly a basic description of interacting BECs, with emphasis on elongated geometries, followed by a presentation of the two-mode model describing the physics of a condensate in a double-well potential.
- Chap. 2 is devoted to a description of the apparatus on which the experiments were conducted, with focus on the techniques of magnetic trapping on an atom chip, in particular the radio frequency-dressing used for the creation of double-well potentials, as well as the imaging systems used to probe the atoms.

- Chap. 3, which is the central part of this thesis, presents each stage of the Mach-Zehnder interferometric sequence and the corresponding results.
- Finally, Chap. 4 gives an outlook on effects beyond the two-mode description of the BJJ in the light of new experimental observations.

References

1. Alexander D. Cronin, David E. Pritchard, Optics and interferometry with atoms and molecules. Rev. Mod. Phys., **81**(3), 1051–1129 (2009).
2. M.H. Anderson, J.R. Ensher, M.R. Matthews, C.E. Wieman, E.A. Cornell, Observation of Bose-Einstein condensation in a dilute atomic vapor. Sci., **269**(5221), 198–201 (1995).
3. M.R. Andrews, Observation of Interference Between Two Bose Condensates. Sci., **275**(5300), 637–641 (1997)
4. W. Ketterle, When atoms behave as waves: Bose-Einstein condensation and the atom laser, 2001.
5. A. Leggett, Bose-Einstein condensation in the alkali gases: Some fundamental concepts. Rev. Mod. Phys., **73**(2), 307–356 (2001).
6. E. Hagley, L. Deng, M. Kozuma, M. Trippenbach, Y. Band, M. Edwards, M Doery, P. Julienne, K. Helmerson, S. Rolston, W. Phillips, Measurement of the Coherence of a Bose-Einstein Condensate, Phys. Rev. Lett., **83**(16), 3112–3115 (1999).

Acknowledgments

This thesis manuscript is the outcome of the research I carried out at the Atom Institut of the Vienna University of Technology between October 2009 and May 2014, together with the people of the Rb2 team, the whole atom chip group and—during several stays at the Institut d'Optique—the Palaiseau chip team. During these four and a half years, I had the chance to work with exceptionally friendly and stimulating people, from whom I got to learn a lot, both scientifically and personally.

Among many people, I would like to thank

- Jörg Schmiedmayer for giving me the opportunity to join the atom chip group, supervising me and sharing his enthusiasm, his curiosity, his creative ideas, his outstanding scientific experience, and occasionally a concert ticket;
- Thorsten Schumm for his close coaching throughout this thesis, his personal and organizational skills, his kindness and permanent dedication, particularly while I was writing this manuscript, as well as for a sustained macarons supply that presumably saved me from starvation;
- Jean-François Schaff, for his scientific rigor, his cheerfulness, and for the exceptional atmosphere inside and outside the lab. The two years he spent as a postdoc on Rb2 were the most scientifically stimulating of my Ph.D. and most of the results presented in this manuscript were achieved in close teamwork;
- Aurélien Perrin for having trained me at the beginning of my Ph.D. and for having taught me rigorous scientific work;
- Isabelle Bouchoule, for her energy, her bubbling enthusiasm, the stimulating experimental and theoretical work, and for having entrusted to me that long rope at the CNRS boat race;
- The founder mother and fathers of the Rb2 experiment: Stephanie Manz, Thomas Betz, Robert Bücker, Wolfgang Rohringer, and Christian Koller, for having warmly welcomed me in the team, having shared their knowledge with me, and for the excellent working atmosphere;

- My current Rb2 teammates: Sandrine van Frank, Marine Pigneur, Mira Maiwöger, Ru Gway Wu, Marie Bonneau, whom I am glad to have been working with and to whom I wish good luck for the future;
- The whole Vienna atom chip group for the excellent working atmosphere and the jolly lab-life;
- Thibaut Jacqmin, Bess Fang, and Aishling Johnson from the Palaiseau atom chip team, with whom I had the chance to spend several research stays, as well as the whole Institut d'Optique team;
- Bruno Juliá-Díaz and Artur Polls from the university of Barcelona for fruitful ongoing collaboration;
- Georg Jäger, Julian Grond, and Ulrich Hohenester for both the past and the coming collaborations;
- Augusto Smerzi, for being my thesis referee; and
- The CoQuS graduate school, and in particular Christiane Losert-Valiente Kroon, for financial and organizational support.

Outside research, I would like to thank my parents Mohammed and Michèle for their unfailing and constructive support, my brother Marouane, as well as Alenka, Gabi, Jason, Julia, Laurent, Mariko, and many others who accompanied me during all these years.

Contents

Chapter 1
Introduction and Theoretical Background

The aim of this chapter is to set the framework and give the theoretical tools to analyze the experiments presented in this thesis. It is organized as follows:

- The first part introduces some basic concepts of the theory of atomic Bose-Einstein condensates. In particular, the many-body Hamiltonian for a system of bosons in the weakly interacting regime is presented. A mean-field picture, leading to the Gross-Pitaevskii equation, is studied with particular emphasis on the ground state properties of elongated condensates. The Bogoliubov approach is described with the aim of obtaining a classical field picture of elementary excitations.
- The second part is devoted to the two-mode description of a condensate in a double-well potential. The two-sites Bose-Hubbard Hamiltonian is derived from the full many-body Hamiltonian, and its different regimes are studied with focus on the fluctuations of the physical observables. A connection is established to the collective spin formalism to introduce the notion of atomic squeezed states. A mean-field picture is derived and used to describe the dynamics of the bosonic Josephson junction.

1.1 Elements of the Theory of Bose-Einstein Condensation in Atomic Gases

The experimental realization of an atomic Bose-Einstein condensate (BEC) in 1995 [1] has been a striking demonstration of the phase transition predicted by Albert Einstein in 1925 [2], as a direct consequence of the statistics Satyendra Nath Bose had proposed one year before for photons [3]. Einstein showed that at fixed temperature, increasing the density of a uniform ideal Bose gas would cause the bosons to pile up in the quantum state with the lowest kinetic energy while all the other excited states would be saturated, in analogy with the condensation of water in

T. Berrada, *Interferometry with Interacting Bose-Einstein Condensates in a Double-Well Potential*, Springer Theses,
DOI 10.1007/978-3-319-27233-7_1

a saturated vapor. The order parameter of this transition is the fraction of particles in the ground state. The occupation of one quantum state by a non-negligible fraction of the total number of bosons is at the center of the enhanced quantum properties of Bose-Einstein condensates.

1.1.1 Condensation of the Ideal Bose Gas

1.1.1.1 Uniform Ideal Bose Gas

The simple case of an ideal Bose gas in a uniform potential already contains some of the essence of the phenomenon of Bose-Einstein condensation.[1] Let us consider N identical, non-interacting bosons in a square box of size L^3 with periodic boundary conditions (PBC). The single particle eigenstates in this uniform potential are plane waves with quantized wave vectors and energies given by:

$$\vec{k}_{\vec{l}} = \frac{2\pi}{L}\left(l_x\hat{x} + l_y\hat{y} + l_z\hat{z}\right), \tag{1.1}$$

$$\epsilon_{\vec{l}} = \frac{\hbar^2|\vec{k}|^2}{2m} = \frac{2\hbar^2\pi^2}{mL^2}\left(l_x^2 + l_y^2 + l_z^2\right). \tag{1.2}$$

where $\left(l_x, l_y, l_z\right)$ are the three integers labeling the state $\vec{l}$, $\hbar$ is the reduced Planck constant (see Appendix B for the list of symbols used in this manuscript), and m the mass of one boson. At thermal equilibrium in the grand-canonical ensemble, the mean number of particles in the state $\vec{l}$ is given by the Bose statistics

$$N_{\vec{l}} = \frac{1}{e^{(\epsilon_{\vec{l}}-\mu)\beta} - 1} = \frac{z}{e^{\epsilon_{\vec{l}}\beta} - z}. \tag{1.3}$$

Here $\beta = 1/k_B T$ where k_B is the Boltzmann constant and T the temperature. The chemical potential μ is implicitely defined by the constraint of the fixed total atom number through $\sum_{\vec{l}} N_{\vec{l}} = N$. In the right hand side, we have introduced the fugacity z defined as

$$z \equiv e^{\beta\mu}. \tag{1.4}$$

z must be between 0 and 1 to ensure that for any state $\vec{l}$, $N_{\vec{l}} \geq 0$. $z \to 0$ corresponds to the classical limit where Maxwell-Boltzmann statistics is recovered. Conversely, Eq. (1.3) shows that in the limit $z \to 1$, the occupation number N_0 of the ground state

[1] Among the many general references on Bose-Einstein condensation in atomic gases, the books by Pitaevskii and Stringari [4] and Pethick and Smith [5] as well as the Yvan Castin's lecture notes for the Les Houches Physics Summer School [6] have been widely used in this section.

diverges.[2] Since $N_{\vec{l}}$ is an increasing function of z, one sees that this can be achieved by increasing the density of the gas at constant temperature.

More precisely, Bose-Einstein condensation corresponds to a saturation of the excited states: since for any state $\vec{l}$, the occupation number is always smaller than $e^{-\beta\epsilon_{\vec{l}}}$, the total population of the excited states N' is bounded. In the thermodynamic limit ($N \to \infty$, $L \to \infty$ but the density $n_0 \equiv N/L$ is kept constant), we can find a simple upper bound for the number of particles in the excited states:

$$\begin{aligned} N' &\equiv \sum_{\vec{l}\neq 0} N_{\vec{l}} \\ &\leq \sum_{\vec{l}\neq 0} e^{-\beta\epsilon_{\vec{l}}} \approx \int_{k=0}^{\infty} \frac{L^3}{2\pi^2} k^2 e^{-\hbar^2 k^2 \beta/2m} \mathrm{d}k \\ &= 2^{3/2} L^3 \left(\frac{m k_B T}{2\hbar^2 \pi}\right)^{3/2}. \end{aligned} \tag{1.5}$$

This means that when the number of particles (or equivalently the density) of the gas is increased, the population of the excited states saturates at a given value depending on the temperature. If the density is further increased, the particles pile up in the ground state. The exact maximum for N' can be computed using the Riemann ζ function and gives the prefactor $\zeta(3/2) \approx 2.61$ instead of $2^{3/2} \approx 2.83$, see for example [7].

Introducing the de Broglie thermal wavelength

$$\Lambda_T = \sqrt{\frac{2\pi\hbar^2}{m k_B T}} \tag{1.6}$$

gives a physical interpretation to Eq. (1.5): the BEC forms when the typical de Broglie wavelength of the bosons becomes of the order of the mean inter-particle distance:

$$n_0 \Lambda_T^3 \sim 1. \tag{1.7}$$

It can be related to the notion of phase space density [8]. In quantum mechanics, the Heisenberg uncertainty relation

$$\Delta x \Delta p \geq \frac{\hbar}{2} \tag{1.8}$$

sets the lower bound $V = (2\pi\hbar)^3$ to the volume a quantum state can occupy in phase space. The phase space density

[2] Here, $\epsilon_0 = 0$. If the origin of the energies is chosen differently, the ground state energy can be absorbed in the chemical potential: $\mu \to \mu - \epsilon_0$.

$$f(\vec{r},\vec{p}) = \frac{N}{(2\pi\hbar)^3}\frac{1}{Z_1}e^{-\epsilon(\vec{r},\vec{p})/k_BT} \tag{1.9}$$

represents the mean number of particles in an elementary cell of phase space of volume V around $(\vec{r},\vec{p})$. The partition function Z_1 is a normalization constant which can be related to the density in real space n_0 through

$$n_0 = \int f(\vec{r},\vec{p})\mathrm{d}\vec{p} = \frac{N}{\Lambda_T^3 Z_1}. \tag{1.10}$$

The condition (1.7) means that the phase space density at the origin $f(0,0)$ is of the order of V^{-1}. In other words, condensation occurs when there is on average more than one boson per elementary cell of phase space. More generally, this condition corresponds—even for a gas of fermions—to the **quantum degeneracy** limit beyond which the classical description is no more appropriate.

Equation (1.7) defines the critical temperature of the Bose-Einstein condensation in a non interacting gas of bosons in a uniform three-dimensional potential

$$T_c = \frac{2\pi\hbar^2}{mk_B}n_0^{2/3}. \tag{1.11}$$

1.1.1.2 Other Geometries

The exact form of the criterion (1.7) for condensation depends—if applicable—on the geometry of the system. For example, for an ideal Bose gas trapped in a harmonic potential, the condensation threshold becomes [6]:

$$n_0\Lambda_T^3 \approx \zeta(3/2) \approx 2.61 \tag{1.12}$$

where in contrast to the uniform case, n_0 is the density at the minimum of the potential. In Chap. 4, we will see that in certain geometries, Bose-Einstein condensation is not possible, and that a degenerate Bose gas may form a quasi-condensate with reduced phase-coherence, affecting the tunneling properties of BJJs.

1.1.2 The Weakly Interacting Bose Gas

The ideal Bose gas model, assuming non-interacting particles, predicts Bose-Einstein condensation and gives for instance fair estimates for the critical temperature T_c, or the condensate fraction, see for example [4–6]. Nevertheless, interactions are a key ingredient to explain many features of trapped BECs.

We will first briefly present a model for atomic interactions steming from the quantum theory of elastic scattering in a dilute gas and then use it to express the

Hamiltonian in second quantized form for an ensemble of bosons in the weakly interacting regime.

1.1.2.1 Ultracold Collisions

This section is largely inspired by the lecture notes by Walraven on the *Thermodynamics and Collisional Properties of Trapped Atomic Gases* [8]. For a review on ultracold collisions, see Ref. [9]. A key result of the quantum scattering theory is that, at sufficiently low energy, and looking at a sufficiently large distance with respect to the range of the interaction potential, the collision between two identical bosons can be described as an isotropic scattering event (s-wave scattering). More precisely, the wavefunction describing the motion of two bosons, written in the relative coordinate system, can be expressed as the sum of an incoming and a scattered wave (see Fig. 1.1). The wavefunction of the scattered wave is given by

$$\psi_{\text{sc}} \underset{r\to\infty}{\approx} \frac{e^{ikr}}{kr} \sin\eta_0 e^{i\eta_0}, \tag{1.13}$$

k is the wave vector of the relative motion of the colliding particles, while r is the relative distance between the two bosons. Here η_0 represents the phase shift of the wave emerging from the scattering center. This is the key quantity describing the scattering process, because far from the origin, this phase shift is the only track left by the collision. It is used to define the **s-wave scattering length**:

$$a_s \equiv -\frac{\eta_0}{k}. \tag{1.14}$$

The s-wave scattering length is related to the collisional cross-section by

$$\sigma_s = \pi a_s^2 \tag{1.15}$$

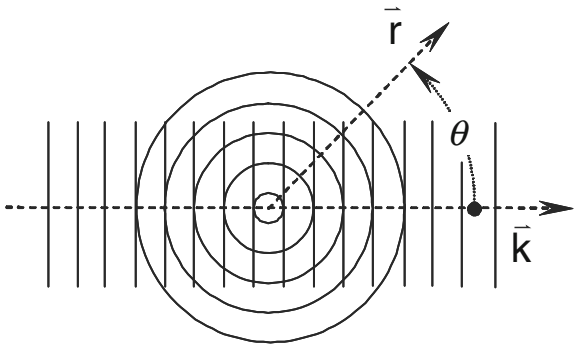

Fig. 1.1 Schematics of s-wave scattering. Adapted from Walraven [8]. Schematic of the s-wave scattering in the center-of-mass coordinate system of the two bosons. k denote the wave vector of the relative motion and $\vec{r}$ is the relative coordinate

which underlines the role of a_s as the measure of the interaction strength in the s-wave regime. The result of Eq. (1.13) is crucial, as it allows to describe the whole scattering process through a single quantity, regardless of the details of the interaction potential. This description of the asymptotic effect of the collision is expected to hold as long as the "collisional size" a_s is much smaller than the typical interparticle distance (*weakly interacting regime*):

$$n|a_s|^3 \ll 1. \tag{1.16}$$

The physical meaning of the sign of a_s becomes clear when looking at how the total energy of a pair of atoms is affected by interactions. Considering two atoms confined in a sphere of radius L, it is shifted by an amount [8]

$$\delta E \approx \frac{\hbar^2 \pi^2}{2mL^3} a_s. \tag{1.17}$$

For $a_s > 0$, the total energy is increased, meaning that the interactions are repulsive, while $a_s < 0$ corresponds to attractive interactions. Remarkably, in some special cases, Feshbach resonances [10] allow tuning both the magnitude and the sign of a_s by changing an external parameter such as the magnetic field.

For the species used in this thesis, the ^{87}Rb isotope in its $F = 1, m_F = -1$ state, the repulsive contact interaction is associated with the scattering length $a_s = 100.4(1)\, a_0 = 5.3$ nm [11], where a_0 is the Bohr radius. It means that the weakly-interacting regime is achieved for a density lower than $\sim 10^{18}$ atoms/cm^3, which is always the case in the experiments presented in this thesis.

A notable consequence of the s-wave scattering description is that there is no need to know the real interaction potential $V_{int}\left(\vec{r} - r'\right)$ to describe the effect of interactions. It can be replaced by a pseudo-potential defined in order to yield the same asymptotic behavior as Eq. (1.13). The simplest mathematical form satisfying this condition is given by the delta-function potential [8]:

$$U(\vec{r}) = \underbrace{\frac{4\pi\hbar^2}{m} a_s}_{g_{3D}} \delta(\vec{r}) \tag{1.18}$$

where δ is the Dirac delta function. The choice of the delta function reflects the assumption of a contact interaction, which only affects the atoms when they are close to each other. The prefactor defines the 3D interaction constant g_{3D}, which measures the strength of the contact interaction. For ^{87}Rb in the $F = 1, m_F = -1$ state, $g_{3D}/h = 7.77 \times 10^{-12}$ cm$^3 \cdot$ Hz. This sets the typical energy scale of interactions: for a typical peak density of $n_0 = 1.3 \times 10^{14}$ atoms/cm^3 in our condensates, the associated energy[3] $g_{3D} n_0$ is of the order of $h \times 1$ kHz.

[3] We will see in Sect. 1.1.3.2 that this energy is precisely equal to the chemical potential in the Thomas-Fermi approximation (Eq. 1.45).

1.1.2.2 Hamiltonian for Weakly Interacting Bosons

To describe a system with a large number (typically $N \sim 1000$ in our experiments) of identical bosons, we work in the formalism of second quantization. For a tutorial introduction to the second quantization, see for example Refs. [12] or [13].

Let us first consider the Hamiltonian $\hat{h}^{(1)}$ for a single particle in an external potential $V(\vec{r})$:

$$\hat{h}^{(1)} = \left[-\frac{\hbar^2}{2m}\Delta + V \right]. \tag{1.19}$$

Its eigenstates $\{|l\rangle\}$ define a basis of modes for the system. We use this single-particle basis to define the operators in second quantization.

The creation and annihilation operator $\hat{a}_l^\dagger$ and $\hat{a}_l$, describing the creation (respectively the destruction) of one boson in the mode $|l\rangle$, obey the bosonic commutation relations:

$$\left[\hat{a}_l, \hat{a}_{l'}\right] = 0, \ \left[\hat{a}_l^\dagger, \hat{a}_{l'}^\dagger\right] = 0, \ \left[\hat{a}_l, \hat{a}_{l'}^\dagger\right] = \delta_{ll'}. \tag{1.20}$$

One also defines the **field operators** $\hat{\Psi}^\dagger$ and $\hat{\Psi}$ corresponding respectively to the creation or annihilation of one boson at position $\vec{r}$:

$$\hat{\Psi}(\vec{r}) = \sum_l \langle \vec{r}|l\rangle \hat{a}_l \tag{1.21}$$

$$\hat{\Psi}^\dagger(\vec{r}) = \sum_l \langle l|\vec{r}\rangle \hat{a}_l^\dagger \tag{1.22}$$

where $|\vec{r}\rangle$ are the eigenvectors of the position operator. They also obey a bosonic commutation relation:

$$\left[\hat{\Psi}(\vec{r}), \hat{\Psi}(\vec{r}\,')\right] = 0, \ \left[\hat{\Psi}^\dagger(\vec{r}), \hat{\Psi}^\dagger(\vec{r}\,')\right] = 0, \ \left[\hat{\Psi}(\vec{r}), \hat{\Psi}^\dagger(\vec{r}\,')\right] = \delta(\vec{r} - \vec{r}\,'). \tag{1.23}$$

The many-body Hamiltonian can be separated into a sum of single-particle terms like $h^{(i)}$ describing the kinetic energy and the potential energy of the ith particle on the one hand, and interaction terms involving several particles on the other hand. In the weakly interacting limit, where binary interactions dominate, and using the pseudo-potential of Eq. (1.18), the full Hamiltonian can be written:

$$\hat{H} = \underbrace{\int \hat{\Psi}^\dagger(\vec{r}) \frac{-\hbar^2}{2m} \Delta \hat{\Psi}(\vec{r}) \mathrm{d}\vec{r}}_{\hat{H}_{\mathrm{kin}}} + \underbrace{\int \hat{\Psi}^\dagger(\vec{r}) V(\vec{r}) \hat{\Psi}(\vec{r}) \mathrm{d}\vec{r}}_{\hat{H}_{\mathrm{pot}}} + \underbrace{\frac{g_{3\mathrm{D}}}{2} \hat{\Psi}^\dagger(\vec{r}) \hat{\Psi}^\dagger(\vec{r}) \hat{\Psi}(\vec{r}) \hat{\Psi}(\vec{r}) \mathrm{d}\vec{r}}_{\hat{H}_{\mathrm{int}}} . \tag{1.24}$$

The Heisenberg equation of motion gives the time evolution of the field operator:

$$\begin{aligned} i\hbar \frac{\partial \hat{\Psi}}{\partial t} &= -\left[\hat{H}, \hat{\Psi}\right] \\ &= \frac{-\hbar^2}{2m} \Delta \hat{\Psi} + V \hat{\Psi} + g_{3D} \hat{\Psi}^\dagger \hat{\Psi} \hat{\Psi} \end{aligned} \tag{1.25}$$

Note the absence of factor 1/2 in front of the interaction term due to the commutation rule for the field operators.

Equation (1.25) allows in principle to compute the full dynamics of the many-body system. In practice, methods to compute the full many-body wavefunction are extremely demanding and it is necessary and useful to resort to approximations.

1.1.3 Mean-Field Model: The Gross-Pitaevskii Equation

Here, we will first consider the case of an almost pure condensate where N is large and most of the atoms occupy the same single-particle wavefunction. If we replace the field operator $\hat{\Psi}$ and its conjugate by a complex function ψ, we can derive a classical field model:

$$\begin{aligned} \hat{\Psi}(\vec{r}, t) &\longrightarrow \sqrt{N} \psi(\vec{r}, t), \\ \hat{\Psi}^\dagger(\vec{r}, t) &\longrightarrow \sqrt{N} \psi^*(\vec{r}, t). \end{aligned} \tag{1.26}$$

We have chosen to normalize ψ to unity: $\int |\psi|^2 d\vec{r} = 1$. Inserting the functions (1.26) in the Hamiltonian (1.24), we find the Gross-Pitaevskii energy functional:

$$E[\psi] = \int \mathrm{d}\vec{r} \left[\frac{\hbar^2}{2m} N |\nabla \psi|^2 + N V |\psi|^2 + \frac{g_{3\mathrm{D}}}{2} N^2 |\psi|^4 \right]. \tag{1.27}$$

As for the Hamiltonian (1.24), we identify the three contributions to the total energy of the gas:

$$E_{\mathrm{kin}} = \frac{\hbar^2}{2m} N \int |\nabla \psi|^2 \mathrm{d}\vec{r} \tag{1.28}$$

$$E_{\text{pot}} = N \int V(\vec{r})|\psi|^2 \mathrm{d}\vec{r} \tag{1.29}$$

$$E_{\text{int}} = \frac{g_{3\text{D}}}{2} N^2 \int |\psi|^4 \mathrm{d}\vec{r}. \tag{1.30}$$

Note that these three terms have to be divided by N to obtain the mean energy per particle. Provided that the origin of energies is fixed at the minimum of V, both kinetic and potential energies are positive. The sign of the interaction term depends only on the sign of $g_{3\text{D}} = 4\pi\hbar^2 a_s/m$, and confirms that repulsive interactions are associated with a positive scattering length while attractive interactions are associated with a negative scattering length.

The ground-state wavefunction ψ_0 can be found by minimizing the Gross-Pitaevskii energy functional with a constraint on the norm of ψ. With the Lagrange multiplier μ for the constraint $\int |\psi|^2 d\vec{r} = 1$, minimizing the functional

$$F[\psi] = E[\psi] - \mu N \int |\psi|^2 \mathrm{d}\vec{r} \tag{1.31}$$

yields the Gross-Pitaevskii equation (GPE), independently derived by Gross [14] and Pitaevskii [15]:

$$-\frac{\hbar^2}{2m}\Delta\psi + V(\vec{r})\psi + g_{3\text{D}} N|\psi|^2\psi = \mu\psi. \tag{1.32}$$

In analogy with the Schrödinger equation, we identify the interaction term $g_{3\text{D}} N|\psi|^2$ to a potential proportional to the local atomic density $n(\vec{r}) \equiv N|\psi|^2$. This mean-field energy can be seen as an effective potential each particle is subjected to because of the interaction with all other atoms. The Lagrange multiplier μ has the dimension of an energy and can be identified with the chemical potential, as can be seen from deriving the energy functional with respect to N [6]:

$$\mu = \frac{\partial E}{\partial N}. \tag{1.33}$$

Inserting Eq. (1.26) into the Heisenberg equation (1.25) yields on the other hand the time-dependent GPE

$$i\hbar\frac{\partial\psi}{\partial t} = -\frac{\hbar^2}{2m}\Delta\psi + V(\vec{r})\psi + g_{3\text{D}} N|\psi|^2\psi. \tag{1.34}$$

Validity of the Mean-Field Treatment

As we will see next, the GPE is a powerful tool to describe many aspects of the equilibrium properties of the condensate as well as its dynamics. The mean-field treatment crucially relies on the assumption that all atoms share the same single-particle wavefunction. An equivalent derivation of the GPE consists in finding an

approximate dynamical equation for the one-body density matrix $\rho_1 = \hat{\Psi}^\dagger \hat{\Psi}$ by replacing the higher-order terms by some function of ρ_1 (see for example [6]). In the presence of a large condensate fraction, one can drop the contribution of all excited states and ρ_1 becomes essentially the projector onto the condensate single-particle wavefunction:

$$\rho_1 = N_0 |\psi_0\rangle\langle\psi_0| + \rho_1' \approx N |\psi_0\rangle\langle\psi_0|. \tag{1.35}$$

From this, we see that the mean-field approximation is expected to hold when the condensate fraction is large, which at thermal equilibrium means that T/T_c is small. This is essentially a classical field approximation, in the sense that it neglects quantum correlation. We will see that it cannot describe many-body correlations, or fluctuations.

In the next sections, we will briefly present some cases where the time-independent GPE has (at least approximate) analytical solutions and mention the numerical resolution methods that have been used in this thesis. We will treat only the case of repulsive interactions ($g_{3D} > 0$).

1.1.3.1 Uniform Potential

The simplest case is that of a uniform potential $V(\vec{r}) = 0$. Let us consider a uniform potential of size L^3 with periodic boundary condition. Although PBC do not correspond to most of the realistic trapping geometries, they offer a simplified description of the bulk of a trapped gas, without caring about the edges. The ground state wavefunction of Eq. (1.32) is simply:

$$\psi(\vec{r}) = \sqrt{\frac{1}{L^3}} \tag{1.36}$$

with the uniform density $n_0 = N/L^3$. The ground state energy E_0 reads:

$$E_0 = E_{\text{int}} = \frac{1}{2} g_{3D} \frac{N^2}{L^3} \tag{1.37}$$

and the chemical potential:

$$\mu = \frac{\partial E_0}{\partial N} = g_{3D} n_0 \tag{1.38}$$

An important property of the mean-field interaction is that it will generally disfavor density fluctuations. Assuming repulsive interactions ($g_{3D} > 0$), a density modulation $\delta n(x) = \delta n \sin kx$ on top of the uniform density n_0 will increase the energy by a relative amount $(\delta n/n_0)^2$. Repulsive interactions therefore generally tend to smoothen the density profile.

1.1.3.2 The Thomas-Fermi Limit

In general, the time-independent GPE cannot be solved analytically for an arbitrary potential. A useful case is however the *Thomas-Fermi* (*TF*) *limit*, for which the interaction and the potential energy dominate over the kinetic energy. In this case, Eq. (1.32) becomes

$$V(\vec{r})\psi + g_{3D}N|\psi|^2\psi \approx \mu\psi. \tag{1.39}$$

The general solution is:

$$\psi(\vec{r}) = \sqrt{\frac{\mu - V(\vec{r})}{g_{3D}N}} \tag{1.40}$$

for $\vec{r}$ such that $\mu > V(\vec{r})$ and 0 elsewhere. For a harmonic potential

$$V(\vec{r}) = \frac{1}{2}m\left[\omega_x^2x^2 + \omega_y^2y^2 + \omega_z^2z^2\right], \tag{1.41}$$

we find that the density profile in each direction is parabolic:

$$n(\vec{r}) = n_0\left[1 - \left(\frac{x}{R_x}\right)^2 - \left(\frac{y}{R_y}\right)^2 - \left(\frac{z}{R_z}\right)^2\right]. \tag{1.42}$$

The extension of the trapped condensate in each spatial direction is given by its Thomas-Fermi radius:

$$R_i = \left[15N\frac{a_s\hbar^2\bar{\omega}^3}{m^2\omega_i^5}\right]^{1/5} \tag{1.43}$$

where $\bar{\omega} = \left(\omega_x\omega_y\omega_z\right)^{1/3}$ is the geometric mean of the trap frequencies and $i = x, y, z$. Note that the TF radii are increasing functions of N: if atoms are added, the repulsive interactions tend to inflate the condensate. The chemical potential μ is related to the number of atoms and to the trap parameters through

$$\mu = \frac{1}{2}\hbar\bar{\omega}\left(15N\frac{a_s}{a_{ho}}\right)^{2/5} \tag{1.44}$$

where $a_{ho} = \sqrt{\hbar/m\bar{\omega}}$ is the harmonic oscillator length. A simple relation links μ to the density $n(0)$ at the center of the cloud:

$$\mu = g_{3D}n(0). \tag{1.45}$$

We can check a posteriori the consistency of the TF approximation by evaluating the different contribution to the total energy using Eq. (1.40). We find using Eqs. (1.29) and (1.30) that:

$$E_{\text{pot}} = \frac{3}{7} N\mu \tag{1.46}$$

$$E_{\text{int}} = \frac{2}{7} N\mu \tag{1.47}$$

The kinetic energy cannot be self-consistently evaluated using (1.40) because the integral in Eq. (1.28) diverges. We can however estimate it for each spatial direction using the TF radii as typical sizes of the condensate:

$$E_{\text{kin},i} \approx N \frac{\hbar^2}{m R_i^2} \tag{1.48}$$

($i = x, y, z$). The condition for the Thomas-Fermi approximation becomes, for each spatial direction:

$$\frac{E_{\text{kin}}}{E_{\text{int}}} \approx \left(\frac{\hbar\omega_i}{\mu} \right)^2 \ll 1. \tag{1.49}$$

The TF approximation is expected to be valid as long as the chemical potential is higher than the typical energy associated with the trapping potential.

1.1.3.3 Condensates in Elongated Harmonic Potentials

Most of the experiments presented in this thesis were performed in elongated traps with aspect ratio $\lambda \equiv \omega_\perp/\omega_\parallel$ up to ~300 (see Fig. 1.2). Typical trapping frequencies for the experiments presented in this thesis are $\omega_\perp \approx 2\pi \times 1.3$ kHz in the radial, tightly confined direction and $\omega_\parallel \approx 2\pi \times 12$ Hz in the longitudinal direction. If we evaluate the chemical potential using Eq. (1.44) for $N = 1200$ atoms, we find $\mu \approx 2\pi\hbar \times 1$ kHz. While this value clearly satisfies condition (1.49) in the longitudinal direction, the kinetic energy cannot be neglected in the transverse direction.

1D Thomas-Fermi Regime

The simplest way to describe such an elongated condensate in the mean-field regime is to assume that due to the large difference in energy scales, the wavefunction is separable into a radial and a longitudinal part [16, 17]

$$\psi(\vec{r}) \equiv \phi(\vec{\rho})\varphi(z). \tag{1.50}$$

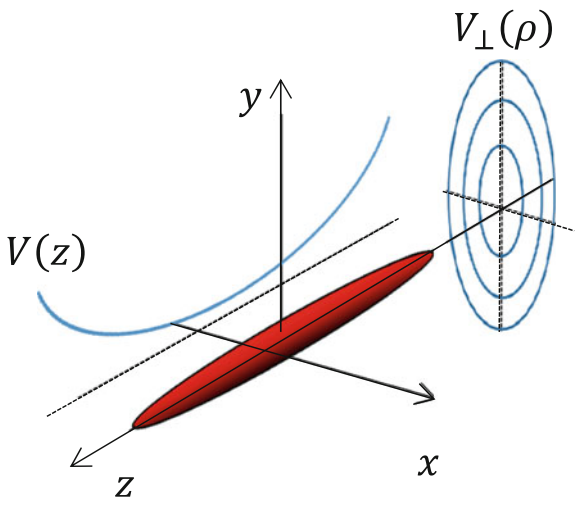

Fig. 1.2 Schematics of an elongated condensate. The z axis corresponds to the direction of shallow confinement $V(z)$ while in the transverse (x, y) plane, the potential $V_\perp(\vec{\rho})$ is strongly confining

Here both φ and ϕ are normalized to unity. We also assume a separable potential

$$V(\vec{r}) = V_\perp(\vec{\rho}) + \frac{1}{2}m\omega_\parallel^2 z^2. \tag{1.51}$$

The GPE (1.32) reads

$$-\frac{\hbar^2}{2m}\frac{\partial^2\varphi}{\partial z^2}\phi + \frac{1}{2}m\omega_\parallel^2 z^2\varphi\phi + g_{3D}N|\phi|^2|\varphi|^2\phi\varphi = \left[\mu + \frac{\hbar^2}{2m}\Delta_\perp\phi - V_\perp\phi\right]\varphi. \tag{1.52}$$

By integration over the radial coordinate $\vec{\rho}$, we get an effective 1D TF equation for the longitudinal wavefunction:

$$-\frac{\hbar^2}{2m}\frac{\partial^2\varphi}{\partial z^2} + \frac{1}{2}m\omega_\parallel^2 z^2\varphi + g_{1D}N|\varphi|^2\varphi = \mu_{1D}\varphi \tag{1.53}$$

with

$$g_{1D} = g_{3D}N\int|\phi|^4 \mathrm{d}\vec{\rho}, \tag{1.54}$$

$$\mu_{1D} = \mu - \int\left(\frac{-\hbar^2}{2m}\phi^*\Delta_\perp\phi + V_\perp|\phi|^2\right)\mathrm{d}\vec{\rho} = \mu - E_\perp^0. \tag{1.55}$$

g_{1D} is the effective 1D interaction parameter. The effective 1D chemical potential μ_{1D} is simply obtained by subtracting the ground-state energy of the radial wave-function $E_\perp^0$ from the true chemical potential μ. The ground state wavefunction reads

$$\varphi(z) = \sqrt{\frac{\mu_{1D}}{g_{1D}N}}\sqrt{1-\left(\frac{z}{R_{1D}}\right)^2} \tag{1.56}$$

Integrating (1.32) over z, we get a similar result for the radial wavefunction

$$\frac{-\hbar^2}{2m}\Delta_\perp\phi + V_\perp\phi + g_\perp N|\phi|^2\phi = \mu_\perp\phi. \tag{1.57}$$

If we assume that radially, the kinetic energy dominates over the interaction energy, we can assume that the radial wavefunction is in the non-interacting ground state. For a radial harmonic potential $V_\perp = m\omega_\perp^2\rho^2/2$, the non-interacting ground state reads

$$\phi(\vec{\rho}) = \frac{1}{a_\perp \pi^{1/2}} e^{-\rho^2/2a_\perp^2}. \tag{1.58}$$

and we get

$$g_{1D} = 2\hbar\omega_\perp a_s, \tag{1.59}$$

$$\mu = \hbar\omega_\perp\left[1+\left(\frac{3}{2\sqrt{2}}Na_s\frac{a_\perp}{a_\parallel^2}\right)^{2/3}\right], \tag{1.60}$$

where we have defined the harmonic oscillator lengths in radial and axial direction $a_{\perp,\parallel} = \sqrt{\hbar/m\omega_{\perp,\parallel}}$. $a_\perp \approx 300$ nm is a typical value for the experiments presented in this thesis. Note that in the 1D Thomas-Fermi limit, the chemical potential and the Thomas-Fermi radius have a different scaling with the atom number N. The 1D Thomas Fermi radius explicitely read

$$R_{TF1D} = \left(\frac{3}{2}\frac{g_{1D}N}{m\omega_z^2}\right)^{1/3}, \tag{1.61}$$

As pointed out in [16, 18], the dimensionless parameter

$$\chi = Na_s a_\perp/a_{\parallel^2} = \frac{g_{3D}N/a_\perp^2 a_\parallel}{\hbar^2/ma_\perp^2} \tag{1.62}$$

appearing in the chemical potential roughly represents the ratio between the interaction energy and the kinetic energy in the radial direction: We can use it to recast the chemical potential in the 3D and in the 1D TF cases

$$\mu_{TF3D} = \frac{1}{2}\hbar\omega_\perp\,(15\chi)^{2/5}\,, \tag{1.63}$$

$$\mu_{TF1D} = \frac{1}{2}\hbar\omega_\perp\left[2+(3\chi)^{2/3}\right]. \tag{1.64}$$

Physically, χ allows to distinguish between the validity range of the 1D and the 3D Thomas-Fermi models. $\chi \gg 5$ corresponds to the 3D Thomas-Fermi limit—sometimes referred to as *three-dimensional cigar* [4]—where the interaction energy dominates over the kinetic energy in all directions. Conversely, when $\chi \ll 5$, the condensate is in the *1D mean-field regime* where the transverse motion is "frozen" and the radial wavefunction is very close to the non-interacting radial ground state, up to some corrections of order $a_s n_{1D}$, where n_{1D} is the linear density (see next section). For the typical parameters given above, we find $\chi = 0.2$, and $\mu_{TF1D} = 2\pi\hbar \times 1.8\,\text{kHz}$, meaning that the experiments have been performed close to the TF 1D limit.

Crossover Between 1D and 3D Thomas-Fermi Regime

In the previous section, we have assumed that the radial and longitudinal degrees of freedom are decoupled. This is of course a crude assumption, since interactions couple all directions. It is still possible to derive a semi-analytical model to find the mean-field ground state wavefunction in the crossover between 1D and 3D Thomas-Fermi regime, where most of the experiments in this thesis take place. Instead of assuming a separable wavefunction, the idea is to compute the radial wavefunction locally, at each position along the longitudinal axis.

Following Refs. [17, 18], we assume local equilibrium in each slice of the elongated condensate (local density approximation). For a harmonic radial potential $V_\perp = \frac{1}{2} m\omega_\perp^2 \rho^2$, it is legitimate to assume that the radial wavefunction is not very different from the non-interacting ground state and to make the following Ansatz

$$\phi(\vec{\rho}) = \frac{1}{2\pi w\,(n_{1D})} e^{-\frac{\rho^2}{2w^2(n_{1D})}} \tag{1.65}$$

whose width w is kept as a variational parameter depending on the local 1D density $n_{1D}(z) = \int n(\vec{r}) d\vec{\rho}$. The expression for $w(n_{1D})$ is found by minimizing the local energy functional and reads:

$$w\,(n_{1D}) = \sqrt{\frac{\hbar}{m\omega_\perp}}\,(1 + 2a_s n_{1D})^{1/4} \tag{1.66}$$

(note that in Ref. [18], the author minimizes the local chemical potential, which yields a factor 4 instead of 2 before in the square root). This means that the local width differs from the non-interacting ground state size by a correction term of the order of $a_s n_{1D}$, which is small but not negligible for the typical 1D densities of the experiment presented in this thesis ($n_{1D} \approx 30$ atoms/μm). Repulsive interactions tend to inflate the cloud transversely, and this effect is stronger in the center of the condensate, where the density is higher. The local-equilibrium chemical potential reads [17]

$$\mu_{\mathrm{1e}}(z) = \hbar\omega_\perp \left(\frac{1 + 3a_s n_{\mathrm{1D}}(z)}{\sqrt{1 + 2a_s n_{\mathrm{1D}}(z)}} \right) \approx g_{\mathrm{1D}} n_{\mathrm{1D}}(z) \tag{1.67}$$

and the longitudinal density profile for a harmonic potential is given by [18][4]

$$n_{\mathrm{1D}}(z) = \frac{\alpha}{16 a_s} \left[\alpha \left(1 - \frac{z}{L} \right)^2 + 4 \right] \left(1 - \left(\frac{z}{L} \right)^2 \right). \tag{1.68}$$

Here $L = a_\parallel^2 \sqrt{\alpha}/a_\perp$ is the longitudinal radius of the condensate (for our typical parameters, $L \approx 25\ \mu\mathrm{m}$, to be compared to $a_\perp \approx 0.3\ \mu\mathrm{m}$) and the value of $\alpha = 2\,(\mu/\hbar\omega_\perp - 1)$ is found by solving numerically the equation:

$$\alpha^3 (\alpha + 5)^2 = (15\chi)^2 . \tag{1.69}$$

α is equal to twice the ratio between the chemical potential (after subtraction of the radial zero-point energy $\hbar\omega_\perp$) over the radial zero-point energy. For the typical parameters given in Sect. 1.1.3.3, $\alpha = 2 \times 0.33$ and $\mu - \hbar\omega_\perp = 2\pi\hbar \times 0.44$ kHz. One can check that depending on the value of χ, the model smoothly interpolates between the predictions of the 1D and 3D TF approximations (see Fig. 1.3). Furthermore, it has been checked [18] that it gives very good agreement with numerical resolution of the 3D GPE for μ and of the axial density profile throughout the crossover.

How Strong Are the Interactions Transversely?

In the rest of this thesis, we will be mostly concerned by the transverse dynamics of a condensate in a double-well potential. Indeed, the geometry of our radio-frequency dressed double wells implies that the splitting occurs transversely, and thus that the tunneling dynamics occurs mostly along one direction. For this reason, we will often resort to approximations or numerical calculations restricted to the transverse dimension.

This is partly motivated by the large aspect ratios of our traps: while the transverse motion of the condensate occurs on the ms timescale, longitudinal oscillations have a typical period of 50 to 100 ms. Moreover, we have seen that the transverse kinetic energy largely dominates over the interaction energy ($\chi \approx 0.2$).

We can evaluate the impact of the interactions on the transverse wavefunction in a (single) harmonic potential from Eqs. (1.66) and (1.68). Using the radial GPE (1.57), we see that in the perturbative approach of Ref. [17], the kinetic, potential and interaction energies (per particle) in the transverse plane read

[4]Note that two numerical factors are wrong in equation (5) of Ref. [18].

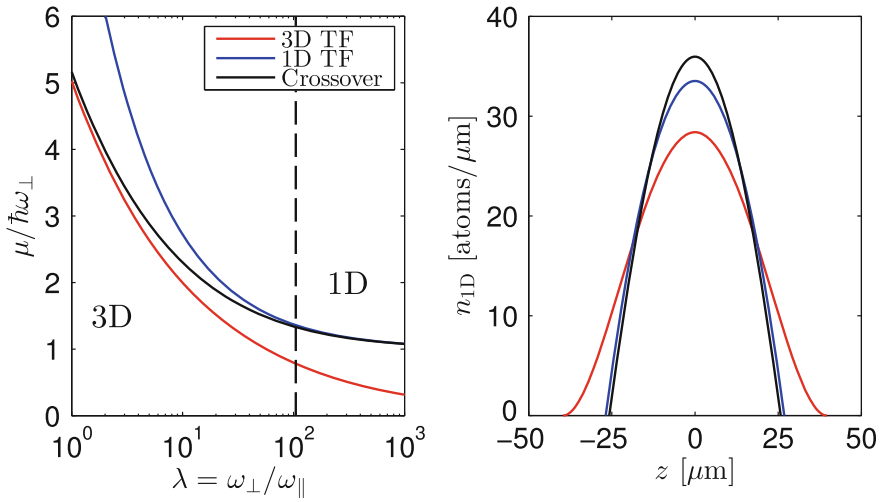

Fig. 1.3 Comparison between the models for elongated condensates. *Left pannel* chemical potential μ evaluated using the 3D Thomas-Fermi (*red*), the 1D Thomas-Fermi (*blue*) or the cross-over model (*black*). N = 1200 atoms, $\omega_\perp$ is kept constant at $2\pi \times 1.3$ kHz while the aspect ratio λ is changed by varying $\omega_\parallel$. *Black dashed line* $\lambda = 105$ ($\omega_\parallel = 2\pi \times 12.4$ Hz), corresponding to typical experimental parameter for the experiments in this thesis. *Right pannel* Linear density profile $n_{1D}(z)$ computed using each model (same color code) for the parameters of to the *black dashed line* of *left panel*

$$E_{\text{kin}} = \hbar\omega_\perp \times [1 - a_s n_{1D}(z)], \tag{1.70}$$

$$E_{\text{pot}} = \hbar\omega_\perp \times [1 + a_s n_{1D}(z)], \tag{1.71}$$

$$E_{\text{int}} = \hbar\omega_\perp \times a_s n_{1D}(z), \tag{1.72}$$

to the first order in $a_s n_{1D}$. For a peak linear density of 30 atoms/μm such as in our condensate before they are split, $a_s n_{1D}(0) = 0.16$, meaning that interactions are responsible by a $\sim$7 % increase of the transverse radius and a 14 % increase of the transverse energy compared to the non-interacting ground state. Transversely, the interaction energy amounts for about 10 % of the total energy. The correction is even weaker after splitting, when the linear density is divided by two.

This justifies why, when the motion of the condensate is excited along one transverse direction only, it is fair to assume that it does not strongly couple to the other transverse directions and to resort to one-dimensional GPE simulations along this direction. In appendix A, we explain how we compute the corresponding effective transverse interaction constant.

1.2 Bose-Einstein Condensate in a Double Well: Two-Mode Theory of the Bosonic Josephson Junction

The aim of this section is to provide the basic theoretical tools to describe the physics of a Bose-Einstein condensate in a double-well potential. Such a *bosonic Josephson junction* (BJJ), consisting of two superfluids weakly tunnel-coupled through a thin potential barrier shows strong similarities with a superconducting Josephson junctions [19, 20]. In this section, we will first introduce the two-mode approximation which allow to simplify the many-body description of an interacting condensate in the double well to a two-sites Bose-Hubbard (BH) model. We will see that within the two-mode approximation, all observables can be computed numerically. We will present the two conjugated macroscopic observables—number difference and relative phase—describing the state of the BJJ and compute their fluctuations in different regimes. We will eventually introduce a mean-field picture which is valid in the limit of large atom numbers and which allows describing the dynamics of the BJJ by mapping it to that of a single fictitious particle.

It is interesting to note that many results presented in this chapter hold for other types of two-mode systems, such as a condensate in a superposition of two internal states (*internal* BJJ, in contrast to the *external* BJJ in a double well), as implemented and studied in Refs. [21, 22]. A comprehensive topical review of the two-mode theory of the BJJ can be found in [23].

1.2.1 Two-Mode Approximation

A natural approximation to describe an ensemble of atoms in a double-well potential is to restrict its wavefunction to a superposition of two static, localized spatial modes, from now on referred to as *left* and *right* mode $\phi_{L,R}(\vec{r})$. This has the effect of limiting the dimension of the Hilbert space which contains all the possible states of the BJJ to 2^N. Furthermore, we will see that if we assume that the particles cannot be distinguished, as in a BEC, the dimension of the Hilbert space is $N+1$, allowing exact calculations even for realistic atom numbers $N \sim 1000$ such as in the experiments presented in this thesis.

In a symmetric double-well potential, the two modes can be built as a linear combination of the ground and the first excited state (see Fig. 1.4):

$$\phi_L = \frac{\phi_g + \phi_e}{\sqrt{2}} \tag{1.73}$$

$$\phi_R = \frac{\phi_g - \phi_e}{\sqrt{2}} \tag{1.74}$$

In a single-particle picture, we can use the two lowest-energy solutions of the Schrödinger equation in the double-well potential:

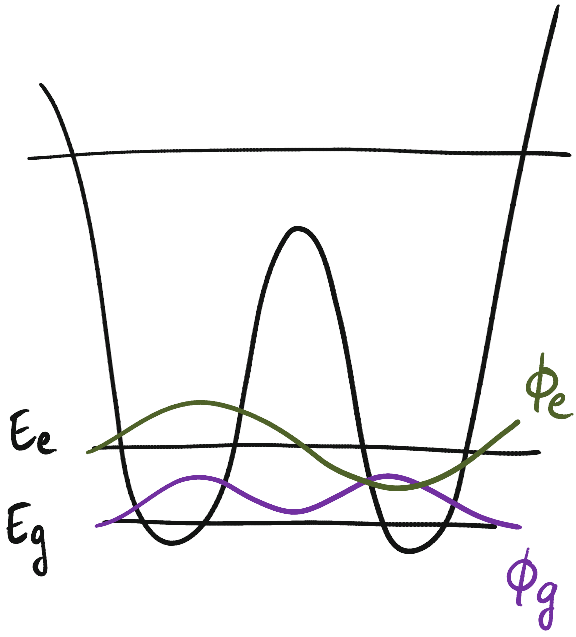

Fig. 1.4 Two-mode approximation. Typical level structure in a symmetric double-well potential. Provided all the energy scales (energy, chemical potential, temperature) are small with respect to the energy of the higher excited states, the dynamics of the system can be restricted to the the two lowest energy levels E_g and E_e. The *left* and *right modes* can be constructed from the ground state (ϕ_g, symmetric) and first excited state (ϕ_e) wavefunctions

$$\hat{h}^{(1)}\phi_{g,e} = E_{g,e}\phi_{g,e}. \tag{1.75}$$

Since $\phi_{L,R}$ are not eigenstates of the system, an atom prepared in one of these two modes will oscillate between left and right at the angular Rabi frequency $\Omega_{\text{Rabi}} = (E_e - E_g)/\hbar$ [24].

For an interacting system, the definition of the spatial modes is less obvious: first, it is not possible to assume static spatial modes since their shape will depend on their occupation. This will be addressed in more detail in Chap. 4. A possible choice is to take the two first stationary solutions of the GPEs.[5] They correspond to a situations where all the atoms are in the ground (respectively the first excited) state. In principle, this choice is not critical as long as the interactions do not significantly modify the spatial modes. As discussed in Sect. 1.1.3.3, this is likely to be a good approximation in the case of elongated double-well potentials.

Secondly, as time evolves, a linear superposition of ground and excited state will not remain in the subspace spanned by ϕ_g and ϕ_e. Still, it is reasonable to restrict the dynamics to the two lowest-lying states as long as no higher-energy state is accessible. This will typically be true as long as the temperature and the energy scale associated with interactions are lower than the energy spacing to the second excited state (see Fig. 1.4).

In an asymmetric double well, there is no general way of defining two localized modes. If the two lowest energy eigenstates are localized each in a different well, it

[5] Which can be readily computed numerically knowing the potential.

seems reasonable to define label them as $\phi_{L,R}$, meaning that in this case, no tunneling will spontaneously occur when the system is initialized in one mode.

In any case, we will derive a two-mode model (2MM) without assumption on the nature of the two modes, and show that all the parameters of the models can be expressed as functions of the spatial modes $\phi_{L,R}(\vec{r})$.

1.2.2 Two-Mode Bose-Hubbard Hamiltonian

1.2.2.1 Derivation from the Full Many-Body Hamiltonian

We want to derive a full many-body description assuming that the atoms can only populate two arbitrary *static* modes. We start from the Hamiltonian (1.24) and follow the derivation presented for example in Refs. [25–28] (double-well potential) or [29, 30] (internal states). An excellent presentation of the model can be found in the topical review by Gati et al. [31].

The first step consists in writing the field operator as a superposition of the left and right modes only[6]:

$$\Psi(\vec{r}) = \phi_L(\vec{r})\, a_L + \phi_R(\vec{r})\, a_R. \tag{1.76}$$

We assume without loss of generality that ϕ_L and ϕ_R are real functions. Here again, we omit the hats on the operators a_L and a_R. They obey the bosonic commutation relations:

$$[a_L, a_R] = 0,\ [a_L^\dagger, a_R^\dagger] = 0,\ [a_L, a_L^\dagger] = [a_R, a_R^\dagger] = 1 \tag{1.77}$$

Following Ref. [25], we insert Eq. (1.76) into the Hamiltonian (1.24) and reorder the terms using the number operators $n_i = a_i^\dagger a_i$

$$\begin{aligned}\hat{H}_{2M} = {} & E_L^0 n_L + E_R^0 n_R + \frac{1}{2} I^{(4,0)}\, n_L\,(n_L - 1) + \frac{1}{2} I_{(0,4)}\, n_R\,(n_R - 1) \\ & - J\left(a_L^\dagger a_R + a_R^\dagger a_L\right) \\ & - I^{(3,1)}\, a_L^\dagger a_R - I^{(1,3)}\, a_R^\dagger a_L + I^{(3,1)}\, n_L\left(a_L^\dagger a_R + a_R^\dagger a_L\right) + I^{(1,3)}\, n_R\left(a_L^\dagger a_R + a_R^\dagger a_L\right) \\ & + 2I^{(2,2)}\, n_L n_R + \frac{1}{2} I^{(2,2)}\left(a_L^\dagger a_L^\dagger a_R a_R + a_R^\dagger a_R^\dagger a_L a_L\right)\end{aligned} \tag{1.78}$$

where E_i^0 is the sum of the mean kinetic and potential energy in the mode i and $I^{(i,j)} = g_{3D} \int \phi_L^i \phi_R^j \mathrm{d}\vec{r}$. Note that each term of the Hamiltonian conserves the total atom number $N = n_L + n_R$. The first line corresponds to the total energy of the left

[6]Note that although the modes are labeled left and right, we don't need at this stage to assume that they are localized.

and right modes, including interactions. The second line describes the tunneling of one particle between the two modes, with the coupling strength:

$$J = -\int \mathrm{d}\vec{r}\left(\frac{\hbar^2}{2m}\nabla\phi_L\nabla\phi_R + \phi_L V\phi_R\right). \tag{1.79}$$

J does not explicitly depend on the interaction strength g_{3D}, but the wavefunctions ϕ_L and ϕ_R usually do. The minus sign is chosen such that J is positive, as will appear below.

The last two lines correspond to interaction-induced transfers of particle between the two modes. In Ref. [28], the authors derived a consistent "improved" two-mode description of the BJJ where they retained all these terms, showing that they could be responsible for significant deviations from the "standard" 2MM generally used in literature. Here we motivate why we can generally neglect these terms. However, it is useful to take them into account to make quantitative predictions over the BJJ (see Sect. 1.2.5.4).

To compare the magnitude of the different terms responsible for particle transfer, we can approximate the double-well potential by two harmonic potentials of frequency ω_0 centered in $\pm x_0$ (see Fig. 1.5) [25]. For simplicity, we treat the problem in one dimension with the effective interaction parameter g in the direction of the double well. We define the left and right mode as the two non-interacting Gaussian ground states centered at $\pm x_0$. The integrals in (1.78) and (1.79) can be perfomed and we find [25]

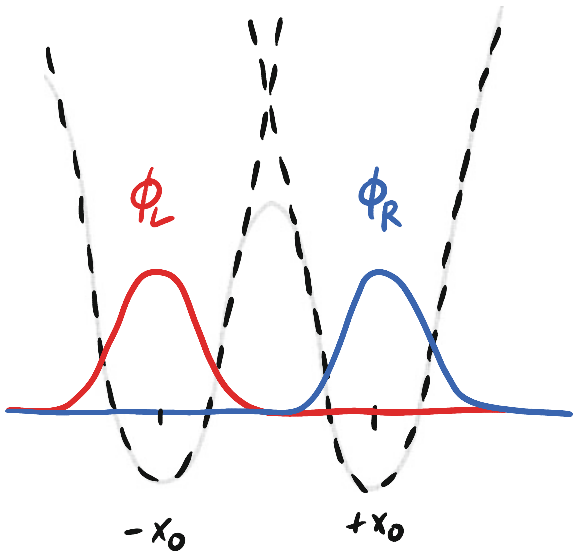

Fig. 1.5 Double well in the harmonic approximation. When the separation is large enough, the double-well potential can usually be approximated by two harmonic potentials, which yields analytical expressions for the tunneling term and the interaction-induced transfer terms

$$J = \frac{\hbar\omega_0}{2}\left(\frac{x_0^2}{a_{\text{ho}}^2} - 1\right) e^{-x_0^2/a_{\text{ho}}^2}, \tag{1.80}$$

$$I^{(1,3)} = I^{(3,1)} = \frac{g}{\sqrt{2\pi}a_{\text{ho}}} e^{-(3/2)\,x_0^2/a_{\text{ho}}^2}, \tag{1.81}$$

$$I^{(2,2)} = \frac{g}{\sqrt{2\pi}a_{\text{ho}}} e^{-2x_0^2/a_{\text{ho}}^2}, \tag{1.82}$$

where $a_{\text{ho}} = \sqrt{\hbar/(m\omega_0)}$ is the the harmonic oscillator length. From this we see that the ratio between the tunnel coupling term and the (dominant) term responsible for interactions-induced particle transfer scales as:

$$\frac{J}{I^{(1,3)}} \propto \frac{\hbar\omega_0 a_{\text{ho}}}{g} e^{x_0^2/2a_{\text{ho}}^2}. \tag{1.83}$$

We find that interaction-induced particle transfer is negligible as long as the kinetic energy dominates over the interaction energy in the direction of the double well, which is precisely one of the condition of validity of the two-mode approximation. Moreover, as discussed in Sect. 1.1.3.3, this condition is generally satisfied for the elongated double-well potentials used in this thesis. Additionally, Eq. (1.80) shows that the tunnel coupling strength J is positive for a large enough x_0 and exhibits a Gaussian decay as a function of the well spacing x_0 on the length scale of the condensate wavefunctions. In practice, the exact dependence of J will depend on the geometry of the barrier, but this scaling has to be kept in mind to evaluate how much the tunneling properties depend on the tuning of the double-well parameters (see Sect. 3.4.4).

Neglecting the interaction-induced transfer terms from the Hamiltonian (1.78) we obtain the two-mode Bose-Hubbard Hamiltonian

$$\begin{aligned}\hat{H}_{\text{BH}} = &- J\left(a_L^\dagger a_R + a_R^\dagger a_L\right) + \frac{\Delta}{2}\left(n_L - n_R\right) \\ &+ \frac{U_L}{2}\left[n_L\left(n_L - 1\right)\right] + \frac{U_R}{2}\left[n_R\left(n_R - 1\right)\right],\end{aligned} \tag{1.84}$$

where

$$\Delta = E_L^0 - E_R^0, \tag{1.85}$$

$$U_{L,R} = g_{3\text{D}} \int \phi_{L,R}^4 \mathrm{d}\vec{r}. \tag{1.86}$$

Figure 1.6 displays a sketch of condensate in the double well and summarizes the parameters of the two-mode Bose-Hubbard Hamiltonian.

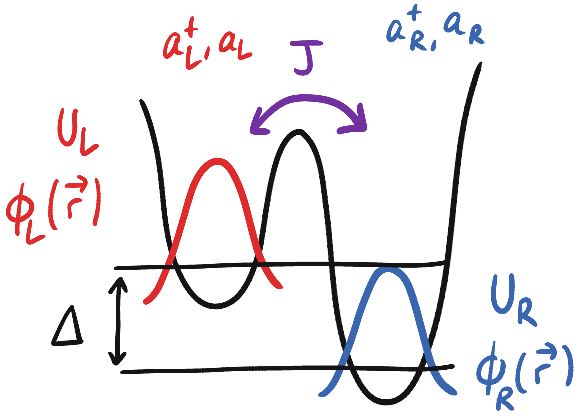

Fig. 1.6 Schematics and notations for the 2-mode BH model. The two sites are denoted *left* and *right*, and are associated to the corresponding bosonic operators $a_{L,R}$ and $a_{L,R}^\dagger$. $\phi_{L,R}$ are the wavefunctions associated to the *left* and *right* mode (we assume that they do not depend on the occupation of the modes). J represents the strength of tunnel coupling, U_L and U_R are proportional to the interaction energies in each site. Δ is the zero-point energy difference between the two wells

1.2.2.2 Link Between $U_{L,R}$ and the Chemical Potential

From the definition (1.30), it is clear that the terms in factor of U_L and U_R correspond to the interaction energies in each mode. In the limit where $J = 0$, we can take ϕ_L and ϕ_R as the ground state of the GPE (1.32) in each well, with the corresponding chemical potentials:

$$\frac{\hbar^2}{2m}\int \nabla\phi_{L,R}^2 \mathrm{d}\vec{r} + \int V(\vec{r})\phi_{L,R}^2 \mathrm{d}\vec{r} + g_{3\mathrm{D}} N_{L,R} \int \phi_{L,R}^4 \mathrm{d}\vec{r} = \mu_{L,R}. \tag{1.87}$$

Neglecting the implicit dependence of the mode wavefunctions with the atom number, we have

$$U_{L,R} \approx \left.\frac{\partial\mu}{\partial N}\right|_{N=N_{L,R}}. \tag{1.88}$$

The interaction constant is equal to the derivative of the chemical potential with respect to the atom number, evaluated for each mode. The meaning of this expression will become clearer in Sect. 3.5.2.

1.2.2.3 Diagonalization in the Basis of Fock States

Since the BH Hamiltonian (1.84) conserves the total atom number N, a natural basis to describe the wavefunction is that of the *Fock states*, containing a well-defined

number of atoms in each mode:

$$\{|N_L = 0, N_R = N\rangle, |1, N-1\rangle \ \ldots \ |N, 0\rangle\}\,. \tag{1.89}$$

It spans a Hilbert space of dimension $N + 1$. This means that withing the two-mode approximation, the full many-body problem can be solved exactly for reasonable total atom numbers (such as $N \sim 1200$ for the experiments carried out in this thesis). All operators can be written as simple $(N + 1) \times (N + 1)$ matrices on this basis (see [31] for details). For example, the tunneling operator reads

$$a_L^\dagger a_R + a_R^\dagger a_L = \begin{pmatrix} 0 & \sqrt{N} & 0 & \cdots & 0 \\ \sqrt{N} & 0 & \sqrt{2\,(N-1)} & \cdots & \vdots \\ 0 & \sqrt{2\,(N-1)} & \ddots & \ddots & \vdots \\ 0 & 0 & \ddots & \ddots & \sqrt{N} \\ 0 & 0 & \cdots & \sqrt{N} & 0 \end{pmatrix}. \tag{1.90}$$

The full Hamiltonian can be diagonalized numerically [25, 31]. A typical spectrum is represented in Fig. 1.7, as well as some of the corresponding eigenstates (Fig. 1.8). It is linear at low energy (like the spectrum of a harmonic oscillator) and quadratic at high energy, where the levels are pairwise (almost) degenerate, corresponding to localized states where most of the atoms are either in the left well or in the right well.

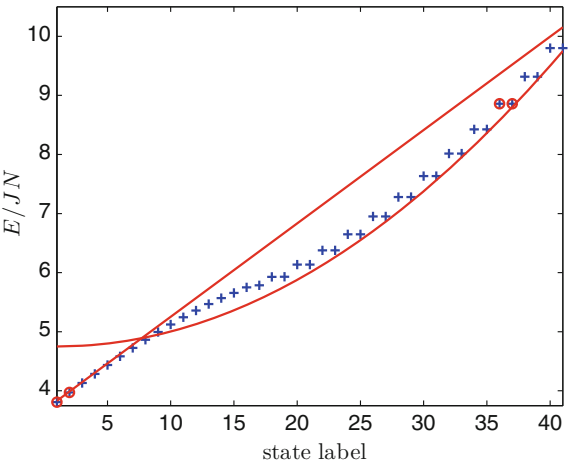

Fig. 1.7 Typical energy spectrum of the two-mode BH Hamiltonian. N = 41 atoms, $\gamma = U/2J = 0.25$ (Josephson regime, see Sect. 1.2.3.2). *Crosses* Energy of the eigenstates in increasing order. *Continuous Lines* approximate expressions in the low energy (*linear*) part and in the high energy (*quadratic part*) of the spectrum. The states surrounded by a *circle* are represented on Fig. 1.8

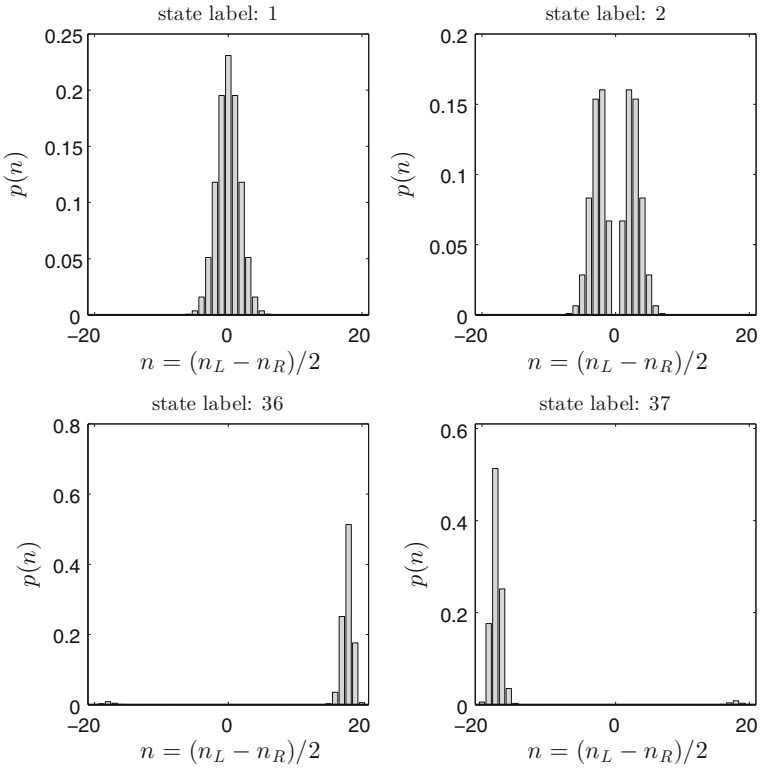

Fig. 1.8 Four eigenstates of the two-mode BH Hamiltonian in number distribution. N = 40 atoms, $\gamma = U/2J = 0.25$. Probability distribution of the half number imbalance $n = (n_L - n_R)/2$ for four eigenstates of the Hamiltonian (1.112). The four eigenstates corresponds to the red circles on Fig. 1.7. Note that the low energy states (linear part of the spectrum) are localized around $n = 0$ while the high energy state are localized pairwise in the *left* or the *right* well

1.2.2.4 Time Evolution

Using the eigenstates $|\psi_i\rangle$ of the Hamiltonian and the corresponding energies E_i, the state of the BJJ can be computed at any time from its initial state $|\Psi(0)\rangle$ through the linear evolution[7]

[7]Note that in the many-body picture of the BH model, the evolution of the $N + 1$-dimensional vector representing the state of the BJJ obeys the linear Schrödinger equation, even in presence of interactions. This is different from the mean-field picture, where the interactions act as a non-linear term in the GPE.

$$|\Psi(t)\rangle = \sum_{i=1}^{N+1} \langle \psi_i \, |\Psi(0)\rangle e^{-iE_i t/\hbar} \, |\psi_i\rangle \, . \tag{1.91}$$

Equivalently, the time evolution of any operator $\hat{A}$ built using the creation and annihilation operators in the left and right mode can be computed from the Heisenberg equation of motion

$$i\hbar \frac{\partial \hat{A}}{\partial t} = -\left[\hat{H}, \hat{A}\right]. \tag{1.92}$$

We will use this result in Sect. 1.2.4.3 to compute the dynamics of the full many-body wavefunction and the physical observables.

1.2.2.5 Macroscopic Observables

In the two-mode approximation, the state of the condensate is characterized by two key observables, similar to a position and a momentum variable: the *population imbalance* and the *relative phase*. As we will see in Sect. 3.2, our setup allows accessing both observables experimentally.

Number Difference

The corresponding observable is defined as the half-number difference operator:

$$\hat{n} \equiv \frac{n_L - n_R}{2} \tag{1.93}$$

which is diagonal in the Fock basis, with eigenvalues ranging from $-N/2$ (all atoms in the left well) to $N/2$ (all atoms in the right well).[8] We can label the Fock states using the eigenvalues of $\hat{n}$

$$|n\rangle \equiv \left| \frac{N}{2} - n, \frac{N}{2} + n \right\rangle. \tag{1.94}$$

[8]The choice of the factor 1/2 is motivated by the fact that conversely to $N_L - N_R$, n is incremented or decremented by 1 when an atom tunnels from one well to the other.

Relative Phase

Defining an operator for the phase difference between left and right is less obvious. This relates to the more general problem of defining a phase operator in quantum mechanics. For a historical (and entertaining) discussion on this topic, see Ref. [32]. Considering for example a single mode of the electromagnetic field, it seems natural to define a Hermitian phase operator $\hat{\phi}$ such that:

$$a = \sqrt{\hat{N}} e^{i\hat{\phi}}, \tag{1.95}$$

$$a^\dagger = e^{-i\hat{\phi}} \sqrt{\hat{N}}. \tag{1.96}$$

Here $\hat{N} = a^\dagger a$ The commutation relation $\left[a, a^\dagger\right] = 1$ imposes that $\hat{\phi}$ would verify the **Lerner criterion**:

$$\left[e^{i\hat{\phi}}, \hat{N}\right] = e^{i\hat{\phi}} \tag{1.97}$$

or the commutation relation proposed by Dirac [33]

$$\left[\hat{\phi}, \hat{N}\right] = i. \tag{1.98}$$

However, this leads to a contradiction: to ensure (1.98), the matrix elements of $\hat{\phi}$ in the basis of Fock states would have to verify:

$$(m - n) \langle n| \hat{\phi} |m\rangle = i\delta_{m,n} \tag{1.99}$$

which doesn't make sense. Furthermore, the commutation relation (1.98) would imply the uncertainty product $\Delta\hat{N}\Delta\hat{\phi} \geq 1/2$, which would impose that $\Delta\hat{\phi} \to \infty$ when $\Delta\hat{N} \to 0$, which is not obvious as the phase is defined on $[-\pi, \pi]$.

It is therefore difficult to rigorously define a phase operator. Still, it is possible to define operators for periodic functions of the phase such as $e^{i\phi}$ or the quadratures $\cos\phi$ and $\sin\phi$ [34, 35].

While the notion of the phase of a single mode of the electromagnetic field, or that of a single Bose-Einstein condensate, remains a delicate question, the experiments in matter-wave interferometry with BECs since the work by Andrews et al. [36] have allowed probing the relative phase between two condensates [37]. They have also shown that in practice, one always measure a quadrature of the phase.

We can try to give a theoretical description of the relative phase between the two modes of the field, following the work by Paraoanu et al. [38], based on the *phase states* defined by Pegg and Barnett [39]

$$\left|\phi_p\right\rangle = \frac{1}{\sqrt{N+1}} \sum_{n=-N/2}^{N/2} e^{-in\phi_p} \left|n\right\rangle . \tag{1.100}$$

They are only defined for discrete values of the phase $\phi_p = 2\pi p/(N+1)$, $p = -N/2, \ldots, N/2$. Note that when $N \to \infty$, we recover a continuous phase over $[-\pi, \pi]$. The $\left\{\left|\phi_p\right\rangle\right\}$ form a complete basis of the Hilbert space. The probability distribution of the phase for any state $\Psi = \sum_n c_n \left|n\right\rangle$ is given by the modulus of the discrete Fourier transform of Ψ

$$p\left(\phi_p\right) = \left|\left\langle\phi_p\right| \Psi\rangle\right|^2 = \frac{1}{N+1} \left| \sum_{n=-N/2}^{N/2} e^{in\phi_p} c_n \right|^2 . \tag{1.101}$$

Note that in the continous limit ($N \to \infty$), we can replace the discrete sums on number or phase states by integrals

$$\begin{aligned} \sum_{n=-N/2}^{N/2} \ldots \left|n\right\rangle &\longrightarrow \int_{-\infty}^{\infty} \mathrm{d}n \ldots \left|n\right\rangle , \\ \sum_{p=-N/2}^{N/2} \ldots \left|\phi_p\right\rangle &\longrightarrow \frac{N+1}{2\pi} \int_{-\infty}^{\infty} \mathrm{d}\phi \ldots \left|\phi_p\right\rangle . \end{aligned} \tag{1.102}$$

The phase states can be used to define the **phase exponential operator**

$$\widehat{e^{i\phi}} \equiv \sum_{p=-N/2}^{N/2} e^{i\phi_p} \left|\phi_p\right\rangle\left\langle\phi_p\right| \tag{1.103}$$

which satisfies the Lerner criterion (1.97). Similarly, the quadrature operators are defined by

$$\widehat{\cos\phi} = \frac{1}{2}\left(\widehat{e^{i\phi}} + \widehat{e^{-i\phi}}\right), \tag{1.104}$$

$$\widehat{\sin\phi} = \frac{1}{2i}\left(\widehat{e^{i\phi}} - \widehat{e^{-i\phi}}\right). \tag{1.105}$$

Even if we have not defined an operator for the relative phase that would satisfy

the commutation relation $[\hat{\phi}, \hat{n}]$, let us introduce the phenomenological uncertainty relation between relative phase and half-number difference[9]

$$\Delta\hat{n}\Delta\hat{\phi} \geq \frac{1}{2}. \tag{1.106}$$

In Sect. 1.2.4, we will show that a N-particle two-mode system can be described by an effective spin verifying angular momentum commutation relations. These commutation relations imply uncertainty relations between certain observables and we will motivate they are consistent with the formal uncertainty relation (1.106) when the number and phase spread are small enough. In Sect. 1.2.5, we will present a mean-field model valid in the "continous limit" $N \to \infty$ and show that the half-number difference and the phase are canonical conjugate variables linked by

$$n = -i\frac{\partial}{\partial\phi}. \tag{1.107}$$

which by the correspondence principle also motivates Eq. (1.106).

Physically, the uncertainty relation (1.106) implies that the number difference and the relative phase of the BJJ cannot be measured simultaneously with arbitrary accuracy.

1.2.2.6 Bose-Hubbard Hamiltonian in Number-Phase Representation

There is a link between the tunneling operator and the operator for the cosine of the phase (1.104). In the Fock basis, the matrix elements of the tunneling operator read (see Eq. 1.90)

$$\begin{aligned}\langle m|\, a_L^\dagger a_R + a_R^\dagger a_L\, |n\rangle = &\sqrt{\left(\frac{N}{2}+m\right)\left(\frac{N}{2}-m+1\right)}\delta_{m,n+1} \\ &+\sqrt{\left(\frac{N}{2}-m\right)\left(\frac{N}{2}+m+1\right)}\delta_{m,n-1}\end{aligned} \tag{1.108}$$

while that of the cosine operator read

$$\langle m|\, \widehat{\cos\phi}\, |n\rangle = \frac{1}{2}\left(\delta_{m,n+1}+\delta_{m,n-1}\right). \tag{1.109}$$

We see that for $n, m \ll N/2$, one can identify both operators:

[9]Note that in the following, unless stated, ΔF^2 represents the variance of the quantity F, and ΔF its standard deviation.

$$\langle m|\, a_L^\dagger a_R + a_R^\dagger a_L \,|n\rangle \approx N \,\langle m|\, \widehat{\cos\phi} \,|n\rangle \,. \tag{1.110}$$

Therefore, an approximate expression for the BH Hamiltonian in number-phase representation (dropping a constant energy offset for clarity) is given by

$$\hat{H}_{\mathrm{BH}} \approx -J\sqrt{N^2 - 4\hat{n}^2}\,\widehat{\cos\phi} + U\hat{n}^2 + \epsilon\hat{n} \tag{1.111}$$

with the interaction constant $U \equiv (U_L + U_R)/2$ and the detuning[10] $\epsilon = (U_L - U_R)(N-1)/2 + \Delta$.

The tunneling term takes the form of a Josephson energy, which associates a flow of particles between the two wells to the cosine of the relative phase between the sites. We will see in Sect. 1.2.5.3 that the analogy with the Josephson effect appears even more clearly in the dynamics of number imbalance and phase. The term in factor of U is quadratic in $\hat{n}$ and represents the interactions energy and corresponds to the cost (for repulsive interactions) of putting more atoms on one side than on the other. The linear term is due to the energy difference between the sites caused by the detuning Δ on one hand, and by the difference of $\partial\mu/\partial N$ on the other hand (see Sect. 1.2.2.2).

1.2.3 Regimes of the Two-Mode Bose-Hubbard Model

In the following, we assume a symmetric double well, such that $\Delta = 0$ and $U_L = U_R = U$:

$$\hat{H}_{\mathrm{BH}} = -J\left(a_L^\dagger a_R + a_R^\dagger a_L\right) + \frac{U}{2}\left[n_L\,(n_L - 1) + n_R\,(n_R - 1)\right] \tag{1.112}$$

$$\approx -J\sqrt{N^2 - 4\hat{n}^2}\,\widehat{\cos\phi} + U\hat{n}^2 + \frac{UN}{4}\,(N-2)\,. \tag{1.113}$$

In this case, the properties of the BH Hamiltonian depend only on the atom number N and the dimensionless parameter

$$\gamma \equiv \frac{U}{2J} \tag{1.114}$$

which represents the ratio of the interaction energy per particle over the total tunneling energy.

[10] We distinguish between the difference in zero-point energy Δ and the detuning ϵ which contains also a difference of interaction energy coming for example from different confinement frequencies in the two wells.

1.2.3.1 Two Limiting Cases

It is useful to look at the two limiting cases $U = 0$ and $J = 0$ [27, 40]:

In the Absence of Interactions (U = 0)

In this case, the BH Hamiltonian is diagonal in the basis of the non-interacting ground and first excited states of the double-well potential (see Fig. 1.4):

$$\hat{H} = E_g a_g^\dagger a_g + E_e a_e^\dagger a_e \tag{1.115}$$

and $J = \left(E_e - E_g\right)/2 = \hbar\Omega_{\text{Rabi}}/2$. At zero temperature, the particles all condense in the single-particle ground state ϕ_g. In the basis of the left and right mode, this corresponds to the product state

$$|\Psi\rangle = \frac{1}{\sqrt{N!}}\left(a_L^\dagger + a_R^\dagger\right)^N |0\rangle \tag{1.116}$$

where $|0\rangle$ is the vacuum state. This is an **atomic coherent state** [41], with relative phase 0 (it is clear from Eq. (1.111) that the phase minimizing the energy is 0). In the Fock basis, it reads[11] [27]:

$$|\Psi\rangle = \frac{1}{\sqrt{2^N}} \sum_{n=-N/2}^{N/2} \sqrt{\binom{N}{N/2+n}}\, |n\rangle\,. \tag{1.117}$$

This shows that the (half-)population imbalance of the ground state follows a binomial distribution between $-N/2$ and $N/2$. This has a simple interpretation: in absence of interactions, the ground state (1.116) is a product state of each atom being in a symmetric superposition of left and right mode. When the number imbalance is measured, each atom is independently projected with equal probability either on the left or the right mode, yielding a binomial distribution. In particular, the variance of the half-number difference in the ground state reads:

$$\Delta\hat{n}^2 = \frac{N}{4} \tag{1.118}$$

(or equivalently, the variance of the number difference $\Delta\left(n_L - n_R\right)^2 = N$). The probability distribution of n and ϕ are represented in Fig. 1.9 for a coherent state

[11] We use the binomial coefficients

$$\binom{n}{k} = \frac{n!}{k!(n-k)!}$$

.

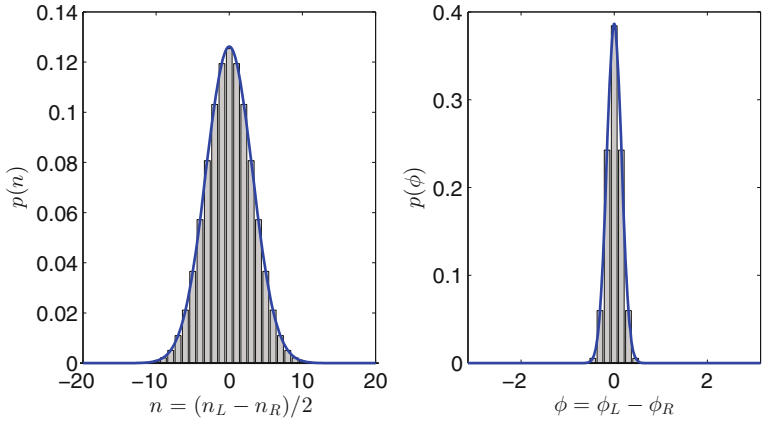

Fig. 1.9 Ground state in absence of interactions. $N = 40$ atoms, $U = 0$. *Grey bars* Histogram of the half-number difference distribution (*left*) and the relative phase distribution (*right*) in the ground state. *Continuous lines* probability distribution in the continous approximation. Note that already for 40 atoms, it matches well the discrete probability distribution

with $N = 40$ atoms. In the limit $N \to \infty$ where $\hat{n}$ and $\hat{\phi}$ have a continuous spectrum, the binomial distributions tend towards normal distributions and the probability distributions for n and the ϕ are given respectively by:

$$p(n) = \frac{1}{\sqrt{2\pi}\sigma_n} e^{-n^2/(2\sigma_n^2)}, \tag{1.119}$$

$$p(\phi) = \frac{1}{\sqrt{2\pi}\sigma_\phi} e^{-n^2/(2\sigma_{\phi^2})}, \tag{1.120}$$

with $\sigma_N^2 = N/4$ and $\sigma_\phi^2 = 1/N$. Note eventually that the coherent state is a **minimum uncertainty state**, i.e. it saturates the Heisenberg uncertainty relation:

$$\Delta n \Delta\phi = \frac{1}{2}. \tag{1.121}$$

In Absence of Tunneling (J = 0)

In this case, the BH Hamiltonian (1.113) is diagonal in the Fock basis and one immediately sees that the state minimizing the energy is the *twin Fock state*[12]

[12] We have assumed an even N. Otherwise, the ground state is

$$\frac{1}{\sqrt{2}} \left(|(N-1)/2, (N+1)/2\rangle + |(N+1)/2, (N-1)/2\rangle\right) \tag{1.122}$$

$$|\Psi\rangle = |n = 0\rangle = |N/2, N/2\rangle \tag{1.123}$$

with well-defined, identical atom number left and right. It has zero number-difference fluctuations, and its phase distribution is uniform (as that of any Fock state), meaning that the phase is completely random. It is a limiting case for the uncertainty relation (1.106), implying infinite variance of the phase (which for a circular variable is to some extent a matter of definition, see below).

1.2.3.2 In-Between: Rabi, Josephson and Fock Regimes

Between these two cases, the regimes of the two-mode Bose Hubbard model can be characterized by looking at the number and phase fluctuations of the ground state (see Fig. 1.10). The number fluctuations are quantified by the variance of the half-number imbalance $\Delta\hat{n}^2$. For the phase distribution, the usual definition of the variance can be extended to angular variables [42]. Here we define the variance of the phase as the square of the **circular standard deviation** S in the state $|\Psi\rangle$

$$\mathrm{S}^2[\phi] = -2\ln\left[\left|\left\langle e^{i\hat{\phi}}\right\rangle\right|\right] = -2\ln\left[\left|\sum_{p=-N/2}^{N/2}\left|\langle\phi_p|\,\Psi\rangle\right|^2 e^{i\phi_p}\right|\right]. \tag{1.124}$$

For a gaussian state, i.e. a state with normally distributed number difference and phase, such as for instance a coherent state with N sufficiently large, we have

$$\int_{-\pi}^{\pi}\cos\phi e^{-\phi^2/2\sigma^2}d\phi \approx e^{-\sigma^2/2}, \tag{1.125}$$

implying that the circular standard deviation coincides with the usual definition of the standard deviation, while that of a Fock state is infinite.

Interestingly, in the case of repulsive interactions, the ground state is always *number-squeezed*, meaning that the half number difference fluctuations in the ground state are always smaller than $\Delta n_{\mathrm{coh}} = \sqrt{N}/2$, and that all the more as $U/2J \to \infty$ [30]. Intuitively, this can be understood by the fact that interactions disfavor number differences, as they are energetically costly. The ground state fluctuations show that three different regimes appear, depending on the the value of γ:

Rabi Regime

As long as

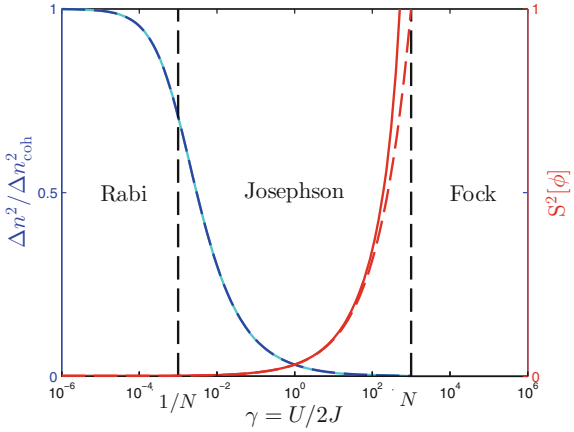

Fig. 1.10 Variance of number and phase difference in the ground state. N = 1000 atoms. *Light blue line* variance of $\hat{n}$, in units of the variance for a coherent state $\Delta n = \sqrt{N}/2$, as a function of $\gamma = U/2J$. *Red line* circular variance $S^2[\phi]$ of the relative phase as a function of γ. The *black vertical dashed lines* correspond respectively to $\gamma = 1/N$ and $\gamma = N$, identifying the Rabi, Josephson and Fock regimes. Note that the harmonic approximation (*red* and *blue dashed lines*) describes extremely well the fluctuations of n and ϕ in the ground state in the Rabi regime and deep into the Josephson regime

$$\frac{U}{2J} \ll \frac{1}{N} \tag{1.126}$$

tunneling dominates over atomic interactions. The physics of the bosonic Josephson junction does not significantly depart from the non-interacting case. The ground state is close to a coherent state with well-defined phase and binomial number difference fluctuations. The many-body spectrum is essentially linear, like that of a harmonic oscillator, with energy levels evenly spaced by the Rabi energy $2J$.

Fock Regime

$$\frac{U}{2J} \gg N \tag{1.127}$$

Conversely, when atomic interactions dominate over tunneling, the ground state exhibits strongly suppressed number difference fluctuations while the phase is almost random. In Ref. [27], an approximate analytical expression for the half-number difference fluctuations in the ground state is derived and reads

$$\Delta\hat{n} = \frac{1}{8\sqrt{2}} \frac{2JN}{U} \ll 1 \tag{1.128}$$

The energy spectrum is essentially quadratic ($\hat{H} \approx U\hat{n}^2$) with pairwise (almost) degenerate states with opposite imbalance ($|N_L, N_R\rangle$, $|N_R, N_L\rangle$, see Fig. 1.8). These states are often said to be fragmented, meaning that they cannot be written as a product of single-particle states.

Josephson Regime

$$\frac{1}{N} \ll \frac{U}{2J} \ll N \tag{1.129}$$

In the intermediate regime, both contributions are comparable and the energy spectrum exhibits both a linear and a quadratic part (see Fig. 1.7). For high energy eigensates, the interaction term dominates in the Hamiltonian

$$\hat{H}_{\mathrm{BH}}^{\mathrm{quad}} \approx U\hat{n}^2 + \frac{UN}{4}(N-2)\,, \tag{1.130}$$

and the energy spectrum is quadratic while at low energy, it is linear. As long as the the low-energy eigenstates have small fluctuations of number-difference and phase (we will check this afterwards), the BH Hamiltonian (1.113) can be linearized and reads

$$\hat{H}_{\mathrm{BH}}^{\mathrm{harm}} = \frac{\hbar\omega_J}{2}\left(\frac{\hat{\phi}^2}{2\sigma_\phi^2} + \frac{\hat{n}^2}{2\sigma_n^2}\right). \tag{1.131}$$

with:

$$\hbar\omega_J = 2J\sqrt{1+\Lambda}, \tag{1.132}$$

$$\sigma_\phi^2 = \frac{\sqrt{1+\Lambda}}{N}, \tag{1.133}$$

$$\sigma_n^2 = \frac{N}{4\sqrt{1+\Lambda}}, \tag{1.134}$$

$$\Lambda = UN/2J. \tag{1.135}$$

We identify the Hamiltonian of a 1D harmonic oscillator where the phase plays the role of the position, and the number difference corresponds to the momentum. The dimensionless parameter $1 \ll \Lambda \ll N^2$ in the Josephson regime represents the ratio between interaction energy and tunneling. The energy scale is given by the Josephson frequency ω_J, which is the frequency of the tunneling oscillations in presence of interactions[13] (see Sect. 1.2.5.3). Equivalently, it is the frequency of the lowest Bogoliubov mode of the bosonic Josephson junction [38]. σ_n^2 and σ_ϕ^2 are respectively

[13] Sometime refereed to as plasma oscillations.

the variance of n and ϕ in the ground state and their product saturates the Heisenberg uncertainty relation (1.106). The fluctuations of n and ϕ in the kth excited state scale as $\sqrt{2\,(k+1/2)}\sigma_{n,\phi}$, their product as $k+1/2$.

Figure 1.7 shows a comparison between the fluctuations of n and ϕ in the ground state computed by the exact numerical diagonalization of (1.112) and the harmonic approximation. This approximation is expected to be valid in the linear part of the energy spectrum, i.e. for state whose energiy is smaller or of the order[14] of JN. This in turn sets a limit to the maximal phase and number spread for which the harmonic approximation is valid

$$\Delta\phi^2 \lesssim 1, \tag{1.136}$$

$$\Delta n^2 \lesssim \frac{N^2}{4\,(1+\Lambda)}. \tag{1.137}$$

The condition on Δn^2 simply tells us that the description of the BJJ as a harmonic oscillator in number and phase difference breaks down when entering the Fock regime. Equivalently, in terms of normalized population imbalance $z = (N_L - N_R)/N$, it reads $\Delta z \lesssim 1/\sqrt{\Lambda+1}$.

1.2.3.3 Link Between Phase Fluctuations and Coherence

The fluctuations of the relative phase can be directly connected to the notion of first-order coherence between the two modes [31, 40]. Provided there is no significant spatial overlap between the two wavefunctions and $n_L \approx n_R$, the first-order coherence function between the left well and the right mode reads

$$\begin{aligned} g^{(1)}(\vec{r}_L,\vec{r}_R) &\equiv \frac{\left\langle \Psi^\dagger(\vec{r}_L)\Psi(\vec{r}_R)\right\rangle}{\sqrt{\left\langle \Psi^\dagger(\vec{r}_L)\Psi(\vec{r}_L)\right\rangle\left\langle \Psi^\dagger(\vec{r}_R)\Psi(\vec{r}_R)\right\rangle}} \\ &\approx \frac{\langle a_L^\dagger a_R + a_R^\dagger a_L\rangle}{N} \\ &\approx \langle\cos\hat{\phi}\rangle. \end{aligned} \tag{1.138}$$

From the definition of the circular standard deviation (1.124) and assuming a symmetric phase distribution,

[14] More precisely, when N is sufficiently large, as it is always the case in our experiments, the crossover energy between the linear and the quadratic part of the spectrum (see Fig. 1.7) occurs between $0.07 \times JN$ ($\Lambda = 1$) and $2 \times JN$ ($\Lambda = N^2$), where the origin of the energies is set to the ground state energy minus $\hbar\omega_J/2$, like in a harmonic oscillator.

$$\begin{aligned} S^2[\phi] &= -2\ln\left(\left\langle\widehat{\cos\phi}\right\rangle\right) \\ &\approx -2\ln\left[g^{(1)}(\vec{r}_L,\vec{r}_R)\right] \end{aligned} \tag{1.139}$$

$\langle\cos\phi\rangle$ is often called the **coherence factor**. It measures the visibility of the average of interference fringes obtained by matter wave interferometry .

1.2.4 Collective Spin Representation

In this section, we will introduce the concept of a collective spin mapped to an ensemble of two-level atoms. We will show the link between the uncertainty product of n and ϕ and the commutation relations for an angular momentum operator. We will see that the collective spin is a useful tool to study and visualize many-body states of the BJJ and introduce the concept of atomic squeezed states. A comprehensive introduction to the notion of collective spins and spin squeezing, particularly in the context of atom interferometry is given in the tutorial by Gross [43].

1.2.4.1 Collective Spin Associated to an Ensemble of Atoms

Spin 1/2 Associated to a Single Two-Level System

A single two-level system can associated to a fictitious spin 1/2 $\hat{\vec{s}}$ [44]. Considering an atom in a double-well potential, the left and right modes can be mapped onto the two eigenstates of $\hat{s}_z$ with eigenvalues respectively $\pm 1/2$. Any coherent superposition of the two modes

$$|\psi\rangle = \cos\frac{\theta}{2}e^{-i\phi/2}|L\rangle + \sin\frac{\theta}{2}e^{i\phi/2}|R\rangle \tag{1.140}$$

can be represented as a point on the **Bloch sphere** (see Fig. 1.11).

The effect of a linear Hamiltonian $\hat{H}$ acting on the two-level system can be represented by an effective external magnetic field $\vec{B}$ the spin is coupled to

$$\hat{H} \propto \vec{B}\cdot\hat{\vec{s}} = B_x\hat{s}_x + B_y\hat{s}_y + B_z\hat{s}_z. \tag{1.141}$$

Collective Spin N⁄2 for N Identical Two-Level Systems

Similarly, an ensemble of N identical two-level systems can be associated with the collective spin $N/2$

$$\hat{\vec{S}} = \sum_{i=1}^{N} \hat{\vec{s}}^{(i)}, \tag{1.142}$$

The connection to a two-mode many-body system in the formalism of second quantization has been established by Schwinger [45, 46]. When all operations done on the spin ensemble act on each spin in the same way, the full Hilbert space of dimension 2^N can be reduced to the $(N+1)$-dimensional subspace corresponding to $\hat{S}^2 = (N/2)(N/2+1)$ [43]. The spin components read[15]

$$\hat{S}_x = \frac{1}{2}\left(a_L^\dagger a_R + a_R^\dagger a_R\right), \tag{1.143}$$

$$\hat{S}_y = \frac{1}{2i}\left(a_R^\dagger a_L - a_L^\dagger a_R\right), \tag{1.144}$$

$$\hat{S}_z = \frac{1}{2}\left(a_L^\dagger a_L - a_R^\dagger a_R\right). \tag{1.145}$$

Importantly, they obey the circular commutation relations for angular momentum operators[16]

$$\left[\hat{S}_k, \hat{S}_l\right] = i\epsilon_{klm}\hat{S}_m, \tag{1.146}$$

and must therefore satisfy the corresponding uncertainty relations

$$\Delta\hat{S}_k \Delta\hat{S}_l \geq \frac{1}{2}\left|\left\langle \hat{S}_m \right\rangle\right|. \tag{1.147}$$

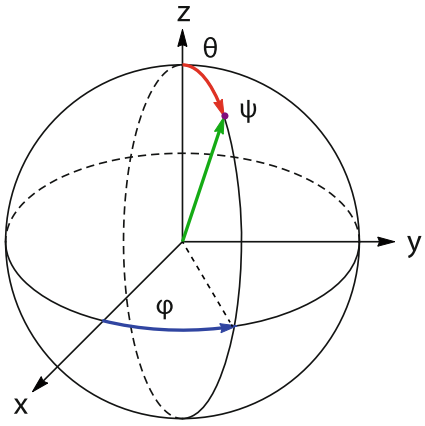

Fig. 1.11 Bloch sphere The *north* and *south poles* correspond respectively to $|L\rangle$ and $|R\rangle$. The latitude is proportional to the probability of measuring the atom in the *left* or the *right* mode, and the angle ϕ of the projection onto the equatorial plane corresponds to the phase of the quantum superposition

[15] We chose to denote the spin components $\hat{S}_i$ to avoid confusions with the coupling energy J.

[16] ϵ_{klm} denotes the Levi-Civita symbol.

N-particle spin states can be visualized employing the Husimi Q-representation on a generalized Bloch sphere [43, 47] (see Fig. 1.12).

1.2.4.2 How Do We Recover the Number-Phase Representation?

The spin picture, through the circular uncertainty relations (Eq. 1.146) between the components of the spin, contains all the uncertainty relations between the physical observables. How does it relate to the number-phase representation introduced in Sect. 1.2.2.5? First, $\hat{n} = \hat{S}_z$. The basis of Dicke states and the Fock basis are exactly the same (the Dicke state with the eigenvalue n for $\hat{S}_z$ coincides with the Fock state $|n\rangle$).

The link to the phase is less straightforward. Let us first note that S_x is equal to the tunneling operator (1.90). For a state which is well-localized around a given position on the Bloch sphere,[17] such as that of Fig. 1.12, we see from Eqs. (1.108) to (1.109) that the phase quadrature operators are approximately given by

$$\hat{S}_x \approx \frac{1}{2}\sqrt{N^2 - 4\left\langle\hat{n}\right\rangle^2}\widehat{\cos\phi}, \tag{1.148}$$

$$\hat{S}_y \approx \frac{1}{2}\sqrt{N^2 - 4\left\langle\hat{n}\right\rangle^2}\widehat{\sin\phi}. \tag{1.149}$$

As in the single particle case, the relative phase corresponds to the angle of the projection of the spin onto the equatorial plane with respect to the x axis.

The link to the phase-number uncertainty can be established (at least formally) if we take such a localized spin state and linearize $\langle\Delta\widehat{\cos\phi}\rangle^2$ and $\langle\Delta\widehat{\sin\phi}\rangle^2$ close to the mean orientation of the spin, we can write

$$\begin{aligned}
\Delta\hat{S}_z\left(\Delta\hat{S}_x + \Delta\hat{S}_y\right) &\geq \frac{1}{2}\left(\left|\langle\hat{S}_x\rangle\right| + \left|\langle\hat{S}_y\rangle\right|\right) \\
\Leftrightarrow \frac{1}{2}\sqrt{N^2 - 4\langle n\rangle^2}\Delta\hat{n}\left(\left|\langle\widehat{\sin\phi}\rangle\right|\Delta\phi + \left|\langle\widehat{\cos\phi}\rangle\right|\Delta\phi\right) &\geq \frac{1}{4}\sqrt{N^2 - 4\left\langle\hat{n}\right\rangle^2}\left(\left|\langle\widehat{\cos\phi}\rangle\right| + \left|\langle\widehat{\sin\phi}\rangle\right|\right) \\
\Leftrightarrow \Delta n\Delta\phi &\geq \frac{1}{2}.
\end{aligned} \tag{1.150}$$

This has a simple geometrical interpretation: when the spin state is well-localized, it is sufficient to consider its immediate vicinity on the generalized Bloch sphere and the problem can be reduced from a 3D representation to a 2D representation on the plane tangent to the mean orientation of the spin. The projection of the state in this plane can be described by only two conjugated observables, for example $\hat{n}$ and $\hat{\phi}$, verifying the uncertainty relation (1.106). But strictly speaking, only the commutation relations and the uncertainty products for the spin components are well-defined.

[17] For example, a coherent state with N large enough, see Sect. 1.2.4.4.

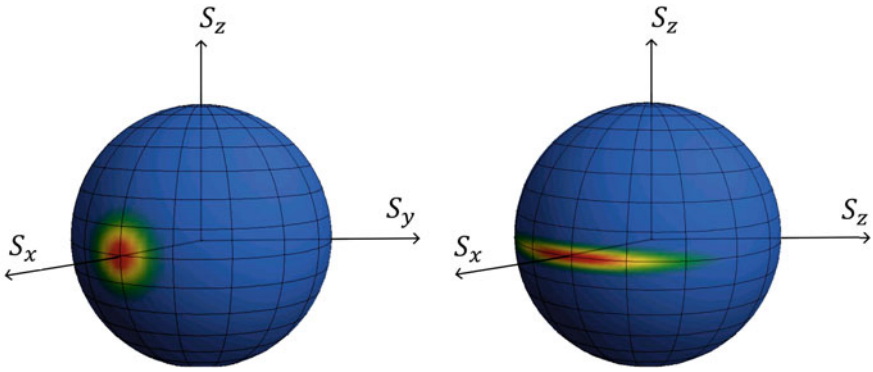

Fig. 1.12 Spin states on the generalized Bloch sphere. Adapted from http://www.stanford.edu/group/kasevich/cgi-bin/wordpress/?page_id=57. N-particle collective spins can be visualized as a density distribution on a generalized Bloch sphere of radius $N/2$. The fuziness of the *red spot* represents the uncertainty on the different spin components. *Left* coherent state. *Right* number-squeezed state (Color figure online)

1.2.4.3 Bose-Hubbard Hamiltonian in Spin Representation

In spin representation, the BH Hamiltonian (1.84) reads

$$\hat{H}_{BH} = -2J\hat{S}_x + \epsilon\hat{S}_z + U\hat{S}_z^2 \tag{1.151}$$

(a constant energy offset has been dropped). The time evolution of an arbitrary state $|\psi\rangle$ under this Hamiltonian follows

$$|\psi(t+dt)\rangle = e^{i\left(2J\hat{S}_x - \epsilon\hat{S}_z - U\hat{S}_z^2\right)dt/\hbar}\,|\psi(t)\rangle\,. \tag{1.152}$$

The tunneling term can therefore be seen as a rotation around the x axis of the Bloch sphere[18] at the angular velocity $2J/\hbar$. In the same way, the detuning term represents a rotation around the z axis at the angular velocity $\epsilon/\hbar$. Note however that as soon as both terms are acting, the motion of the collective spin is not a rotation anymore.

The interaction term on the other hand represents a shearing transformation. It can be seen as a rotation around the z axis, but with an angular velocity $\sim Un/\hbar$ depending on the latitude on the Bloch sphere.

The time evolution of the spin components is obtained from the Heisenberg equation of motion (1.92), making use of the commutation relations (1.146). It yields the three equations [25]

[18] A rotation of angle θ around the i axis reads $R_i(\theta) = e^{-i\theta\hat{S}_i}$.

$$\frac{\mathrm{d}\hat{S}_x}{\mathrm{d}t} = -\frac{\epsilon}{\hbar}\hat{S}_y - \frac{U}{\hbar}\left(\hat{S}_y\hat{S}_z + \hat{S}_z\hat{S}_y\right), \tag{1.153}$$

$$\frac{\mathrm{d}\hat{S}_y}{\mathrm{d}t} = \frac{2J}{\hbar}\hat{S}_z + \frac{\epsilon}{\hbar}\hat{S}_x + \frac{U}{\hbar}\left(\hat{S}_x\hat{S}_z + \hat{S}_z\hat{S}_x\right), \tag{1.154}$$

$$\frac{\mathrm{d}\hat{S}_z}{\mathrm{d}t} = -\frac{2J}{\hbar}\hat{S}_y. \tag{1.155}$$

They will be used in Sect. 1.2.5.3 to compute the time evolution of the macroscopic observables n and ϕ in the classical limit.

1.2.4.4 Some Many-Body States in the Spin Representation

The spin representation is a convenient tool to study and visualize many-body states of the bosonic Josephson junction. Two types of states are particularly relevant for the work presented in this thesis:

Coherent Spin States (CSS)

CSS are product states obtained from putting all the atoms in the same superposition of the two modes [41]

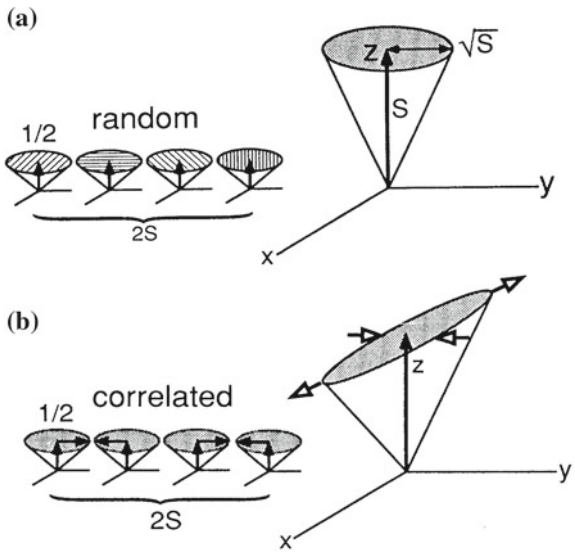

Fig. 1.13 Schematic illustration of a collective spin. Taken from Kitagawa et al. [48]. **a** Coherent spin state constructed from $2S$ uncorrelated spin 1/2. **b** Squeezed state constructed from $2S$ correlated spin 1/2

$$|\theta, \phi\rangle_{\text{coh}} = \frac{1}{\sqrt{N!}} \left(\cos\frac{\theta}{2} e^{-i\phi/2} a_L^\dagger + \sin\frac{\theta}{2} e^{i\phi/2} a_R^\dagger \right)^N |\text{vac}\rangle \tag{1.156}$$

($|\text{vac}\rangle$ denotes the vacuum state). The ground state of the BJJ in absence of interactions (see Eq. (1.116)) is a CSS with $\theta = \pi/2$ and $\phi = 0$. Without loss of generality, let us consider $|\pi/2, 0\rangle_{\text{coh}}$. The spin points along x ($\langle \hat{S}_y \rangle = \langle \hat{S}_z \rangle = 0$) with the length $\langle \hat{S}_x \rangle = N/2$. Transversely to the mean spin direction x, the fluctuations are isotropically distributed (see Fig. 1.12, left panel)

$$\Delta \hat{S}_y^2 = \Delta \hat{S}_z^2 = \Delta \hat{S}_\perp^2 = N/4, \tag{1.157}$$

where $\hat{S_\perp} = \cos\alpha \hat{S}_y + \sin\alpha \hat{S}_z$. CSS are miminum uncertainty states saturating the product (1.147)

$$\Delta \hat{S}_y \Delta \hat{S}_z = \frac{1}{2} \left| \langle \hat{S}_x \rangle \right|. \tag{1.158}$$

Figure. 1.13a, taken from Kitagawa et al. [48], illustrates this result: the variance of the orthogonal components of a single spin 1/2 pointing in x direction are given by $\Delta \hat{s}_\perp^2 = 1/4$. Summing up N such uncorrelated spins, the variances simply add up to $N/4$. CSS are minimum uncertainty states with isotropic fluctuations in the direction orthogonal to the mean spin orientation.

Squeezed States

In 1993, M. Kitagawa and M. Ueda introduced the concept of spin-squezed states to describe states such that the variance of one spin component normal to the mean spin vector is smaller than the standard quantum limit [48]. Such states involve an anisotropical redistribution of the fluctuations of the collective spin, which still has to satisfy the uncertainty relation (1.147). This means that noise reduction for one spin component implies excess noise in another direction.

A state such that $\Delta \hat{S}_z^2 \leq N/4$, or equivalently $\Delta (N_L - N_R)^2 \leq N$, is said to be *number squeezed* (see Fig. 1.12, right panel). The *number squeezing factor*

$$\xi_N \equiv \frac{\Delta \hat{S}_z}{\sqrt{N}/2} = \frac{\Delta (N_L - N_R)}{\sqrt{N}} \tag{1.159}$$

quantifies the amount of number squeezing by comparing the fluctuations of the number difference to that of a coherent state. Number squeezed states are characterized by $\xi_N < 1$. A Fock state for example is perfectly number-squeezed (it can be represented by a circle of latitude on the Bloch sphere). As pointed out by Kitagawa et al. [48], correlations between the atoms are necessary to produce number squeezing (see Fig. 1.13b). However, these correlations can be classical: for example, the state of two condensates produced independently with a given finite number of atoms

(in each condensate) is number-squeezed, although there exists no phase coherence between both.

Importantly, as mentioned in Sect. 1.2.3.2, the ground state of the BH Hamiltonian in presence of repulsive interactions is always number-squeezed (see Fig. 1.10). In the Rabi and the Josephson regimes, the square of the number squeezing factor reads

$$\xi_N^2 = \frac{1}{\sqrt{\Lambda + 1}} \leq 1. \tag{1.160}$$

By extension, one can also define *phase-squeezed states* as states with a phase spread smaller than $1/\sqrt{N}$. They are characterized by the phase squeezing factor

$$\xi_\phi \equiv \frac{\Delta\phi}{1/\sqrt{N}}. \tag{1.161}$$

Because it is saturating the Heisenberg number-phase inequality, the ground state of the two-modes BH Hamiltonian with repulsive interaction is always anti phase-squeezed. In the Josephson and Rabi regimes, it reads

$$\xi_\phi^2 = \sqrt{\Lambda + 1} \geq 1. \tag{1.162}$$

Coherent Spin Squeezed State (CSSS)

In 1994, Wineland et al. defined a particular class of atomic squeezed states characterized by the measure of *useful* (or *coherent*) *spin squeezing* [49]

$$\xi_S = \sqrt{N}\frac{\Delta\hat{S}_{\perp,\min}}{\langle\hat{\vec{S}}\rangle} < 1. \tag{1.163}$$

ξ_S measures the ratio of the minimal fluctuations transversely to the spin mean direction over the spin mean length. In particular, for a spin pointing along x and where the direction of minimal uncertainty is z, this definition translates into

$$\xi_S = \frac{\Delta\hat{n}}{\sqrt{N}/2\widehat{\langle\cos\phi\rangle}} = \frac{\xi_N}{\widehat{\langle\cos\phi\rangle}} \tag{1.164}$$

Not all atomic squeezed states satisfy the definition (1.163), as it requires a high coherence together with suppressed fluctuations of one observable. The Fock states, for which $\Delta\hat{n} = 0$ and $\widehat{\langle\cos\phi\rangle} = 0$ are a particular case for which the amount of useful spin squeezing is not defined. Importantly, the ground state of a BJJ with repulsive interactions and finite tunnel coupling is always spin-squeezed [30]. In the Rabi and the Josephson regime ($\Lambda \ll N^2$), the square of the useful squeezing factor reads

$$\xi_S^2 = \frac{1}{\sqrt{\Lambda+1}} \exp\left(\sqrt{1+\Lambda}/N\right) \leq 1. \tag{1.165}$$

We will show in Sect. 3.4.3 that the state that we produce by coherently splitting a Bose-Einstein condensate is also a coherent spin squeezed state.

1.2.4.5 Spin Squeezing and Interferometry

The concept of atomic spin squeezing has been largely investigated as a potential resource for enhanced precision in interferometry. The idea of enhancing the sensitivity of an interferometric measurement by engineering the noise fluctuations of the quantum state in the interferometer originated in the field of quantum optics with photons [50].

A prototypical interferometer is the Ramsey/Mach-Zehnder interfometer (MZI, see Fig. 3.1). In Sect. 3.1, we will come back to the distinctions between the different schemes investigated in literature, but conceptually, they are all based on the same principle: an ensemble of particles is prepared in a coherent superposition of two modes by means of a first $\pi/2$ pulse (separation beam splitter). They are allowed to evolve for a given time during which the superposition picks up a relative phase ϕ. A second $\pi/2$ pulse (recombination beam-splitter) eventually maps the phase ϕ onto the population of the two modes. The phase ϕ can be inferred from the measured population imbalance.

The Non-interacting Case

In the collective-spin picture, and assuming no interactions, the Ramsey/MZI sequence can be represented by a series of rotations on the generalized Bloch sphere. The beam-splitters correspond to rotations of angle $\pi/2$ around the (x)-axis, while the phase accumulation corresponds to a rotation of angle ϕ around the (z)-axis (see Sect. 1.2.4.3). For example, if the atoms initially all share the same mode, which is similar to illuminating only one input port of an optical MZI, the initial state corresponds to the Dicke state located on one of the poles of the Bloch sphere. The first $\pi/2$ pulse brings the spin onto the equator, then the phase accumulation rotates it by an angle ϕ in the equatorial plane. The second $\pi/2$ pulse eventually rotates the spin in a way such that ϕ is mapped onto the projection of the spin along the vertical axis of the Bloch sphere.

Alltogether, in absence of interactions, the MZI sequence is equivalent to a rotation of angle ϕ around the y-axis of the Bloch sphere[19] [51]:

[19] Note that the choice of the axes and the orientation of the rotations may differ depending on the conventions and on the exact procedure. For example, in traditional optical MZI built with half-

$$|\Psi_{\text{out}}\rangle = e^{i\frac{\pi}{2}\hat{S}_z} e^{-i\phi\hat{S}_z} e^{-i\frac{\pi}{2}\hat{S}_x} |\Psi_{\text{in}}\rangle$$
$$= e^{-i\phi\hat{S}_y} |\Psi_{\text{in}}\rangle . \tag{1.166}$$

The phase picked-up during the phase accumulation stage is mapped onto the population imbalance in the output state

$$\langle\hat{S}_z\rangle_{\text{out}} = -\sin\phi\langle\hat{S}_x\rangle_{\text{in}} + \cos\phi\langle\hat{S}_z\rangle_{\text{in}}. \tag{1.167}$$

In classical wave optics, it is common to present MZI setups where only one input port is illuminated, yielding $\langle\hat{n}\rangle_{\text{out}} = \cos\phi$. In a double-well matter-wave interferometer, the input state is generally a symmetric superposition of left and right mode ($\langle\hat{S}_z\rangle = 0$), in which case

$$\langle\hat{n}\rangle_{\text{out}} = -\langle\hat{S}_x\rangle_{\text{in}} \sin\phi. \tag{1.168}$$

The imbalance of the output state varies sinusoidally with the accumulated phase. In an ideal interferometer, the contrast[20] of the interference fringes is determined only by the degree of coherence $\langle\hat{S}_x\rangle$ of the input state. If an atomic coherent state is sent into the interferometer, the contrast is maximal and equal to one.

The sensitivity of the MZI to phase shifts, i.e. its ability to detect a small deviation $\Delta\phi$ from a given phase ϕ_0, is commonly estimated from Eq. (1.168) by error propagation to the first order[21] and reads

$$\Delta\phi = \frac{\Delta\hat{n}_{\text{out}}(\phi_0)}{|\partial\langle\hat{n}_{\text{out}}\rangle/\partial\phi|_{\phi_0}} \tag{1.169}$$

Figure 1.14 illustrates the meaning of Eq. (1.169): the sensitivity to small phase shifts is equal to the ratio of the uncertainty on the population imbalance over the slope of the averaged fringe.

The variance of $\hat{n}_{\text{out}}$ is given by

$$\Delta\hat{n}^2_{\text{out}} = \sin^2\phi(\Delta\hat{S}^2_x)_{\text{in}} + \cos^2\phi(\Delta\hat{S}^2_z)_{\text{in}} - 4\sin\phi\cos\phi\langle\hat{S}_x\hat{S}_z\rangle_{\text{in}}, \tag{1.170}$$

where we have assumed that the input state is symmetric ($\langle\hat{S}_z\rangle_{\text{in}} = 0$) and that its spin is aligned along x ($\langle\hat{S}_y\rangle_{\text{in}} = 0$) [51]. The last term is linked to the correlations between number and phase fluctuations of the input state. If we assume that they are independent,[22] we get

---

silvered mirrors, care has to be taken about the fact that reflexions on the front or the rear face of the beam-splitters have a different phase shift.

[20] In the following, we will use equivalently the terms *contrast* and *visibility*.

[21] For $\phi_0 = \pi/2$, it is not a meaningful quantity since both numerator and denominator are equal to zero.

[22] Such a state can be represented by a noise ellipse with eigenaxes parallel to (y) and (z), such as displayed in Fig. 1.12.

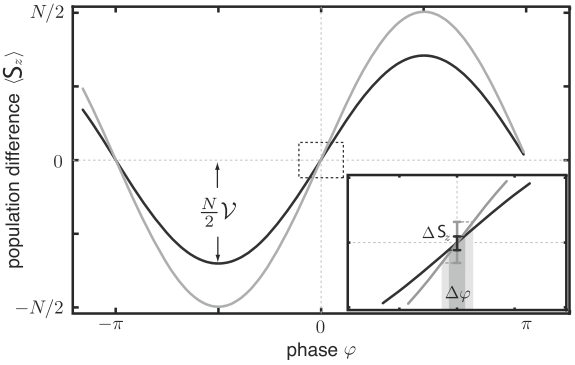

Fig. 1.14 Phase sensitivity in Mach-Zehnder interferometry. Adapted from Gross [43]. Comparison between the phase sensitivity achieved with a coherent state, and with a spin-squeezed state. The visibility V of the MZI/Ramsey fringes is higher with a coherent state ($V = 1$) than with a spin-squeezed state. Nevertheless, the precision of the phase estimation with a spin-squeezed state outperforms that of a coherent state, because the projection noise is suppressed by a larger amount (see caption)

$$\Delta\phi^2 = \frac{\sin^2\phi_0(\Delta\hat{S}_x^2)_{\text{in}} + \cos^2\phi_0(\Delta\hat{S}_z^2)_{\text{in}}}{\langle\hat{S}_x\rangle_{\text{in}}^2\cos^2\phi_0}. \tag{1.171}$$

In an ideal, i.e. noise-less and interaction-free MZI, the sensitivity depends only on the input state and the working point ϕ_0. Equation 1.171 is minimal at the points of steepest fringe slope $\phi_0 = 0$ and $\phi_0 = \pi$, and reads

$$\Delta\phi_{\text{min}}^2 = \frac{(\Delta\hat{S}_z^2)_{\text{in}}}{\langle\hat{S}_x\rangle_{\text{in}}^2}. \tag{1.172}$$

If the input state of the interferometer is a coherent atomic state, Eq. (1.172) yields the standard quantum limit (SQL), also referred to as quantum projection noise:

$$\Delta\phi_{\text{SQL}} = \frac{1}{\sqrt{N}}. \tag{1.173}$$

This result simply reflects the fact that the absence of correlation between the atoms implies a binomial number distribution between the two output ports (shot noise). The SQL represents the best sensitivity achievable with uncorrelated atoms.

On the other hand, Eq. (1.172) indicates that sub-shot noise sensitivity can be achieved with coherent spin-squeezed states. The condition $\Delta\phi_{\text{min}} < \Delta\phi_{\text{SQL}}$ corresponds precisely to the definition of useful squeezing introduced in Ref. [49]. The value of ξ_S expresses the potential sensitivity gain achievable with the resource of a given spin-squeezed state. As shown in Fig. 1.14, the states defined by Eq. (1.163)

yield reduced fluctuations of the output imbalance (number squeezing) at the expense of a moderate loss of fringe contrast, allowing for an overall sensitivity gain.

The sensitivity defined in Eq. (1.172) is fundamentally limited by the fact that the number of atoms in each mode can be at best counted one by one, while the coherence is smaller or equal to 1. This defines the Heisenberg limit

$$\Delta\phi_{\mathrm{H}} = \frac{1}{N}, \tag{1.174}$$

which is believed to be the best precision achievable by an interferometric measurement [52]. Note however that the simple expression (1.169) for the phase sensitivity assumes Gaussian probability distributions, which is not in general the case for non-classical states. Finding the best possible sensitivity requires to find both an optimal input state and an optimal estimation method [53–55].

The Interacting Case

The above discussion is however only valid in the non-interacting limit. If interactions are present, the Hamiltonian describing the evolution of $|\Psi\rangle$ is not linear anymore, and the sensitivity of the interferometer depends also on the details of the interferometer sequence. It was recognized in Ref. [56] that sub-shot noise sensitivity could be achieved in a double-well interferometer by taking advantage of the strong correlations appearing in the Fock regime. In Ref. [57], the authors derived the scaling of the sensitivity for a MZI with interacting BECs in the Rabi ($\Delta\phi \propto N^{-1/2}$), Josephson ($\Delta\phi \propto N^{-3/4}$) and Fock regimes ($\Delta\phi \propto N^{-1}$).

Experimentally, interferometric measurements beyond the SQL have been recently achieved in internal BJJ [58, 59]. In Ref. [58], controlled interaction during the first $\pi/2$ beam-splitter resulted in the creation of a strongly spin-squeezed state. It yielded a 15 % metrology gain over a similar sequence in which the first beam-splitter was well into the Rabi regime.

Whether or not such a scheme is extendable to an external BJJ in a double-well potential is still an open question. Several aspects of this question will be discussed in the next chapters. Nevertheless, numerical simulations of the full many-body dynamics in a realistic 1D double well, together with the use of Bayesian phase estimation protocols, suggest that sub shot-noise measurements should be achievable with an interacting BEC [60].

1.2.4.6 Spin Squeezing and Entanglement

Entanglement in many-body systems is defined as the non-separability of the density matrix (see the review [61]), meaning that the density matrix of the system cannot be written as a product of single-particle density matrices

$$\rho = \sum_k p_k \rho_k^{(1)} \otimes \cdots \otimes \rho_k^{(N)}. \tag{1.175}$$

The difficulty in characterizing many-body entanglement comes from the exponentially increasing number of measurements necessary to reconstruct the full density matrix. However, entanglement criterions based on collective measurements were proposed. Sørensen et al. [62] showed that for distinguishable bosons, the same criterion that quantifies useful (or coherent spin-) squeezing (Eq. 1.163) detects entanglement. The same year, a criterion to quantify the depth of entanglement from a measurement of two collective operators was derived in Ref. [63].

The idea of this criterion is that, for a collection of spin-S particles, there exists a lower bound for the fluctuation of one component of the associated collective spin, given the value of its mean projection onto an orthogonal direction [63]:

$$\begin{aligned}\Delta \hat{S}_z^2 &\geq \frac{1}{2}\left[S(S+1) - \langle \hat{S}_x \rangle^2 - \sqrt{\left(S(S+1) - \langle \hat{S}_x \rangle^2\right) - \langle \hat{S}_x \rangle^2}\right] \\ &\equiv F_S\left(\langle \hat{S}_x \rangle\right).\end{aligned} \tag{1.176}$$

In other words, this inequality sets a lower bound to the fluctuations of $\hat{n}$ for a given coherence $\langle \cos\phi \rangle$ and a given atom number N. It can be used to estimate the optimal spin-squeezed state for an interferometric measurement, given the requirement of a certain contrast. F is not a tight bound but is close to the actual minimum when the coherence is large.

Inequality (1.176) can be used to define a measure of the extent to which a system of distinguishable bosons is entangled. Any separable state of M spin-J particles ($\vec{j}_i, i = 1 \ldots M$) verifies

$$\Delta \mathcal{J}_z^2 \geq MJ\, F_J\left[\langle \mathcal{J}_x \rangle / (MJ)\right] \tag{1.177}$$

where $\vec{\mathcal{J}} \equiv \sum_{i=1}^{M} \vec{j}_i$ [63]. For example, with $J = 1/2$, we recover the coherent spin-squeezing condition Eq. (1.163). For two values M and J such that $MJ = N/2$, if the measured values of $\Delta \mathcal{J}_z^2/(MJ) = \xi_N$ and $\langle \mathcal{J}_x \rangle / MJ \approx \langle \cos\phi \rangle$ do not satisfy the inequality (1.177), the degree of spin-squeezing excludes that the density matrix of the system can be written as a direct product of blocks all involving less than M particles.

It must be however underlined that originally, the criterion (1.177) has been derived for distinguishable particles [43]. The question of whether atoms in a BEC are distinguishable, has been heavily debated and is beyond the scope of this thesis manuscript. A discussion of entanglement and spin-squeezing in BECs can be found in the tutorial by Gross [43] .

1.2.5 Mean-Field Model in the Josephson Regime

The aim of this section is to derive a mean-field version of the BH Hamiltonian to gain more insight into the dynamics of the macroscopic observables as well as their fluctuations.

1.2.5.1 Continuous Limit

We have seen in Sect. 1.2.2.5 that in the limit $N \to \infty$, the (half-)number difference operator and the phase quadrature operators have a continuous spectrum. In this "continous limit", we assume that there exist real functions n and ϕ such that the creation and annihilation operators in the left and right mode can be replaced by the complex numbers [38]

$$\hat{a}_L \longrightarrow \sqrt{N+n}e^{-i\phi/2}, \tag{1.178}$$

$$\hat{a}_R \longrightarrow \sqrt{N-n}e^{i\phi/2}. \tag{1.179}$$

This approximation is expected to hold as long as the fluctuations on the number difference and the phase spread are small enough, as it is typically the case in the Josephson and in the Rabi regime when $N \gg 1$.

In the continuous limit, the spin components read

$$\hat{S}_x \longrightarrow \frac{1}{2}\sqrt{N^2-4n}\cos\phi, \tag{1.180}$$

$$\hat{S}_y \longrightarrow \frac{1}{2}\sqrt{N^2-4n}\sin\phi, \tag{1.181}$$

$$\hat{S}_z \longrightarrow n, \tag{1.182}$$

and the full BH Hamiltonian (1.84) becomes

$$H_{\mathrm{MF}} = -J\sqrt{N^2-4n^2}\cos\phi + Un^2 + \epsilon n. \tag{1.183}$$

Inserting Eqs. (1.180)–(1.182) into the Heisenberg equations of motion (1.153)–(1.155) yields the two coupled differential equations for the time evolution of the macroscopic observables

$$\dot{n} = -\frac{J}{\hbar}\sqrt{N^2-4n^2}\sin\phi, \tag{1.184}$$

$$\dot{\phi} = \frac{\epsilon}{\hbar} + \frac{2U}{\hbar}n + \frac{4J}{\hbar}\frac{n}{\sqrt{N^2-4n^2}}\cos\phi. \tag{1.185}$$

On the other hand, partial derivation of H_{MF} with respect to n and ϕ shows that they obey Hamilton's equations

$$\frac{\partial H_{\mathrm{MF}}}{\partial n} = \hbar\dot{\phi}, \tag{1.186}$$

$$\frac{\partial H_{\mathrm{MF}}}{\partial \phi} = -\hbar\dot{n}. \tag{1.187}$$

This proves that in the continuous limit, n and ϕ are two canonical conjugated variables and motivates the uncertainty relation (1.106) between n and ϕ in the quantum limit. Furthermore, it implies that

$$n = -i\frac{\partial}{\partial \phi}. \tag{1.188}$$

ϕ can be identified to a position variable and n to a momentum variable.

1.2.5.2 Effective Schrödinger Equation in Phase Representation

Considering the BJJ in the continous limit allows to developing an intuitive mean-field picture for the dynamics and the fluctuations of the full many-body wavefunction. The state of the system can be described by an effective single-particle wavefunction $|\psi\rangle$ evolving under the mean-field Hamiltonian (1.183). It can be either written in phase or in half-number difference representation, both beeing linked by Fourier transform

$$\psi_n(n,t) = \frac{1}{\sqrt{2\pi}}\int \psi_\phi(\phi,t)e^{-in\phi}\mathrm{d}\phi. \tag{1.189}$$

The wavefunction in phase representation $\psi(\phi,t)$ obeys the effective Schrödinger equation[23]

$$i\hbar\frac{\partial\psi}{\partial t} = \left(-U\frac{\partial^2}{\partial\phi^2} - J\sqrt{N^2 + 4\frac{\partial^2}{\partial\phi^2}}\cos\phi - i\epsilon\frac{\partial}{\partial\phi}\right)\psi. \tag{1.190}$$

Equation (1.190) maps the evolution of the many-body wavefunction to the motion of a fictitious particle of mass $\propto 1/2U$ in a cosine potential with the unusual feature that its steepness depends on the momentum of the particle. It is often compared to the motion of a classical momentum-shortened pendulum, i.e. a pendulum, the length of which decreases as a function of its angular momentum.

[23] (from now on, we consider only the wavefunction in phase representation and omit the subsript $_\phi$).

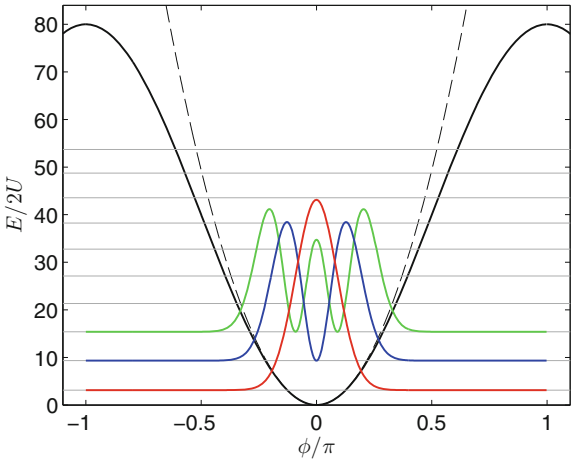

Fig. 1.15 Effective potential and some eigenstates in the mean-field approximation. Effective potential $V_{\text{eff}}(\phi) = \eta \cos\phi$ (*continuous black line*) and harmonic approximation (*dashed black line*) for the mean-field Hamiltonian ($\eta = 40$). *Gray lines* energies of the ten lowest eigenstates. *Red*, *blue*, *green lines* phase distribution (non normalized) for the three lowest eigenstates. Note that the picture of an effective potential is only meaningful for small population imbalances (Color figure online)

Neglecting this term, which is possible when $\Delta n \ll N/2$, and rewriting Eq. (1.190) using the dimensionless time[24] $\tau = 2Ut/\hbar$ yields

$$i\frac{\partial\psi}{\partial\tau} = \left(-\frac{1}{2}\frac{\partial^2}{\partial\phi^2} - \eta\cos\phi - i\tilde{\epsilon}\frac{\partial}{\partial\phi}\right)\psi, \tag{1.191}$$

with

$$\eta = \frac{NJ}{2U} = \frac{N^2}{4\Lambda}, \tag{1.192}$$

$$\tilde{\epsilon} = \frac{\epsilon}{2U}. \tag{1.193}$$

For large values of η, the effective potential $V_{\text{eff}}(\phi) = \eta\cos\phi$ is deep, corresponding to localized ground state with a narrow phase width (see Fig. 1.15). It illustrates the fact that tunneling tends to lock the relative phase between the condensates. On the contrary, when η is small, interactions cause a spread of the phase distribution, giving rise to interaction-induced phase diffusion (see Sect. 3.5.2, where the crossover value of η is discussed).

[24] In the following, we will sometimes also use the dimensionless time $\tau = 2J/\hbar t$. In one case, it mean measuring the time in units of $\hbar/2J$, in the other, in units of $\hbar/2U$. Which variable is used depends on whether one is interested respectively in the limit $U \to 0$ or $J \to 0$.

In the case of an inbalanced double well, the term containing $\tilde{\epsilon}$ represents a constant momentum applied to the fictitious particle. We can perform the transformation

$$\phi - \tilde{\epsilon}\tau \longrightarrow \phi, \tag{1.194}$$

$$\psi(\phi - \tilde{\epsilon}\tau) \longrightarrow \psi(\phi), \tag{1.195}$$

to get

$$i\frac{\partial\psi}{\partial\tau} = \left(-\frac{1}{2}\frac{\partial^2}{\partial\phi^2} - \eta\cos\left(\phi - \tilde{\epsilon}\tau\right)\right)\psi. \tag{1.196}$$

It corresponds to going to a frame moving with the velocity $\tilde{\epsilon}$. In this frame, the fictitious particle is evolving in a time-dependent cosine potential shifting at the velocity $\tilde{\epsilon}$.

When $n \ll N/2$ and $\phi \ll 1$, we can develop the Hamiltonian (1.183) to the second order to recover the harmonic approximation[25] of Sect. 1.2.3.2

$$i\hbar\frac{\partial\psi}{\partial t} = \left[-\left(U + \frac{2J}{N}\right)\frac{\partial^2}{\partial\phi^2} + \frac{JN}{2}\phi^2\right]\psi \tag{1.197}$$

(we have assumed $\epsilon = 0$). This the Schrödinger equation of an effective particle of mass $\propto \left(U + \frac{2J}{N}\right)^{-1}$ in a harmonic potential of frequency $\omega_J = 2J\sqrt{1+\Lambda}/\hbar$. The harmonic approximation consists in restricting the motion of the fictitious particle to the quadratic part of the cosine potential.[26] The validity condition $E \ll JN$ ensures that this condition is satisfied.

1.2.5.3 Dynamical Modes in the Mean-Field Regime

Without resorting to the small imbalance approximation, Eqs. (1.184) and (1.185) can be used to describe the dynamics of the BJJ by computing the time evolution of the mean phase and number difference. It is convenient to rewrite them using the dimensionless time $\tau = 2Jt/\hbar$ and the normalized population imbalance $z \equiv (n_L - n_R)/N = 2n/N$. In dimensionless form, they read

$$\dot{z} = -\sqrt{1 - z^2(\tau)}\,\sin\phi(\tau), \tag{1.198}$$

$$\dot{\phi} = \frac{\epsilon}{2J} + \Lambda z(\tau) + \frac{z(\tau)}{\sqrt{1 - z^2(\tau)}}\cos\phi(\tau). \tag{1.199}$$

[25] Actually, the condition on n is more stringent, as we have seen from the many-body results (Sect. 1.2.3.2) that the harmonic approximation breaks down already when $n \sim N/2 \cdot (1+\Lambda)^{-1/2}$.

[26] Note that if the momentum-shortening term is neglected, one gets $\omega_J = 2J\sqrt{\Lambda}$. In the Josephson regime ($1 \ll \Lambda \ll N^2$), both expression coincide.

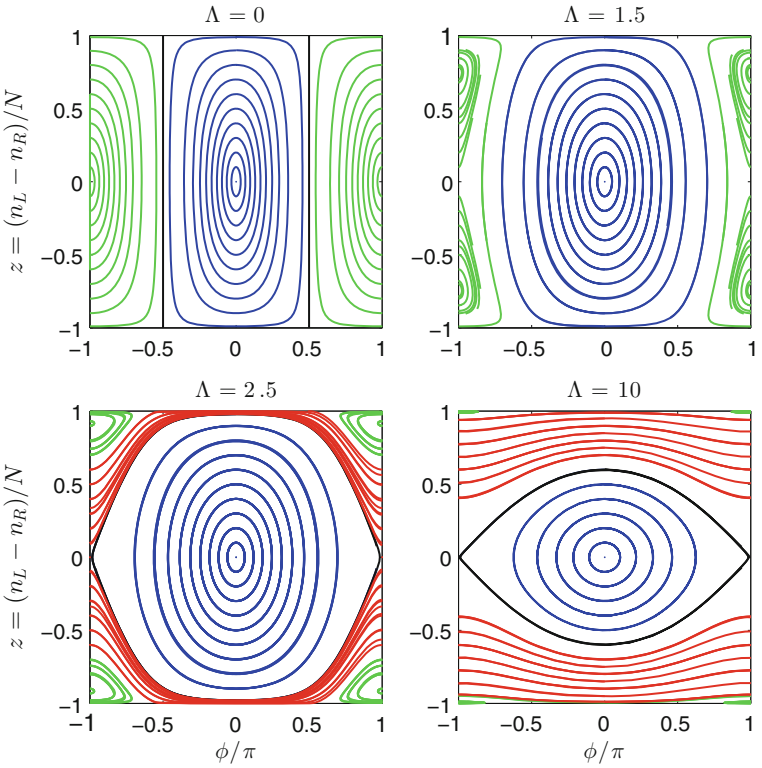

Fig. 1.16 Phase portraits of the classical BJJ. Trajectories of the state of the symmetric BJJ in phase space $\{n, \phi\}$ for four different values of Λ. In absence of interactions ($\Lambda = 0$), all trajectories are closed paths around the two fixed points $(0, 0)$ (*blue*) and $(0, \pi)$ (*green*, corresponding to the π-modes). The black lines correspond to the maximum-amplitude oscillation between $z = -1$ and 1. Interactions change the topology of the phase portrait. When Λ exceeds 1, a bifurcation occurs: the point $(0, \pi)$ bifurcates in two new stable fixed points with opposite population imbalances, while $(0, \pi)$ becomes a hyperbolic fixed point. For even larger interactions ($\Lambda > 2$), self-trapped modes appear with a free running phase (*red lines*) while the π-phase mode are wedged in the corners of the phase portrait (*green lines*). MQST modes and π-modes are parted from the Josephson oscillations (*blue lines*) by a separatrix (*black line*)

These equations can also be derived directly from a mean-field picture by inserting a two-mode Ansatz in the time-dependent GPE [64]. The dynamics of $z(t)$ and $\phi(t)$ result from the interplay between tunneling, detuning and interactions. Figure 1.16 displays the phase portrait of the BJJ for different values of Λ. Let us review three dynamical modes which have been studied in the experiment presented in this thesis.

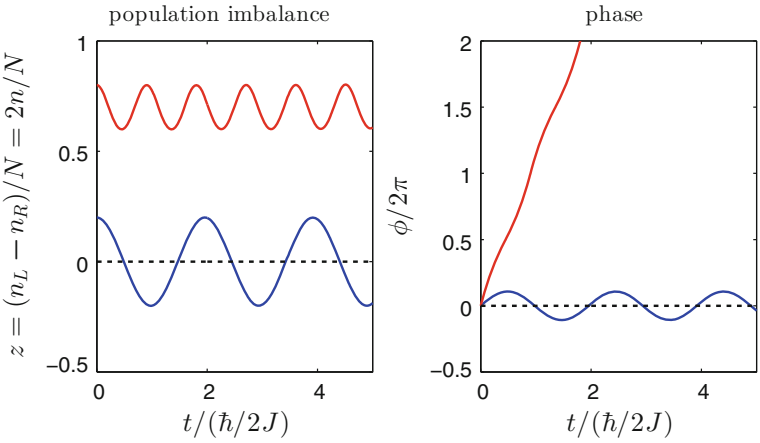

Fig. 1.17 Josephson oscillations and self-trapping. Evolution of the population imbalance $z(t)$ and the relative phase $\phi(t)$ from the dynamical equations (1.198) and (1.199) in two different modes: Josephson oscillations (*blue*) and Macroscopic Quantum Self-Trapping (*red*). $\Lambda = 10$, $\epsilon = 0$

Josephson Oscillations

Here and in the following paragraph, we assume $\epsilon = 0$. To treat small oscillations close to the minimum of V_{eff} (see Fig. 1.15), we can linearize Eqs. (1.198) and (1.199) to find the oscillatory solutions

$$z(t) \approx z\,(0) \cos\left[\omega_{\text{J}} t + \phi\,(0)\right], \tag{1.200}$$

$$\phi(t) \approx \frac{z\,(0)}{(\Lambda + 1)} \sin\left[\omega_{\text{J}} t + \phi\,(0)\right] \tag{1.201}$$

(see Fig. 1.17, blue lines). Physically, this represents small-amplitude tunneling oscillations of the atoms between the two wells at the Josephson angular frequency ω_{J} given by Eq. (1.132). Note that in presence of interactions, the Josephson frequency can be significantly larger than the Rabi frequency $2J/\hbar$ for the tunneling of non-interacting atoms.

At higher amplitude, the tunneling oscillation become increasingly anharmonic, and their period increases, as the system undergoes a critical slowing-down with a logarithmic divergence [64]. It means in particular, as we will see in Sect. 3.6.1.3, when tunneling oscillations are initiated with $\phi(0)$ close to π and $z(0) = 0$, their period diverges like $\ln(1/|\phi(0) - \pi|)$.

Macroscopic Quantum Self-Trapping (MQST)

Solving Eqs. (1.198) and (1.199) for a stronger initial population imbalance (red lines) shows that z and ϕ do not undergo symmetric oscillations around zero. Instead, z exhibits small amplitude oscillations around a non-zero value $\bar{z}$ while ϕ essentially winds up linearly (see Fig. 1.17, red lines). Making the corresponding approximations in Eqs. (1.198) and (1.199) yields

$$z(t) \approx \bar{z} - \frac{\sqrt{1-\bar{z}^2}}{\Lambda} \cos\phi(t), \tag{1.202}$$

$$\phi(t) \approx \bar{z} U N t/\hbar + \phi(0). \tag{1.203}$$

We can understand MQST by looking at how the (conserved) total energy is distributed between the tunneling energy E_{tun} and the interaction energy E_{int} (see Fig. 1.17, right pannel). At any time, the Hamiltonian (1.183) imposes that

$$-JN < E_{\text{tun}} < JN, \tag{1.204}$$

$$0 < E_{\text{int}} < \frac{1}{4} U N^2. \tag{1.205}$$

This means that as long as the total energy (which is determined by Λ and the initial conditions $z(0), \phi(0)$) is smaller than the maximum value allowed by the tunnel coupling, it will oscillate between the tunneling term and the interaction term, resulting in oscillations of ϕ and z which are symmetric around 0. In the opposite case, only a fraction of the interaction energy can be converted into tunneling energy, resulting in oscillations of z around an non zero value. This sets the condition for self-trapping [64] (see Fig. 1.18)

$$\frac{\Lambda}{2} z(0)^2 - \sqrt{1-z(0)^2} \cos\left[\phi(0)\right] > 1. \tag{1.206}$$

In particular, this condition determines the maximum amplitude of the Josephson oscillations (see Fig. 1.16)

$$|z_c| = 2\frac{\sqrt{\Lambda - 1}}{\Lambda}. \tag{1.207}$$

Note that Macroscopic Quantum Self-Trapping, despite its name, is an effect of interactions already contained in the mean-field description.

Since the first prediction of an "oscillatory exchange of atoms between two trapped condensates" in 1986 [19], Josephson oscillations between BECs have been intensively studied theoretically (see for example [25, 65]). The concept of MQST has been introduced in Ref. [65]. Both effects were observed for the first time by Albiez et al. in 2005 [66] in an optical double well. A comprehensive experimental study of

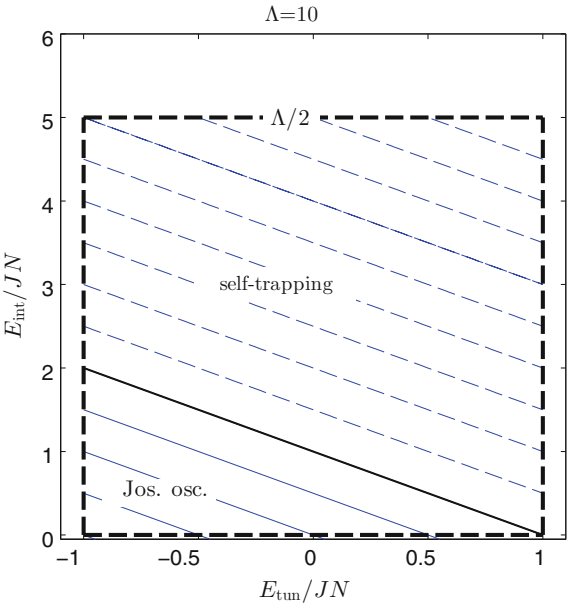

Fig. 1.18 Energetical interpretation of self-trapping. For any given initial conditions allowed by the parameters of the BJJ (inside the *dashed box*), the total energy $E = E_{\rm tun} + E_{\rm int}$ must be conserved, meaning that the state of the BJJ evolves along lines of slope -1 on the graph. *Below* the self-trapping threshold, the whole energy can oscillate between tunneling and interactions (*continuous lines*). *Above* the self-trapping threshold, only a fraction of the total energy can be transferred (*dashed lines*). The *black line* corresponds to the self-trapping condition

the modes of an internal BJJ has been carried out in [22], demonstrating a classical bifurcation when $\Lambda = 1$.

Running Phase

Let us now assume a double well with an arbitrary detuning ϵ and no tunnel coupling ($J = 0$). In this case, the phase evolves linearly at a rate depending on the energy difference

$$\phi(t) \approx \left(\frac{\epsilon}{\hbar} + \frac{UN}{\hbar}\bar{z}\right) t. \tag{1.208}$$

It contains both the difference in zero-point energy between the wells and differential terms due to interactions.

1.2.5.4 Improved Two-Mode Model

In the derivation of the Hamiltonian of the BJJ in the two-mode approximation, we have neglected the "mixed terms" involving overlap integrals between the two modes of order higher than one $I^{(1,3)}$, $I^{(3,1)}$ and $I^{(2,2)}$. It has allowed us deriving a simple two-mode Bose Hubbard Hamiltonian where the strength of the tunnel coupling J and the on-site interaction energy U are expressed as integrals of the wavefunctions

of the two modes. For static orbitals, these two parameters are constant and do not depend on the state of the BJJ.

Retaining all the terms in the two-mode expansion, Ananikian and Bergeman derived a refined version of the mean-field two-mode model, often refereed to as "improved two-mode model" (I2MM) [28]. It contains corrections from the standard two-mode model (S2MM). In particular, the coupling terms responsible for the transfer of atoms between the two mode becomes explicitly dependent on the time-dependent occupation of the two orbitals and read

$$J_{\mathrm{I2MM},L} = \frac{\Delta\mu}{2} - \frac{\Delta\gamma}{4}\,|\psi_R(t)|^2 - C\psi_R^*(t)\psi_L(t) \tag{1.209}$$

(similar expression for $J_{\mathrm{I2MM},R}$) where $\Delta\mu$ is the chemical potential difference between the ground and the first excited GPE eigenstate in the potential, γ and C are time-independent factors involving integrals of the ground and first excited state wavefunctions and $i = L, R$ [28]. The complex numbers $\psi_i(t)$ represent the occupation of the two modes and a linked to the total mean-field wave function through

$$\psi(t) = \sqrt{N}\left[\psi_L(t)\phi_L(\vec{r}) + \psi_R(t)\phi_R(\vec{r})\right]. \tag{1.210}$$

Although it relies on the assumption of two static orbitals, the I2MM turns out to reproduce the predictions of the full multimode mean-field dynamics (GPE) much more accurately than the S2MM. Figure 1.19 shows for example a comparison between the Josephson oscillation frequency in different double wells (labeled by the parameter $\mathrm{RF}_{\mathrm{Amp}}$) computed with the standard two-mode model, the improved two-mode model as well as the one-dimensional GPE in the transverse potential and the 3D GPE. In the rest of this manuscript, we have been mostly using the standard version of the two-model model, because it yields much insight into the interplay between tunneling and interactions. However, when quantitative predictions are needed, the I2MM often gives reliable results.

1.3 Conclusion of the Theoretical Part

In the first part of this chapter, we have reviewed some basic concepts of Bose-Einstein condensation and sketched the framework for the description of a system of interacting bosons. We have applied the GPE to give a mean-field description of our elongated condensates in the ground state. The main result is that, for our typical parameters, the cloud is well within the 1D Thomas-Fermi regime. It implies that while interactions determine the longitudinal shape of the condensate, transversely, the system is close to its non-interacting ground state. Aspect ratio of the order of several hundreds allow us very often to restrict the dynamics of the BEC during the experimentally relevant timescales to one or two dimensions.

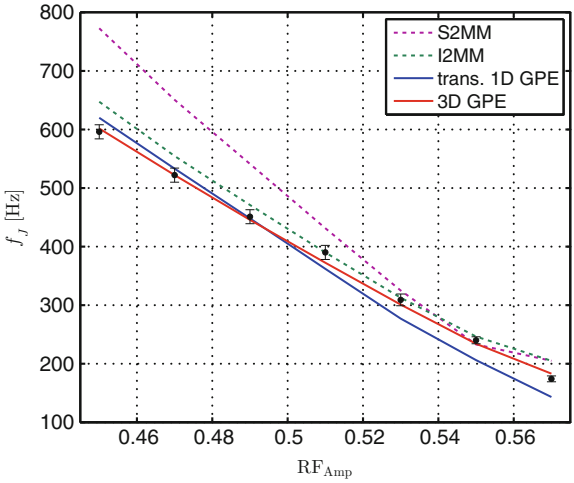

Fig. 1.19 Josephson oscillation frequency in different double wells. Comparison between measured Josephson oscillation frequencies in different double wells (data of Fig. 4.2) and the frequencies computed using the standard two-mode model (S2MM), the improved two-mode model (I2MM), a 1D GPE simulation in a transverse cut of the potential and a full 3D GPE simulation in the double-well potential. The parameter $\mathrm{RF_{Amp}}$ represents the intensity of the splitting (a higher value means a weaker tunneling and thus a lower Josephson oscillation frequency)

Interestingly, although interactions appear transversely as a perturbative term, we have seen that not only they are a key feature to understand the physics of the condensate in a double well, but very often they drive the evolution of the many-body wavefunction.

In the second part of this chapter, we have seen that the state of a condensate in a double-well potential can be described in a two-mode approximation, assuming that its wavefunction can only occupy two static spatial modes $\phi_L(\vec{r})$ and $\phi_R(\vec{r})$. In the formalism of second quantization, this approximation allows restricting the system to a $N+1$-dimensional Hilbert space in which all observables can be computed exactly. In particular, the quantities n (half number difference) and ϕ (relative phase) appear like two natural conjugate observables defining the many-body state of the BJJ. In fact, care has to be given to the exact definition of ϕ, and it is generally preferable to work instead with the coherence factor.

We have seen that within this approximation, the many-body problem could be solved exactly. In particular, the two-mode Bose Hubbard Hamiltonian can be diagonalized, yielding the eigenstates of the BJJ and allowing to compute the time-evolution of any initial state. An important feature of the symmetric BJJ with repulsive interactions is that its ground state is always number- and spin-squeezed. We have seen that the 2MM can be recast in a collective spin formalism which illustrates more precisely the number-phase uncertainty and turns out to be particularly adapted for interferometry.

In the limit of large atom numbers, and provided the number imbalance is sufficiently small, it is possible to derive a mean-field picture in the Josephson regime

which allows gaining insight into both the equilibrium properties and the dynamics of the BJJ.

However, it is crucial to keep in mind that by writing the state of the BEC as a time-dependent superposition of the two static "orbitals" $\phi_L(\vec{r})$ and $\phi_R(\vec{r})$, we ignore its spatial dynamics. In fact, the motion of the wavefunction is absorbed in the time-evolution of the amplitudes of the two static modes. This model, which is very powerful to describe the tunneling dynamics of the BJJ, cannot capture its coupling to the spatial degree of freedom. This is true both for the external BJJ, where the 2MM ignores the motion of the condensate in the double well [67], as for the internal BJJ, where it for example fails to describe the demixing dynamics observed in superpositions of internal states [68]. In Chap. 4, we will present observations which clearly go beyond the two-mode approximation, and discuss extensions to the theoretical models.

References

1. M.H. Anderson, J.R. Ensher, M.R. Matthews, C.E. Wieman, E.A. Cornell, Observation of Bose-Einstein condensation in a dilute atomic vapor. Science **269**(5221), 198–201 (1995)
2. A. Einstein, Quantentheorie des einatomigen idealen Gases, Zweite Abhandlung. Sitzungsberichte der Preußischen Akademie der Wissenschaften, **3**(14) (1925)
3. S.N. Bose, Plancks Gesetz und Lichtquantenhypothese. Z. Phys **26**(1), 178–181 (1924)
4. L. Pitaevskii, S. Stringari, *Bose-Einstein Condensation* (Oxford University Press, Oxford, 2003)
5. C.J. Pethick, H. Smith, *Bose-Einstein Condensation in Dilute Gases* (Cambridge University Press, Cambridge, 2008)
6. Y. Castin, Bose-Einstein condensates in atomic gases: simple theoretical results, in *Coherent Atomic Matter Waves, Lecture Notes of Les Houches Summer School*, vol. 2 (Springer, 1999), pp. 1–136
7. C.J. Pethick, H. Smith, The non-interacting Bose gas, in *Bose-Einstein Condensation in Dilute Gases* (Cambridge University Press, Cambridge, 2008), pp. 21–22
8. J.T.M. Walraven, *Thermodynamic and Collisional Properties of Trapped Atomic Gases* (2010)
9. J. Weiner, P.S. Julienne, Experiments and theory in cold and ultracold collisions. Rev. Mod. Phys. **71**(1), 1–85 (1999)
10. C. Chin, R. Grimm, P. Julienne, E. Tiesinga, Feshbach resonances in ultracold gases. Rev. Mod. Phys. **82**(2), 1225–1286 (2010)
11. E.G.M. van Kempen, S.J.J.M.F. Kokkelmans, D.J. Heinzen, B.J. Verhaar, Interisotope determination of ultracold rubidium interactions from three high-precision experiments. Phys. Rev. Lett. **88**(9), 093201 (2002)
12. J. Dalibard, *Systèmes de Bosons et de Fermions* (1990)
13. H. Bruus, K. Flensberg, *Many-Body Quantum Theory in Condensed Matter Physics, an Introduction* (Oxford University Press, Oxford, 2004)
14. E.P. Gross, Structure of a quantized vortex in boson systems. Il Nuovo Cimento **20**(3), 454–477 (1961)
15. L. Pitaevskii, Zh. Eksp. Teor. Fiz. (1961) **40**(646) (1961)
16. C. Menotti, S. Stringari, Collective oscillations of a one-dimensional trapped Bose-Einstein gas. Phys. Rev. A **66**(4), 043610 (2002)
17. L. Salasnich, A. Parola, L. Reatto, Effective wave equations for the dynamics of cigar-shaped and disk-shaped Bose condensates. Phys. Rev. A **65**(4), 043614 (2002)

18. F. Gerbier, Quasi-1D Bose-Einstein condensates in the dimensional crossover regime. Europhys. Lett. (EPL) **66**(6), 771–777 (2004)
19. J. Javanainen, Oscillatory exchange of atoms between traps containing Bose condensates. Phys. Rev. Lett. **57**(25), 3164–3166 (1986)
20. A. Leggett, Bose-Einstein condensation in the alkali gases: some fundamental concepts. Rev. Mod. Phys. **73**(2), 307–356 (2001)
21. P. Böhi, M.F. Riedel, J. Hoffrogge, J. Reichel, T.W. Hänsch, P. Treutlein, Coherent manipulation of Bose-Einstein condensates with state-dependent microwave potentials on an atom chip. Nat. Phys. **5**(8), 592–597 (2009)
22. T. Zibold, E. Nicklas, C. Gross, M.K. Oberthaler, Classical bifurcation at the transition from Rabi to Josephson dynamics. Phys. Rev. Lett. **105**(20), 204101 (2010)
23. B.J. Dalton, S. Ghanbari, Two mode theory of Bose-Einstein condensates: interferometry and the Josephson model. J. Mod. Opt. **59**(4), 287–353 (2012)
24. C. Cohen-Tannoudji, B. Diu, F. Laloë, A simple model of the ammonia molecule, in *Quantum Mechanics I* (1977), pp. 455–469
25. G.J. Milburn, J. Corney, E.M. Wright, D.F. Walls, Quantum dynamics of an atomic Bose-Einstein condensate in a double-well potential. Phys. Rev. A **55**(6), 4318–4324 (1997)
26. R. Spekkens, J. Sipe, Spatial fragmentation of a Bose-Einstein condensate in a double-well potential. Phys. Rev. A **59**(5), 3868–3877 (1999)
27. J. Javanainen, M. Ivanov, Splitting a trap containing a Bose-Einstein condensate: atom number fluctuations. Phys. Rev. A **60**(3), 2351–2359 (1999)
28. D. Ananikian, T. Bergeman, Gross-Pitaevskii equation for Bose particles in a double-well potential: two-mode models and beyond. Phys. Rev. A **73**(1), 013604 (2006)
29. J. Cirac, M. Lewenstein, K. Mølmer, P. Zoller, Quantum superposition states of Bose-Einstein condensates. Phys. Rev. A **57**(2), 1208–1218 (1998)
30. M. Steel, M. Collett, Quantum state of two trapped Bose-Einstein condensates with a Josephson coupling. Phys. Rev. A **57**(4), 2920–2930 (1998)
31. R. Gati, M.K. Oberthaler, A bosonic Josephson junction. J. Phys. B: At. Mol. Opt. Phys. **40**(10), R61–R89 (2007)
32. M.M. Nieto, Quantum phase and quantum phase operators: some physics and some history. Physica Scripta **48**(T48), 5–12 (1993)
33. P.A.M. Dirac, The quantum theory of the emission and absorption of radiation. Proc. Roy. Soc. **114**, 243 (1927)
34. W.H. Louisell, Amplitude and phase uncertainty relations. Phys. Lett. **7**, 60 (1963)
35. L. Susskind, J. Glogower, Quantum mechanical phase and time operator. Physics **1**, 49 (1964)
36. M.R. Andrews, Observation of interference between two Bose condensates. Science **275**(5300), 637–641 (1997)
37. Y. Castin, J. Dalibard, Relative phase of two Bose-Einstein condensates. Phys. Rev. A **55**(6), 4330–4337 (1997)
38. G.-S. Paraoanu, S. Kohler, F. Sols, A.J. Leggett, The Josephson plasmon as a Bogoliubov quasiparticle. J. Phys. B: At. Mol. Opt. Phys. **34**(23), 4689–4696 (2001)
39. D. Pegg, S. Barnett, Phase properties of the quantized single-mode electromagnetic field. Phys. Rev. A **39**(4), 1665–1675 (1989)
40. D. Guéry-Odelin, T. Lahaye, Basics on Bose-Einstein condensation, in *Les Houches 2009—Ultracold Gases and Quantum Information* (Oxford edition, 2009), pp. 54–55
41. F. Arecchi, E. Courtens, R. Gilmore, H. Thomas, Atomic coherent states in quantum optics. Phys. Rev. A **6**(6), 2211–2237 (1972)
42. N.I. Fisher. *Statistical Analysis of Circular Data* (Cambridge University Press, Cambridge, 1995)
43. C. Gross, Spin squeezing, entanglement and quantum metrology with Bose-Einstein condensates. J. Phys. B: At. Mol. Opt. Phys. **45**(10), 103001 (2012)
44. C. Cohen-Tannoudji, B. Diu, F Laloë, Fictious Spin 1/2 associated with a two-level system, in *Quantum Mechanics (I)*, Chapter IV (1977), pp. 424–429

45. J. Schwinger, in *On Angular Momentum*, ed by L.C. Biedenharn, H. van Dam. Quantum Theory of Angular Momentum (Academic Press edition, New York, 1965), p. 229
46. J.J. Sakurai, *Schwinger's Oscillator Model of Angular Momentum*, Revised edn., in Modern Quantum Mechanics, Chapter 3.8 (1994), pp. 217–223
47. C. Lee, Q representation of the atomic coherent states and the origin of fluctuations in superfluorescence. Phys. Rev. A **30**(6), 3308–3310 (1984)
48. M. Kitagawa, M. Ueda, Squeezed spin states. Phys. Rev. A **47**(6), 5138–5143 (1993)
49. D. Wineland, J. Bollinger, W. Itano, D. Heinzen, Squeezed atomic states and projection noise in spectroscopy. Phys. Rev. A **50**(1), 67–88 (1994)
50. D.F. Walls, G. Milburn. *Quantum Optics* (Springer, New York, 1995)
51. B. Yurke, S. McCall, J. Klauder, SU(2) and SU(1,1) interferometers. Phys. Rev. A **33**(6), 4033–4054 (1986)
52. M. Holland, K. Burnett, Interferometric detection of optical phase shifts at the Heisenberg limit. Phys. Rev. Lett. **71**(9), 1355–1358 (1993)
53. B. Sanders, G. Milburn, Optimal quantum measurements for phase estimation. Phys. Rev. Lett. **75**(16), 2944–2947 (1995)
54. L. Pezzé, A. Smerzi, Phase sensitivity of a Mach-Zehnder interferometer. Phys. Rev. A **73**(1), 011801 (2006)
55. J. Chwedeńczuk, P. Hyllus, F. Piazza, A. Smerzi, Sub-shot-noise interferometry from measurements of the one-body density. New J. Phys. **14**(9), 093001 (2012)
56. M. Jääskeläinen, W. Zhang, P. Meystre, Limits to phase resolution in matter-wave interferometry. Phys. Rev. A **70**(6), 063612 (2004)
57. L. Pezzé, L. Collins, A. Smerzi, G. Berman, A. Bishop, Sub-shot-noise phase sensitivity with a Bose-Einstein condensate Mach-Zehnder interferometer. Phys. Rev. A **72**(4), 043612 (2005)
58. C. Gross, *Spin squeezing and non-linear atom interferometry with Bose-Einstein condensates*. Ph.D. thesis, Ruperto-Carola University of Heidelberg (2010)
59. C.F. Ockeloen, R. Schmied, M.F. Riedel, P. Treutlein, Quantum metrology with a scanning probe atom interferometer. Phys. Rev. Lett. **111**(14), 143001 (2013)
60. J. Grond, U. Hohenester, J. Schmiedmayer, A. Smerzi, Mach-Zehnder interferometry with interacting trapped Bose-Einstein condensates. Phys. Rev. A, **84**(2) (2011)
61. L. Amico, A. Osterloh, V. Vedral, Entanglement in many-body systems. Rev. Mod. Phys. **80**(2), 517–576 (2008)
62. A. Sørensen, K. Mølmer, Entanglement and extreme spin squeezing. Phys. Rev. Lett. **86**(20), 4431–4434 (2001)
63. A. Sørensen, L.M. Duan, J.I. Cirac, P. Zoller, Many-particle entanglement with Bose-Einstein condensates. Nature **409**(6816), 63–64 (2001)
64. S. Raghavan, A. Smerzi, S. Fantoni, S. Shenoy, Coherent oscillations between two weakly coupled Bose-Einstein condensates: Josephson effects, Pi oscillations, and macroscopic quantum self-trapping. Phys. Rev. A **59**(1), 620–633 (1999)
65. A. Smerzi, S. Fantoni, S. Giovanazzi, S.R. Shenoy, Quantum coherent atomic tunneling between two trapped Bose-Einstein condensates. Phys. Rev. Lett. **79**(25), 4950–4953 (1997)
66. M. Albiez, R. Gati, J. Foelling, S. Hunsmann, M. Cristiani, M.K. Oberthaler, Direct observation of tunneling and nonlinear self-trapping in a single bosonic josephson junction. Phys. Rev. Lett. **95**(1) (2005)
67. L. LeBlanc, A. Bardon, J. McKeever, M. Extavour, D. Jervis, J. Thywissen, F. Piazza, A. Smerzi, Dynamics of a tunable superfluid junction. Phys. Rev. Lett **106**(2) (2011)
68. R. Anderson, C. Ticknor, A. Sidorov, B. Hall, Spatially inhomogeneous phase evolution of a two-component Bose-Einstein condensate. Phys. Rev. A **80**(2), 023603 (2009)

Chapter 2
Experimental Setup and Techniques

Most of the experiments presented in this thesis have been performed on the Vienna atom chip setup internally labeled as "Rb2". The current setup has been developed in Heidelberg starting from 2002 and moved, rebuilt and extended in Vienna from 2006. The first section will be devoted to a brief description of the apparatus. The second section will focus on the techniques used to create, control and characterize magnetic double-well potentials on our atom chip setup. The last section will present the imaging systems used to probe the atoms.

2.1 Experimental Setup

As in most BEC experiments, a different atomic sample (a cold thermal cloud or a Bose-Einstein condensate) is prepared at each experimental cycle, before it is manipulated and eventually released and destructively imaged. A Magneto Optical Trap (MOT) is used to trap Rubidium atoms from the background gas. The atoms are optically cooled down by an optical molasses an then optically pumped and confined in a magnetic Ioffe-Pritchard-type trap created by a macroscopic copper structures behind the atom chip. After a first step of radio-frequency evaporative cooling, the atoms are transferred into the actual chip trap and further cooled down. Eventually, the condensate is released from the trap and imaged in time of flight (tof), either by an absorption or a fluorescence imaging system. Each experimental cycle of the Rb2 machine lasts about 37 s, including 18 s in the MOT and 10 s of cooling and trapping in the the two magnetic traps. The aim of this section is to present the main steps of the experimental cycle and the hardware used to realize them. Figure 2.1 shows an overview of the Rb2 setup.

The status of the experiment, as presented in this thesis, shows little difference to that described in the previous theses of the students who worked on the experiment, in particular the Ph.D. thesis of Bücker [1] (2013). The following sections will briefly recapitulate the most important features of our setup, with emphasis on the techniques

T. Berrada, *Interferometry with Interacting Bose-Einstein Condensates in a Double-Well Potential*, Springer Theses,
DOI 10.1007/978-3-319-27233-7_2

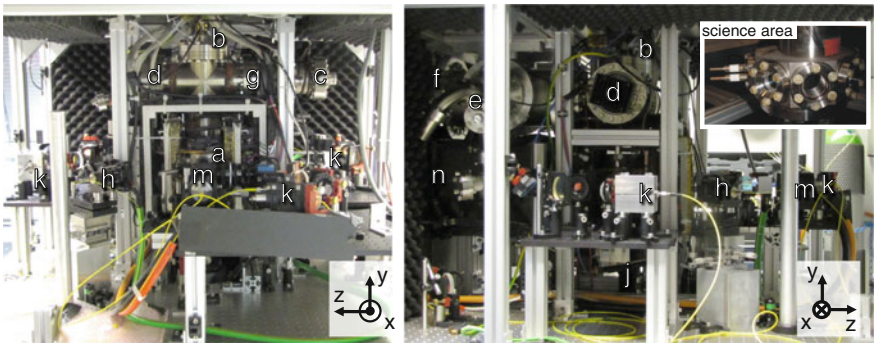

Fig. 2.1 Overview pictures of the Rb2 setup. Adapted from Ref. [1]. *Left* front view, *right* side view. **a** Science area, surrounded by Helmholtz coil pairs, **b** Chip mounting flange, **c** Ti-sublimation pump, **d** LIAD viewport, **e** Cluster flange with vacuum valve and ion gauge, **f** (behind panel) Ion getter pump, **g** NEG pump, **h** Light sheet illumination optics, **j** Light sheet objective (facing upwards), **k** Various fiber couplers for optical pumping beams, **m** Fiber coupler for absorption imaging, **n** (behind panel) Absorption imaging camera. *Inset* science area (*octagon*) with viewports and dispenser current feedthrough (*left*)

used in the experiments presented in this thesis. More specific information can be found in the Ph.D. and diploma theses of the students who worked on the Rb2 experiment in Heidelberg and Vienna, as well as in the publications of the Rb2 team:

- initial design and general aspects of atom chip experiments: Krüger [2], Wildermuth [3], Gimpel [4], Becker [5], Haupt [6] and Hofferberth [7]
- radio-frequency dressed potentials, in particular double wells: Schumm [8], Hofferberth [9], Betz [10] and Refs. [11–14]
- chip manufacturing and characterization: Groth [15], Manz [16] and Ref. [17]
- upgrades performed after the move to Vienna: Manz [16], Betz [10], Bücker [1, 18]
- imaging systems: Bücker [1, 18] and Refs. [19–21].
- micro-wave and radio-frequency systems: Koller [22], Plisson [23].
- experiment control: Bradjic [24], Rohringer [25] and Ref. [26]

2.1.1 Vacuum Chamber and Rubidium Source

The experiments take place in a single stainless steel ultrahigh vacuum chamber. It contains the atom chip and its mounting, which is suspended by a large vacuum flange at the top of the vessel. The vacuum pumps (an ion pump,[1] a passive non-evaporative getter pump[2] and a Titanium sublimation pump (TSP), the filaments of which are

[1] Varian StarCell, 500 L/s.

[2] SAES Getters.

heated every few weeks) are mounted in the chamber on dedicated flanges. The chip is located in the lower half of the chamber and is surrounded by an octagonal vessel equipped with anti-reflection coated viewports ($\geq$1 in. clear aperture diameter) on seven of its faces, providing optical access for the MOT, optical pumping and imaging beams, as well as the Rubidium dispensers on the eighth face. Another dispenser is placed directly behind a viewport to be used as a Light Induced Desorption source (LIAD, not implemented yet). The bottom flange is a large viewport used for two of the MOT beams as well as the fluorescence imaging.

On the one hand, experiments with BECs require a low background pressure (of the order of 10^{-11} mbars) to ensure a good lifetime, but on the other hand, a background pressure of 10^{-9} mbars is necessary to load the MOT from the ambient Rb vapor. This means that the pressure changes by two order of magnitude during each experimental cycle. This is achieved by pulsing the current in the dispensers for about 17 s at the beginning of each cycle to desorb gaseous Rb. The MOT is held for another $\sim$1.5 s with dispenser off to allow the pumps to capture the remaining hot background gas before the rest of the cooling sequence starts.

2.1.2 External Coils

Coils

Uniform magnetic fields are required throughout the sequence. They are created by six pairs of coils located outside the vacuum chamber. For each spatial direction, each of the two pairs is operated close to Helmholtz configuration to produce a homogeneous magnetic field close to the center, but with opposite orientation, labeled as *Big and Small Bias field* in the horizontal x direction, *Big and Small Ioffe field* in the horizontal z direction and *Big and Small Up-Down field* in the vertical y direction (see Fig. 2.1 for the orientation of the axes). For each direction, one pair of coils is made of thick copper wires (*Big*-) to create fields up to tens[3] of Gauss, while the other pair (*Small*-) is made of thinner wires to provide smaller fields of a few G. This configuration with two sets of coils is advantageous when changes in field magnitude and direction are needed on a timescale which cannot be met by the current sources. It also allows using unipolar current supplies and matching the current and voltage ranges to the requirements of each coil.

Current Sources

The current sources[4] are operated in current-stabilized mode to output a constant current and avoid long-term thermal drift. The current target is set by an analog control voltage from the sequencer. The only exception is the offset field providing

[3]Fields magnitude larger than 100 G should be achievable but not required in the current experimental cyclee.

[4]HP/Agilent 65xx series, excepted for the small Up-Down field, where a bipolar supply (High-Finesse BCS-5/5) is used.

the trap bottom in the final chip trap (small Ioffe field, see Sect. 2.2.1.2). In particular for extremely cold samples obtained by radio-frequency evaporative cooling close to the trap bottom, the stability of the small Ioffe field determines the reproducibility of the BEC production. It is also crucial for the stability of the dressed double wells, because fluctuations of the small Ioffe field translate into fluctuations of the RF dressing detuning (see Sect. 2.2.2.2), and hence of the shape of the potential. Particularly in the kHz regime (of the order of the transverse trapping frequency), noise at the mG level has to be suppressed, because it would result in a technical heating of the BEC.

To take advantage of the fact that the supply for the small Ioffe turns out to be less noisy in controlled-voltage mode, it is voltage-stabilized on a 1 Ω precision resistor[5] (temperature coefficient < 1 ppm/K) connected in series with the coil, yielding a relative current stability better than 10^{-5} at 0.5 G. Details of the small Ioffe stabilization setup and noise characteristics can be found in Bücker's Ph.D. thesis [1].

Switches

Fast switching (<0.1 ms) is achieved using home-made field-effect transistor (FET) switches to stand currents up to 60 A and induced voltages uo to 400 V. Still, the coils switches are among the devices which break more frequently on the experiment.

2.1.3 Chip Mounting and Copper Structure

The chip mounting (see Fig. 2.2a) hangs upside down in the vacuum chamber so that the atoms can levitate below the chip surface (see Fig. 2.2b), allowing to perform tof measurements. The chip mounting consists of 10 copper rods and ceramic spacers, as well as "macroscopic" copper wires (∼1 mm thickness) embedded in a ceramic block ensuring electrical insulation as well as heat conductivity. These copper wires form an additional layer of current carrying structures approx. 1 mm behind the chip surface in order to produce non-homogenous magnetic fields (see Fig. 2.2c):

- a broad **H-shaped structure**, electrically connected as a U wire, is used together with the big Bias field and the big Up-Down field to create the MOT quadrupole approximately 1 cm below the chip surface, in a region where the MOT beams intersect [5, 27, 28]. In contrast to the standard MOT configuration with three pairs of counterpropagating beams, the mirror MOT is created by replacing two beams by reflection of the beams impinging on the surface of the atom chip, tilting the beam configuration by 45° with respect to the chip surface [28]. Scanning the magnitude of the two external fields allows changing the position of the MOT as well as the orientation of the quadrupole axes, in order to match the beam configuration. It is often necessary to optimize iteratively these parameters, for

[5] Isabellenhütte RUG-Z.

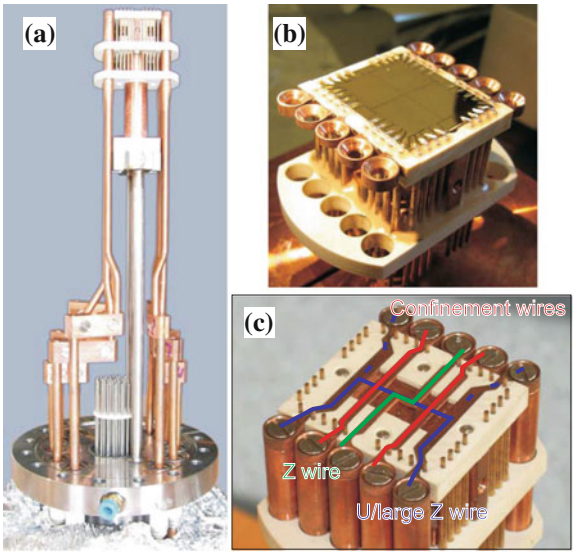

Fig. 2.2 The atom chip and its mounting. Adapted from Ref. [1]. **a** Chip mounting. At the *bottom*, the vacuum flange with feedthroughs for high-current copper rods and chip wires is seen. The steel tube in the center can be used for water cooling. Near the *top*, the copper rods and chip connection pins are guided by a ceramic (Shapal) block. When mounted, the copper structrue hangs upside down. **b** Atom chip, glued to ceramic mounting block. Near the edges of the atom chip, bond wires between connection pins and pads on the chip are seen. **c** Copper structures underneath the atom chip. Z-, U- and outer confinement wires are traced in *green*, *blue*, and *red*, respectively

example to ensure that the MOT is not located in the shadow of one of the chip wire.

Besides, the copper U is also used as a radio-frequency antenna for evaporative cooling.

- a **Z-shaped wire** is used together with the big Bias field and the small Ioffe field to create a Ioffe-Pritchard magnetic trap [27, 29, 30]. After the molasses phase, the atoms are optically pumped into the magnetically trappable state $F = 1, m_F = -1$ (see Sect. 2.2.1.1) and transferred into the Z trap located a few mm below the chip surface, where the RF evaporative cooling starts.
- any of the two **I shaped wires** perpendicular to the long axis of the chip trap can be used to create a longitudinal gradient for Stern and Gerlach separation of the magnetic spin states during tof (see Sect. 3.2).

The copper mounting is connected to the top vacuum flange which is equipped with electrical high current feedthroughs (up to 60 A) for the macroscopic copper wires, as well as pins for the Kapton wires connected to the atom chip ($I \leq 1$ A).

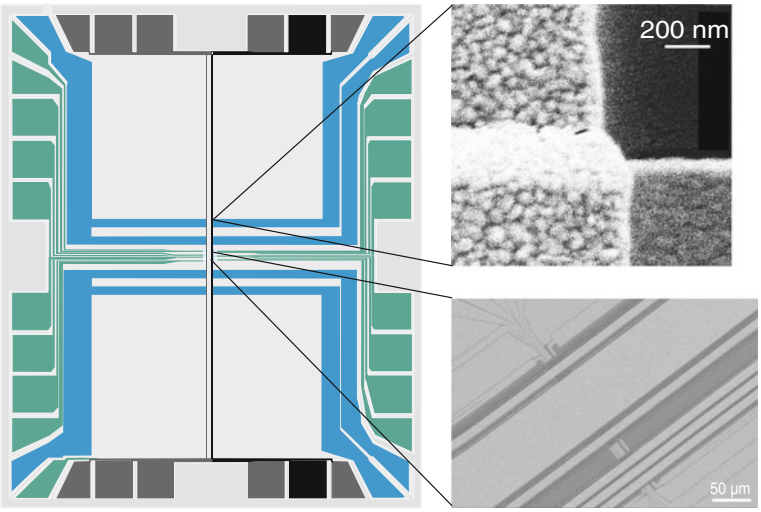

Fig. 2.3 Layout and of the Rb2 chip. Adapted from Ref. [16]. *Left* The *blue* and *green* wires (perpendicular to the long axis of the trap) belong to the first layer (deepest with respect to the chip surface). The *black* and *gray* wires (parallel to the long axis of the trap) belong to the second layer (closest to the surface). The *light gray* area is coated with gold as well, and serves as a mirror for the MOT beams. *Top Right* Wire in the second layer climbing up an insulation pad. *Bottom right* electron microscope image of the central part of the chip showing six wires in the second layer, in particular the main trapping wire (80 µm wide) and the two wires used for the RF dressing (10 µm wide) (Color figure online)

2.1.4 Atom Chip

The chip currently used on the Rb2 setup has been designed and manufactured by Groth in the group of I. Bar-Joseph at the Weizmann institute [17]. Details of the manufacturing can be found in Ref. [17] and in the Ph.D. thesis of Groth [15], characterization in the Ph.D. thesis of Manz [16]. It consists of a double-layer gold surface on a silicon substrate (see Fig. 2.3). The current-carrying structures are gold wires on two levels separated by an insulating layer to allow wire crossings. The rest of the surface is coated with gold and serves as a mirror for the MOT. A simplified sketch of the layout can be found in Sect. 2.2.

Currents up to 1 A (depending on the wires) are sent through connection pads placed all around the chip, excepted in the middle of each edge to ensure good optical access. Each pad is bonded with a copper pin connected to an electrical feedthrough on the base flange. The atom chip is directly glued onto the mounting. The heat produced by current flowing in the microwires is evacuated through the substrate into the mounting, which is water cooled.

Despite insulation pads at the position of the wire crossing, it turned out that some of the wires were electrically in contact. To avoid current leaks, the current driver for each wire is floating and connected to an independent set of car batteries (± 12 V) to supply the wire and the current source. Great care has to be taken to avoid grounding of the wire. In the long run, the heat dissipated by the microwires slightly bends

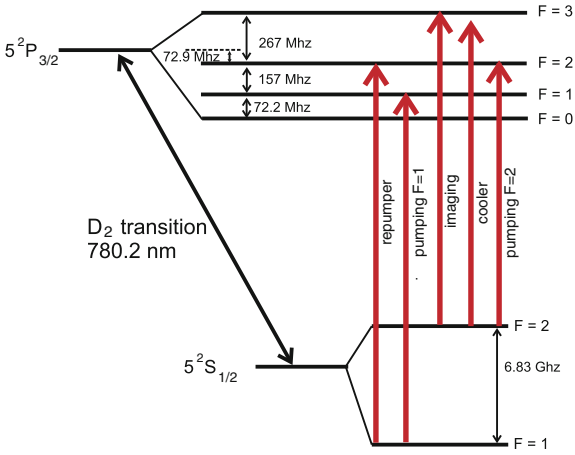

Fig. 2.4 Hyperfine structure and lasers. Adapted from Ref. [1]. Hyperfine structure of the D2 line of Rubidium 87 and laser frequencies used on the experiment

the chip surface, which affects the position of the mirror MOT and the molasses. To operate the experiment in steady state, current is always sent in the wires during the same amount of time at each experimental cycle, implying a buffer time at the end of the sequence. When used continuously, the car batteries have to be reloaded every week.

2.1.5 Optics and Laser System

Lasers are used for the MOT, repumping, optical pumping and imaging of the atoms (see Fig. 2.4). One laser source is used for each of the transitions between the two hyperfine states $F = 1$ and 2 of the ^{87}Rb electronic ground state ($5^2S_{1/2}$) and the excited state $5^2P_{3/2}$ (D2 line). Their wavelength is approximately 780.2 nm (the frequencies of the lasers differ by $\nu \approx 6.85$ GHz). Both lasers are external-cavity diode lasers (ECDL). Each is locked on the corresponding line (or crossover line) of a Rb vapor in a cell at room temperature through a Doppler-free saturated spectroscopy scheme (the description of a locking system similar to the one used on our experiment can be found in the diploma thesis of Wilzbach [31]). The structure of the laser system is sketched on Fig. 2.5.

Cooler Laser

The cooler laser[6] is mounted in a Master Oscillator Power Amplifier (MOPA) configuration. The Tappered Amplifier (TA) produces up to 1 W optical power which is launched into a single-mode, polarization-maintaining (SMPM) fiber. About 90 % of the optical power at the output of the fiber is transferred to a second fiber which outputs about 240 mW. Most of it is used for imaging, allowing to tune the intensity of

[6]Toptical Photonics TA100.

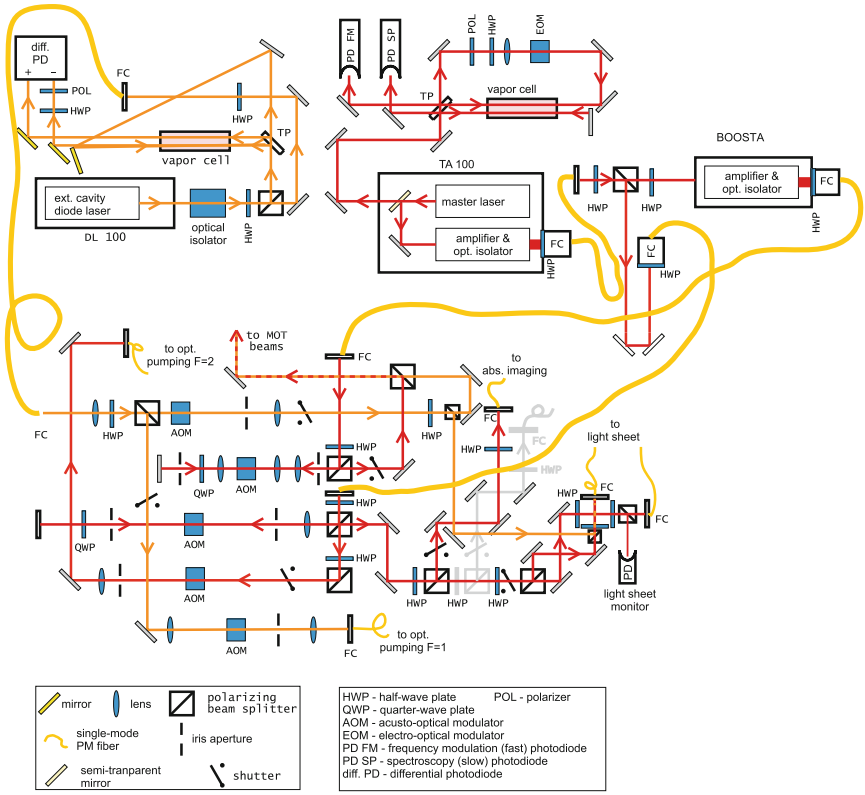

Fig. 2.5 Laser setup. Updated from Ref. [1]. *Red* and *orange lines* indicate F = 2 (cooler) and F = 1 (repumper) beam paths, respectively. The *greyed-out* parts belong to the former longitudinal imaging, which is not in use currently. The *upper part* of the drawing shows the laser spectroscopy setups for the F = 1 (*left*) and F = 2 (*right*) lasers, which are placed in a separate box to provide better thermal and acoustic isolation from the environment. The F = 2 laser uses a dual spectroscopy setup to simultaneously provide a normal Doppler-free spectroscopy and an additional path for Pound-Drever-Hall locking using an electro-optical modulator (EOM) for sideband modulation. Both lasers are coupled into single-mode polarization-maintaining fibers and brought to the BOOSTA amplifier (*right*) and to the AOM and beam distribution setup shown in the *lower part*. Finally the beams are guided to their destinations by free-field beam lines (MOT) or single-mode fibers (imaging, optical pumping)

the absorption imaging system up to 8 times the saturation intensity (see Sect. 2.3.1). The rest (a few mW) is used to drive the transition[7] $F = 2,\ F' = 2$. It has been used in the past to optically pump atoms into the magnetically trapped ($F = 2, m_F = 2$) state. Currently, since we trap the atoms in ($F = 1, m_F = -1$), we only employ this line to "repump" atoms from the $F = 2$ state into $F = 1$ after the molasse phase,

[7]The notation $F = n$ denotes a hyperfine state of the ground state while $F' = m$ denotes a hyperfine state of the excited state.

before optically pumping them with the $F = 1 \leftrightarrow F' = 1$ transition. The remaining output power of the TA (∼40 mW) is used to seed a second laser amplifier,[8] which is also coupled to a SMPM fiber (about 600 mW available optical power at the output of the fiber). It is used exclusively for the MOT beams.

Repumper

Since repumping and optical pumping on the other hand do not require large intensities, the repumper[9] consists of a single ECDL coupled into a SMPM fibre, yielding an output power of 40 mW. It is used for standard repumping during the MOT + molasse phase as well as to bring the atoms into the imaging transition. A small fraction of the light is used for the optical pumping into $(F = 1, m_F = -1)$.

Frequency Shifting

The hyperfine splittings in the excited state of ^{87}Rb are small enough (tens of MHz) to be addressed by Acousto-Optical Modulators (AOM) downstream in the beam paths (see Fig. 2.5) and in the same time large enough to be well-resolved. The cooler (MOT + molasses) beams, the detuning of which need to be dynamically changed during the cycle, as well as the imaging beam, are frequency-shifted by a double-pass AOMs. Typical detunings (with respect to the $F = 2 \leftrightarrow F' = 3$ transition) lie between −15 MHz (MOT) and −70 MHz (molasse). The other beams are sent through single-pass AOMs and are frequency shifted by a fixed amount to be resonant with the corresponding transitions.

2.1.6 *Radio-Frequency Evaporative Cooling*

Radio-Frequency Cooling Electronics

The radio-frequency (rf) source used for evaporative cooling is a digital arbitrary waveform generator.[10] The rf field frequency has to range from several MHz down to the Larmor frequency at the center of the trap (typically a few hundred kHz). This is achieved in Direct Digital Synthesizer (DDS) mode by concatenating waveforms consisting of a single period of a cosine wave at different frequencies spanning the desired range. This way, no phase jump occurs, but the frequency changes by discrete steps. The size of the frequency steps is chosen to decrease exponentially as the frequency approaches the trap bottom. While loading all the wave forms into the memory of the signal generator can take several minutes, the instruction sequence sent at each experimental sequence only contains the order of the basic waveforms and the number of times they have to be looped, and can be uploaded in a few s, during the MOT loading phase. This way, arbitrary frequency ramps can be produced and optimized in order to improve the cooling process.

[8] Toptica Photonics BoosTA.

[9] Toptica Photonics DL100.

[10] Tabor Electronics, WonderWave Series.

The rf field is radiated onto the atoms through the macroscopic copper U-wire on the chip mounting (see Fig. 2.2c). The waveform generator produces a constant-amplitude voltage and is not current-stabilized.

Cooling Sequence

Forced rf evaporative cooling starts after the atoms have been optically pumped to the $(F = 1, m_F = -1)$ state and loaded into the Z trap. After the first ramp (3 s), the Z trap is compressed and brought closer to the chip. Approximately 2 million atoms at $T \sim 50$ mK are transferred into the chip trap. Further evaporation is performed in the chip trap for another 3 s, before the chip trap is compressed and brought to its final position ∼60 μm below the surface of the chip. A final evaporation ramp (2 s) is performed to reach degeneracy and produce a Bose-Einstein condensate with typically a few thousand atoms.

Other Oscillating Fields

Note that besides rf evaporative cooling, time-varying magnetic fields in the kHz to GHz frequency range are used on the Rb2 setup for rf dressing of the potential (∼900 kHz), controlled displacement of the trap (∼3 kHz) and addressing of the ground state hyperfine transition (6.834 GHz). While the rf dressing electronics will be addressed in detail in Sect. 2.2.2, a description of the electronics for the trap position modulation ("shaking") can be found in Bücker's Ph.D. thesis [1] and Refs. [32, 33]. A description and a characterization of the rf/microwave setup which has been used in particular to address the *clock states* $F = 1, m_F = -1$ and $F = 2, m_F = 1$ can be found in Koller's Ph.D. thesis [22] and in Plisson's Master thesis [23].

2.1.7 Computer Control and Acquisition

The sequencer[11] is the spinal cord of the experiment. It is a stand-alone, real-time computer controlling 32 analog voltage channels (16 bits, ±10 V) and 64 digital Transistor-Transistor Logic (TTL) channels (0–5 V) used a triggers. The whole experimental cycle is coded as a matrix describing a sequence of values for each channel—in a similar fashion as a musical score [34]—with a minimal time step size of 25 μs. The sequence is transmitted from a dedicated computer through an link at the beginning of each cycle. Programming the sequence occurs through a Matlab interface which is also used to address devices which are not controlled by the sequencer, including the imaging cameras and the rf sources. The acquisition also relies on a Matlab interface for the read-out of analog control probes,[12] the read-out and the storage of camera pictures and the real time preprocessing of the data. Informations are exchanged between the computers (currently 6 different computers + the sequencer) through a local network by shared Windows drives and TCP/UDP connections.

[11] Jäger ADwin Pro.

[12] National Instruments USB-6218.

2.2 Trapping Atoms Magnetically with an Atom Chip

In this section, we will present the techniques used to trap atoms with magnetic fields on our atom chip setup. In particular, we will describe how the technique of rf dressing can be employed to create a tunable double-well potential.

2.2.1 Magnetic Trapping with Static Fields

2.2.1.1 Magnetic Trapping of Neutral Atoms

Magnetic trapping of neutral atoms relies on the local interaction between the magnetic field and the magnetic moment of the atoms. When the magnetic field is sufficiently weak so that the Zeeman shift is small compared to the hyperfine splitting (see Ref. [35] for the ^{87}Rb data), the total angular momentum $\vec{F}$ is a good quantum number to describe the coupling of an atom to the field and the interaction Hamiltonian reads

$$H = \vec{\mu}_F \cdot \vec{B}. \tag{2.1}$$

In the ^{87}Rb ground state ($5^2S_{1/2}$), the hyperfine splitting between $F = 1$ and $F = 2$ is approximately 6.8 GHz. For typical magnetic fields of a few G, the Zeeman shift is of the order of a few MHz. Furthermore, if the Larmor angular frequency $\omega_{\mathrm{L}} = g_{\mathrm{F}}\mu_{\mathrm{B}}|\vec{B}|/h$, where μ_{B} is the Bohr magneton, is large compared to the rate at which the field probed by the atoms changes

$$|\partial\vec{B}/\partial t| < \omega_{\mathrm{L}}|\vec{B}|, \tag{2.2}$$

the magnetic moment aligns adiabatically to the local magnetic field, so that the interaction takes the form of a potential

$$V_{\mathrm{mag}}(\vec{r}) = m_{\mathrm{F}} g_{\mathrm{F}} \mu_{\mathrm{B}} |\vec{B}(\vec{r})|. \tag{2.3}$$

In the $F = 1$ hyperfine state, the Landé factor $g_{\mathrm{F}} \approx -1/2$. Since Wing's theorem forbids the existence of a local field maximum in free space [36], the only Zeeman substate of $F = 1$ which can be trapped is $m_{\mathrm{F}} = -1$. The conversion factor between potential energy and field magnitude is $\kappa \equiv |g_{\mathrm{F}}|\,\mu_{\mathrm{B}} = h \times 0.7$ MHz/G. Note that atoms in $F = 2$, $m_{\mathrm{F}} = 1, 2$ can also be trapped. The choice of $F = 1$ on the Rb2 setup was partly motivated by observations showing that the three-body loss rate in a BEC was higher for $F = 2$ [37, 38]. Experiments coupling the two *clock states* ($F = 1, m_{\mathrm{F}} = -1$; $F = 2, m_{\mathrm{F}} = 1$), which experience the same potential, with a two-photon (microwave + rf) transition were also performed on the Rb2 setup [23].

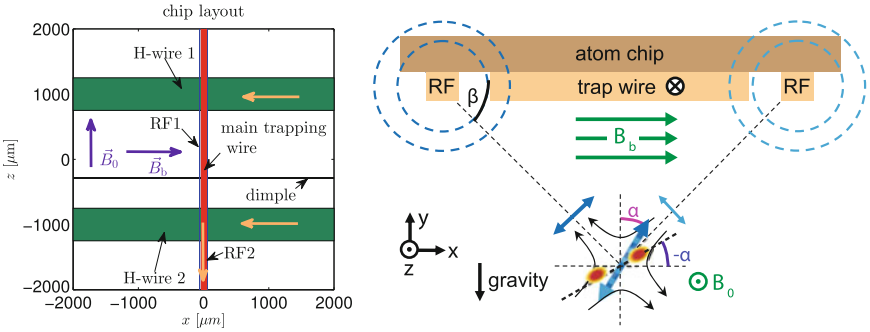

Fig. 2.6 Chip wires layout and schematics. *Left* Layout of the chip wires (at scale). *Red* main trapping wire (width: 80 μm), flanked by the two RF wires (*blue*, width: 10 μm). *Green* the two H-wires responsible for the longitudinal confinement (width: 500 μm). The dimple wire (width: 18 μm), located at 290 μm from the origin, can be used to locally deform the longitudinal potential for measurements of ω_z. The *orange arrows* indicate the orientation of the DC currents. The *purple arrows* indicate the orientation of the uniform external fields. The trap is located close to the origin. The typical length (in the z direction) of a BEC is 50 μm. The height of the wires (in y direction) is about 1 μm. *Right* Schematics of the configuration to create a double well. The DC current in the main trapping wire, together with the Bias field $\vec{B}_\mathrm{b}$, creates a magnetic quadrupole ∼60 μm below the chip. The external Ioffe field $\vec{B}_0$ completes the Ioffe-Pritchard configuration. AC currents in the two RF wires located at 55 μm on each side of the main trapping wire create a linearly polarized RF field. Its orientation (angle α) can be tuned by changing the current balance and the relative phase between the RF wires. They produce a tunable double well oriented along an axis tilted by the angle $-\alpha$ with respect to the horizontal direction (*red spots*)

For an atom oscillating in a trap at the angular frequency $\omega_\perp$ (amplitude of the order of $a_\perp = \sqrt{\hbar/m\omega_\perp}$) around the potential minimum characterized by the Larmor angular frequency ω_L, the adiabaticity criterion (2.2) imposes $\omega_\perp \ll \omega_L$.

2.2.1.2 Static Trap

A few years after the first demonstration of atom trapping with a free-standing wire [39], microfabricated structures were developed to trap atoms [40, 41], before Bose-Einstein condensation on an atom chip was achieved in 2001 [42, 43]. Atom chips can produce strong confinements in the vicinity of the current carrying microstructures, while offering a high degree of control and robustness. Besides the review by Folman et al. [27], the book edited by Reichel and Vuletic [44] gives a comprehensive overview on atom chips and their applications for cold atoms, ions and molecules.

The Vienna Rb2 setup implements the so-called *side guide trap* [27] geometry to create a single elongated harmonic potential a few tenths of microns below the chip surface. Figure 2.6 sketches the layout of the chip structures used to produce the trapping potential. The following sections describe how the confinement is obtained and discuss the details of the implementation.

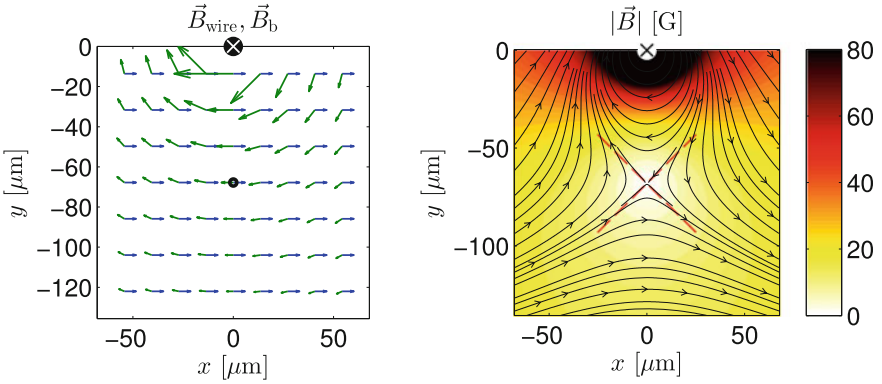

Fig. 2.7 Static transverse confinement. *Left* The uniform bias field (*blue*) and the field created by the trapping wire (*green*) cancel each other in only one point, defining the center of the guide (*black dot*). The direction of the current in the trapping wire is indicated by the cross. *Right* Field magnitude (colorscale) and field lines using the infinite wire approximation. In the vicinity of the point of zero-field, the magnetic field can be approximated by a quadrupole field tilted by 45° with respect to the (x, y) axis (*red lines*) (Color figure online)

Transverse Confinement

An elongated magnetic guide for atoms can be created using a DC current I in a single microwire in combination with a uniform bias field $\vec{B}_{\rm b} = B_{\rm b}\hat{e}_x$ orthogonal to the wire. In the following, we always assume $B_{\rm b} > 0$ and the current I oriented in the same direction as z. In the plane (x, y) orthogonal to the wire, both fields cancel each other in only one point (see Fig. 2.7, left panel). This defines a line of zero-magnetic field parallel to the wire, at a distance

$$d = \frac{\mu_0 I}{2\pi B_{\rm b}} \tag{2.4}$$

(we have assumed a infinitely long and thin trapping wire). For typical parameters $B_b = 29.5$ G and $I = 1$ A, we find $d = 68$ μm. Expanding the field to the first order in the vicinity of the field minimum yields the quadrupole configuration (the origin of the coordinate system is chosen at the point where the magnetic field vanishes)

$$\begin{aligned} B_x &= -Gr\sin\theta = -Gy, \\ B_y &= -Gr\cos\theta = -Gx, \end{aligned} \tag{2.5}$$

with the magnetic gradient at the origin

$$G \equiv \left|\nabla\vec{B}\right| = \frac{B_b}{d} \tag{2.6}$$

(see Fig. 2.7, right panel). This elongated guide does not allow confining atoms efficiently because close to the line of zero-field, they have a high probability to undergo spin flips into non-trapped states [45]. The guide hence has to be plugged by adding a constant offset field B_0 in z direction (Ioffe field). In the vicinity of the potential minimum, the potential reads

$$V_\perp(x, y) = V_0 + \frac{1}{2} m\omega_\perp^2 \left(x^2 + y^2\right) \tag{2.7}$$

with

$$V_0 = \kappa B_0 \tag{2.8}$$

$$\omega_\perp = \sqrt{\frac{\kappa}{m}} \frac{G}{\sqrt{B_0}} = \sqrt{\frac{\kappa}{m}} \frac{2\pi B_\mathrm{b}^2}{\mu_0 I \sqrt{B_0}} \propto \frac{B_\mathrm{b}^2}{I\sqrt{B_0}}. \tag{2.9}$$

For $B_0 = 1.17$ G, the Larmor frequency at the trap bottom[13] $V_0/h \approx 820$ kHz and $\omega_\perp \approx 2\pi \times 3.5$ kHz, satisfying the adiabaticity criterion (2.2). Note that atom chips allow much higher field gradients, and therefore higher trapping frequencies than magnetic trapping geometries using only external coils. In practice, the transverse confinement is varied by changing the Bias field, which also shift the position of the trap.

Longitudinal Confinement

The geometry presented so far creates a cylindrical guide with an isotropic harmonic confinement in the (x, y) plane. To create a confinement in all three directions, the translational invariance along z is broken by a pair of wires (*H-wires*) located at a distance $L/2 = 1$ mm on each side of the main trapping wire (see Fig. 2.6) and orthogonal to the main trapping wire. When a current I_h is sent in each wire (both with the same orientation), a field oriented along z is produced, creating a harmonic potential $V_z(z) = V_\mathrm{TB} + \frac{1}{2} m\omega_z^2 z^2$ with

$$V_\mathrm{TB} = \kappa \left(B_0 + \frac{4d\mu_0 I_h}{\pi L^2}\right), \tag{2.10}$$

$$\omega_z = \sqrt{\frac{\kappa}{m}} \frac{4\mu_0}{\pi L^2} \frac{I_h}{\sqrt{B_0}} \propto \frac{I_h}{\sqrt{B_0}}, \tag{2.11}$$

provided $z, d \ll L$. Since L is much larger than the other length scales, the longitudinal potential is very shallow. The resulting 3D trap is in good approximation an elongated harmonic potential. For a typical current $I_h = 0.5$ A, the correction to the trap bottom due to the H-wires is of the order of 10 % and the expected longitudinal

[13] Simply referred to as: the trap bottom.

frequency is approximately $\omega_z \approx 2\pi \times 15$ Hz, yielding an aspect ratio $\omega_\perp/\omega_z \sim 200$. In practice, however, it is difficult to control the longitudinal frequency close to the chip, as will be explained in the next section.

2.2.1.3 Realistic Static Trap

Finite Size Wires

The model of infinitely long and thin wires presented above gives fair estimates of the trap frequencies and of the trap bottom. In practice, the finite size of the wires cannot be neglected, in particular when d becomes comparable to the width and height of the wires. The dimensions of the wires are given in the caption of Fig. 2.6. In Ref. [9], an analytical expression is given for the field produced by a rectangular wire in three dimensions. We use it to model the chip layout and compute the static field. The parameters of the computation (fields, currents) are calibrated with measured trap parameters (see Sect. 2.2.3). The trap frequencies along the three eigen-axes of the potential are computed by diagonalizing its Hessian matrix at the center of the trap.

The trap frequency is proportional to the field gradient as the position of the trap. As explained in Ref. [46], for a square wire of width and height a, the gradient of the field saturates at a value proportional to I/a. The maximal current applicable is limited by the heat transfer out of the wire, and scales as $a^{3/2}$ [47], so that the maximal gradient scales as $1/\sqrt{a}$, motivating the interest in miniaturized structures.

Gravity

The effect of gravity can also be accounted for in the simulations. It is responsible for a shift of the potential minimum downwards (gravitational sag) of the order of $\Delta y = g/\omega_\perp^2 \sim 30$ nm for typical parameters. For comparison, the half-width of the radial wavefunction is $a_\perp \approx 200$ nm.

Corrugation

An effect which cannot be easily accounted for is the corrugation of the longitudinal potential [8, 46, 48, 49]. Bulk inhomogeneities in the wires, as well as the roughness of the wire surface and edges distort the current flow into directions orthogonal to the wire orientation z. This produces a spatially disordered but temporally constant magnetic field along z, and hence a disordered longitudinal potential $V(z)$. This effect is particularly deleterious close to the chip, where it causes the longitudinal fragmentation of cold atomic clouds when their temperature is of the order of the potential roughness (μK), and sets a limit to the highest achievable aspect ratios of chip traps. For our parameters, corrugation is already dominant in the longitudinal direction, yielding measured trap frequencies significantly higher than the one com-

puted from the finite-size-wire simulations. It seems that the condensate forms in a potential dip created by the corrugation. Still, the additional field in z direction caused by corrugation remains negligible compared to the offset Ioffe field, so that the trap bottom is hardly affected.

It is possible to attenuate the effect of corrugation averaging it out through a rapid modulation of the wire current [50]. This requires however a trapping geometry based on microwires only, since the high inductance of external coils forbids modulation in the kHz range.

2.2.2 *Double-Well Potentials Created by Radio-Frequency Dressing*

The dressing of the internal states of an atom by a strong laser field has been studied extensively and is at the foundation of optical trapping techniques [51]. Using strong rf magnetic fields to couple different internal states of an atom, that experience different spatial potentials, is at the heart of the concept of rf-dressed adiabatic potentials. The spatial dependence of the new energy eigenstates (*dressed states*) emerging from the coupling of the bare atomic states to the rf field can be engineered to create new trapping geometries. A tutorial introduction to rf dressed adiabatic potentials can be found in the Les Houches summer school lecture notes by Perrin [52]

The first rf-dressed adiabatic potentials were proposed in 2001 [53] to realize a 2D curves sheet at the bottom of a magnetic "shell"-potential, and implemented 3 years later [54]. The approach of Ref. [53] was extended by accounting for the vector nature of the magnetic field to propose various trapping geometries including double wells [55], ring traps [55, 56] and periodic arrays of microtraps [57].

The most promiment application of radio-frequency dressing has been the realization of tunable double-well potentials on atom chips. They were used for BEC interferometry [14, 58–61] and to study the dynamics of a superfluid junction [62]. Elongated rf-dressed double wells served as a playground to study pairs of independent [63, 64] or tunnel-coupled [11] 1D quasicondensates. In Refs. [12, 13] and [33], we used rf-dressing to control the anharmonicity of a single elongated potential in order to manipulate coherently motional states of a trapped BEC. Very anisotropic dressed magnetic traps have also been used to study 2D degenerate Bose gases [65].

In Sect. 2.2.2.3, we present the electronics used to radiate the rf fields on the atoms. In Sect. 2.2.2.1, we describe the coupling of a ^{87}Rb atom to an oscillating magnetic field. In Sect. 2.2.2.2, we use the rotating wave approximation (RWA) to derive an approximate expression of the adiabatic potential and show how rf dressing can be used to create a double-well potential. Eventually, we explain how the potential can be computed beyond the RWA (Sect. 2.2.2.4).

2.2.2.1 Coupling of an Atom to an Oscillating Field

Following Lesanovsky et al. [55], we describe the coupling of a ^{87}Rb atom in $F = 1$, $m_F = -1$ to a combination of a static, spatially varying magnetic field, and a uniform oscillating RF field

$$\vec{B} = \vec{B}_s(\vec{r}) + \vec{B}_{RF}\cos(\omega t). \tag{2.12}$$

Since the coupling term (2.1) is local, the Hamiltonian has to be diagonalized for each position in space. For an arbitrary point $\vec{r}$, it is convenient to use a local coordinate system $\{x', y', z'\}$ such that $\vec{B}_s = B_s\widehat{e}_{z'}$ and $\vec{B}_{RF} = B_{RF,\parallel}\widehat{e}_{z'} + B_{RF,\perp}\widehat{e}_{x'}$. In this coordinate system, as a consequence of the adiabaticity hypothesis (2.2), the total angular momentum $\vec{F}$ is also oriented along z'. It means that only the component of the RF field which is orthogonal to z' can couple the different Zeeman states. We introduce the Rabi frequencies for the static and the oscillating field

$$\Omega_s(\vec{r}) = \frac{\kappa}{\hbar}B_s, \tag{2.13}$$

$$\Omega_{RF}(\vec{r}) = \frac{\kappa}{\hbar}B_{RF,\perp}. \tag{2.14}$$

In the basis of the m_F states ($\{-1, 0, 1\}$), the wavefunction obeys the time-dependent Schrödinger equation

$$i\frac{\partial}{\partial t}\begin{pmatrix} c_{-1}(t) \\ c_0(t) \\ c_1(t) \end{pmatrix} = \begin{pmatrix} \Omega_s & \frac{\Omega_{RF}}{\sqrt{2}}\cos(\omega t) & 0 \\ \frac{\Omega_{RF}}{\sqrt{2}}\cos(\omega t) & 0 & \frac{\Omega_{RF}}{\sqrt{2}}\cos(\omega t) \\ 0 & \frac{\Omega_{RF}}{\sqrt{2}}\cos(\omega t) & -\Omega_s \end{pmatrix}\begin{pmatrix} c_{-1}(t) \\ c_0(t) \\ c_1(t) \end{pmatrix}. \tag{2.15}$$

In absence of RF coupling, the stationary solution of (2.15) are the three *bare* m_F states ($\{-1, 0, 1\}$) with the corresponding energies $\{\hbar\Omega_s, 0, -\hbar\Omega_s\}$. The off-diagonal terms mix the bare states into new states **dressed** by the RF field, which are solution of Eq. (2.15).

2.2.2.2 Rotating Wave Approximation

The simplest way to solve Eq. (2.15) consists in making the substitution

$$c_{-1}(t) = \tilde{c}_{-1}(t)e^{-i\omega t}, \tag{2.16}$$

$$c_0(t) = \tilde{c}_0(t), \tag{2.17}$$

$$c_1(t) = \tilde{c}_1(t)e^{i\omega t}, \tag{2.18}$$

which is equivalent to moving to a frame rotating at the frequency of the rf photons. Provided the rf Rabi frequency Ω_{RF} and the detuning $\delta(\vec{r}) \equiv \omega - \Omega_s$ are both small compared to the static Rabi frequency Ω_s, the "rapidly oscillating terms" at $\sim 2\omega$ can be neglected (rotating wave approximation, RWA). This yields the time-independent

Hamiltonian

$$H_{\mathrm{RWA,rot.fr.}} = hbar \cdot \begin{pmatrix} -\delta & \frac{\Omega_{\mathrm{RF}}}{2\sqrt{2}} & 0 \\ \frac{\Omega_{\mathrm{RF}}}{2\sqrt{2}} & 0 & \frac{\Omega_{\mathrm{RF}}}{2\sqrt{2}} \\ 0 & \frac{\Omega_{\mathrm{RF}}}{2\sqrt{2}} & \delta \end{pmatrix}. \tag{2.19}$$

The new "dressed" energy levels

$$V\left(\vec{r}\right) = m'_{\mathrm{F}}\hbar\sqrt{\delta^2\left(\vec{r}\right) + \frac{1}{4}\Omega^2_{\mathrm{RF}}\left(\vec{r}\right)}. \tag{2.20}$$

arising from the coupling of the atom to the magnetic field are found by diagonalizing the RWA Hamiltonian. Their are labeled by the new quantum number $m'_{\mathrm{F}} \in \{-1, 0, 1\}$. Inserting the approximate expression for the static field

$$\vec{B}_{\mathrm{s}}\left(\vec{r}\right) = -Gr\left(\sin\theta\hat{e}_x + \cos\theta\hat{e}_y\right) + B_0\hat{e}_z, \tag{2.21}$$

the RWA potential reads, in polar coordinates [55]:

$$V_{\mathrm{RWA}}\left(r,\theta\right) = m'_{\mathrm{F}}\kappa\sqrt{\left(B_{\mathrm{s}} - \frac{\hbar\omega}{\kappa}\right)^2 + \left(\frac{B_{\mathrm{RF}}}{2\left|B_{\mathrm{s}}\right|}\right)^2\left[B_0^2 + G^2r^2\left(\cos\alpha\sin\theta + \sin\alpha\cos\theta\right)^2\right]}, \tag{2.22}$$

where α is the angle between the direction of the rf magnetic field and the vertical axis:

$$\vec{B}_{\mathrm{RF}} = B_{\mathrm{RF}}\left(-\sin\alpha\hat{e}_x + \cos\alpha\hat{e}_y\right). \tag{2.23}$$

(see Fig. 2.8).

The static potential is approximately harmonic and transversely isotropic. If the rf amplitude is increased (keeping the rf frequency constant), the potential smoothly becomes anisotropic and flattens along a direction tilted by $-\alpha$ with respect to the x-axis. In Refs. [12, 13, 33], we took advantage of the anisotropy and anharmonicity induced by weak rf dressing to single out the two lowest vibrational levels and manipulate non-classical motional states of a trapped BEC. The axis of splitting (red line in Fig. 2.8) corresponds to the direction where the quadruopole component of the static magnetic field is parallel to the rf field [59].

Above a certain critical value B_{c} of the rf dressing amplitude, a potential hump emerges at the center of the trap, creating two minima along the splitting axis. If the rf intensity is further increased, the distance between the minima gets larger while the potential barrier rises. This geometry hence allow to create a tunable double well controlled by the amplitude[14] of the rf field. In Ref. [55], Lesanowsky et al. give

[14] It is also possible to split the potential by ramping the rf frequency towards the Larmor frequency of the static trap, as was done for example originally in Ref. [58].

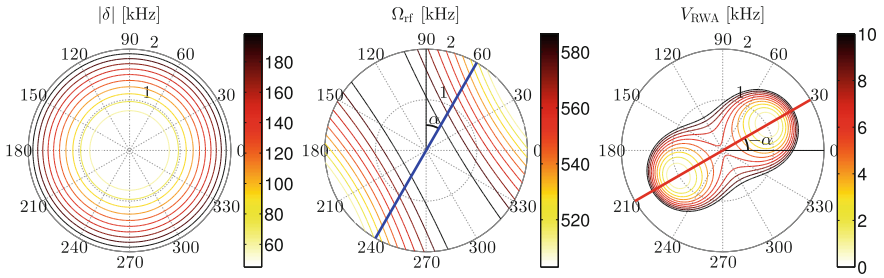

Fig. 2.8 Dressed double-well potential within the RWA. All energies are given in kHz, polar representation in the transverse (x, y) plane (polar radius in μm, polar angle in °). *Left* Detuning term. For a negative detuning ($\omega < \Omega_s$), it simply corresponds to the transversely isotropic parabola of the static potential. *Center* RF Rabi frequency. *Blue line* direction of polarization of the RF field ($\alpha = -30°$). The coupling to the RF breaks the polar symmetry by creating a potential barrier oriented along $-\alpha$ with respect to the y axis. *Right* The resulting RWA potential (Eq. (2.22)) exhibits two local minima along an axis (*red line*) tilted by an angle $-\alpha$ with respect to the x axis. The origin of energies is chosen at the minima of the potential. Same parameters as in Sect. 2.2.1.2 and $\delta = -2\pi \times 30$ kHz and $B_{RF} = 0.85$ G (Color figure online)

useful approximate expressions for the position $\pm r_0$ of the potential minima, the angular trap frequency ω_{dw} of each well along the splitting axis, the correction to the trap bottom B_{TB} and the critical splitting field B_c:

$$r_0 = \frac{1}{\sqrt{2}G}\sqrt{B_{RF}^2 - B_c^2}, \tag{2.24}$$

$$\omega_{dw} = \sqrt{\frac{\kappa}{mB_{TB}}}\frac{G^2 r_0}{B_0}, \tag{2.25}$$

$$B_{TB} = \frac{B_{RF}}{2}\sqrt{1 - \frac{\hbar\delta_0}{\kappa B_0}}, \tag{2.26}$$

$$B_c = 2\sqrt{-B_0\frac{\hbar\delta_0}{\kappa}} \tag{2.27}$$

($\delta_0 \equiv \omega - \kappa/\hbar B_0$ is the detuning at the minimum of the static trap. For our parameters, $\delta_0 < 0$). Equations (2.24)–(2.27) do not always give accurate quantitative predictions, but they capture the right dependence on the rf amplitude B_{RF} and the detuning δ_0.

Conveniently, the transverse double-well potential can generally be well approximated by the simple polynomial [59]

$$V_{DW} = bx^2 + dx^4. \tag{2.28}$$

It is important to keep in mind that when tuning the double well with one control parameter only (in our case the rf dressing amplitude), r_0 and ω_{dw} cannot be adjusted independently. We will see in Sects. 3.4.1 and 3.6.1 that this sets some constraints on ensuring adiabatic motion of the condensate in the double well.

It is also interesting to note that Eq. (2.22) allows also to realize a double well with positive detuning ($\hbar\omega > \kappa B_0$). The main difference is that the spatial dependence of the detuning term has the shape of the bottom of a bottle-of-wine, with a "resonant ring" of points where the detuning term vanishes ($\Omega_s(\vec{r}) = \omega$). This causes a larger well spacing than in the negative detuning case, for the same rf amplitude (see Eq. (2.24)), but also a higher sensitivity of the well position to noise on the Ioffe field. For a full analysis of the effects of noise on the double well, see the Ph.D. thesis of Schumm [8].

2.2.2.3 Implementation

The rf magnetic field is induced by AC currents sent through two wires (width: 10 μm) parallel to the main trapping wire, located on each side at a distance of $l = 55\,\mu\text{m}$ (see Fig. 2.6, right panel). Peak-to-peak intensities up to ∼100 mA can be sent through each wire, resulting in rf field amplitudes up to ∼2.5 G. In first approximation, the rf field can be considered uniform over the region where the atoms are trapped. Its polarization can be tuned by varying the relative intensity between both wires as well as their relative phase

$$\begin{aligned} I_{\text{RF1}} &= I_1 \left(\cos \omega t\right), \\ I_{\text{RF2}} &= I_2 \left(\cos \omega t + \phi_{12}\right), \end{aligned} \tag{2.29}$$

where ω is the angular frequency of the RF (by convention, the amplitudes $I_1, I_2 \geq 0$). To create double-well potentials with an arbitrary splitting axis in the (x, y) plane, the rf field must be linearly polarized, meaning that $\phi_{12} = 0$ or π. To rotate the double well in the (x, y) plane by an angle $-\alpha$ with respect to the horizontlal (x)-axis (see Fig. 2.8), $\vec{B}_{\text{RF}}$ must be rotated by an angle $+\alpha$ with respect to the vertical (y)-axis (see Fig. 2.6, right panel). To keep the well spacing constant when changing α, the amplitudes I_1, I_2 and the relative phase ϕ_{12} must obey

$$\begin{aligned} I_1 &= I_0 \left|\cos\alpha - \frac{\sin\alpha}{\tan\beta}\right|, \\ I_1 &= I_0 \left|\cos\alpha + \frac{\sin\alpha}{\tan\beta}\right|, \\ \phi_{12} &= 0 \text{ if } \alpha \bmod [\pi] \in [\beta, \beta + \pi/2], \ \phi_{12} = \pi \text{ otherwise.} \end{aligned} \tag{2.30}$$

Here $\tan\beta = d/l = 42.5°$ and I_0 is the amplitude in each wire for a vertical polarization ($\alpha = 0$), as required for a horizontal double well: $I_1 = I_2 = I_0, \phi = \pi$. Note that the polarization axis can be rotated on $[0, 2\pi]$ without discontinuity of the current because each time ϕ_{12} jumps between 0 and π, either I_1 or I_2 is equal to 0.

To achieve full control over amplitudes and phase, each rf wire is connected to a separate output of the digital arbitrary waveform generator. Although it can be programmed to generate arbitrary signals, we used it only to produce sinusoidal

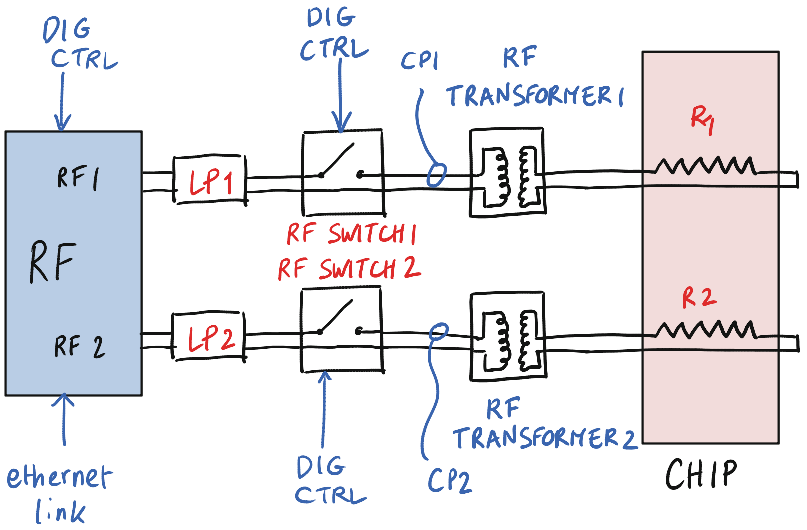

Fig. 2.9 Schematics of the rf electronics. The two rf microwires, with resistance $R_{1,2} \approx 44\,\Omega$ are connected each to one output of the digital arbitrary waveform generator through a low-pass filter ($LP_{1,2}$), a rf switch (MiniCircuits ZX80-DR230-S+) and a 1:1 rf isolation transformer (MiniCircuits T1-1T) to ensure a floating ground. The rf source is controlled digitally through an Ethernet link and can be triggered with a TTL signal. Both channels ($RF_{1,2}$) can be controlled independently. Two low pass filters (cutoff frequency: 1.9 MHz) are used to suppress higher harmonics of the DDS generator. The rf switches can also be triggered, bust most of the time the switching on and off was performed using the rf output. Two alternative current probes (Tektronix CT-6, $CP_{1,2}$) were used to monitor the rf currents on an oscilloscope. Note that although the two rf circuits are in principle identical, they may have different response functions, so that the current balance and the relative phase have to be adjusted carefully on a common probe

signals with time-dependent amplitudes. Figure 2.9 shows a schematics of the RF control electronics. The main limitation to the complexity of the rf control sequence is set by the capacity of the memory of the digital RF source. Although basic patterns, such as a period of a sine wave at constant amplitude, can be indefinitely looped, the rf amplitude *ramps* had to be programmed point by point. To allow decreasing the sampling rate of the arbitrary waveform generator without distorting the signal, low-pass filters (cutoff frequency: 1.9 MHz) were added at the output of each rf channel. The maximum ramp duration for our rf dressing carrier frequency of 880 kHz allowed a maximum total ramp duration (for each channel) of more than 55 ms, limited by the size of the memory. An analog control of the amplitude of the RF source is also available, but it doesn't allow tuning each output independently, as needed to turn the polarization of the RF field, and it is expected to be noisier than the sole digital control.

For the experiments presented in the next chapters, RF currents up to $I_0^{\max} = 79.5$ mA pp (in the case of horizontal splitting, $\alpha = 0$) were used. In the rest of this thesis, instead of giving the absolute value of the current in mA pp, we will often refer

to the RF amplitude $\mathrm{RF}_{\mathrm{Amp}}$ in units of $I_0^{\max}$ ($0 \leq \mathrm{RF}_{\mathrm{amp}} \leq 1$). The corresponding values of $I_{1,2}$ and ϕ_{12} for a tilted RF polarization are given by Eq. (2.30).

2.2.2.4 Beyond the Rotating Wave Approximation

For the dressed potential presented in this thesis, $|\delta| = 30$ kHz $\ll \Omega_{\mathrm{s}} = 910$ kHz at the center of the trap. Nevertheless, high rf amplitudes, up to $\Omega_{\mathrm{RF}} \gtrsim \Omega_{\mathrm{s}}$ are commonly used to achieve large splitting distances ($2r_0 \sim 4$ μm). It is therefore necessary to compute the dressed potential beyond the RWA. The standard method to solve a Schrödinger equation with any periodic, time-dependent Hamiltonian has been given by Shirley in 1965 [66]. In our case, it consists in transforming the system of three differential equations (2.15) into an infinite system of linear equations with time-independent coefficients. This is achieved by expanding the time-dependent coefficients of the wavefunction as Fourier series

$$c_{-1}(t) = \sum_{n\in\mathbb{Z}} c_{-1}^{(n)} e^{-i(n+1)\omega t}, \tag{2.31}$$

$$c_0(t) = \sum_{n\in\mathbb{Z}} c_0^{(n)} e^{-in\omega t}, \tag{2.32}$$

$$c_1(t) = \sum_{n\in\mathbb{Z}} c_1^{(n)} e^{-i(n-1)\omega t}. \tag{2.33}$$

Solving Eq. (2.15) (for each point of space) is then exactly equivalent to diagonalizing the infinite-dimension matrix

$$M = \begin{pmatrix}
\ddots & & & & & & & & & & & & & \\
0 & 0 & 0 & a+\omega & b & 0 & 0 & 0 & 0 & b & 0 & 0 & 0 & 0 \\
0 & 0 & 0 & b & 0 & b & 0 & 0 & 0 & 0 & b & 0 & 0 & 0 \\
0 & 0 & 0 & 0 & b & -a+\omega & 0 & 0 & 0 & 0 & 0 & 0 & 0 & 0 \\
0 & 0 & 0 & 0 & 0 & 0 & a & b & 0 & 0 & 0 & 0 & b & 0 \\
b & 0 & 0 & 0 & 0 & 0 & b & 0 & b & 0 & 0 & 0 & 0 & b \\
0 & b & 0 & 0 & 0 & 0 & 0 & b & -a & 0 & 0 & 0 & 0 & 0 \\
0 & 0 & 0 & 0 & 0 & 0 & 0 & 0 & 0 & a-\omega & b & 0 & 0 & 0 \\
0 & 0 & 0 & b & 0 & 0 & 0 & 0 & 0 & b & 0 & b & 0 & 0 \\
0 & 0 & 0 & 0 & b & 0 & 0 & 0 & 0 & 0 & b & -a-\omega & 0 & 0 \\
 & & & & & & & & & & & & & \ddots
\end{pmatrix}, \tag{2.34}$$

with

$$a \equiv \Omega_{\mathrm{s}}, \tag{2.35}$$

$$b \equiv \frac{\Omega_{\mathrm{RF}}}{2\sqrt{2}}. \tag{2.36}$$

M consists of 3×3 diagonal blocks (for example, red block in the center) and off-diagonal terms (blue). M has an infinite number of eigenvalues which, due to the invariance by the transformation $\omega \rightarrow p + \omega$ (for any integer p) are all equal to one of three principal eigenvalues, modulo ω. In practice, it can be diagonalized approximately by truncating M to a finite sized matrix and keeping the three central eigenvalues.

The physical meaning of these blocks becomes obvious when writing the magnetic field in the formalism of second quantization (see for example Ref. [67]). They are associated to processes implying the exchange of more than one rf photon. Diagonalizing the full quantum-mechanical Hamiltonian shows that the dressed states are grouped into three-state manifolds separated by one rf photon energy (see Fig. 2.10, taken from Perrin's lecture notes [67]). The summation over $\mathbb{Z}$ in the Fourier series expansion implicitly means that the field is assumed to contain an infinite (very large) number of photons, as it is the case with a classical coherent field. Retaining only one Floquet multiplicity (red central block in (2.34)) is equivalent to applying the RWA, see Eq. (2.19) for comparison. It implies neglecting the non-resonant coupling terms

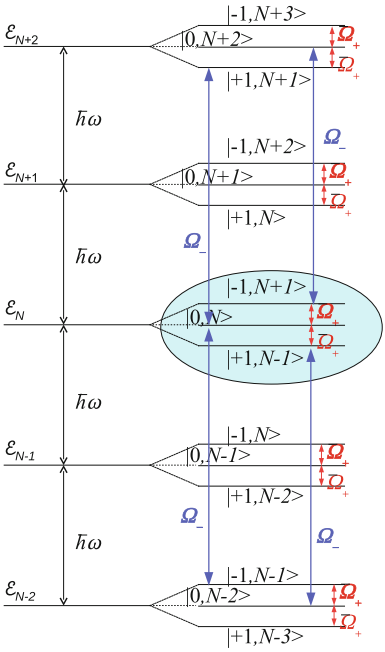

Fig. 2.10 Schematics of the dressed states picture. Taken from Perrin's lecture notes [67]. The dressed states of the atom and the electromagnetic field can be groupped into three-state manifolds separated by one photon energy $\hbar\omega$. In the RWA, only the coupling terms within one manifold are retained (*red arrows* and *red* terms in Eq. 2.34), and each manifold can be treated independently (*blue bubble*). The *blue* terms (*blue arrows*) couple the nth manifold to $n + 2$ and $n - 2$ and are responsible for beyond RWA effects, which cannot be neglected when Ω_{RF} or Δ become comparable to Ω_s and the manifolds are not clearly decoupled (Color figure online)

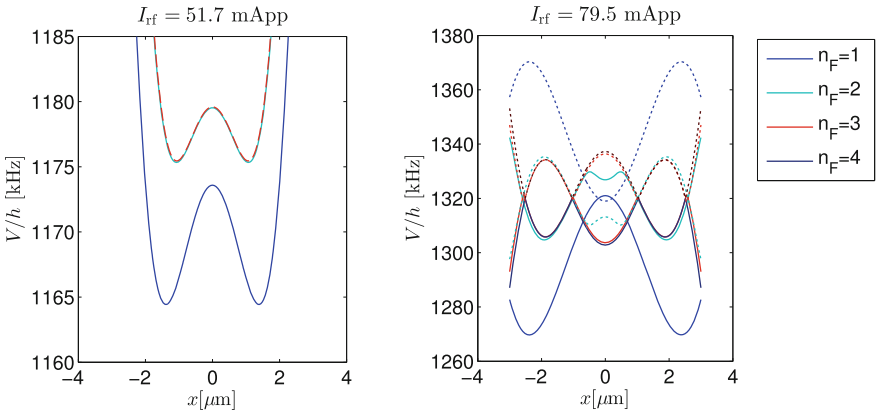

Fig. 2.11 Beyond RWA calculation of the dressed potential. *Left* Potential computed retaining $n_{\rm F} = 1, 2, 3$ Floquet multiplicities at a moderate rf intensity. Taking into account the first order correction to the RWA ($n_{\rm F} = 2$) differs significantly from the RWA result ($n_{\rm F} = 1$). However, increasing $n_{\rm F}$ above 2 doesn't improve much the result. *Right* (For each $n_{\rm F}$, both $m'_{\rm F} = \pm 1$ are represented by a *full* and *dashed line* respectively). For even higher rf intensities, needed for the full separation of the clouds, the coupling between the multiplicities leads to avoided crossings which complicate the calculation of the potential experienced by the atoms. Whether or not the atoms see the avoided crossing depends on their velocity (see Sect. 2.2.1.1)

to the $n+2$ and $n-2$ multiplicities (blue terms in (2.34) and blue arrows in Fig. 2.10). This is valid as long as the detuning is small enough so that the multplicities do not overlap, and as long as the rf Rabi frequency is weak enough to neglect the coupling between different multiplicities. In practice, for our parameters, it is enough to retain up to $n_{\rm F} = 5$ Floquet multiplicities for the numerical computations (see Fig. 2.11).

2.2.3 *Characterization of the Potential and Calibration of the Simulations*

The quantitative description of the dynamics of the condensate in the double well requires a precise knowledge of the shape of the potential. This is achieved by computing it as explained in the previous section. The parameters of the simulations are adjusted using measurements of the trap. This section describes the whole calibration procedure which has been used to simulate the traps in which the experiments of Chap. 3 have been performed. The good agreement between measurement and simulations of many different quantities is a convincing demonstration of the reliability of the calibration procedure. This section is organized as follows: first, the calibration of the static trap is presented, then that of the rf dressing and of the dressed potentials.

2.2.3.1 Static Trap

To calibrate the static trap, we use the fact that the trap bottom V_{TB} depends essentially on the Ioffe field B_0 and the current in the longitudinal confinement wires I_{h} (see Eq. 2.10), while the radial trap frequency depends mainly on the bias field B_{s} and the current I in the main trapping wire (with a weak dependence on the Ioffe field, see Eq. 2.9). The trap bottom is measured by means of rf spectroscopy, while the trap frequencies along the three eigenaxes of the potential are measured by exciting dipolar oscillations of a condensate (see Fig. 2.12).

Trap Bottom Spectroscopy

The value of the Larmor frequency at the center of the trap $\nu_{\mathrm{TB}} = V_{\mathrm{TB}}/h$ is probed by means of rf spectroscopy [68]. We use the same rf electronics as for the evaporative cooling, but strongly reduce the rf intensity to resonantly couple atoms between the trapped state $m_{\mathrm{F}} = -1$ and the untrapped state $m_{\mathrm{F}} = 0$ without dressing the potential. We apply a $T = 20$ ms pulse rf pulse at constant frequency ν_{RF} onto the trapped condensate. At resonance, i.e. when $\nu_{\mathrm{RF}} = \nu_L$, atoms are maximally coupled

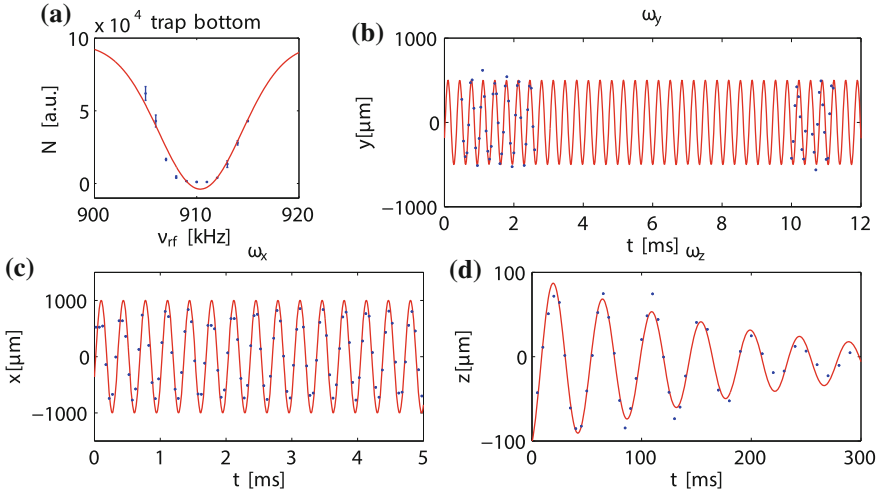

Fig. 2.12 Static trap characterization. **a** Trap bottom spectroscopy. A weak rf pulse is applied to resonantly outcouple atoms from the trap. The maximum losses (dip) is achieved when the rf frequency is equal to the Larmor frequency in the center of the trap. The *red line* is a guide to the eye. **b**–**d** Trap frequencies in transverse horizontal (**b**), transverse vertical (**c**) and longitudinal (**d**) direction, obtained by exciting dipolar oscillations (sloshing) and measuring the position of the center-of-mass after expansion. Note the difference of time scale between transverse and longitudinal oscillations, as well as the damping of the longitudinal sloshing. It is probably due to the anharmonicity of the longitudinal potential caused by corrugation, as well as technical heating. The values of the trap parameters are summarized in Table 2.1 (Color figure online)

to $m_F = 0$ and fall off the trap. After a few ms of holding time ensuring that the outcoupled atoms leave the imaging region, the remaining atoms are released and counted. The trap bottom is inferred from the frequency of the loss dip in the number of remaining atoms when ν_{RF} is scanned (see Fig. 2.12a).

The width of the loss dip is influenced by several effects, including: power broadening (the intensity of the rf spectroscopy pulse has to be chosen weak enough), the resolution in frequency (the pulse duration $T = 20$ ms imposing $\Delta\nu = 1/T = 0.05$ kHz was chosen in order to average over one period of the characteristic 50 Hz electric noise), the stability of the trap bottom (dominated by the stability of the Ioffe field B_0, see [1]), the chemical potential of the condensate ($\mu/h \sim 1$ kHz) and the gravitational sag [69]. For most experiments, the typical rms width of the static trap spectroscopy was about 4 kHz.

Note that the same technique can be used in rf dressed trap to measure the effective trap bottom by coupling atoms between the trapped dressed state and $m'_F = 0$. In Ref. [70], this technique has been used to demonstrate the existence of beyond RWA resonances between different Floquet multiplicities. We observe that resonances in the dressed potentials are typically twice narrower than in the static trap (see Fig. 2.14, upper panel). This might come from the fact that the effective trap bottom is twice less sensitive to fluctuations of B_0 (see Eq. (2.26)), because a variation of B_0 is partly compensated by a variation of the detuning, similarly to what has been investigated in Ref. [71].

Trap Frequencies

The trap frequencies are probed by exciting dipolar (sloshing) oscillations of the condensante along each of the three eigenaxis of the nearly harmonic potential.

In the **vertical transverse direction** (y), a small kick is applied by suddenly ($< 25\,\mu$s) varying the current in the main trapping wire by $\sim$1 %. It excites a center-of-mass oscillation of amplitude approximately four times the transverse oscillator length. The motion is recorded by imaging the atoms in the (z,y) plane with the absorption imaging system (see Sect. 2.3.1) after 17 ms tof (see Fig. 2.12b).

In the **horizontal transverse direction** (x), the condensate is prepared in one well of a horizontal (dressed) double-well potential (this is achieved by slowly splitting the condensate in the vertical direction, and then leveling the double well). The rf current is then rapidly ramped off so that the position of the cloud does not change. The atoms find themselves displaced horizontally with respect to the center of the static trap and start oscillating (see Sect. 3.2.2.1. The motion is recorded by imaging the atoms with the "light sheet" imaging system Sect. 2.3.2 in the (x, y) horizontal plane after 46 ms of tof (see Fig. 2.12c).

The **longitudinal frequency** ω_z is measured by slowly, slightly distorting the longitudinal potential, and returning abruptly to the original potential. This is achieved by means of a weak current pulse produced by a wire (see Fig. 2.6) orthogonal to the main trapping wire. The measurement of the slow longitudinal sloshing (typical frequency: 20 Hz) is limited by its damping time (typically 200 ms, see Fig. 2.12d),

Table 2.1 Trap calibration

Measured parameters	
Trap bottom V_{TB}/h	910 ± 1 kHz
Horizontal transverse trap freq. $\omega_x/2\pi$	2.97 ± 0.01 kHz
Vertical transverse trap freq. $\omega_y/2\pi$	2.98 ± 0.01 kHz
Longitudinal trap freq. $\omega_z/2\pi$	22.3 ± 0.3 Hz
Settings used for simulations	
Current in main trapping wire I	1 A
Current in longitudinal confinement wires I_{h}	0.5 A
Bias field B_{b}	29.5 G
Ioffe field B_0	1.17 G
Max. rf current (in each wire) $I_0^{\max}$	79.5 mApp
rf relative phase ϕ_{12}	$-2°$

Upper part measured trap parameters, with the corresponding experimental uncertainty. *Lower part* Parameters used in the chip trap simulations

associated to the heating of the cloud and the anharmonicity caused by potential corrugation.

Calibration of the Static Trap Simulations

The currents in the main trapping wire and in the longitudinal confinement wire I and I_{h} are measured with a precision multimeter meter[15] and the values are used for computation of the potential. The value of B_0 for the simulation is adjusted to match approximately the measured trap bottom. Both values of B_0 and B_{b} are iteratively fine-tuned to reproduce exactly the measured radial trap frequencies and trap bottom. This leaves some indeterminacy between B_0 and B_{b}, which can then be lifted from the measurements of the dressed trap (see next section). The potential simulations usually strongly underestimate the longitudinal trap frequency (typically by a factor 4) because they do not take corrugation into account. Table 2.1 summarizes the values of the measured trap parameters and the corresponding settings for the simulations.

2.2.3.2 RF Dressing

Once the static trap has been characterized, the rf dressing must be calibrated. The first step is to characterize and adjust the rf amplitudes I_1 and I_2 in each wire as well as the relative phase ϕ_{12} (see Eq. (2.29)). The second step is to adjust and check these parameters in the simulation by comparing them to measurements of

[15] Keithley 2000 digital Multimeter.

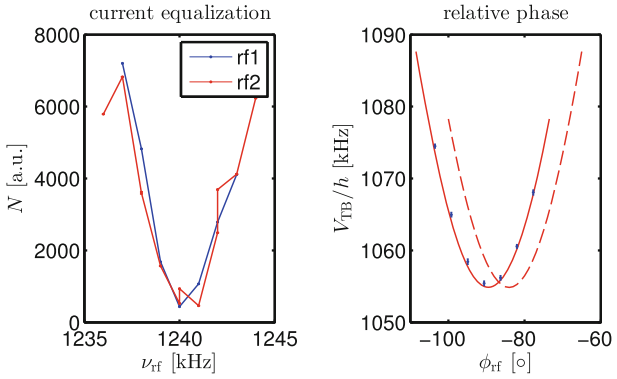

Fig. 2.13 Adjustment of the RF intensity balance and the relative phase. *Left* The trap bottom spectroscopies for a trap dressed by only RF wire at a time overlap, ensuring that $I_1 = I_2$. *Right* The effective trap bottom is measured as a funtion of the relative phase ϕ_{12} between the two wires (*blue dots*). The result of the simulations has to be shifted by approximately 6° to match the measurement. This is probably caused by some differential filtering in the RF electronics of each channel (Color figure online)

the effective trap bottom, trap frequencies, well spacing etc. in a series of dressed potentials obtained for different rf intensities.

Balance of the RF Currents in the Two Wires

The rf generator produces a given AC voltage. Since the resistance of each wire (including the leads and the rf electronics for each output port) may be different, the currents have to be balanced using a common probe. The high-frequency current probes mounted on each wire give an estimate of the currents, but the atoms are a much more precise probe of the magnetic field. For some arbitrary intensity I_0, the effective trap bottom is measured by rf spectroscopy with one rf wire on at a time. The voltage of each output port of the rf source is tuned to equalize the trap bottoms (see Fig. 2.13, left panel), ensuring $I_1 = I_2$. Furthermore, comparing the measured value of the trap bottom to simulations enables to calibrate the absolute values of $I_{1,2}$.

Relative Phase Between the RF Wires

The control of the relative phase between the two rf wires is important to ensure the right linear polarization to turn the axis of the double well. Different delays due to different filtering in the rf leads may shift ϕ_{12} with respect to the value defined by the rf generator. This effect is accounted for by correcting the phase difference between the two output of the rf generator by an amount which is determined by

measuring the dependence of the trap bottom with respect to the relative phase (see Fig. 2.13, right panel). The dependence of the effective trap bottom with ϕ_{12} is not trivial but can be simulated. It is related to the relative contribution of the σ^+ and σ^- polarization which couple the different m_F states. Note that the geometry of the dressed potential can change between a double well and a ring trap, depending on ϕ_{12} [55]. We found that ϕ_{12} had to be corrected by 6° with respect to the nominal value to get a linear polarization. For the experiments presented in chapter , this value has been slightly over-corrected. For this reasons, all simulations of the potential were performed with $\phi_{12} = -2°$.

Additional Checks

In principle, the calibration procedure presented above is sufficient to constraint all parameters of the static trap and of the rf dressing. Nevertheless, a series of additional measurements were performed to benchmark the simulations of the potential.

The dependence of the effective trap bottom with the rf amplitude was checked, recovering the linear behaviour given by Eq. (2.26) (see Fig. 2.14).

The transverse trap frequencies in each well of the dressed potentials were also compared to simulations (see Fig. 2.15, left pannel). The vertical trap frequency was measured in the same way as in Sect. 2.2.3.1. The horizontal trap frequency ω_{dw} (Eq. (2.25)) was measured by slightly changing the rf amplitude to excite an oscillation of the spacing between the two parts of the condensate in the double-well. This results in an oscillation of the fringe spacing of the interference pattern measured after tof (see Sect. 3.2.1). Note that in this strongly anharmonic direction, the notion of trap frequency is less obvious, explaining partly the poor agreement of experiment and simulation.

The spacing $d = 2r_0$ between the two wells (Eq. (2.24)) was also inferred from the fringe spacing of the interference patterns. Assuming Gaussian wave packets and a ballistic expansion during a time t, the fringe spacing is

$$\lambda \approx \frac{ht}{dm}. \tag{2.37}$$

It shows a very good agreement with the simulations for strongly split double wells, where the effect of interactions is less significant [58].

Note that for both d and ω_{dw}, the beyond-RWA simulations are in excellent agreement with the dependence on the rf dressing amplitude expected from the approximate RWA expressions (2.24) and (2.25). Fitting them to the data of Fig. 2.15, we found that the critical splitting point is reached for $\mathrm{RF}^{c}_{\mathrm{Amp}} = 0.42$.

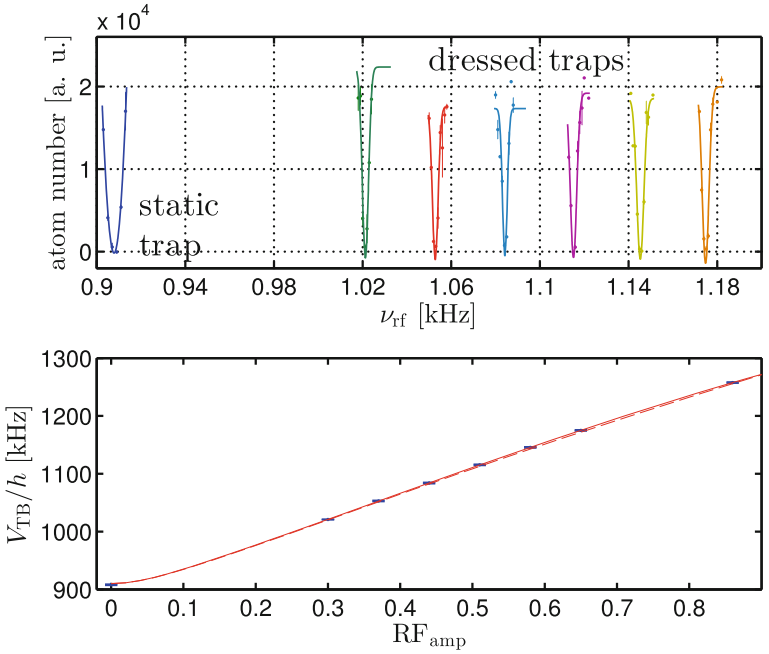

Fig. 2.14 RF amplitude calibration. The effective trap bottom $V_{\rm TB}$ is measured by rf spectroscopy for different values of the amplitude of the rf current ($I_1 = I_2$). *Top panel* rf spectroscopies for 5 values of $RF_{\rm Amp}$ between 0 and 0.65 (five first points of *bottom panel*). Note that the loss dips are narrower in the dressed potentials as compared to the static trap. *Bottom panel* effective trap bottom $V_{\rm TB}/h$ as a function of $RF_{\rm Amp}$, showing good agreement with the beyond RWA simulations. Note that the RWA prediction (*dashed curve*) underestimates the trap bottom by a few kHz only

2.3 Imaging Systems

Most of the experimental information gathered on Bose-Einstein condensates in atomic gases has been obtained by optical measurements, that is to say photographs of the atoms. Notable exceptions are for example the temporally and spatially resolved detection of a BEC of metastable Helium with a microchannel plate [72] or the use of scanning electron microscopy (SEM) [73].

Among the various optical imaging methods used to probe ultracold gases [74], two independent systems are implemented on the Rb2 setup (see Fig. 2.16):

- an absorption imaging system,
- and a fluorescence imaging (often referred to as *Light Sheet*).

Both allow imaging destructively the atom cloud in tof, meaning that for each experimental cycle, the atomic sample can be observed only once. Figure 2.17 shows typical images of condensates taken with both imaging systems. The following section briefly presents both imaging systems, with emphasis on the methods we

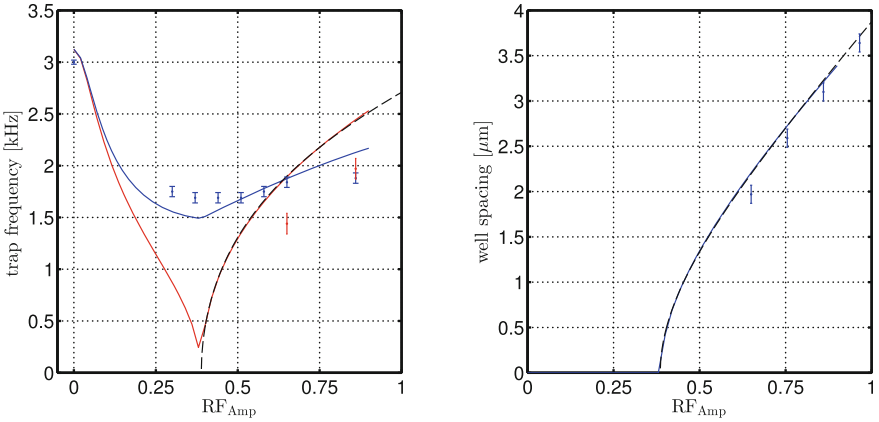

Fig. 2.15 Transverse trap frequencies and well spacing. *Left* Transverse trap frequencies (quadratic term in the Taylor expansion of the potential) in the double-well (*red* ω_{dw} in the direction of splitting, *blue* orthogonal direction) as a function of the rf amplitude. *Points* measurements. *Lines* beyond RWA simulations. *Black dashed* fit of the beyond RWA simulation with the approximate expression (2.25). Note the typical kink of ω_{dw} at the critical value $\mathrm{RF}^{\mathrm{c}}_{\mathrm{Amp}} = 0.42$, corresponding to the splitting point. *Right* Spacing between the potential wells, inferred from (3.2). *Points* measurement. *Blue line* beyond RWA simulation. *Black dashed line* fit of the beyond RWA simulation with the approximate expression (2.24). Note that both quantities are very well described qualitatively by the RWA approximate analytical expressions (Color figure online)

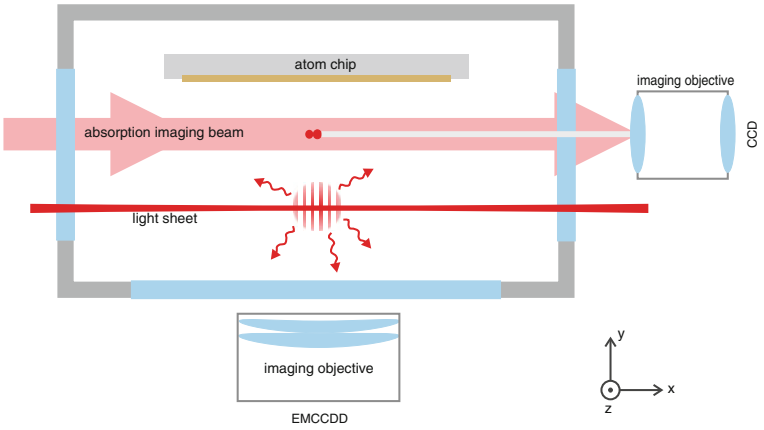

Fig. 2.16 Schematics of the two imaging systems. The absorption beam is oriented along the x-axis to image the atoms in a plane parallel to the long axis of the trap (z). The shadow cast by the atoms is imaged through an objective on a CCD camera. The fluorescence imaging is oriented along the y-axis to image photons scattered by the atoms while falling through the light sheet. Light is collected by an objective located below the chamber and detected by a EMCCD camera. When the BEC is released from a horizontal double well, imaging along (x) integrates over the matter-wave interference pattern, while the fringes can be resolved with the fluorescence imaging system

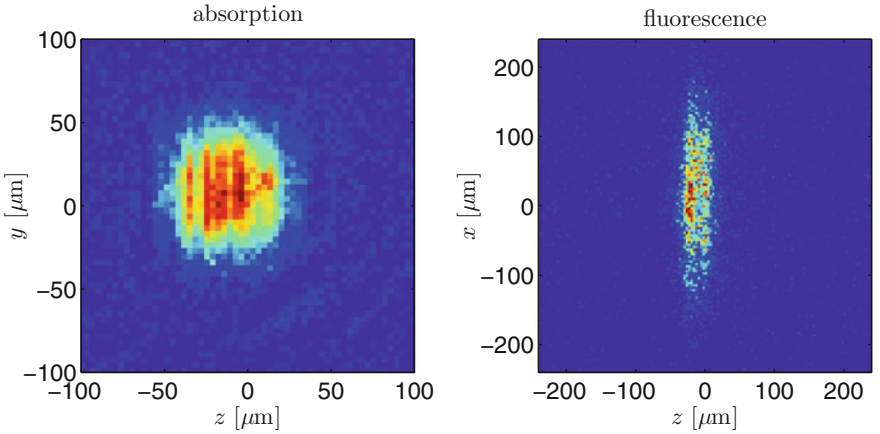

Fig. 2.17 Images of quasi-condensates. Pictures of quasi-BECs with ∼1000 atoms taken 6 ms (absorption imaging system, *left*) and 46 ms (fluorescence imaging systems, *right*) after release from a (in this case single-well) trap. The axes are the same as in Fig. 2.16: (z) is the axis of shallow confinement and gravity is oriented along (y). Note that both pictures exhibit characteristic patterns perpendicular to the (z)-axis. They correspond to density fluctuations emerging in tof as a result of the initial longitudinal phase fluctuations [16]

used to determine the absolute atom number in our condensates. A more detailed description of the hardware as well as the characterization of both imaging systems can be found in the diploma and Ph.D. thesis of Bücker [1, 18] as well as in the Ph.D. theses of Manz [16] and Betz [10].

2.3.1 Absorption Imaging

Absorption imaging is probably the most commonly used imaging technique in cold atom experiments [74]. A comprehensive discussion of absorption imaging on atom chip setups can be found in Ref. [75]. The Ph.D. theses of Gring [76] and Jacqmin [77] contain detailed descriptions of absorption imaging systems implemented in different configurations on atom chip experiments similar to our setup.

The absorption imaging system implemented on Rb2 is oriented along the x-axis to image the atoms in the (y, z) plane. It allows inferring the integrated column density $\tilde{n}(y, z) = \int n(\vec{r})dx$ from the attenuation of a laser beam passing through the atomic cloud [74]. The shadow cast by the atoms is imaged onto a back illuminated Charge Coupled Device camera[16] (CCD) through an objective consisting of two doublet lenses, each operating at near-infinite conjugate ratio. The optics is adjusted to obtain a magnification of $\times 3.78$. The corresponding pixel size (in object space) is $3.44 \times 3.44\ \mu\text{m}^2$. The numerical aperture (NA) of 0.12 determines the diffraction

[16] Princeton Instruments MicroMax 1024 BFT.

limit, which lies slightly below 4 μm. The field of view (3 × 3 mm) allows for tofs up to ∼25 ms. When the cloud is imaged too close to the chip (tof $\lesssim$ 2 ms), unavoidable reflection and refraction of the imaging light on the surface of the chip cause distortions of the image [75]. The fast frame-transfer readout enables taking the absorption and the reference picture within tens of ms, in order to mitigate the effect of mechanical vibrations.

The absorption imaging system can be used to image thermal clouds (after short tofs) or BECs. We use it routinely to monitor center-of-mass oscillations in order to measure trap frequencies (see Sect. 2.2.3.1), image BECs after short tofs (2 ms) to access their *in-situ* density profile, and to measure the atom number in our BECs (see next section). In Ref. [20], it was used to measure density fluctuations (*density ripples*) of expanding 1D quasi-condensates. The fast frame-transfer readout has also been used to image successively atoms in the two hyperfine states $F = 2$ (without repumper) and $F = 1$ (with repumper), which would be necessary for experiments with internal states of a BEC (see Sect. 3.1.2.1).

Note that it cannot be used to image the matter-wave interference patterns obtained from releasing a BEC from a horizontal double well (see Sect. 3.2.1) since the fringes, which are parallel to the (y, z) plane, are integrated out (see Fig. 2.16).

2.3.1.1 Atom Number Calibration by Saturation Absorption Imaging

As we will see in Sect. 3.4.3, precise number-squeezing measurements imply a correct estimation of the absolute atom number in our BECs. So far, N can only be inferred from absorption pictures. For this reason, it is absolutely necessary to characterize our absorption imaging system to obtain a reliable estimation of N.

We followed the approach proposed in Ref. [78], comparing the optical density of identical atomic samples measured at different intensities, well below and above saturation. At resonance, the photon scattering rate of a two-level atom reads

$$\dot{N}_{\mathrm{ph}} = \frac{\Gamma}{2} \frac{I/I_{\mathrm{sat}}}{1 + I/I_{\mathrm{sat}}}, \tag{2.38}$$

where Γ is the natural line width of the optical transition. For the optical transitions of the D2 line of ^{87}Rb, $\Gamma = 2\pi \times 6.07$ MHz [35]. The saturation intensity I_{sat} is connected to the resonant cross section σ_0 through

$$I_{\mathrm{sat}} = \Gamma \frac{\hbar\omega}{\sigma_0}. \tag{2.39}$$

To maximize the absorption signal, we chose to work in the configuration yielding the highest cross section, namely by using σ^+ polarized light to address the cycling transition $F = 2, m_{\mathrm{F}} = 2 \leftrightarrow F' = 3, m_{\mathrm{F}} = 3$. For this transition, $\sigma_0 = 2.91 \times 10^{-9}\,\mathrm{cm}^2$ and $I_{\mathrm{sat}} = 1.67\,\mathrm{mW/cm}^2$ [35]. Note that to access this transition, we must first repump the atoms (see Sect. 2.1.5) from $F = 1$ to $F' = 2$. The repumper light,

which is superimposed to the path of the imaging beam, is shone for ∼200 μs right before the imaging pulse.

In practice, however, the actual cross section is likely to be smaller than this value, depending on the exact configuration of the beam direction, polarization and the orientation of the magnetic field defining the quantization axis. To ensure that the atoms experience a σ^+ polarization, we use the small Bias coil (see Sect. 2.1.2) to apply a uniform magnetic field parallel to the optical axis (see Ref. [1]). Nevertheless, besides the imperfect alignment of the quantization field with respect to the optical axis, transient pumping effects are also expected to slightly reduce the effective cross section.

Following Ref. [78], we take into account the specific configuration of our absorption imaging by defining an effective cross section

$$\sigma_{\text{eff}} = \frac{\sigma_0}{\alpha} \tag{2.40}$$

with $\alpha \geq 1$ and the corresponding effective saturation intensity $I_{\text{sat}}^{\text{eff}} = \alpha I_{\text{sat}}$.

From the scattering rate (2.38), we can express the attenuation of a laser beam passing through an atomic cloud. After it has traveled through an infinitesimal distance dx in a cloud of density $n(\vec{r})$, the intensity of the imaging beam drops by

$$\mathrm{d}I = -\sigma_{\text{eff}} \frac{I}{1 + I/I_{\text{sat}}^{\text{eff}}} n(\vec{r}) \mathrm{d}x. \tag{2.41}$$

Integrating Eq. (2.41), we can express the optical density (OD) $\sigma_0 \tilde{n}$ as the sum of two terms:

$$\sigma_0 \tilde{n}(y, z) = \underbrace{\alpha \ln\left(\frac{I_{\text{i}}}{I_{\text{f}}}\right)}_{\log} + \underbrace{\frac{I_{\text{i}} - I_{\text{f}}}{I_{\text{sat}}^0}}_{\text{sat}}, \tag{2.42}$$

where I_i and I_f are respectively the intensity of the imaging beam before and after propagation through the atomic cloud. Far below the saturation intensity ($I_i \ll I_{\text{sat}}$), the logarithmic term dominates. This is the regime where most absorption imaging systems are operated. The column density is given by the Beer-Lambert law

$$\tilde{n}(y, z) = \sigma_{\text{eff}} \ln\left(\frac{I_i}{I_f}\right), \tag{2.43}$$

which has the important property that $\tilde{n}$, and hence the total atom number $N = \int\int \tilde{n} \mathrm{d}y \mathrm{d}z$ do not depend on the intensity of the imaging beam, provided it is sufficiently small.[17] However, it depends linearly on α, meaning that the atom number computed by absorption might be systematically underestimated when using the theoretical value σ_0 of the resonant cross section.

[17] Typically, this is true as long as $I \lesssim I_{\text{sat}}/10$.

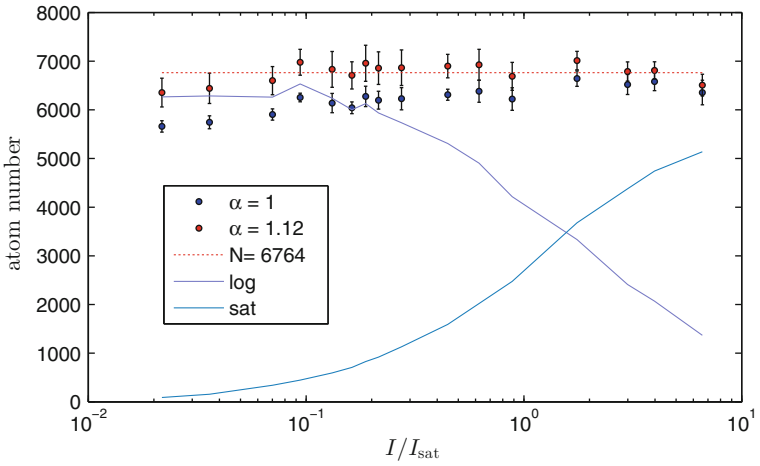

Fig. 2.18 Calibration of the absolute atom number in absorption. Measured atom number N in a BEC for different imaging beam intensities. For each intensity, the atom number was computed using Eq. (2.42). *Black points* atom number assuming $\alpha = 1$. *Red points* atom number corrected for $\alpha = 1.12$, in order to ensure a constant N regardless of I/I_{sat} (note that the points corresponding to the two lowest intensities, for which the pictures were very noisy, were not used to estimate α). *Continuous lines* logarithmic (*lavender blue*) and saturation (*medium turquoise*) terms (the logarithmic term has been computed for $\alpha = 1.12$). Both contributions are equal for $I = I_{\mathrm{sat}}^{\mathrm{eff}}$

The second term becomes dominant above saturation, i.e. when $I_i, I_f \gg I_{\mathrm{sat}}$. It does not depend on the effective cross section, because if all the atoms are saturated, their scattering rate is simply equal to $\Gamma/2$.

The method proposed in Ref. [78] consists in inferring α from absorption pictures of identical atomic clouds taken at different intensities, spanning a large range below and over I_{sat}. It relies on the assumption that (a) the atom number of all the observed atomic samples is the same, (b) the correction factor α is independent on the intensity of the probe beam. While the first assumption depends on the atom number stability of the experiment, which for us is of the order of 10 %, the second one was checked within our group by solving the optical Bloch equations for different imaging configuration close to ours.

We calibrated our absorption imaging system by taking images of a BEC with ∼6000 atoms at different intensities ranging from 0.02 I_{sat} to 8 I_{sat}. The number of scattered photons N_{ph} was kept approximately constant by adjusting the imaging pulse duration. We also checked experimentally that no significant Doppler shift was reducing the effective cross section even for the largest number of photons ($N_{\mathrm{ph}} \approx 300$).[18]

Figure 2.18 shows an example of the atom numbers computed with the full Eq. (2.42). Assuming $\alpha = 1$ (black points), we observed that the computed N was slightly increasing with increasing intensity, indicating that the logarithmic term in Eq. (2.42) was underestimated. Repeating the measurement for different values of

[18] It needs approximately 350 scattered photons for a ^{87}Rb atom to be Doppler-shifted by $\Gamma/2$.

N_{ph}, we found that the values of α ensuring a constant atom number (red points) was lying between 1.05 and 1.15. Furthermore, independent measurements of the axial Thomas-Fermi radius of a trapped condensate (see Sect. 1.1.3.3.) confirmed that we can exclude underestimating the atom number by more than 20 %.

2.3.2 *Fluorescence Imaging System (Light Sheet)*

Most of the data presented in the next chapters has been acquired with our fluorescence imaging system [1, 18, 19]. It is aligned along the vertical y-axis to image atoms in the horizontal (x, z) plane. It consists of a thin (waist radius: 20 μm) horizontal "sheet" of resonant (or slightly red-detuned) laser light located roughly 1 cm below the atom chip. When atoms are released from the trap, they expand and fall through the *light sheet* (LS) after a ∼46 ms tof. Each atom typically scatters hundreds of photons during the ∼100 μs it spends in the LS. A small fraction (around 2 %) of the fluorescent light is captured by an objective located below the vacuum chamber, and detected by an electron multiplying CCD camera[19] (EMCCD), yielding a typical sensitivity of $\bar{p} = 15$ detected photons per atom on average.

The LS is created by superimposing two identical counter-propagating laser beams, each of them coupled out of an optical fiber outside the chamber and sent through a cylindrical lens to obtain a highly anisotropic "flat" sheet of light (waist in horizontal direction: 4.5 mm). The optical axis of the LS is rotated by 45° with respect to the x and z-axis. A lin-⊥-lin polarization configuration was chosen to avoid creating an intensity grating, resulting in a polarization grating perpendicular to the optical axis. The total optical power (a few μW) can be adjusted to tune $\bar{p}$. It is actively stabilized against slow drifts by sampling a fraction of the optical power and readjusting the AOM amplitude accordingly every second experimental cycle, i.e. once per minute.

The custom objective [1] was sized in such a way that the geometric spot size and the diffraction limit remain smaller than the object space camera pixel size ($4 \times 4\,\mu\mathrm{m}^2$) over the whole field of view ($2 \times 2\,\mathrm{mm}^2$). An advantage of the LS configuration is that the depth of field can be matched to the thickness of the LS. This allows imaging thermal clouds after long tofs, which are generally larger than the depth of field set by our relatively high NA of 0.34 and would otherwise look blurred. The vertical position of the LS determines the tof. It can be adjusted by means of a translation stage, but changing the tof implies refocussing the optics, so that in practice, conversely to the absorption imaging system, we have to work with a fixed tof (46 ms), although we can adjust the duration of the LS pulse to image slices of the atomic cloud [21]. Imaging several slices of the same atomic cloud should be in principle possible, but is currently limited by the readout speed of the camera.

Currently, the main factor limiting the resolution of our fluorescence imaging system is the diffusion of the atoms in the LS [18]. The atoms perform a random

[19] Andor iXon+ 897.

walk in momentum space due to the stochastic absorption and re-emission events. This result in a real-space spot size for the fluorescence signal coming from each atom of typically 10 μm rms size, whereby the shape of the anisotropic fluorescence pattern depends on the detail of the scattering events.

The main asset of our fluorescence imaging system is its high sensitivity together with a high dynamical range [18], allowing us to detect single atoms as well as dense BECs. For each atom crossing the LS, we detect on average a number of photons sufficiently large so that the probability of not detecting an atom can be made vanishingly small. The mean number of detected photons per atom $\bar{p}$ can be increased by increasing the LS intensity, at the expense of the spatial resolution. We usually worked with $\bar{p} \approx 15$. Together with an extremely low background noise (the CCD chip is thermoelectrically cooled down to $-90\,^{\circ}\mathrm{C}$), our single-atom sensitivity has been a crucial condition to detect strong number squeezing [12, 14], as will be detailed in Sect. 3.2.2.2. It should be noted however that single-atom sensitivity does not mean the ability to resolve atoms in dense clouds, because of our limited resolution. Nevertheless, high signal-to-noise ratio associated with a relatively long tof are particularly advantageous to probe the high-k tails of the momentum distribution of thermal clouds and BECs, and has allowed studying the emission of high-momentum correlated atom pairs [12, 79].

The LS imaging system is oriented as to image the atoms from below, which is well-suited to image matter-wave interference patterns emerging from the recombination of a horizontally split condensate (see Sect. 3.2.1). In particular, it allowed probing the spatial phase correlations of a 1D BJJ [11]. It was also used to demonstrate Hanbury Brown and Twiss (HBT) correlations across the BEC threshold [21].

2.3.2.1 Calibration of Fluorescence Picture

In an EMCCD camera, each photon impinging on a pixel of the CCD chip is converted into a primary electron, which is amplified to a large number (up to about 1000) of secondary electrons. To calibrate the raw fluorescence picture, the gain of the electron multiplying unit is calibrated from a second picture taken immediately afterward, but without light. The second picture hence only contains technical noise, which is essentially due to clock-induced charges, i.e. charges created before the amplification process and therefore indistinguishable from real photons. Nevertheless, since the EM amplification is a stochastic process, the distribution of counts per pixel in the calibration picture can be fitted to retrieve the amplification gain (see Fig. 2.19, left pannel) [19]. It also provides information on the background level and the additional noise added by the readout stage. The fitted values are used to compute the processed fluorescence picture (in photon number/pixel) from the raw picture. An important consequence from the stochastic amplification is that it adds extra shot noise: the variance of the signal on a camera pixel with on average $\bar{s}$ photons is two times $\bar{s}$ (see Sect. 3.4.3.1).

An additional background contribution is caused by stray light from the LS beams. When working with cold condensates well-located in the center of the picture, this

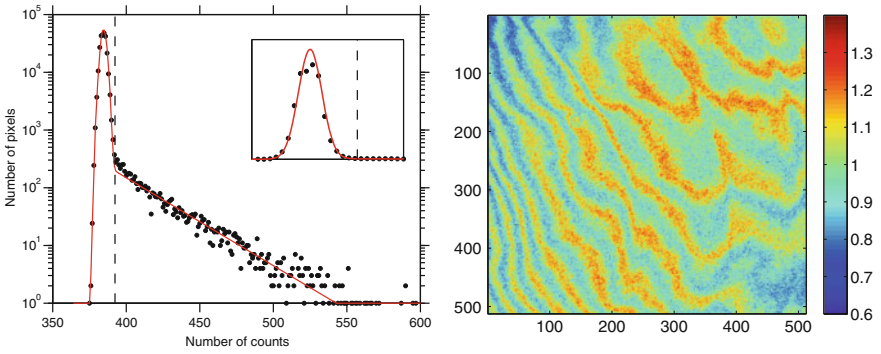

Fig. 2.19 Calibration of the fluorescence pictures. *Left* Taken from Ref. [19]. Distribution of the number of counts per pixel in a single image acquired without any light. The detected signal is only due to CIC. The continuous line is a fit of the distribution (see Ref. [19] for the fit model) allowing to extract the EM gain, the baseline and the readout noise. The *dashed line* marks the threshold of the readout cutoff. The *inset* shows the same distribution in linear scale. *Right* Etaloning. Reflections between the nearly parallel front and back surface of the narrow, back-illuminated CCD chip interfere, causing distortions of the images. Since it is constant over time, etaloning can be characterized from averaging hundreds of images of a hot thermal cloud to ensure uniform illumination, and accounted for as a position-dependent gain factor

usually uniform background can be calibrated from the edges of the images and subtracted. Another, non-uniform, contribution is due to etaloning, i.e. the interference of coherent light on the CCD chip acting as a non uniform Fabry-Perot etalon. While this does not affect significantly the signal integrated over a sufficiently large area, it leads to local distortions of the image. It can be highlighted by averaging hundreds of pictures of a sufficiently hot thermal cloud (to ensure a uniform illumination), see Fig. 2.19. Fortunately, as it doesn't change over time, it can be corrected for, for example to fit the profile of a cloud.

So far, the absolute column density (in atom/pix) cannot be easily deduced from the fluorescence pictures only, although alternative schemes based on the correlation properties of the fluorescence signal are currently being investigated. The average number of detected photons per atom $\bar{p}$ is hence inferred from imaging a series of (typically 20) condensates prepared in the same conditions, alternating between fluorescence and absorption imaging. It yields an uncertainty on $\bar{p}$ of the order of 10 %.

2.4 Conclusion of the Experimental Part

In this chapter, we have presented the apparatus on which the experiments presented in this thesis have been conducted. The main features of our compact ^{87}Rb BEC machine are

- the atom chip, which enable the creation of elongated magnetic traps with transverse frequencies in the kHz range and longitudinal frequencies between 10 and 20 Hz,
- the possibility to apply rf-dressing to manipulate the transverse confinement and realize a tunable double-well geometries,
- a light sheet fluorescence imaging system which allows probing the BECs with single-atom sensitivity.

References

1. R. Bücker, *Twin-atom beam generation in a one-dimensional Bose gas*. Ph.D. thesis, Vienna University of Technology, 2013
2. P. Krüger, *Coherent matter waves near surfaces*. Ph.D. thesis, Heidelberg, 2004
3. S. Wildermuth, *One-dimensional Bose-Einstein condensates in micro-traps*. Ph.D. thesis, Heidelberg, 2005
4. H. Gimpel, *Magnetische Oberflächenfallen für Atom-Interferomete*. Diploma thesis, Heidelberg, 2002
5. C. Becker, *Eine neuartige magneto-optische Falle für Atomchip-Experimente.* Diploma thesis, Heidelberg, 2002
6. S. Haupt, *Setup of a new experiment with ultracold 87Rb Atoms: towards quantum information processing on an atom chip*. Ph.D. thesis, Heidelberg, 2003
7. S. Hofferberth, *Experiments with ultracold atoms and Bose-Einstein condensated in microtraps near surfaces*. Diploma thesis, Heidelberg, 2004
8. T. Schumm, *Bose-Einstein condensates in magnetic double well potentials*. Ph.D. thesis, Université Paris 11, 2005
9. S. Hofferberth, *Coherent manipulation of Bose-Einstein condensates with rf adiabatic potentials*. Ph.D. thesis, Heidelberg, 2007
10. T. Betz, *Phase correlations of coupled one-dimensional Bose gases*. Ph.D. thesis, Vienna University of Technology, 2011
11. T. Betz, S. Manz, R. Bücker, T. Berrada, Ch. Koller, G. Kazakov, I. Mazets, H.-P. Stimming, A. Perrin, T. Schumm, J. Schmiedmayer, Two-point phase correlations of a one-dimensional Bosonic Josephson junction. Phys. Rev. Lett. **106**(2) (2011)
12. R. Bücker, J. Grond, S. Manz, T. Berrada, T. Betz, C. Koller, U. Hohenester, T. Schumm, A. Perrin, J. Schmiedmayer, Twin-atom beams. Nat. Phys. **7**(8), 608–611 (2011)
13. R. Bücker, T. Berrada, S. van Frank, J.-F. Schaff, T. Schumm, J. Schmiedmayer, G. Jäger, J. Grond, U. Hohenester, Vibrational state inversion of a Bose-Einstein condensate: optimal control and state tomography. J. Phys. B: At. Mol. Opt. Phys. **46**(10), 104012 (2013)
14. T. Berrada, S. van Frank, R. Bücker, T. Schumm, J.-F. Schaff, J. Schmiedmayer, Integrated Mach-Zehnder interferometer for Bose-Einstein condensates. Nat. Commun. **4**, 2077 (2013)
15. S. Groth, *Development, fabrication, and characterisation of atom chips*. Ph.D. thesis, University of Heidelberg, 2006
16. S. Manz, *Density correlations of expanding one-dimensional Bose gases*. Ph.D. thesis, TU Vienna, 2011
17. M. Trinker, S. Groth, S. Haslinger, S. Manz, T. Betz, S. Schneider, I. Bar-Joseph, T. Schumm, J. Schmiedmayer, Multilayer atom chips for versatile atom micromanipulation. Appl. Phys. Lett. **92**(25), 254102 (2008)
18. R. Bücker, *Fluorescence imaging of ultracold atoms*. Diploma thesis, Heidelberg, 2008
19. R. Bücker, A. Perrin, S. Manz, T. Betz, C.H. Koller, T. Plisson, J. Rottmann, T. Schumm, J. Schmiedmayer, Single-particle-sensitive imaging of freely propagating ultracold atoms. New J. Phys. **11**(10), 24 (2009)

20. S. Manz, R. Bücker, T. Betz, C. Koller, S. Hofferberth, I.E. Mazets, A. Imambekov, E. Demler, A. Perrin, J. Schmiedmayer, T. Schumm, Two-point density correlations of quasicondensates in free expansion. Phys. Rev. A **81**(3), 031610 (2010)
21. A. Perrin, R. Bücker, S. Manz, T. Betz, C. Koller, T. Plisson, T. Schumm, J. Schmiedmayer, Hanbury Brown and Twiss correlations across the Bose Einstein condensation threshold. Nat. Phys. **8**(3), 195–198 (2012)
22. C. Koller, *Towards the realization of hybrid quantum systems*. Ph.D. thesis, Vienna University of Technology, 2012
23. T. Plisson, *Coherent manipulation of Bose-Einstein condensates with microwave and radio frequency fields*. Diploma thesis, Télécom Paristech, 2009
24. M. Brajdic, *Entwicklung einer Computersteuerung und ihre Anwendung in einem Experiment zur vereinfachten Bose-Einstein Kondensation in einer Oberflächen- falle*. Diploma thesis, Heidelberg, 2003
25. W. Rohringer, *Stochastic optimization in an ultracold atom experiment*. Diploma thesis, Vienna University of Technology, 2008
26. W. Rohringer, R. Bücker, S. Manz, T. Betz, C. Koller, M. Göbel, A. Perrin, J. Schmiedmayer, T. Schumm, Stochastic optimization of a cold atom experiment using a genetic algorithm. Appl. Phys. Lett. **93**(26), 264101 (2008)
27. R. Folman, P. Krüger, J. Schmiedmayer, J. Denschlag, C. Henkel, Microscopic atom optics: from wires to an atom chip. Adv. At. Mol. Opt. Phys. **48**, 263–356 (2002)
28. S. Wildermuth, P. Krüger, C. Becker, M. Brajdic, S. Haupt, A. Kasper, R. Folman, J. Schmiedmayer, Optimized magneto-optical trap for experiments with ultracold atoms near surfaces. Phys. Rev. A **69**(3), 030901 (2004)
29. A. Haase, D. Cassettari, B. Hessmo, J. Schmiedmayer, Trapping neutral atoms with a wire. Phys. Rev. A **64**(4), 043405 (2001)
30. S. Schneider, A. Kasper, Ch. vom Hagen, M. Bartenstein, B. Engeser, T. Schumm, I. Bar-Joseph, R. Folman, L. Feenstra, J. Schmiedmayer, Bose-Einstein condensation in a simple microtrap. Phys. Rev. A **67**(2), 023612 (2003)
31. M. Wilzbach, *Aufbau eines Experiments zur miniaturisierten und integrierten Detektion neutraler Atome*. Diploma thesis, Heidelberg, 2002
32. R. Bücker, T. Berrada, S. van Frank, J.-F. Schaff, T. Schumm, J. Schmiedmayer, G. Jäger, J. Grond, U. Hohenester, Vibrational state inversion of a Bose-Einstein condensate: optimal control and state tomography, arXiv:1212.4173. Accessed Dec 2012
33. S. van Frank, A. Negretti, T. Berrada, R. Bücker, S. Montangero, J.-F. Schaff, T. Schumm, T. Calarco, J. Schmiedmayer, Interferometry with non-classical motional states of a Bose-Einstein condensate, p. 7, Feb 2014
34. J.F. Scharf, Eine Partitur der atomaren Bewegung. Wiener Zeitung, 2012
35. D.A. Steck, Rubidium 87 D Line Data. Technical report, 2008
36. C. Cohen-Tannoudji, Atomes ultrafroids - Piègeage non dissipatif et refroidissement évaporatif, in *Notes de Cours au Collège de France*, p. II (1996)
37. E. Burt, R. Ghrist, C. Myatt, M. Holland, E. Cornell, C. Wieman, Coherence, correlations, and collisions: what one learns about Bose-Einstein condensates from their decay. Phys. Rev. Lett. **79**(3), 337–340 (1997)
38. J. Söding, D. Guéry-Odelin, P. Desbiolles, F. Chevy, H. Inamori, J. Dalibard, Three-body decay of a rubidium Bose-Einstein condensate. Appl. Phys. B: Lasers Opt. **69**(4), 257–261 (1999)
39. J. Schmiedmayer, Guiding and trapping a neutral atom on a wire. Phys. Rev. A **52**(1), R13–R16 (1995)
40. J. Reichel, W. Hänsel, T. Hänsch, Atomic micromanipulation with magnetic surface traps. Phys. Rev. Lett. **83**(17), 3398–3401 (1999)
41. R. Folman, P. Krüger, D. Cassettari, B. Hessmo, T. Maier, J. Schmiedmayer, Controlling cold atoms using nanofabricated surfaces: atom chips. Phys. Rev. Lett. **84**(20), 4749–4752 (2000)
42. W. Hänsel, P. Hommelhoff, T.W. Hänsch, J. Reichel, Bose-Einstein condensation on a microelectronic chip. Nature **413**(6855), 498–501 (2001)

43. H. Ott, J. Fortagh, G. Schlotterbeck, A. Grossmann, C. Zimmermann, Bose-Einstein condensation in a surface microtrap. Phys. Rev. Lett. **87**(23), 230401 (2001)
44. J. Reichel, V. Vuletic, *Atom Chips* (Wiley, New York, 2010)
45. T.H. Bergeman, P. McNicholl, J. Kycia, H. Metcalf, N.L. Balazs, Quantized motion of atoms in a quadrupole magnetostatic trap. J. Opt. Soc. Am. B, **6**(11), 2249 (1989)
46. T. Schumm, Atom chips in the real world: the effects of wire corrugation. EPJD **32**, 171–180 (2005)
47. S. Groth, P. Krüger, S. Wildermuth, R. Folman, T. Fernholz, J. Schmiedmayer, D. Mahalu, I. Bar-Joseph, Atom chips: fabrication and thermal properties. Appl. Phys. Lett. **85**(14), 2980 (2004)
48. J. Estève, C. Aussibal, T. Schumm, C. Figl, D. Mailly, I. Bouchoule, C. Westbrook, A. Aspect, Role of wire imperfections in micromagnetic traps for atoms. Phys. Rev. A **70**(4), 043629 (2004)
49. P. Krüger, L. Andersson, S. Wildermuth, S. Hofferberth, E. Haller, S. Aigner, S. Groth, I. Bar-Joseph, J. Schmiedmayer, Potential roughness near lithographically fabricated atom chips. Phys. Rev. A **76**(6), 063621 (2007)
50. J.-B. Trebbia, C. Garrido, Alzar, R. Cornelussen, C. Westbrook, I. Bouchoule, Roughness suppression via rapid current modulation on an atom chip. Phys. Rev. Lett. **98**(26), 263201 (2007)
51. R. Grimm, M. Weidemüller, Y.B. Ovchinnikov, Optical dipole traps for neutral atoms. Adv. At. Mol. Opt. Phys. **42**, 95–170 (2000)
52. H. Perrin, *Adiabatic Potentials*, Lecture on Adiabatic Potentials, Les houche edition, 2013
53. O. Zobay, B. Garraway, Two-dimensional atom trapping in field-induced adiabatic potentials. Phys. Rev. Lett. **86**(7), 1195–1198 (2001)
54. Y. Colombe, E. Knyazchyan, O. Morizot, B. Mercier, V. Lorent, H. Perrin, Ultracold atoms confined in rf-induced two-dimensional trapping potentials. Europhys. Lett. (EPL) **67**(4), 593–599 (2004)
55. I. Lesanovsky, T. Schumm, S. Hofferberth, L. Andersson, P. Krüger, J. Schmiedmayer, Adiabatic radio-frequency potentials for the coherent manipulation of matter waves. Phys. Rev. A **73**(3), 033619 (2006)
56. O. Morizot, Y. Colombe, V. Lorent, H. Perrin, B. Garraway, Ring trap for ultracold atoms. Phys. Rev. A **74**(2), 023617 (2006)
57. P.W. Courteille, B. Deh, J. Fortágh, A. Günther, S. Kraft, C. Marzok, S. Slama, C. Zimmermann, Highly versatile atomic micro traps generated by multifrequency magnetic field modulation. J. Phys. B: At. Mol. Opt. Phys. **39**(5), 1055–1064 (2006)
58. T. Schumm, S. Hofferberth, L.M. Andersson, S. Wildermuth, S. Groth, I. Bar-Joseph, J. Schmiedmayer, P. Krüger, Matter-wave interferometry in a double well on an atom chip. Nat. Phys. **1**(1), 57–62 (2005)
59. S. Hofferberth, I. Lesanovsky, B. Fischer, J. Verdu, J. Schmiedmayer, Radiofrequency-dressed-state potentials for neutral atoms. Nat. Phys. **2**(10), 710–716 (2006)
60. G.-B. Jo, J.-H. Choi, C.A. Christensen, Y.-R. Lee, T.A. Pasquini, W. Ketterle, D.E. Pritchard, Matter-wave interferometry with phase fluctuating Bose-Einstein condensates. Phys. Rev. Lett. **99**(24), 240406 (2007)
61. F. Baumgärtner, R.J. Sewell, S. Eriksson, I. Llorente-Garcia, J. Dingjan, J.P. Cotter, E.A. Hinds, Measuring energy differences by BEC interferometry on a chip. Phys. Rev. Lett. **105**(24), 243003 (2010)
62. L. LeBlanc, A. Bardon, J. McKeever, M. Extavour, D. Jervis, J. Thywissen, F. Piazza, A. Smerzi, Dynamics of a tunable superfluid junction. Phys. Rev. Lett. **106**(2) (2011)
63. S. Hofferberth, I. Lesanovsky, B. Fischer, T. Schumm, J. Schmiedmayer, Non-equilibrium coherence dynamics in one-dimensional Bose gases. Nature **449**(7160), 324–327 (2007)
64. M. Gring, M. Kuhnert, T. Langen, T. Kitagawa, B. Rauer, M. Schreitl, I. Mazets, D. Adu, Smith, E. Demler, J. Schmiedmayer, Relaxation and prethermalization in an isolated quantum system. Science (New York, N.Y.) **337**(6100), 1318–1322 (2012)

65. K. Merloti, R. Dubessy, L. Longchambon, A. Perrin, P.-E. Pottie, V. Lorent, H. Perrin, A two-dimensional quantum gas in a magnetic trap. New J. Phys. **15**(3), 033007 (2013)
66. J. Shirley, Solution of the Schrödinger equation with a Hamiltonian periodic in time. Phys. Rev. **138**(4B), B979–B987 (1965)
67. H. Perrin, *Spin and Fields*, Lecture on Adiabatic Potentials, Les houche edition, 2013
68. A. Martin, K. Helmerson, V. Bagnato, G. Lafyatis, D. Pritchard, rf Spectroscopy of trapped neutral atoms. Phys. Rev. Lett. **61**(21), 2431–2434 (1988)
69. I. Bloch, T. Hänsch, T. Esslinger, Atom laser with a cw output coupler. Phys. Rev. Lett. **82**(15), 3008–3011 (1999)
70. S. Hofferberth, B. Fischer, T. Schumm, J. Schmiedmayer, I. Lesanovsky, Ultracold atoms in radio-frequency dressed potentials beyond the rotating-wave approximation. Phys. Rev. A **76**(1), 013401 (2007)
71. J. van Es, S. Whitlock, T. Fernholz, A. van Amerongen, N. van Druten, Longitudinal character of atom-chip-based rf-dressed potentials. Phys. Rev. A **77**(6), 063623 (2008)
72. A. Robert, O. Sirjean, A. Browaeys, J. Poupard, S. Nowak, D. Boiron, C.I. Westbrook, A. Aspect, A Bose-Einstein condensate of metastable atoms. Science (New York, N.Y.) **292**(5516), 461–464 (2001)
73. T. Gericke, P. Würtz, D. Reitz, T. Langen, H. Ott, High-resolution scanning electron microscopy of an ultracold quantum gas. Nat. Phys. **4**(12), 949–953 (2008)
74. W. Ketterle, D.S. Durfee, D.M. Stamper-Kurn, Making, probing and understanding Bose-Einstein condensates, p. 90, Apr 1999
75. A. David, Smith, S. Aigner, S. Hofferberth, M. Gring, M. Andersson, S. Wildermuth, P. Krüger, S. Schneider, T. Schumm, J. Schmiedmayer, Absorption imaging of ultracold atoms on atom chips. Opt. Exp. **19**(9), 8471–8485 (2011)
76. M Gring, *Prethermalization in an isolated many body system*. Ph.D. thesis, Vienna University of Technology, 2012
77. T. Jacqmin, *Mesures de corrélations dans un gaz de bosons unidimensionnel sur puce*. Ph.D. thesis, Université Paris Sud, 2012
78. G. Reinaudi, T. Lahaye, Z. Wang, D. Guéry-Odelin, Strong saturation absorption imaging of dense clouds of ultracold atoms. Opt. Lett. **32**(21), 3143 (2007)
79. R. Bücker, U. Hohenester, T. Berrada, S. van Frank, A. Perrin, S. Manz, T. Betz, J. Grond, T. Schumm, J. Schmiedmayer, Dynamics of parametric matter-wave amplification. Phys. Rev. A **86**(1), 013638 (2012)

Chapter 3
A Mach-Zehnder Interferometer for Trapped, Interacting Bose-Einstein Condensates

In this chapter, we present the main results of this thesis:

- the implementation of a Mach-Zehnder interferometer (MZI) for trapped, interacting BECs on our atom chip setup, including the development of a novel type of BEC recombiner,
- the generation of number- and spin-squeezed states of a BEC with $N \approx 1200$ atoms in a double-well potential,
- the first direct experimental demonstration of the link between number fluctuations and interaction-induced phase diffusion, underlining how the use of a non-classical state can help extending the interrogation time of a matter-wave interferometer.

These results have been summarized in our 2013 publication [1]. Here we motivate our research, explain in detail how our results have been achieved, discuss their physical meaning and consider them in the light of related findings reported on other BEC experiments.

3.1 Introduction

3.1.1 A Prototypical Interferometer

The BEC interferometer implemented on our atom chip is meant to be a matter-wave analogue of the prototypical interferometer developed by Ludwig Mach and Ludwig Zehnder at the end of the XIXth century (see Fig. 3.1). An optical interferometer is a device that makes use of the effect of interference of light waves. Most interferometers rely on the splitting of one input beam on a beam-splitter (*separation BS*). Each beam is exposed to a different external influence, such as transmission through media

T. Berrada, *Interferometry with Interacting Bose-Einstein Condensates in a Double-Well Potential*, Springer Theses,
DOI 10.1007/978-3-319-27233-7_3

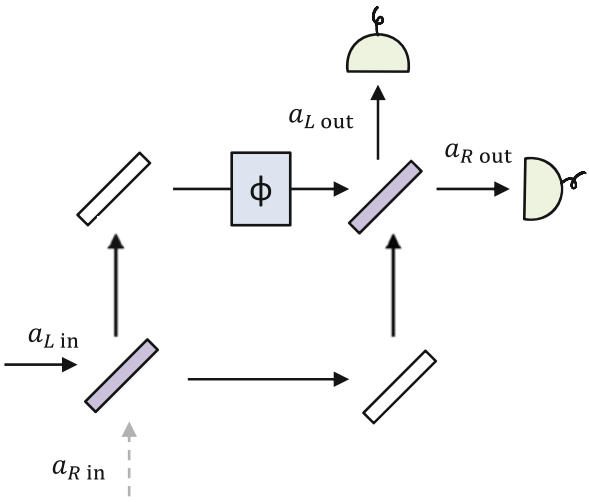

Fig. 3.1 Mach-Zehnder interferometer. Photons (or atoms, neutrons, molecules...) entering each of the two input ports are coherently split by the separation beam-splitter. The two paths pick up a phase difference ϕ before beeing recombined on the second beam-splitter. The atoms exiting the interferometer are counted separately by two detectors. Generally, particles enter only from one input port

with different refractive indices, or propagation along paths of different length, and picks up a certain phase. The two beams are recombined on a second beam-splitter[1] (*recombiner*). The differential phase between the two beams is read out either from the difference of intensities between the two output ports (*number fringes*) or from the spatial distribution of the intensity (*spatial fringes*).

Note that the MZI can be operated in both ways: if the interferometer is perfectly aligned (full mode overlap), the phase information is encoded in the intensity difference between the two output ports only. For example, it can be adjusted in a way such that all the power exits through one single output port. If the beams are slightly misaligned, both outputs will exhibit spatial fringe patterns. The phase will be encoded in the spatial intensity distribution, while the total power in each output-port will be hardly phase-dependent. MZI can also be used for *white-light interferometry*, i.e. using a broad-band source, in which case interference is observed in a narrow range around the point of zero arm length difference.

3.1.2 Interferometry with Bose-Einstein Condensates

Particle-wave duality enables the construction of interferometers for matter-wave [2]. Atom interferometry requires the ability to manipulate coherently the internal and external (motional) state of atoms, making use of techniques developed for atom optics [3] and atomic spectroscopy [4]. It is a key experimental technique to probe quantum properties of matter and fundamental laws of nature, and yields rich applications in metrology.

[1] Some interferometers, like the Michelson interferometer, make use of the same BS to split and recombine the light.

Bose-Einstein condensates are particular matter waves with macroscopic coherence properties. They have often been compared to atom lasers [5]. It is natural to wonder whether macroscopic spatial coherence and high phase density would make BECs an ideal bright, single-mode source for atom interferometry. In particular in the context of Bragg interferometers (see next section), the narrow momentum spread $\delta p \ll \hbar k$, where k is the wave vector of the light, allows achieving close to 100 % contrast [6]. It has also been underlined that trapped BECs could constitute a small, localized probe for weak shot-range interactions such as the Casimir-Polder force [7], and recently, a BEC has been used as a scanning probe to map out the microwave field near the surface of an atom chip [8].

However, the analogy between lasers and BECs should not conceal the fact that they are two very different physical systems. A fundamental distinction is the presence of atom-atom interactions. While they can usually be neglected in freely expanding atomic clouds, interactions dominate the physics of confined BECs, leading to mean-field shifts and dephasing effects, which ultimately limit the coherence time of interferometers [1, 9–11]. On the other hand, we have seen in Sects. 1.2.4.4 and 1.2.4.5 that interactions can be utilized to generate non-classical correlations between the atoms, which can be used to improve the phase sensitivity of a BEC interferometer beyond the SQL. We will show that it can also reduce the effect of interaction-induced dephasing and extend the interrogation time of an interferometer (see Sect. 3.7). The question still remains open how and to which extent the detrimental effects of interactions can be overcome and whether precision measurements can be performed with trapped BECs. However, as we will motivate below, a BEC interferometer certainly is as a powerful tool to probe interacting quantum many-body systems.

In the next sections, we give a brief review on the techniques that have been used to realize BEC interferometry and list some examples of the physical questions that have been addressed with BEC interference experiments. Many examples of BEC interferometers are given in the 2009 review on atom interferometry by Cronin et al. [2], as well as in the 2014 Varenna lecture notes by Schaff et al. [12], with focus on double-well interferometers.

3.1.2.1 BEC Interferometry Experiments: State of the Art

BEC interferometry has been a very active field of research on ultracold atoms since the first demonstration of the macroscopic coherence of a Bose-Einstein condensate in 1997 [13].

BEC interferometer rely on the coherent splitting and recombination of a BEC between (at least) two external and/or internal modes, and on the possibility to apply and read out a phase shift. This basic scheme, illustrated schematically in Fig. 3.1 should not conceal one fundamental difference between interferometers based on the interaction of a two-level atom with an electromagnetic field (for example Bragg interferometers, or interferometers with internal-state labeling, see below), and

interferometers where splitting and recombination are carried out by transforming the confining potential (for example double-well interferometers).

In the first case, the electromagnetic (rf, microwave or laser) coupling drive has also the function of a reference oscillator [14]. Once the first $\pi/2$ pulse has put the BEC in a coherent superposition of the two modes, the phase between them evolves at a rate proportional to their energy difference. During this time, the coupling drive also accumulates a certain phase. The second $\pi/2$ pulse eventually recombines the two halves, comparing the phase accumulated by the condensates to that accumulated by the drive. The resulting phase-dependent number or spatial fringes stem from the beat note between the condensate and the reference oscillator. This has the important consequence that such interferometers can serve locking the reference oscillator on the atomic transition (like in atomic clocks) or measuring a shift of the atoms with respect to a moving, standing wave (like in Bragg gravimeters).

Several denominations are used concurrently in literature to distinguish the different types of interferometer: while many schemes where the two modes are spatially separated are called *Mach-Zehnder interferometers* (including in particular the interferometer presented in this thesis), some authors prefer calling *Michelson interferometer* systems where the separation and recombination BS are at the same spatial position [15]. The term *Ramsey interferometer* generally refers to schemes with internal-state labeling, but we also chose to refer to the vibrational-state interferometer presented in Ref. [16] as a (temporal) Ramsey-like interferometer, to underline the fact that both modes are located in the same (single-well) potential.

Although the denominations are sometime not consistent, the main distinction concerns schemes involving a finite enclosed area, i.e. where the center-of-mass of the two modes are spatially separated and recombined, such as for example the Mach-Zehnder, Ramsey-Bordé or spatial Ramsey interferometer; and the schemes where the center-of-mass of the two modes stay essentially at the same location (temporal Ramsey interferometers). While the first can be used to measure inertial forces (acceleration and rotations), the latter are only sensitive to effects that cause the two states to acquire phase at different rates, such as an intrinsic energy difference (hyperfine splitting in clocks) or different Zeeman or Stark shifts.

Most BEC interferometers to date can be assigned to one of these three broad categories:

Interferometers with Internal-State Labeling

A first group consists of "time-domain separated-oscillatory-field" Ramsey interferometers [4], where rf or microwave fields are used to drive coherent transitions between internal atomic states. Following the first measurement of the relative phase in a two-component BEC in 1998 [14], several interferometers with internal-state labeling (ISLI) were implemented with optically trapped condensates [17–19]. Ramsey interferometry has also been performed with magnetically trapped BECs, using rf pulses to couple the different Zeeman states [20], enabling the realization of multi-path interferometers [21]. A related approach, inspired by the progress on

atom lasers [22] has consisted in using rf pulses to coherently outcouple and recombine atoms from a BEC [23, 24], with the distinction that interference is detected in spatial fringes instead of number fringes.

Even if the recoil due to rf or microwave photons can generally be neglected in experiments with trapped condensates, the transition between internal states is always accompanied by a modification of the external wavefunction. The coupling between internal and external degrees of freedom is particularly spectacular in experiments where the two internal states experience different external potentials. This is for example the case in Ref. [25] where a bimodal condensate was confined in a microwave-dressed state-dependent potential. In Ref. [24], free-falling as well as trapped condensates were split and recombined using Stern-Gerlach field-gradient BS. Another example of the coupling between internal and external dynamics is the dramatic loss of Ramsey contrast in two-components BECs caused by demixing effects [9] as well as (in magnetic traps) the relative center-of-mass motion of the different Zeeman states [20, 21].

Stimulated Raman transitions can also serve as BS between low-lying internal states. Although Raman interferometers have been widely used with non-condensed atoms since 1991 [26], there are very few examples of BEC Raman interferometers. One exception is the interferometer described in Ref. [27], where atoms coherently rf-outcoupled from a BEC fall through two Raman BS implemented using copropagating beams, resulting in a negligible momentum-transfer.

Bragg Interferometers

Bragg interferometers (BI) rely on the coherent splitting of a matter-wave in momentum space, i.e. the diffraction on a light grating caused a momentum transfer, which then translates into a spatial shift. Along with the first experiments on temporal [28] and spatial [29] coherence of BECs, the first BIs for condensates were developed around 2000 [6, 30], resorting to the three light grating configuration already implemented with cold atoms [31, 32]. Three optically induced Bragg pulses ($\pi/2$-π-$\pi/2$), created by two off-resonant (to avoid spontaneous emission) counterpropagating laser beams with different wave vectors are used to coherently split, reflect and recombine a BEC. Owing to the possibility of large momentum transfer using nth-order Bragg pulses [33, 34] and long expansion times [35], the two arms of the interferometer can be separated by hundreds of μm. Extensions to this scheme included asymmetric MZI [29, 35], where a temporal mismatch causes a partial spatial overlap of the wavefunctions and encodes the relative phase into spatial interference fringes; a three-path interferometer [36], where the phase is encoded into the contrast of the spatial interference pattern; or guided Michelson interferometers [15, 37], where the BECs are split and recombined at the same location in space. While some condensate BIs—together with most of the BIs using cold, non-condensed atoms—are operated with free falling BECs, including the extreme case of BECs in microgravity [35], experiments were also performed with trapped [10, 29, 38], or guided [10, 15, 29, 34, 37, 39] condensates.

A related approach, also based on the diffraction of a matter wave on a light grating, is the Bloch oscillation interferometer (BOI) [40–43], where the macroscopic interference between different Wannier states gives rise to oscillations of the density pattern at a frequency proportional to the applied phase shift.

Double-Well Interferometers

The interferometer presented in this chapter belongs to the category of double-well interferometers (DWI), i.e. trapped BEC interferometers where the atoms share the same internal state while their external wavefunction is in a superposition of two localized modes in a double-well potential [12]. Coherent splitting is achieved by smoothly deforming the external potential from a single well to a double well. Splitting occurs in position space, in contrast to Bragg interferometers, where it happens in momentum space.

A few years after the observation of interferences from independent condensates in an optical double well [13], the first DWI was realized in 2004 with an optically trapped BEC [44]. One year later, the first magnetic DWI was implemented on an atom chip [45], using the same technique of rf dressing as in the experiments presented in this thesis (see Sect. 2.2.2). Double wells created by rf dressing have been widely used for BEC interference experiments, owing to their high degree of control allowing to access different regimes of tunnel coupling [1, 11, 46, 47]. In particular, many experiments were performed with phase fluctuating BECs in elongated double wells [48–52].

BEC interference experiments have also been performed in double wells, or arrays of wells in one [53], two [54] or three [55] dimensions created using optical lattices.

Most DWI rely on time-of-flight recombination: the condensates are released, expand and overlap in tof, creating a fringe density pattern similar to a double slit interference experiment, from which the phase can be extracted (see Sect. 3.2.1). Some exceptions are for example the technique presented in Ref. [56], where the phase was inferred from a phase-dependent heating when the two halves of the condensate are merged, and the trapped recombiners presented in this thesis (see Sect. 3.6) [1].

Other Types of BEC Interferometers

Besides these three categories, one should also mention a BEC interferometer based on the coherent diffraction of a BEC on a magnetic lattice [57] as well as the Ramsey-like interferometer with vibrational states of a trapped BEC that we recently developed on our experiment [16].

3.1.2.2 Example of BEC Interference Experiments

Matter-wave interferometry (MWI) has proven to be a powerful tool to probe many-body quantum systems. In particular, it is the only experimental technique which allows accessing the quantum phase, nearly without equivalent in other fields of physics.

MWI has been performed to demonstrate the temporal [28] and spatial [29] coherence of BECs and has allowed probing the phase fluctuations of degenerate Bose gases in low dimensions [38, 48, 50, 51]. It has also been used to observe phase defects such as vortices [23, 58] or solitons [30] in BECs.

Since the first observation of Bloch oscillations as a macroscopic quantum interference effect [40], MWI has been used to observe Josephson oscillations and macroscopic quantum self-trapping through the evolution of the phase between two condensates in an optical double-well potential [55], illustrate the difference between independently created and coherently split BECs [46] and study the thermal phase fluctuations at equilibrium in a pair of coupled condensate in 1D [51], 2D [54] and 3D [59].

Atomic interactions, which seem currently to be the main factor limiting the interrogation time of BEC interferometers, have been studied by means of MWI. Mean-field effects have been observed in trapped or guided BECs, including the demixing dynamics of coherent superpositions of two internal states with slightly different scattering lengths [9, 14] and spatially inhomogeneous, density-dependent phase dynamics [10, 19]. Many-body effects, such as interaction-induced phase diffusion, which will be discussed in detail in Sect. 3.5.2, have been studied in Ref. [1, 11]. It has also been experimentally demonstrated that these effects could be limited by controlling interactions with a Feshbach resonance [39, 41, 43]. Magnetic dipolar intractions have also been studied by MWI [60].

MWI has allowed characterizing non-classical many-body states of a BEC in a double well [1, 61, 62]. Quantum enhanced interferometry was demonstrated with internal states of a BEC [8, 17].

Recently, in our group, a series of MWI experiments with a pair of 1D quasi-condensates has brought new insight in the physics of out-of-equilibrium quantum systems, highlighting the mechanisms of prethermalization [49, 52, 63] and the emergence of thermal correlations [64, 65] after a quench.

Although currently most matter-wave metrology experiments such as clocks or inertial sensors use cold, non-condensed atoms, the three-path Bragg contrast interferometer of Ref. [36] has been used to measure precisely the photon recoil energy.

3.1.3 The Vienna BEC Mach-Zehnder Interferometer

The design of our BEC interferometer is based on previous work of our group in Heidelberg and Vienna [45, 46, 51]. It relies on the coherent splitting and recombination of a BEC in a tunable rf-dressed double-well potential, where the matter

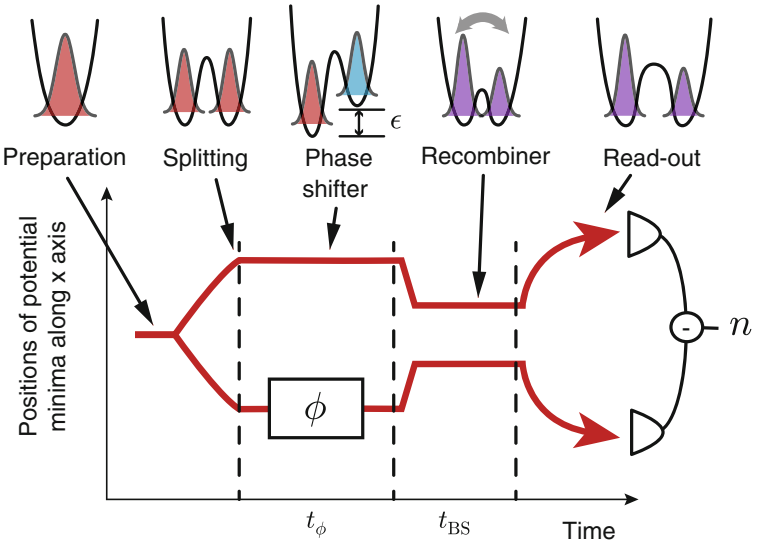

Fig. 3.2 Schematics of the Mach-Zehnder interferometric sequence. A Bose-Einstein condensate is coherently split by transforming a single trap into a double-well potential. A relative phase ϕ between the two arms is imprinted by tilting the double well during a time t_ϕ (phase accumulation time). A phase sensitive recombination, similar to the action of a beam-splitter, is performed during the time t_{BS}, to transform the phase ϕ into a population imbalance between the two wells. The atoms are eventually separated and the atom number in each well is read out by fluorescence imaging

wave is confined at all times. Figure 3.2 shows a schematics of the interferometric sequence: a single BEC is first coherently split by smoothly transforming the single well into a double well. Thanks to a spatial separation of $\sim$2 μm between the two wave packets, our setup is sensitive to inertial forces. A relative phase between the two arms is imprinted by tilting the double well. By adjusting the time during which the double well is tilted out of the horizontal plane, we can tune the relative phase between the two interferometer arms. The two condensates are then recombined by reducing the splitting between the two wells in a way such that the double well acts an atomic beam splitter, transforming the relative phase into a population imbalance. We have implemented two different strategies based on a slow, adiabatic deformation of the double-well potential (Josephson recombiner) and on a fast, non-adiabatic deformation of the potential (non-adiabatic recombiner). After recombination, the atom clouds are separated and the particle number is read out using our fluorescence imaging system. The state of the condensate can be characterized at each step of the interferometric sequence by interrupting the MZI transformation and measuring the two macroscopic observables *number* and *phase* difference.

In the following sections, we describe, characterize and discuss each stage of the interferometric sequence. We start by presenting the methods used to probe the state of the BEC (Sect. 3.2). We then turn to the matter-wave source (Sect. 3.3). In Sect. 3.4, we present the splitting stage and show that the output state is strongly spin-squeezed

and features reduced number fluctuations compared to a classical coherent state. In Sect. 3.5, we study the evolution of the phase during the phase accumulation stage and show that the deterministic phase accumulation is accompanied by a randomization of the phase distribution that we attribute to interaction-induced phase diffusion. In particular, we compute the phase diffusion rate and connect it to the number fluctuations of the BEC in the interferometer. In Sect. 3.6, we present and compare the two BEC recombiners. Eventually, in Sect. 3.7, we present and discuss the interferometric signal resulting from the full MZI sequence, underlining the effect of phase diffusion and demonstrating how the use of a number-squeezed state extends the interrogation time of our interferometer by more than a factor of 2.

3.2 Number and Phase Estimation

During each experimental run, we can interrupt the sequence at any stage to measure either one or the other conjugate observable *phase* and *number difference* (see Sect. 1.2.2.5). This way, we can characterize the state of the condensate after each step of the interferometric sequence. The fact that we can experimentally infer the relative phase for each individual realization is an important feature of bosonic Josephson junctions, which has no counterpart in superconducting Josephson junctions or superfluid helium. One should however keep in mind that beyond the two-mode approximation, the two macroscopic observables are not enough to characterize the state of the BEC.

The following section discusses the methods used on our setup to estimate both phase and number difference, and evaluates the sensitivity of each.

3.2.1 Relative Phase Measurement

3.2.1.1 Principle

We have seen in Sect. 1.2.2.5 that it is not obvious to give an unambiguous definition of the relative phase between the two parts of a Bose-Einstein condensate. Nor is it to relate the concept of a quantum phase to the outcome of a phase measurement process. An enlightening discussion has been led in the 1997 article by Castin and Dalibard [66], where the authors showed that no measurement, nor series of measurements, could allow distinguishing between a coherent state with random phase and a Fock state. In this section, we assume that the BEC has been prepared in a coherent state with a well-defined phase $\phi = 0$ (see Sect. 1.2.4.4).

The relative phase between two condensates cannot be directly measured. Instead, it can be inferred from observables which are functions of the quadratures of the phase. For this, some kind of beam-splitter is needed. In Sect. 3.6, we will discuss some of the techniques which have been used to recombine BECs and read-out their

phase. Here, we focus on the time-of-flight recombination method, which is the BEC analogue of the famous Young's double-slit experiment. It was first used in 1997 to observe the interference between two independently created BECs [13].

Although recombining a split double-well allows the readout of the relative phase as a population imbalance between the two modes, as we will show in Sect. 3.6, interactions make this operation hard to control. Because the free expansion reduces strongly the non-linearity, tof recombination has generally been preferred in double-well interferometers [44, 45]. Time-of-flight recombination has also been used in asymmetric Bragg MZIs [29], particularly in the drop tower setup Ref. [35], where the choice of a method where interference can be seen at each single shot was justified by the expense of the experiment. Local information can be extracted from the spatial fringes, particularly with quasi-condensates in low dimensions [48, 49, 51, 52, 54], or to demonstrate phase defects [23]. For all the experiments presented in this chapter, although our experiment provides sufficient resolution to probe axial phase fluctuations [51], we chose to discard all spatial information by integrating the interference pattern along the longitudinal direction of the cloud (z). In Chap. 4, we will discuss what information could be extracted from spatial phase fluctuations.

Implementation

In our setup, tof recombination is achieved by abruptly switching off the double-well potential to release the atoms, letting them expand for 46 ms and imaging them with the LS fluorescence detector (see Fig. 3.3a). Due to the high transverse trapping frequency in the direction of splitting (several kHz), the two BEC clouds quickly expand and overlap. A characteristic interference pattern emerges in the density distribution in tof (see Fig. 3.3c). Assuming that the double well can be approximated by two harmonic potentials (see Fig. 1.5) of frequency ω, located in $\pm d/2$, and that the transverse wavefunctions remain Gaussian during expansion with the time-dependent rms width $\sigma(t)$, the transverse density profile reads

$$|\psi(t)|^2 \approx \underbrace{\frac{N}{\sqrt{\pi\sigma^2(t)}} e^{-x^2/2\sigma^2(t)}}_{\text{envelope}} \left[1 + \underbrace{\cos\left(k_0(t)x + \phi\right)}_{\text{interference term}} \right], \tag{3.1}$$

where ϕ denotes the relative phase and N is the total atom number. The interference pattern consists of a Gaussian envelope modulated by an interference term. The phase appears as a shift in the position of the fringes with respect to the envelope. Note that for two spatially phase-coherent BECs, and in absence of any technical noise, the contrast of each single realization, i.e. the amplitude of the interference term, is expected to be maximal and equal to 1. We will see in Chap. 4 that this is also true for 1D quasi condensates immediately after splitting, as long as the axial phase fluctuations are equal in each cloud. The time-dependent fringe spacing

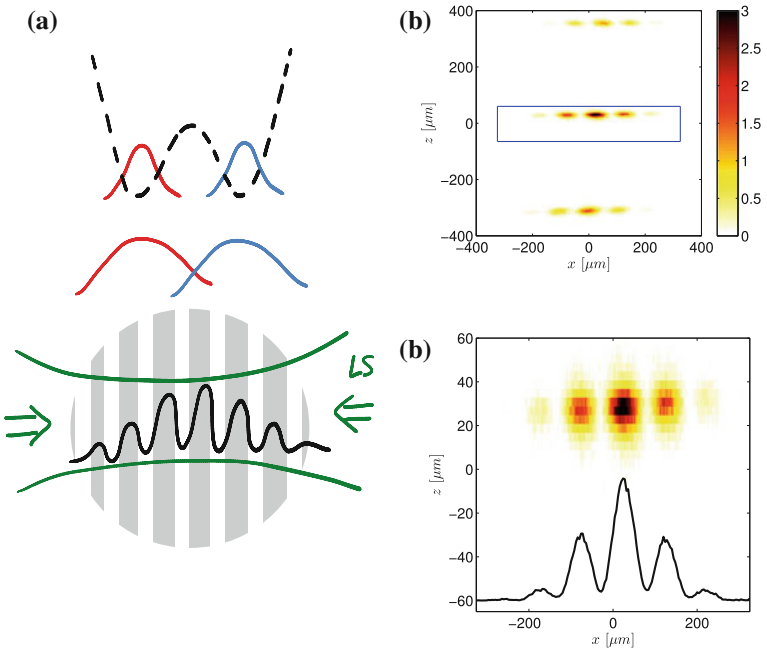

Fig. 3.3 Double-slit experiment with Bose-Einstein condensates. **a** Schematics of the time-of-flight recombination. After 46 ms, the transverse width of each cloud is much larger than the distance between the two wells and an interference pattern emerges in the density profile imaged with the Light Sheet. **b** Fluorescence image (averaged over 20 identical experimental runs) of the three m_F components after time of flight. The Stern & Gerlach separation is achieved by applying a magnetic field gradient along the longitudinal z-direction. Only the central cloud ($m_F = 0$, insensitive to magnetic fields), which contains up to half of the atoms, is used for phase analysis. *Color scale* 2D density in atoms/pixel. **c** Zoom on the central cloud (*blue box* in pannel b) showing a typical interference pattern. *Black line* density profile after integration along z, as used for the phase estimation. The bright fringe in the center of the cloud indicates a phase close to 0. The contrast is of the order of 80 % (Color figure online)

$$\lambda_{\mathrm{fr}}(t) \equiv \frac{2\pi}{k_0(t)} = \frac{h}{tdm\omega^2}\left(1+\omega^2 t^2\right) \underset{t^2 \gg \omega^{-2}}{\approx} \frac{ht}{dm}, \tag{3.2}$$

is a decreasing function of the splitting distance d. Atomic interactions during the early stage of the expansion tend to increase the fringe spacing compared to Eq. (3.2), but this effect becomes negligible when d is sufficiently large [67]. To ensure a constant fringe spacing regardless of the actual working trap, we chose to always ramp the rf dressing intensity to the same final value $\mathrm{RF_{Amp}} = 0.65$ (corresponding to the splitting trap, see Fig. 3.11) before releasing the atoms. Given the 46 ms tof, and $d = 2\,\mu\mathrm{m}$, it yields a fringe spacing $\lambda_{\mathrm{fr}} \approx 105\,\mu\mathrm{m}$, to be compared to the rms width of the optical point spread function, which is of the order of $10\,\mu\mathrm{m}$, and to the transverse extension of the expanded BEC ($4\sigma = 360\,\mu\mathrm{m}$), so that about 5 bright fringes fit into the envelope (see Fig. 3.3c).

Because of unavoidable mismatches between the switch-off time of the rf dressing and the trapping wire (<1 μs) on the one hand, and that of the bias field (0.1 ms) on the other hand, the atoms experience a rapidly varying magnetic field. When their Larmor frequency becomes lower than the rate of change of the local magnetic field, the adiabaticity hypothesis (Eq. (2.2)) breaks down and the atoms are projected onto the three m_F states. We observe that the transverse positions of the three clouds are slightly shifted, probably under the effect of spurious magnetic gradients during the tof. This reduces the contrast of the interference pattern after integration along z. Furthermore, since the projection depends on the exact configuration of the fields at switch off, the ratio between the m_F states occupation, and hence the contrast of the fringes, depends on the experimental parameters.

To mitigate this issue, we chose to deliberately apply a magnetic field gradient in the longitudinal direction (z) by pulsing current in one of the I-shaped copper wires (see Fig. 2.2). This realizes Stern and Gerlach separation of the three Zeeman components. Furthermore, we chose to perform phase analysis only on the magnetic-field insensitive $m_F = 0$ state (see Fig. 3.3b). When possible, the switch off was optimized[2] to maximize the population in $m_F = 0$ (up to 50 % of the total atom number). Adiabatic rapid passage (ARP) of all the atoms into a field insensitive state using a rf or microwave pulse [68] is currently under study.

3.2.1.2 Analysis of the Interference Pattern

Two methods to extract the relative phase from the interference patterns have been tested and compared. In both cases, the phase is extracted from the transverse density profile $n(x)$ obtained from integrating the fluorescence picture along the z-axis of the cloud , so that no information about the local axial phase is retained, and axial phase fluctuations are integrated out (see Fig. 4.1).

It is important to note that since the phase is a 2π periodic angular variable, the usual definitions of ensemble average, standard deviation etc. have to be adapted to extract meaningful statistical quantities [69]. Considering a set of phases $\{\phi_n\}$, $n = 1, \ldots, m$, the following quantities will be used throughout this thesis:

- the **resultant** $R = \frac{1}{m}\sum_{n=1}^{m} e^{i\phi_n}$ is a complex number inside the trigonometric disc, the argument of which corresponds to the average phase, while its modulus is a measure of the coherence (see Sect. 1.2.3.3). For a sample of m uniformly distributed phases, the mean modulus of R scales like $1/\sqrt{m}$.
- the **circular mean** is defined as $\langle\phi\rangle \equiv \arg R$.
- the **circular standard deviation** $\Delta\phi \equiv \sqrt{-2\ln|R|}$ is defined in such a way that it coincides with the rms width for a circular normal distribution. For a sample of m uniformly distributed phases, the mean circular standard deviation scales like $\sqrt{\ln m}$.

[2]The projection ratio onto the three m_F states can be tuned by changing the phase of the rf dressing field at the moment when the potential is switched off.

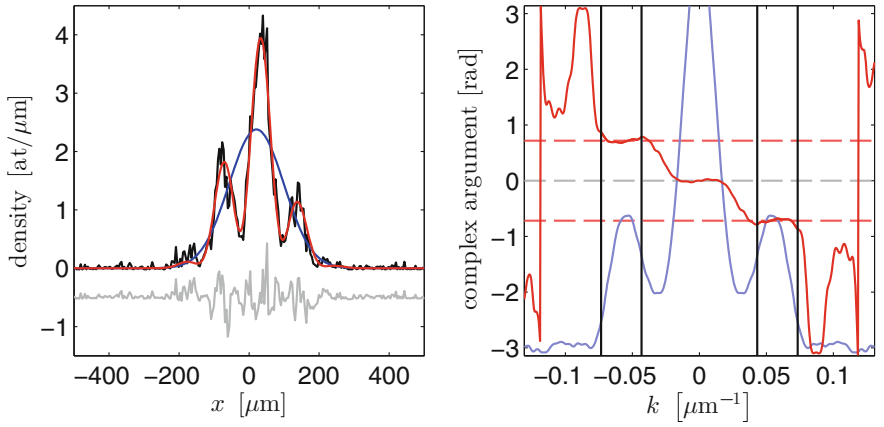

Fig. 3.4 Interference pattern analysis. *left* fit. *Black* interference pattern obtained from a single experimental realization ($N \approx 600$ atoms, retaining only the atoms in $m_F = 0$). Note that the central bright fringe is shifted with respect to the center of the envelope, indicating $\phi \neq 0$. *Red line* fit with the model of Eq. (3.3), yielding $\phi_{\text{fit}} = -0.73$ rad. *Blue* Gaussian envelope only. *Gray* residual (shifted by -0.5 for clarity). *right* Fourier transform. *Red line* complex argument of the Fourier transform $G(k)$ of the same density profile as in the *left panel*, displaying three plateaus. The central plateau, with value around 0, corresponds to the envelope of the cloud, while the side plateaus with opposite argument around $k = \pm 0.05\,\mu\text{m}^{-1}$ stem from the interference term. The relative phase is extracted from one of the side plateau by averaging $G(k)$ in the region defined by the two vertical *black lines*. This yields $\phi_{\text{FT}} = -0.72$ rad (*dashed red lines*). *Pale blue line* modulus $|G(k)|$

Fit

The first method consists in fitting the density profile $n(x)$ with a model following Eq. (3.1)

$$n_{\text{fit}}(x) = A_{\text{fit}} e^{-(x-x_{0,\text{fit}})^2/2\sigma_{\text{fit}}^2} \left[1 + C_{\text{fit}} \cos\left(k_{\text{fit}}(x - x_{\text{ref}}) + \phi_{\text{fit}}\right)\right]. \tag{3.3}$$

Details of the implementation can be found in T. Betz's PhD thesis [70]. The contrast term $0 \leq C \leq 1$ accounts for finite imaging resolution, averaging over spatial fluctuations of $\phi(z)$ as well as a slight angle between the camera and the splitting axis. x_{ref} is not a fit parameter but a fixed reference point on the camera image (see discussion in Sect. 3.2.1.3). Figure 3.4, left panel, displays an example of the fit of the interference pattern obtained from a single experimental realization. An advantage of the fit procedure is that most fitting routines readily give confidence intervals and estimators of the goodness of the fit which can be used to automatically reject some realizations when analyzing large amount of data.

Fourier Transform

The main drawback of the fit model (3.3) is that it relies on a harmonic approximation of the double-well and neglects interactions in the trap and in tof. One could in principle simulate numerically the whole expansion, but it wouldn't yield a simple analytical model. A less model-dependent method consists in extracting the phase from the complex argument of the Fourier transform of $n(x)$. Assuming that a generic interference pattern consists of an generic envelope $g(x)$ modulated by an interference term

$$n(x) = g(x)\left[1 + C\cos\left(k_0 x + \phi\right)\right], \tag{3.4}$$

the Fourier transform of n reads

$$F(k) = \sqrt{2\pi}G(k) * \left[\delta(k) + \frac{C}{2}\left(e^{i\phi}\delta(k - k_0) + e^{-i\phi}\delta(k + k_0)\right)\right] \tag{3.5}$$

where $G(k)$ is the Fourier transform of the envelope, $\delta(k)$ is the Dirac distribution and $*$ denotes the convolution product. The pale blue line in Fig. 3.4, right panel, shows the modulus of $G(k)$. It consists of three peaks corresponding to the envelope and the two sidebands around $\pm k_0$. The phase is computed by averaging the complex argument of the Fourier transform over one side band

$$\phi_{\mathrm{FT}} = \arg\left[\int_{k_0-\Delta k/2}^{k_0+\Delta k/2} G(k)\right]. \tag{3.6}$$

As long as the side bands can be resolved from the central peak (in other words: as long as a sufficiently large number of fringes fit within the envelope), the result does not crucially depend on Δk. The choice of the origin of the x axis however is not incidental, since a shift in real space corresponds to a phase gradient for the complex argument. In practice, it is chosen as the center of the envelope.

3.2.1.3 What is the Best Way of Extracting the Phase?

The measured value of the phase always depends on the estimation method. The phase can be extracted from a fit or from the Fourier transform of the interference pattern. In either case, it can be defined with respect to a fixed pixel on the image or with respect to the center of the cloud (center of mass, or center of the envelope...) for each realization. To the best of our knowledge, there is no definite argument as what method is more appropriate. It probably depends on what source of technical noise (vibrations of the double-well, momentum kick when the cloud is released...) dominates during the formation of the interference pattern. Arguably, this issue relates to the distinction between phase shift and envelope shift discussed for example in Ref. [71]. In Ref. [44], the phase was defined with respect to a fixed position, while

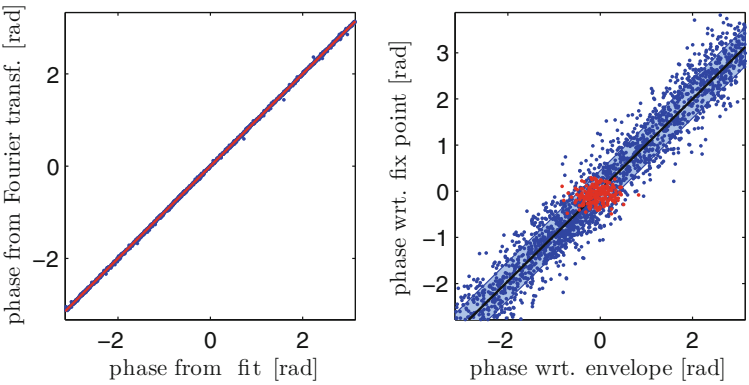

Fig. 3.5 Comparison between the phase extraction procedures. *Left Blue dots* phase extracted from the Fourier transform procedure versus phase extracted from the fit procedure for 2000 experimental interference patterns ($N_d \approx 600$ atoms in $m_F = 0$) with different phases spanning the interval $[0, 2\pi]$. *Red line* $y = x$. The width of the *blue* trace indicates the average discrepancy between the two methods $\Delta(\phi_{FT} - \phi_{fit}) = 0.018$ rad. In both cases, the phase was defined with respect to a fixed pixel on the camera. *Right Red dots* phase defined with respect to a fixed reference pixel on the camera ϕ_{ref} versus phase defined with respect to the center of the envelope (for each realization) ϕ_{env}, for 234 experimental interference patterns created in the same conditions ($\phi \sim 0$). In both cases, the phase was extracted from the Fourier transform. ϕ_{env} exhibit larger fluctuations than ϕ_{ref}. *Blue* same for the data of the *left panel* ($\phi \in [0, 2\pi]$). The *pale blue* area shows the average discrepancy $\Delta(\phi_{ref} - \phi_{env}) = 0.44$ rad between both methods. *Black line* $y = x$

in Ref. [47], the authors chose to define it with respect to the fitted center of the Gaussian envelope.

Both fit and Fourier transform methods were tested by estimating the phase of over 2000 experimental interference patterns (see Fig. 3.5, left panel). They yielded similar results, with an average discrepancy between both methods $\Delta(\phi_{FT} - \phi_{fit}) = 0.018$ rad, to be compared to the SQL (see Sect. 1.2.4.5) for $N_d = 600$ detected atoms, $\Delta\phi_{SQL} = 0.041$ rad. Besides being faster than the fit, the Fourier transform procedure proved also to be more robust (fewer outliers) and was preferred for phase analysis.

To decide whether to use a fixed reference pixel on the camera or the center of the envelope as the origin of phases, over 200 interference patterns recorded in the same experimental conditions ($\phi \sim 0$) were compared, yielding $\Delta\phi_{ref} = 0.16$ rad, $\Delta\phi_{env} = 0.26$ rad and $\sqrt{\text{covar}(\phi_{ref}, \phi_{env})} = 0.07$ rad (see Fig. 3.5, right panel). The discrepancy between both definitions of the phase, computed on over 2000 realizations with different phases amounts to 0.44 rad, which is ten times larger than $\Delta\phi_{SQL}$.

A possible reason why the phase defined with respect to the envelope displays stronger fluctuations is that it relies on an extra fitted parameter ($x_{0,fit}$). For these reasons, we chose to always define the phase with respect to an absolute reference point on the camera

3.2.1.4 Noise of the Phase Estimation

In order to observe non-classical states of a bosonic Josephson junction, one must be capable of measuring precisely phase fluctuations. One way of stating the question is: what is the most narrow phase distribution which is measurable by our setup? One difficulty is that the phase spread depends on the state of the BEC. Assuming that there is an intrinsic readout noise $\Delta\phi_\mathrm{d}$ of the phase extraction procedure, one could think of measuring it using a perfectly phase squeezed state. Since we cannot produce such a state, we chose to resort to numerical simulations. Instead of a non-classical state, which involves computing the $(N+1)\times(N+1)$ density matrix, we estimated the detection noise $\Delta\phi_\mathrm{d}$ for a coherent state.

Simulation of the Interference Patterns

We assume that the BEC is in a product state where all atoms share the wavefunction of Eq. (3.1). The intrinsic phase uncertainty for such a state is $\Delta\phi_\mathrm{SQL} = 1/\sqrt{N}$ (see Fig. 1.9), which sets the fundamental limit for the sensitivity of the phase inference procedure. We estimate $\Delta\phi_\mathrm{d}$ from applying our phase extraction procedure on a large number of artificial interference patterns with $\phi = 0$. The simulated interference patterns are generated stochastically in the following way, extending the simulations performed by Betz [51]:

- The position x_i of each of the N_d detected atoms is picked up independently by sampling the spatial probability distribution (3.1).
- For each atom, the number of detected photons n_i is picked up from a normal distribution with average $\bar{p}$ and variance $\sigma_p = 2\bar{p}$ reflecting both photon shot noise and the amplification noise of the camera.
- the position $x_{i,j}$ at which each photon is detected is picked up from a normal distribution of width $\sigma_\mathrm{LS} = 10\,\mu\mathrm{m}$ centered around x_i, crudely modeling the diffusion of the atoms in the Light Sheet and the finite optical resolution.
- Eventually, all the photon positions are binned on a grid with a camera object space pixel size of $4\,\mu\mathrm{m}$

Figure 3.6, left panel, shows an example of such a simulated interference pattern. For each numerical realization, the phase is estimated using the Fourier routine.[3] The circular standard deviation $\Delta\phi_\mathrm{d}$ is computed over the results of the estimation[4] (see Fig. 3.6, right panel). Table 3.1 shows the cumulative error budget for typical experimental parameters. The main contribution turns out to be the fit error linked to the atomic shot noise on the grid, i.e. the fact that when the condensate wavefunction is sampled, the number of atom n_i in the ith pixel has $\sqrt{n_i}$ fluctuations. Computing

[3] Note that the fit procedure yields slightly lower phase uncertainty since the artificial interference patterns precisely implement the fit model.

[4] Note that the error of the estimation process is actually $\Delta\phi_\mathrm{d}/\sqrt{m}$ (standard error of the mean), where m is the number of measurement.

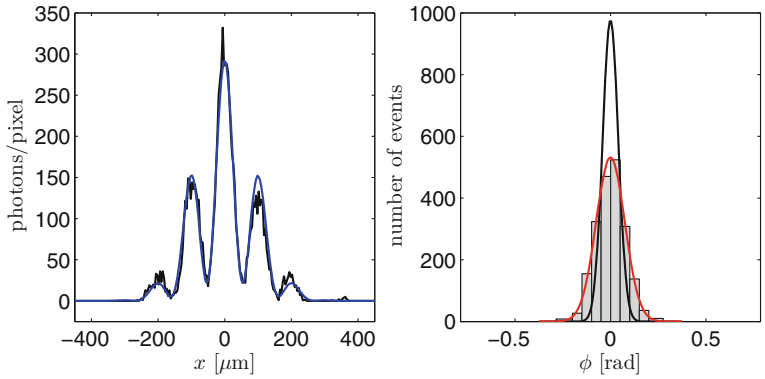

Fig. 3.6 Simulation of the phase estimation procedure. *Left* Numerical simulation of interference patterns for typical experimental parameters. *Black* one single numerical realization, *blue* average over 2000 realizations. *Right* Histogram of the phases estimated from the 2000 numerical runs. *Red* Gaussian fit to the histogram, yielding $\Delta\phi_{\mathrm{d}} = 0.078$. *Black* Gaussian distribution with RMS width $\Delta\phi_{\mathrm{SQL}}$ (Color figure online)

Table 3.1 Noise of the phase estimation method

	$\Delta\phi_{\mathrm{d}}$
Standard quantum limit ($N = 1100$)	$1/\sqrt{N} = 0.030$ rad
Standard quantum limit ($N_{\mathrm{d}} = 550$)	$1/\sqrt{N_{\mathrm{d}}} = 0.043$ rad
Atom shot noise ($N_{\mathrm{d}} = 550$)...	0.073 rad
$\cdots +$ photon shot noise	0.076 rad
$\cdots +$ diffusion in LS	0.078 rad

Circular standard deviation of the phase estimated from 4000 simulated interference patterns with $\phi = 0$, taking into account successively (a) the atom shot noise (b) the photon shot noise (c) the diffusion of the atoms in the Light Sheet

$\Delta\phi_{\mathrm{d}}$ for different numbers of detected atoms yields $\Delta\phi_{\mathrm{d}} \approx 2/\sqrt{N_{\mathrm{d}}}$ (see Fig. 3.7). In particular, assuming we perform the phase estimation on half of the atoms, $\Delta\phi_{\mathrm{d}} \approx 2.8 \times \Delta\phi_{\mathrm{SQL}}$. Increasing the fraction of detected atoms (for example by ARP transfer to $m_{\mathrm{F}} = 0$) would improve the sensitivity by a factor $\sqrt{2}$ to $\Delta\phi_{\mathrm{d}} = 0.55$ rad.

Optimal Sensitivity

It is not obvious to obtain an analytical expression to see how the phase sensitivity scales with the different parameters of the model. Nevertheless, neglecting photon and camera shot noise, as well as imaging resolution, we can estimate the best sensitivity for a phase estimation strategy based on a fit of the interference pattern [72]. We assume that for each pixel Δx_i ($i = 1, \ldots, M$) on the spatial grid, the probability distribution of the number of detected atoms n_i (ϕ) conditional to the phase ϕ is

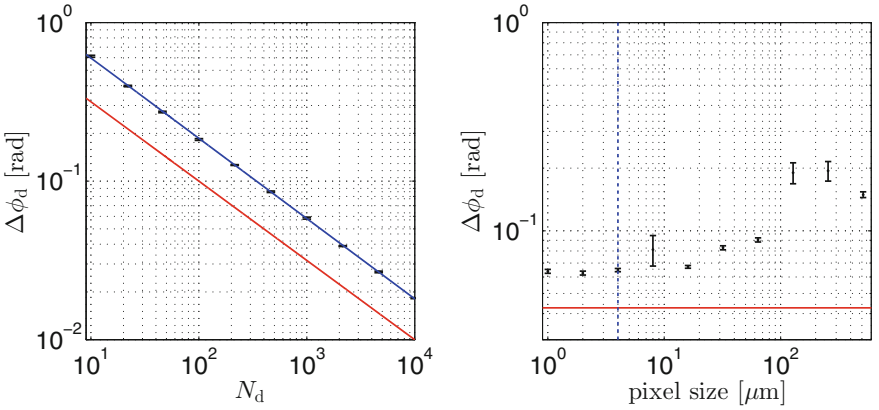

Fig. 3.7 Sensitivity of the phase estimation procedure (simulations). *Left Black dots* Noise on the phase measurement $\Delta\phi_d$ computed for different values of the number of detected atoms N_d. *Red* standard quantum limit ($\Delta\phi_{SQL} = 1\sqrt{N_d}$). *Blue* fit to the data, yielding $y = 1.91x^{-0.51}$. *Right* Noise on the phase measurement $\Delta\phi_d$ computed for different pixel sizes ($N_d = 550$). *Red* $y = \Delta\phi_{SQL}$. *Blue* pixel size (4 μm) (Color figure online)

known. This is in particular the case for a coherent state when the single particle wavefunction is known. For example, the expectation value of n_i reads

$$\bar{n}_i(\phi) = N \int_{\Delta x_i} \left|\psi_\phi(x)\right|^2 \mathrm{d}x \tag{3.7}$$

where $\psi(\phi)$ is the wavefunction of Eq. (3.1). In this case, the best sensitivity is obtained from a fit of the density profile, because this method precisely implements the maximum likelihood estimator for the phase [73]. The best sensitivity is given by the Cramer-Rao bound $\Delta\phi^2 = F^{-1}$ where F is the Fisher information (see Ref [72] and references therein)

$$F \underset{m\gg 1}{\sim} m \sum_{i=1}^{M} \frac{1}{\Delta n_i^2} \left(\frac{\partial \langle n_i \rangle}{\partial \phi}\right)^2. \tag{3.8}$$

Equation (3.8) reflects the fact that the sensitivity is improved when (a) the average density $\bar{n}_i$ on each pixel is more sensitive to a variation of the parameter ϕ (b) when the statistical fluctuations in each pixel are reduced.[5] In Ref. [74], the authors evaluate F and find that for a coherent state, it precisely corresponds to the SQL: $F = mN$. The fact that our estimation method is still at least twice less sensitive than the optimal method comes from technical limitations as well as the fact that in practice, the wavefunction (conditional to ϕ) is not known in advance. It has been

[5]The prefactor m simply indicates that the standard error scales as $1/\sqrt{m}$ for m independent measurements.

proposed [74] to first conduct a calibration where the actual interference patterns would be recorded for different, well-controlled values of ϕ, before proceeding to the phase estimation for an unknown ϕ.

Increasing the pixel size, for example by binning adjacent pixels, decreases the atom shot noise fluctuations but also decreases the sensitivity of the mean profile to the fit parameter (in the limit where all the data is binned in one pixel, no phase can be extracted). This suggests that there is an optimal pixel size. However, our numerical simulations (see Fig. 3.7, right panel) do not indicate any improvement above the (object space) camera pixel size $\Delta x = 4\,\mu\text{m}$, which was therefore kept for the analysis.

Note eventually that the model did not take into account effects such as the finite contrast of the interference pattern (e.g. due to phase axial fluctuation), fluctuations of N_d or of the fringe spacing etc. which would further deteriorate the phase sensitivity.

3.2.2 Number Difference Measurement

3.2.2.1 Methods

Conceptually, at least, it is more obvious to measure the number difference between the two modes of the BEC than their relative phase. It consists, ideally, in projecting the many-body wavefunction on the basis of Fock states (see Sect. 1.2.2.5). For this, tunnel coupling must be instantaneously turned off. When $J = 0$, the Fock states are the eigenstates of the system, so that the number difference distribution $p(n)$ cannot evolve.

In practice, this is achieved by ramping up the barrier between the two wells non-adiabatically with respect to the inverse Josephson frequency and then increasing the separation between the two clouds so that they can be resolved on the camera pictures after tof. The atom number difference can then be deduced from the difference of fluorescence intensity from each cloud. We have used to different techniques to separate the clouds:

- **Method 1** (see Fig. 3.8a). It consists in rapidly increasing the splitting between the two potential wells by ramping up the rf dressing amplitude. This gives a transverse kick with opposite outward momentum to each cloud. Then the potential is switched off and the two clouds fly away from each other. After a 46 ms tof, they are imaged with the LS detector.
- **Method 2** (see Fig. 3.8b) [47]. This method is inspired from a technique used to produce collisions between condensates [75]. It consists in rapidly switching off the RF dressing, so that the atoms find themselves in the static (harmonic) potential, but displaced from its minimum. For that, the switch off must be non-adiabatic with respect to the motion in the static trap. On the other hand, it must be adiabatic with respect to the variation of the Larmor frequency, to avoid projecting some of the atoms onto non-trapped m_F states. In practice, we ramped down the

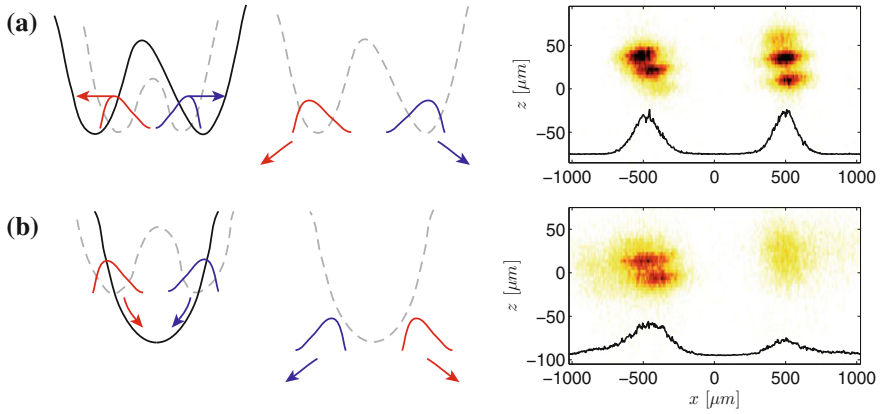

Fig. 3.8 Atom clouds separation. **a** *Left* Method 1. The RF dressing amplitude is raised to $\mathrm{RF}_{\mathrm{amp}} = 1$ within 0.1 ms in order to apply a transverse kick in opposite direction for each cloud. The potential is switched off immediately after, and the two clouds separate during tof. *Right* Typical f luorescence picture (averaged over 10 realizations with identical settings). When they are imaged, the two clouds are separated by about 1mm. Note that due to stray magnetic gradients during tof, the three m_{F} components of each cloud are slightly shifted longitudinally. **b** *Left* Method 2. The RF dressing is rapidly switched off (360 μs), so that the atoms find themselves shifted with respect to the minimum of the bare harmonic potential and start accelerating towards the center. The potential is switched off when they have gained maximum velocity. The two clouds cross each other while expanding and can be resolved after tof. *Right* Typical fluorescence picture (averaged over 10 realizations), exhibiting a population imbalance of the order of 40 %. Note that for method 2 the position of the *left* and *right* clouds are swapped

dressing in 360 μs. After the first quarter of an oscillation in the static trap, i.e. when the clouds have attained maximal inwards velocity, the potential is switched off. The clouds cross each other, separate and can be resolved once they fall through the LS.

The main advantage of method 1 is that the two clouds do not need to cross each other and that the overlap between the two clouds, as well as their transverse extension after tof, turns out to be smaller (see Fig. 3.9, right panel). For this reason, it was preferred for measurements where a precise counting of the atoms in each cloud was needed (see Sect. 3.4.3.1). On the other hand, when the splitting between the two wells is too weak, method 1 fails because of the atoms which remain on the tunnel barrier while it is ramped up and end up between the two clouds after expansion. Method 2 proved to be robust for a large variety of initial double-wells, and was used for all measurements were atom counting was not critical.

Collisions

Furthermore, atom collisions while the two clouds cross each other turn out not to be a limitation. The two parts of the BEC cross each other with a relative velocity

$v_{\mathrm{rel}} \approx 40$ mm/s, ensuring that collisions occur in the s-wave regime ($a_s \times v_{\mathrm{rel}} < \hbar$, see Sect. 1.1.2.1). A rough estimate of the total number of collisions when the BEC cross is [75]

$$n_{\mathrm{col}} = \frac{1}{2} N n_0 \pi a_s^2 v_{\mathrm{rel}} \tau_{\mathrm{col}} \tag{3.9}$$

where N is the total atom number, n_0 the peak density of one cloud and $\tau_{\mathrm{col}} = 2\sqrt{2} a_\perp / v_{\mathrm{rel}} \approx 20\,\mu\mathrm{s}$ is the time during which the two clouds overlap. For an elongated condensate in the 1D Thomas-Fermi regime (see Sect. 1.1.3.3),

$$n_{\mathrm{col}} = \frac{(3N)^{2/3}}{2\sqrt{2}} a_s^{5/3} a_\perp^{-1/3} a_\parallel^{-4/3} \tag{3.10}$$

where $a_\perp$ and $a_\parallel$ are the harmonic oscillator lengths in transverse and longitudinal direction respectively. For typical parameters, $n_{\mathrm{col}} \approx 2$. This relatively low value (note that it is an upper bound, because the density is overestimated) is a consequence of the elongated geometry of the cloud in the direction orthogonal to the collision, as well as the relatively small atom number.

It was checked experimentally (by not switching off the static trap and letting the clouds undergo several oscillations through each other) that the first hints of atom scattering events appeared only after ~10 consecutive collisions. Note that by increasing n_{col}, BEC collisions could be studied, benefiting from the high detection efficiency of the Light Sheet imaging.

3.2.2.2 Analysis and Noise

To estimate the number difference from the fluorescence images, a region of integration (ROI) is defined around each cloud (see Fig. 3.9). Note that to keep the area of the ROI small and minimize background intensity, no Stern-Gerlach gradient was applied. In our setup, the precise determination of the number difference benefits from the almost background-free fluorescence imaging. It has to be stressed that single atom sensitivity is crucial for number-squeezing measurements (see below). It has already allowed demonstrating strong number squeezing between correlated atom pairs in our experiment [76]. We will show in Sect. 3.4.3.1 how we could aslo show number-squeezing in a double well.

The model to describe the fluorescence signal has been described extensively in the PhD thesis of R. Bücker [77]. Let us review it here briefly to estimate the noise on a number difference measurement. The starting point are raw fluorescence camera pictures, namely a 512×512 matrix of counts. Using the values for the gain g_{cam} and the baseline c_0 fitted on the background image (see Sect. 2.3.2.1), the fluorescence signal (in photon/pixel) is reconstructed by computing

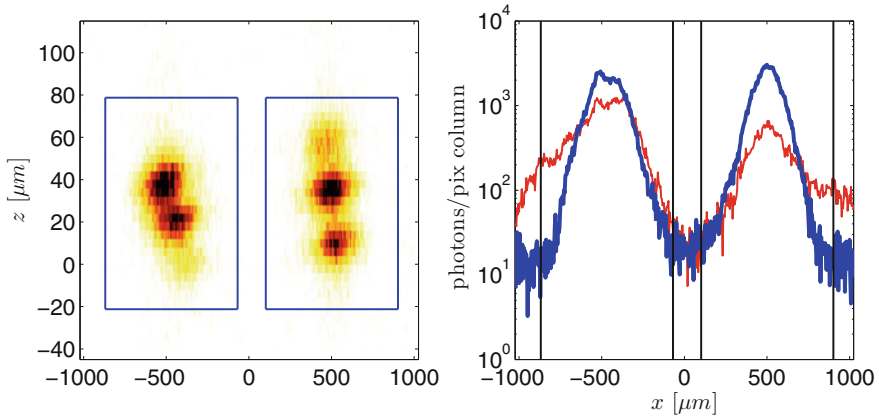

Fig. 3.9 Number difference measurement. *Left* Region of integration of the fluorescence signal from each of the two cloud for atom counting. *Right* Fluorescence signal (integrated along z—integration length: 80 pixels). The *black lines* correspond to the x-boundaries of the integration regions defined in the *left panel*. *Blue* signal from the left panel, obtained with separation method 1 (without crossing). Between the two integration regions, the signal is close to its background level. *Red* signal from Fig. 3.8a, obtained with separation method 2 (with crossing). The overlap is more significant, as well as the fraction of atoms outside the field of view, which would increase the measured number fluctuations (Color figure online)

$$I(x, y) = [c(x, y) - c_0] / g_{\text{cam}}. \tag{3.11}$$

Calling the number of atoms in the left (respectively: right) ROI $N_{L,R}$, the total fluorescence signal in each ROI is modeled by assuming that:

- for each atom, a certain number of photons p_i is detected. We model the p_i's by independent realization of a random process of mean $\bar{p}$ and variance σ_p^2. Due to the amplification noise of the camera, the variance is $\sigma_p^2 \approx 2\bar{p}$ [78].
- electronic noise on the CCD as well as stray light from the Light Sheet and fluorescence light reflected on the chip are responsible for a non-zero background. Assuming that the background is uniform,[6] we model it by a random noise $\hat{b}$ (average $\bar{b}$, variance σ_b^2) and assume that each pixel implements an independent realizations b_i of $\hat{b}$.

The total fluorescence signal $S_{L,R} \equiv \int_A I(x, y)\, \mathrm{d}x\, \mathrm{d}y$ in each ROI reads

$$S_L = \sum_{i=1}^{N_L} p_i + \sum_{j=1}^{A} b_j, \tag{3.12}$$

$$S_R = \sum_{i=1}^{N_R} p_i' + \sum_{j=1}^{A} b_j', \tag{3.13}$$

[6] Background photons are out of focus.

where A is the number of pixels in each ROI. This allows to estimate the noise on the fluorescence signal difference $s \equiv S_L - S_R$. In the case of a perfectly number-squeezed sample ($N_L = N_R = N/2$), the variance of s reads

$$\Delta s^2 = 2N\bar{p} + 2A\sigma_b^2. \tag{3.14}$$

This shows that the ROI must be kept as small as possible to minimize background. On the other hand, assuming a perfect background-free detector and exactly $\bar{p}$ detected photons per atoms, the signal variance would be

$$\Delta s^2 = \bar{p}^2 \Delta \left(N_\mathrm{L} - N_\mathrm{R}\right)^2. \tag{3.15}$$

The detection noise scales like $\sqrt{\bar{p}}$ while the signal scales like $\bar{p}$. For most of the experiments presented in this thesis, $\bar{p} \approx 16$ photons/atom, but higher values can be achieved, at the expense of a reduced spatial resolution. Eventually, this sets a limit to the best observable squeezing. Equating (3.14) to (3.15), we get the estimate

$$\xi^2_{\mathrm{N,d}} = \frac{2}{\bar{p}} + \frac{2A\sigma_b^2}{N\bar{p}^2}. \tag{3.16}$$

For $\bar{p} = 16$ photons/atom and $N = 1200$ atoms, the second term is almost negligible and $\xi_\mathrm{d} \approx 0.38$. Equation (3.16) shows that owing to its high sensitivity and low background, fluorescence imaging can give access to number fluctuations beyond the standard quantum limit. It also suggests that for squeezing measurements, we should crank up the LS intensity, as long as the two clouds remain clearly separated on the images. It also

3.2.3 Conclusion on Number and Phase Measurements

We have seen in this section that different detection methods exist for the two macroscopic observables. Importantly, they can be used at any time in the sequence to characterize the state of the condensate at each step of the interferometric sequence. We modeled our fluorescence imaging system to estimate the detection noise on each measurement, showing that while detecting number fluctuations below the standard quantum limit should be possible, the noise on the phase measurement using interference pattern is more than two times above the SQL.

This doesn't tell us how strongly phase-squeezed a BEC should be for us to be able to detect sub-shot noise phase fluctuations, but answering this question requires simulations of the full density matrix, which are beyond the scope of this thesis. Furthermore, this analysis underlines the fact that, owing to the highly sensitive detection methods already currently available, counting atoms can be much more precise than inferring the phase from an interference pattern [61, 79, 80]. It motivates

Table 3.2 Preparation trap parameters

Preparation trap ($RF_{Amp} = 0.3$)	
Horizontal transverse single-particle level spacing (simulated)	$E_x/h = 1.02\,\text{kHz}$
Vertical transverse trapping frequency	$\omega_y/2\pi = 1.75\,\text{kHz}$
Longitudinal trapping frequency	$\omega_z/2\pi = 12.4\,\text{Hz}$

Unless stated, all parameters have been directly measured

the search for new recombination methods for double-well interferometers allowing to map a phase difference into a number difference, as will be discussed in Sect. 3.6.

How the sensitivity of both phase and number difference measurements vary with the atom number is currently being investigated. It raises interesting questions about how a measurement performed on a fraction of the atoms impacts the state of the quantum superposition. Furthermore, while so far either one or the other observable could be measured in each experimental cycle, one could think of methods to measure both number and phase in the same time, for example by changing the switch off procedure.

3.3 Matter Wave Source

The matter wave source for the BEC interferometer is a single quasi-condensate in a slightly anharmonic trap. Instead of preparing the condensate in the static, harmonic trap, we chose to perform the last stage of the rf evaporative cooling in a weakly dressed trap ($RF_{Amp} = 0.3$), below the splitting point $RF^c_{Amp} = 0.42$, in order to minimize excitations of the collective modes during the splitting (see Fig. 3.11). The potential is essentially harmonic along the longitudinal (z) and transverse vertical (y) direction, while it has a significant quartic component in the horizontal (splitting) direction (see schematics in Fig. 1.2). Table 3.2 summarizes the trap parameters.

The atom number $N \approx 1200$ is controlled by the final frequency of the rf evaporation knife (10 % fluctuations from shot to shot). For these parameters, the condensate is well described by a 1D Thomas-Fermi model (see Fig. 1.3) and $\mu \approx h \times 450$ Hz.[7] The temperature of about 20 nK is estimated from the longitudinal profile after expansion using a stochastic model to describe the phase fluctuations along the quasi-condensate [81] (see Fig. 3.10). This rough estimate is compatible with the absence of an isotropic thermal fraction and excludes a temperature higher than 50 nK.

The fact that $k_B T, \mu \leq h\nu_{x,y}$ cloud lies in the weakly interacting 1D quasi-condensate regime [82, 83]. The corresponding phase coherence length [] (computed from the peak 1D density of 35 atoms/μm) lies between 10 and 20 μm, which is less than the length of the cloud $L \approx 50\,\mu\text{m}$. However, as will be discussed in Sect. 3.4.5, it seems that for matter-wave interferometry, only the coherence properties of the

[7] Here, the zero-point energy is substracted from the chemical potential.

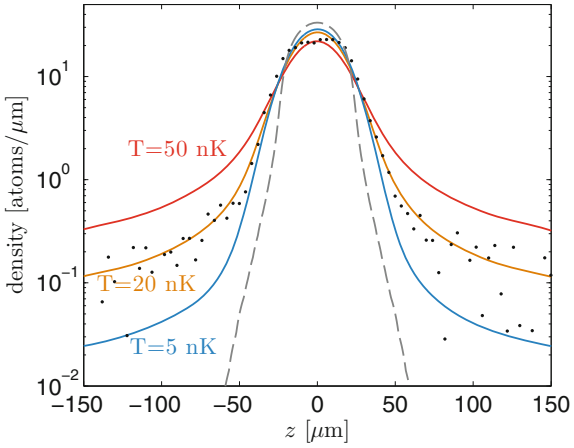

Fig. 3.10 Temperature estimation. The temperature of the initial quasi-condensate is estimated from its longitudinal profile (averaged over several realizations) after expansion, using a stochastic model to model the thermal axial phase fluctuations and assuming ballistic expansion. Blue, orange, red lines: density profiles computed for T = 5, 20 and 50 nK respectively. *Dashed line* computed in situ profile. Note that in the longitudinal direction, the expansion is much slower than in the transverse, tightly confined directions. The wings of the density distribution are compatible with a temperature of 20 nK, yielding an axial phase coherence length of 20 μm at the center of the cloud (Color figure online)

relative phase between the two halves of the condensate are relevant, regardless of the phase coherence of a single BEC.

For this reason, in the following, we will most of the time refer to our quasi-1D condensate simply as a Bose-Einstein condensate, and apply tools which, strictly speaking, have been developed for true condensates. In Chap. 4, we will question this simplistic assumption and discuss the implications of the multimode nature of our matter-wave source.

3.4 Coherent Splitting and Generation of Atomic Squeezed States

The first step of the interferometer sequence consists in splitting a single condensate into a quantum superposition of two spatially separated, localized modes with a well-defined (i.e. reproducible) relative phase. The dynamics of splitting must be always be considered with respect to different timescales: on the one hand, the timescales associated to the external degree of freedoms (motion of the condensate along the different spatial directions in the trap), on the other hand, that associated to the tunneling of the particles. Adiabaticity or non-adiabaticity of the splitting always refers to one particular timescale.

In Sect. 3.4.1, we explain how adiabatic splitting of the external wavefunction of the BEC is achieved on our atom chip using rf dressed potentials. In Sect. 3.4.2, we show how near-to-adiabatic splitting of the interacting many-body wavefunction of the BEC inherently produces a spin-squeezed state. In Sect. 3.4.3, we present the results of the measurements of the number and phase distributions to characterize the state of the BEC right after splitting, and we evaluate the achieved degree of squeezing. Eventually, in Sect. 3.4.4, we compare our results to the prediction of a simple model for the evolution of the many-body wavefunction in the two-mode approximation.

3.4.1 Coherent Splitting of a Condensate

3.4.1.1 Coherent Splitting Techniques

Coherent splitting of a BEC is achieved by means of an atomic beam splitter. Different types of BS have been developped for BEC interferometry. In interferometers with internal-state labeling, the BS consists generally in a $\pi/2$ rf and/or microwave pulse, see for example Ref. [14], or in a two-photon Raman coupling pulse [27]. In Bragg interferometers, coherent splitting relies on the diffraction of the atoms by a moving light grating, which acts as a phase grating for the atomic de Broglie waves and creates coherent, displaced copies of the BEC [6, 32]. A related approach relies on the coherent diffraction of a BEC on a magnetic phase grating created by the superposition of a static lattice potential and an oscillating field on an atom chip [84].

In double-well interferometers, coherent splitting is achieved by smoothly deforming the confining potential from a single well to a double well. In the limit where the rate of transformation of the potential is slow compared to the timescale of the transverse motion (typically the inverse transverse trap frequency), a BEC prepared in the transverse ground state of the initial single-well potential will adiabatically follow the instantaneous ground state and end up in the ground state of the double-well potential.[8] Hence, in a symmetric double well, adiabatic splitting produces a superposition of two localized states (one in each well) with the same phase. In a sense, this is merely a consequence of the definition of the two modes: we have seen in Sect. 1.2.1 that in a symmetric double well, it is natural to define the left and right modes as the sum and the difference of the to first eigenstates. In this case, the ground state corresponds necessarily to a symmetric superposition of left and right modes with $\phi = 0$. Restricting the dynamics of the BEC to the two lowest-lying eigenstates also underlines the fact that an adiabatic separation BS realizes a unitary operation. The second input port of a "Y-shaped beam splitter" such as the one presented in this thesis corresponds to the first excited state.

[8]Note that, at least for a non-interacting system, this argument remains true for any eigenstate of the potential and has motivated the proposal of a multimode interferometer [85].

Note that the situation is different in an asymmetric double well, where the eigenstates "collapse" in the left and right mode when the energy difference between the trap minima becomes comparable to the energy difference between the two lowest eigenstates (see Ref. [12] for a discussion of the sensitivity of adiabatic splitting to potential asymmetry in the non-interacting case.). Asymmetric splitting can instead be used to prepare a BEC with a finite population imbalance [86]. Adiabatic splitting of an interacting BEC in a double-well created using the corrugation of a magnetic film has even been used to characterize the potential asymmetry [87].

A beam splitter for cold atoms realized with a Y-shaped magnetic guide was demonstrated in 2000 [88]. Coherent, i.e. phase-preserving splitting of a BEC was first achieved in 2004 with an optical double-well implemented with a focused laser beam passed through an AOM driven by two rf signals [44]. One year later, the first DWI using rf-dressed potentials was demonstrated on atom chip [45]. The same year, the first BJJ was realized by superimposing a 1D optical lattice to an optical harmonic potential, realizing a single weak link [55].

In Ref. [16], we were able to demonstrate symmetric coherent splitting of a BEC between the ground and the first excited state of a single well through a non-adiabatic manipulation of the potential ("shaking"). In principle, in a given anharmonic trap (for example a double well) where two modes can be singled-out, it is possible to create any coherent superposition by appropriately manipulating the confining potential, if needed by means of optimal control methods [89]. Arguably, this is similar to the splitting methods used in Ramsey or Bragg interferometers, where the phase of the coherent superposition is imprinted by the driving field (rf, microwave or laser).

3.4.1.2 Implementation in Our Setup

As explained in Sect. 2.2.2, we use essentially the same splitting technique as in Ref. [45], with the minor difference that we tune the rf dressing intensity instead of the rf detuning. Figure 3.11 shows how the rf dressed potential is smoothly transformed from a single well to a double well as $\mathrm{RF}_{\mathrm{Amp}}$ is increased. Transversely, the potential first flattens until a point where the quadratic term completely vanishes. At the splitting point $RF^{\mathrm{c}}_{\mathrm{amp}} = 0.42$, a local maximum emerges in the center. As the dressing amplitude is further increased, the height of the barrier, the well spacing and the trapping frequency increase in each well (see Sect. 2.15). Table 3.3 summarizes the parameters of the final double well used in most of the experiments presented in this thesis ($\mathrm{RF}_{\mathrm{Amp}} = 0.65$).

To prepare a population imbalance, the splitting axis is tilted by an angle α with respect to the horizontal plane (see Fig. 2.8) by scaling the intensities in each RF wire following Eq. (2.30). This way, a larger fraction of the wavefunction is localized in the lowest potential well (see Fig. 3.12).

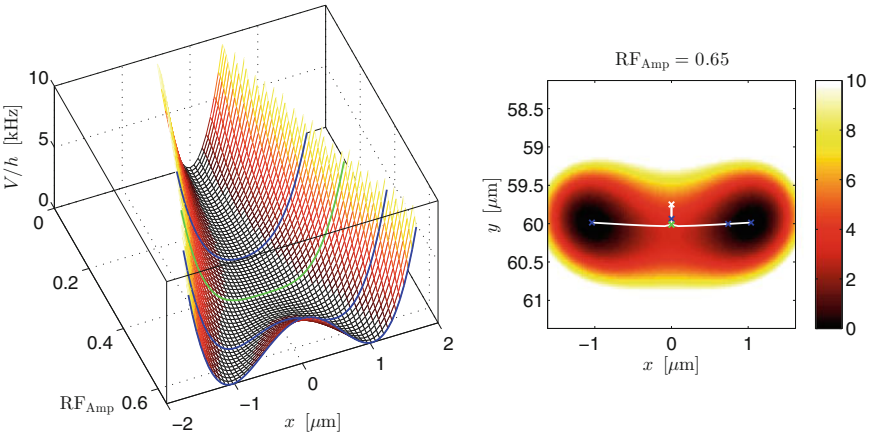

Fig. 3.11 Splitting the rf dressed potential. *Left* 1D cut along the splitting axis (x) of the simulated potential for different values of the rf dressing intensity. In absence of dressing (RF$_{\rm amp} = 0$), the potential is harmonic. When the RF amplitude is increased over the critical value RF$^{\rm c}_{\rm amp} = 0.42$ (*green line*), two minima appear which are separated by a potential barrier. The *blue lines* represent respectively the preparation trap (RF$_{\rm Amp} = 0.3$), the trap used for the recombination (RF$_{\rm amp} = 0.55$) and the splitting trap (RF$_{\rm Amp} = 0.65$). *Right* 2D cut of the RF$_{\rm amp} = 0.65$ potential in the transverse (x, y) plane ($z = 0$, gravity is pointing *downwards*). The *white line* represents the trajectory of the potential minima from RF$_{\rm Amp} = 0$ to 0.65 (*White cross* static trap, *green* and *blue crosses* same as in *left panel*). Note the *downward* sag before RF$^{\rm c}_{\rm Amp}$ is reached, which is mostly caused by gravity. The typical transverse rms size of the ground state wavefunction is of the order of 200 nm. Color map (in both panels): potential in kHz.

Table 3.3 Parameters of the double well at the end of the splitting ramp

Splitting double well (RF$_{\rm Amp} = 0.65$)	
Horizontal trap frequency (in each well)	$\omega_x/2\pi = 1.44\,$kHz
Vertical transverse trap freq. (in each well)	$\omega_y/2\pi = 1.84\,$kHz
Longitudinal trap freq. (in each well)	$\omega_z/2\pi = 13.2\,$Hz
Well spacing (simulated, in agreement with fringe spacing)	2.1 μm
Barrier height (simulated)	$h \times 3.7\,$kHz
Tunnel coupling energy (simulated)	$J/h \approx 0.1\,$Hz

Unless stated, all parameters have been directly measured. Note the finite value of the estimated coupling

3.4.1.3 Motion of the Condensate During Splitting

Adiabaticity in the Direction of Splitting

One common requirement for coherent splitting is that the deformation of the potential should be adiabatic with respect to the motion of the trapped condensate. Otherwise, excitations in the BEC will cause heating and decoherence. In Ref. [44], axial breathing modes excited by the splitting led to a strong curvature of the spatial interference fringes, eventually rendering phase readout impossible after a few ms.

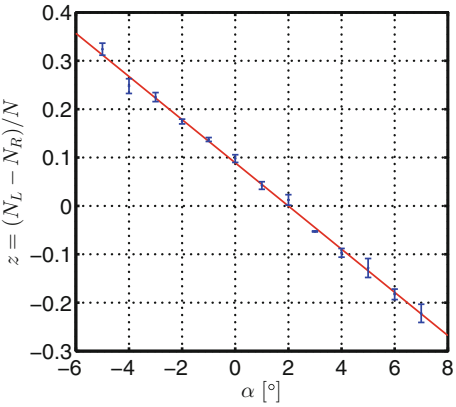

Fig. 3.12 Splitting with imbalance. Normalized population imbalance as a function of the splitting angle (α parameter used in Eq. (2.30)). Note that for this particular measurement, α is offset by 2°, probably because of a slight asymmetry of the currents in the supposedly balanced configuration ($\alpha = 0$). This offset was carefully checked and readjusted whenever needed. The linear fit (*red*) yields a sensitivity for the number difference preparation of 53 ± 2 atoms by degree ($N = 1200$) (Color figure online)

Our elongated geometry is characterized by two timescales: transversely, trapping frequencies in the kHz range impose to manipulate the potential at the ms timescale. Longitudinally, the trapping frequency is of the order of 10–20 Hz, corresponding to hundreds of ms. Considering a system initially in the eigenstate $|n\rangle$ of the Hamiltonian (energy E_n), a commonly used criterion for adiabaticity is

$$\sum_{m \neq n} \left| \frac{\hbar \langle m|\dot{n}\rangle}{E_n - E_m} \right| \ll 1, \tag{3.17}$$

where the summation is performed over all other eigenstates [90]. For a single particle initially in the ground state of a harmonic trap with a time-dependent frequency $\omega(t)$ and position $x_0(t)$, it translates into

$$\underbrace{\frac{1}{4\sqrt{2}} \frac{|\dot{\omega}(t)|}{\omega^2(t)}}_{\text{(de)compression}} + \underbrace{|\dot{x}_0(t)| \sqrt{\frac{m}{2\hbar\omega(t)}}}_{\text{displacement}} \ll 1. \tag{3.18}$$

This criterion can never be fulfilled during the entire splitting because when $\mathrm{RF}_{\mathrm{Amp}} = 0.42$, the transverse trapping frequency vanishes ($\omega \to 0$)[9] while in the same time, x_0 grows like the square root of the dressing amplitude (see Fig. 2.15).

[9] Strictly speaking, at the splitting point, the transverse potential becomes quartic so that the criterion (3.18) does not apply anymore. Nevertheless, the adiabaticity constraint becomes more stringent since the spacing between the energy levels diminishes.

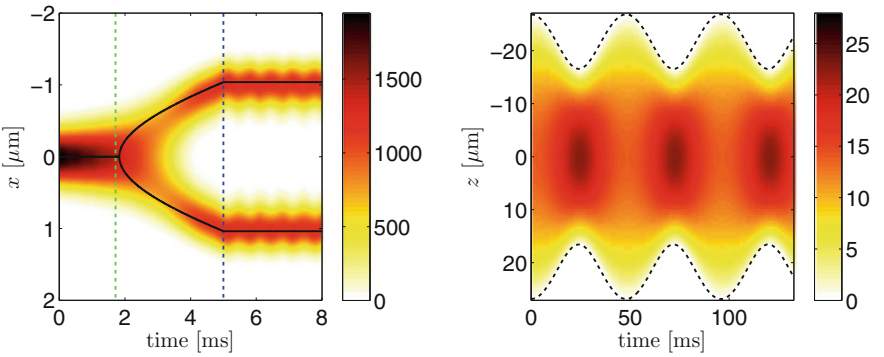

Fig. 3.13 Splitting a Bose-Einstein condensate. *Left* Transverse density profile (in atoms/μm) as a function of time (1D GPE simulation, the initial state is the ground state of the preparation trap $\mathrm{RF}_{\mathrm{amp}} = 0.3$). Starting at $t = 0$, the RF intensity is ramped up linearly for 5 ms, and then held at the final value $\mathrm{RF}_{\mathrm{amp}} = 0.65$. The *green dotted line* indicates the splitting point ($\mathrm{RF}_{\mathrm{amp}} = 0.42$), the *blue* one the end of the splitting ramp. The *black line* indicates the position of the minima of the potential at each time. Note the small residual transverse oscillation after the end of the splitting. *Right* Breathing of the longitudinal density profile (in atoms/μm) of one cloud after symmetric splitting, obtained by solving numerically the scaling equation (3.19). The *dotted lines* show the evolution of the Thomas-Fermi Radius. Between a maximum and a minimum of the axial breathing oscillation, the length of each cloud shrinks by 40 % while its peak density is increased by 80 % (Color figure online)

We chose to minimize the excitations by starting from an already dressed potential and increase linearly the dressing amplitude in 5 ms from $\mathrm{RF}_{\mathrm{amp}} = 0.3$ to the final value $\mathrm{RF}_{\mathrm{amp}} = 0.65$. We checked that no transverse excitation was detectable after the end of splitting, in agreement with simulations predicting an overlap better than 90 % with the instantaneous ground state at all times (see Fig. 3.13, left panel). In contrast, for ramps shorter than 1 ms, a strong heating of the cloud was observed. Optimal control techniques may enable faster splitting with high fidelity [16].

Axial Breathing

The splitting occurs on a time scale much shorter than the longitudinal motion. This results in an axial breathing mode (see Fig. 4.1). Two effects contribute unequally to the breathing: first, each part of the condensate has only half of the initial atom number (or any other proportion, depending of the choice of the imbalance). Secondly, the longitudinal frequency of the final trap ($\omega_z = 2\pi \times 13.2$ Hz) is slightly different from the initial one. After splitting, each condensates initially sees its shape unaffected, while its atom number and the potential it experiences suddenly changes. The cloud is thus "too long" compared to its new equilibrium size, and it begins to breath inwards, as could be observed in tof.

More precisely, using the explicit expression for the 1D Thomas-Fermi radius at equilibrium (Eq. 1.61) with the number N_i atoms ($i = L, R$) in each well, we see that

in the case of a symmetric splitting ($N_L = N_R = N/2$), the cloud is 25 % too long. Following the scaling approach of Refs. [91–93], the evolution of the Thomas-Fermi radius can be described by a scaling factor $b(t) \equiv R(t)/R_{TF}$ which in 1D evolves according to

$$\ddot{b} + \omega_z^2 b = \frac{\omega_z^2}{b^2} \tag{3.19}$$

(see Fig. 3.13, right panel). For a small perturbation ($b(t) = 1 + \epsilon(t)$ with $\epsilon \ll 1$), the oscillation of the TF radius is close to harmonic at the frequency $\omega_Q = \sqrt{3}\omega_z \approx 2\pi \times 22.8$ Hz (we measured $\omega_b = 23 \pm 5$ Hz). Importantly, it implies that after splitting, both condensates are out-of-equilibrium, causing the phase to evolve both in space and time (see Sect. 3.5.3). One way of mitigating this effect would be to take advantage of the dependence of ω_z with the dressing amplitude. By choosing a preparation trap such that the change of trap frequency compensates the change of interaction energy after the atom number has been divided by two, we hope to strongly suppress the breathing mode.

3.4.2 Squeezing and Adiabatic Splitting

We now turn to the dynamics of the many-body wavefunction during the splitting. As we have seen in Sect. 1.2.3, the ground state of a bosonic Josephson junction with repulsive contact interaction is always number-squeezed (see Fig. 1.10). The basic idea of number squeezing generation by adiabatic splitting is to reduce fluctuations of the number imbalance by increasing the ratio $\Lambda = UN/2J$—generally by decreasing J—between interaction energy and tunnel coupling.

Number squeezing in a BEC was observed in an array of weakly linked traps (optical lattice) in 2001 [94]. In 2008, the number and the phase distribution of a condensate in an optical double well (as well as an optical few-well potential) were measured to demonstrate number and spin squeezing [61]. Sub-binomial numer fluctuations were also observed in a cloven BEC in a magnetic double well on an atom chip [95]. In the last years, number or spin squeezing between internal states of a BEC was reported in various setups [17, 62]. An extreme case of number-squeezing is the generation of twin atomic states, for example in our setup using collisions in an elongated BEC [76], or spin exchanging collisions [80, 96].

Figure 3.14 shows how the characteristic energy scales of our BJJ depend on the control parameter of the double well (the dressing amplitude RF_{Amp}). How these parameters were computed is detailed in appendix A. As RF_{Amp} is increased, the tunnel coupling energy drops by several orders of magnitude while the interaction energy varies by less than a factor of 2. Note that our simulations indicate that as long as $RF_{\mathrm{Amp}} \leq 0.53$ (vertical black dotted line), the chemical potential of the first excited state is larger than the barrier height, meaning that the two-mode approximation is not expected to give accurate quantitative results. According to the simulations, the

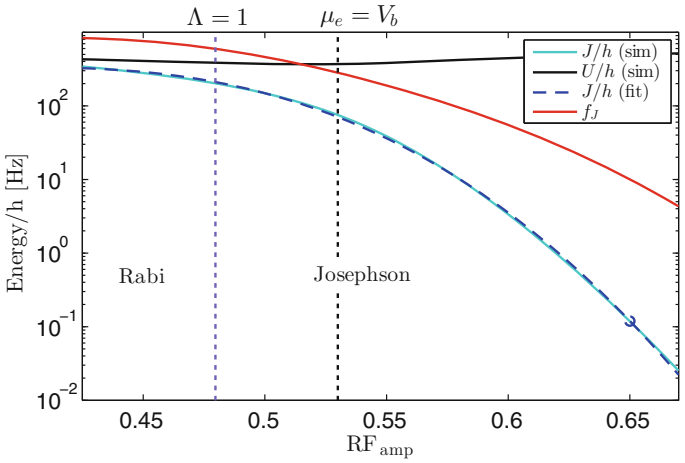

Fig. 3.14 Parameters of the bosonic Josephson junction. Result of numerical simulations of the BJJ for different rf dressing amplitudes and $N = 1200$ atoms. *Pale blue line* tunnel coupling energy, *black line* interaction energy, *red* Josephson frequency. The *dashed blue line* is a fit to the simulated coupling energy with the analytical model (3.31). The splitting point, where a second potential minimum appears, corresponds to $\mathrm{RF_{Amp}} = 0.42$. At the end of the splitting ramp, $\mathrm{RF_{Amp}} = 0.65$ (the *blue circle* shows the expected final value of the coupling $J/h \approx 0.1$ Hz). The vertical *dotted line* represents the crossover between Rabi and Josephson regimes $\Lambda = 1$ (*purple*) and the point where the chemical potential μ_e of the first excited state is equal to the barrier height V_b, setting a lower bound for the validity range of the two-mode approximation. Note that the crossover between the Josephson and the Fock regime is outside the plotting range (Color figure online)

transition between the Rabi and the Josephson regime occurs around $RF_{\mathrm{Amp}} \leq 0.48$ (vertical purple dotted line). Importantly, it means that our BJJ can essentially be tuned in the Josephson and Fock regimes. This is an important limitation of our BJJ: for our typical atom numbers ($N \sim 1000$), the interaction energy (roughly measured by the chemical potential) and the oscillation frequencies are both of the order of 1 kHz. For this reason, it is impossible to reach the Rabi regime within the validity range of the two-mode approximation. One could think of strongly reducing U by reducing the atom number, but besides the technical challenge of preparing a stable, low number of atoms, at some point, the mean-field description of the BJJ would break down.

We recall here the expressions given in Sect. 1.2.4.4 for the number-, phase- and spin squeezing factors in the ground state of the BJJ, in the Rabi and Josephson regimes:

$$\xi_N^2 = \frac{1}{\sqrt{\Lambda + 1}}, \tag{3.20}$$

$$\xi_\phi^2 = \sqrt{\Lambda + 1}, \tag{3.21}$$

$$\xi_S^2 = \frac{1}{\sqrt{\Lambda + 1}} \exp\left(\sqrt{1 + \Lambda}/N\right) \approx \xi_N^2 \tag{3.22}$$

In the final $\mathrm{RF}_{\mathrm{amp}} = 0.65$ double well, $\sqrt{\Lambda} \approx 2400$, so that the spin squeezing factor is approximately equal to the number-squeezing factor.

Starting from the ground state of a BJJ with finite (and usually small) Λ, an arbitrarily high amount of number squeezing could be in principle achieved as long as the system adiabatically follows its instantaneous ground state. In the limit $J = 0$, the ground state is nothing else than the perfectly number-squeezed twin Fock state [97]. Of course, this would require splitting infinitely slowly because in this limit, the inverse Josephson frequency ω_J^{-1} diverges. In practice, splitting can be adiabatic in the beginning, until a point where it breaks down and the number distribution is frozen (no atom can tunnel). Note that in this regard, the breakdown of adiabaticity is necessary to achieve coherent splitting, since the relative phase of the twin Fock state is completely undetermined.

We expect this to happen in our double well, where simulations predict that the final value of the coupling energy is $J/h \approx 0.1\,\mathrm{Hz}$, corresponding to a Josephson period of the order of 100 ms, much longer than the splitting time. We will come back in Sect. 3.5.2.4 on the implications of the fact that the final coupling has a finite value.

3.4.3 Results: State of the BEC After Splitting

To characterize the state of the condensate right after splitting, we measured the distribution of the two conjugated macroscopic observables *number difference* and *relative phase* (see Fig. 3.15). This was achieved by inferring either number or phase for a large number of condensates prepared in the same conditions, using the methods explained in Sect. 3.2.

3.4.3.1 Number Distribution

The number difference distribution was computed from fluorescence images of the two clouds after separation (see Fig. 3.8). For each picture, the total fluorescence coming from each of the two cloud (S_L, S_R) was integrated over a region located around the cloud (see Fig. 3.9). Figure 3.15, top pannel, shows the histogram of the fluorescence signal difference $s \equiv S_L - S_R$ from around 230 independent experimental realizations. We observed a bell-shaped distribution centered around 0 with a sample variance $\Delta s^2 = 8.5 \times 10^4$. The statistical uncertainty on the variance was estimated to be of the order of $\pm 0.8 \times 10^4$. To deduce the fluctuations of n from that of s, we resorted to the model presented in Sect. 3.2.2.2. Assuming a fixed total number of atoms $N = N_L + N_R$ and using the law of total variance, the variance Δs^2 of the fluorescence signal is connected to $\Delta(N_L - N_R)^2$ by

$$\Delta s^2 = \underbrace{2A\sigma_b^2}_{\text{background noise}} + \underbrace{2N\bar{p}}_{\text{photon detection noise}} + \bar{p}^2 \Delta\left(N_L - N_R\right)^2 . \tag{3.23}$$

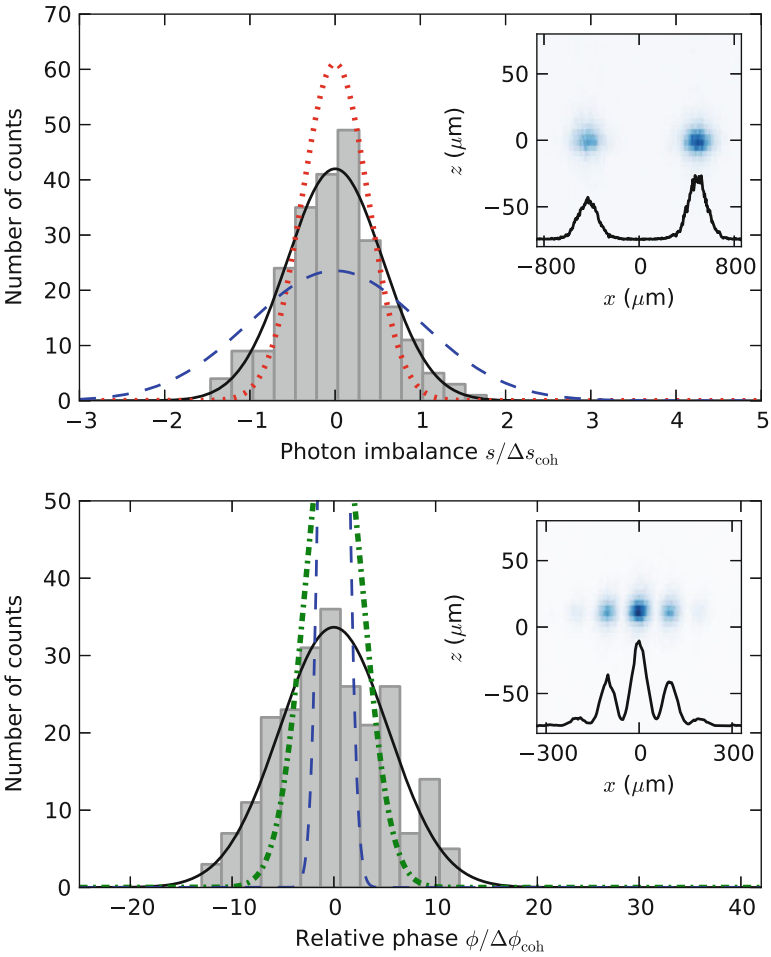

Fig. 3.15 Number and phase distributions after splitting. *Top*, Histogram of the difference between the fluorescence signals of the *left* and *right* clouds $s = S_{\mathrm{L}} - S_{\mathrm{R}}$, in units of the standard deviation expected for a coherent state Δs_{coh}. The curves indicate a normal distribution corresponding to the measured number squeezing factor $\xi_{\mathrm{N}} = 0.41 \pm 0.04$ (*solid black*); the distribution expected in the limit $\xi_{\mathrm{N}} = 0$, where only detection noise is responsible for fluctuations (*dotted red*); and the distribution expected for a coherent state in the absence of detection noise (*dashed blue*). The inset shows a typical fluorescence picture used for measuring S_L and S_R. *Bottom*, Histogram of the measured relative phases ϕ in units of the circular standard deviation of a coherent state $\Delta\phi_{\mathrm{coh}}$. The *curves* indicate a normal distribution with the measured standard deviation $\Delta\phi = 5.4 \pm 0.5 \times \Delta\phi_{\mathrm{coh}}$ (*solid black*); and the distributions expected for a coherent state in the absence (*dashed blue*) and in the presence (*dash-dot green*) of detection noise. The inset shows a typical matter-wave interference pattern from which the phase is extracted. Each histogram was obtained from ∼230 independent experimental realizations (Color figure online)

(see Ref. [77] for a more detailed and comprehensive analysis of number fluctuation measurements). The first two terms correspond to the detection noise (dashed red curve of Fig. 3.15, see also Eq. (3.14)), while the third term describes the actual quantity we want to measure. The mean number of photons per atom $\bar{p} = 15.6 \pm 1.3$ is estimated by comparing images of condensates prepared in the same conditions taken either with the absorption or the fluorescence imaging. We replace N by the average atom number $\bar{N} = 1110$. The background noise is estimated from a region of area $2A$ containing no atom, and amounts to 6 % of the total variance, while the photon detection noise contributes to about 40 %. This sets an upper bound to the atom number fluctuations. If we first neglect the background noise and assume that we detect exactly $\bar{p}$ photons per atom, the non-corrected number squeezing factor is

$$\xi_{N,\mathrm{unc}} \equiv \sqrt{\frac{\Delta s^2}{\bar{p}^2 \bar{N}}} = 0.56 \pm 0.04. \tag{3.24}$$

Correcting for detection noise, we get from Eq. (3.23)

$$\xi_N = \sqrt{\frac{\Delta s^2 - 2\bar{N}\bar{p} - 2A\sigma_b^2}{\bar{p}^2 \bar{N}}} = 0.41 \pm 0.04. \tag{3.25}$$

It is also common to express the number squeezing factor in decibel: $\xi_N^2 = -7.8 \pm 0.8$ dB. It indicates that the fluctuations of the atom number difference $\Delta (N_L - N_R) = 13$ atoms are more than a factor of two smaller than that expected for a classical coherent state (dashed blue curve in Fig. 3.15). This proves that the splitting process generates a number-squeezed state. However, this value is about three times higher than the value expected in the ground state of the split trap ($\xi_N \approx 0.14$), suggesting that the splitting is not truly adiabatic and/or that the BEC is not initially in the ground state.

The uncertainty on ξ_N was computed by error propagation, assuming that the measured parameters (Δs^2, $\bar{p}$, ...) were uncorrelated. The main contribution comes from the uncertainty on Δs^2, which scales like $1/\sqrt{k}$, k beeing the number of measurements. The main potential source of systematic error is the value of $\bar{p}$ (or equivalently the mean number of atoms), which is calibrated using the absorption imaging system (see Sect. 2.3.1.1). Overestimating $\bar{p}$ by 20 % yields a higher value $\xi_N \approx 0.46$. It would be useful to compare the measured fluctuations to a binomial distribution, such as the fluctuations expected from splitting a non-interacting cloud. A method to mimic this situation, for example by performing a rf or microwave Rabi $\pi/2$ pulse between two internal states, is currently under investigation.

3.4.3.2 Phase Distribution

Here as well, the phase distributions was reconstructed from the results of the analysis of ~230 independent interference patterns obtained in the same condi-

tions (see Fig. 3.15, bottom panel). The phase was extracted by Fourier transform (see Sect. 3.2.1.2). It displays a bell-shaped distribution with vanishing average and circular standard deviation

$$\Delta\phi = 0.16 \pm 0.01 \text{ rad}, \tag{3.26}$$

(black curve, the error reflects the uncertainty on the sample variance). The phase spread is larger than the intrinsic phase uncertainty for a classical coherent state $\Delta\phi_{\text{SQL}} = 0.03$ rad (dashed blue curve). It is also larger than the circular standard deviation expected for a coherent state, taking into account our detection noise $\Delta\phi_d = 0.08$ rad (dashed green curve, see Sect. 3.2.1.4). Unlike the atom number difference, there is no easy way to correct the phase distribution for detection noise. Still, the phase fluctuations are smaller than that expected in the ground state of the split trap ($\Delta\phi \approx 0.22$ rad), indicating again that the splitting is not fully adiabatic.

The coherence $\alpha = \langle \cos\phi \rangle = 0.987 \pm 0.001$ is very close to 1, due to the relatively small phase fluctuations.[10]

3.4.3.3 Uncertainty Product and Spin Squeezing

From the measured values of the phase and number-difference spread, we compute the uncertainty product

$$\Delta\,(N_L - N_R)\,\Delta\phi = 2.3 \pm 0.4, \tag{3.27}$$

which is about twice the minimal value allowed by the Heisenberg uncertainty relation. Altogether, the state of the condensate exhibits reduced number fluctuations and a high coherence, yielding a spin squeezing factor (see Eq. 1.164)

$$\xi_S = \frac{\xi_N}{\langle \cos\phi \rangle} = 0.41 \pm 0.04. \tag{3.28}$$

Note that the value of ξ_S is here identical to that of ξ_N thanks to the large coherence factor.

It proves that the output state of the separation beam splitter is a spin-squeezed state with a potential metrology gain of 7.8 ± 1 dB over the standard quantum limit (see Sect. 1.2.4.5). It also demonstrates that splitting produces a non-separable state (see Sect. 1.2.4.6). According to the criterion (1.177), the measured fluctuations and the coherence factor imply that our BEC contains ~150 entangled particles. We can exclude entanglement of less than 67 atoms with more than 90 % probability (see Fig. 3.16).

This figure can be compared to depth of entanglement reported in different experiments with BECs. In Ref. [17], $M = 170$-atom entanglement was demonstrated in a

[10] Note that α is insensitive to $\Delta\phi$ to the first order.

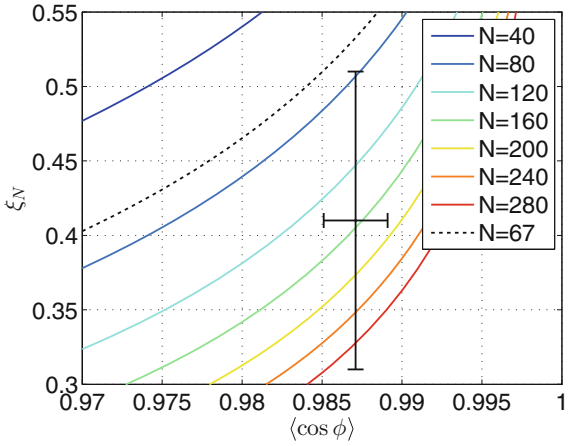

Fig. 3.16 Depth of entanglement. Each *curve* displays the lower bound Eq. (1.177) for ξ_N as a function of the coherence factor $\langle \cos \phi \rangle$, for a collection of spin $N/2$ particles. Our measured number and phase fluctuations (*black points*) exclude that the density matrix of the system can be written as a direct product of blocks all involving less than ∼150 atoms. The error *bars indicate* two times the standard error of the mean, allowing to exclude entanglement of less than 67 atoms with more than 90 % probability

BEC containing $N = 2300$ atoms following the one-axis twisting scheme proposed in Ref. [98]. The same year, $M = 4$-atom entanglement for $N = 1250$ was reported in an experiment using state-dependent potentials [62]. Very recently, Dicke states with at least 28 entangled atoms (out of 8000) [99] and 13 (out of 40) [100] were demonstrated.

3.4.4 A Simple Model to Describe Adiabatic Splitting

The main hurdle when trying to get a quantitative description of adiabatic splitting lies in the fact that the parameters of the BJJ can vary over several orders of magnitude during splitting, making direct dynamical simulations strenuous [101]. Involved numerical methods have been used to compute [102] and optimize [103] number squeezing.

In order to get an intuition about the amount of squeezing we expect from adiabatic splitting, we make a simple two-step model following that proposed by Legget and Sols [104] and extended by Javanainen and Ivanov [101]. We assume that, initially, the BEC is in the ground state of the BJJ for $\mathrm{RF}_{\mathrm{Amp}} = 0.42$, i.e. the point where the trap starts to split in two wells. At this stage, tunnel coupling dominates over interaction ($\Lambda \lesssim 1$). As the dressing intensity is increased, the system follows adiabatically its instantaneous ground state, meaning that the number fluctuations decrease while the phase fluctuations increase. We assume that, at some point, adiabaticity breaks down

and that the number fluctuations are immediately frozen at their current value (at this stage, conversely to Ref. [102] we neglect further evolution of the phase fluctuations. We will come back to this in Sect. 3.5.2). With this model, the amount of number squeezing is hence fully determined by the point at which adiabaticity breaks down.

Adiabaticity condition

To define a condition for the breakdown of adiabaticity, we apply the criterion (3.17) to the Hamiltonian of the BJJ in the mean field description (see Sect. 1.2.5.2). In the Josephson regime ($1 \ll \Lambda \ll N^2$), the Hamiltonian (1.197) reads

$$H_{\text{harm}} = \frac{JN}{2}\phi^2 + Un^2. \tag{3.29}$$

It is the Hamiltonian of a harmonic oscillator of angular frequency $\omega_J \approx \sqrt{2JUN}$ and (effective) mass $M = 1/2U$ (see Fig. 1.15). In our setup, J varies over almost four orders of magnitude while U stays essentially constant (see Fig. 3.14). The splitting is thus formally equivalent to the decompression of a harmonic trap, and the adiabaticity criterion (3.18) becomes

$$A(t) = \frac{1}{8\sqrt{2}}\frac{1}{\omega_J(t)}\frac{\left|\dot{J}(t)\right|}{J(t)} \ll 1. \tag{3.30}$$

To model the variation of J with the control parameter (amplitude of the rf dressing), we consider its dependence as a function of the well spacing and well frequencies in the harmonic approximation (Eq. (1.80)) and resort to the description of the dressed double-well potential in the RWA (Eqs. (2.24) and (2.25)) to find that the coupling should scale $\propto \exp[-\left(I_{\text{RF}}^2 - I_{\text{RF,c}}^2\right)^{3/2}]$, where I_{RF} is the dressing intensity and $I_{\text{RF,c}}$ is its value at the point where the second minima appears. This motivates the Ansatz

$$J\left(I_{\text{RF}}\right) = J_0 \exp\left[-\left(\frac{\mathrm{I}_{\text{RF}} - \mathrm{I}_{\text{RF,c}}}{\sigma_{\text{RF}}}\right)^{5/2}\right] \tag{3.31}$$

which we find to be in fair agreement over four orders of magnitude with the numerical simulations of the double well beyond the RWA (see Fig. 3.14) with $J_0 = h \times 355$ Hz, $\mathrm{I}_{\text{RF}}^{\text{c}} = 0.39$ and $\sigma_{\text{RF}} = 0.11$ (both intensities are given like RF_{Amp} in units of $I_0^{\max} = 79.5$ mA pp). Note that this dependence reflects both the effect of the increasing spacing between the wells and that of the compression of each well during splitting, and is therefore stronger than the exponential decay assumed for example in Refs. [101–103].

Linear splitting ramp

We consider a linear ramp of the dressing intensity

$$I_{\text{RF}} = I_{\text{RF}}^c + \alpha t \tag{3.32}$$

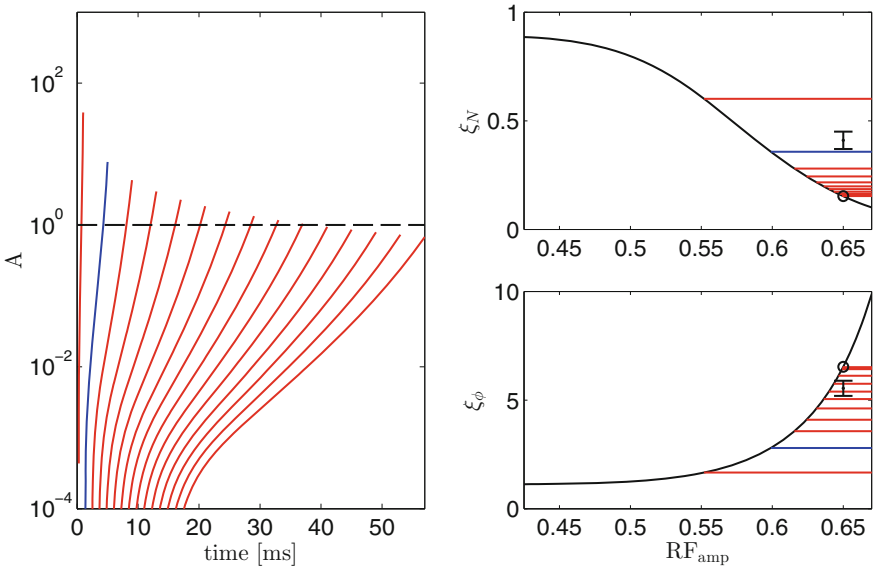

Fig. 3.17 Breakdown of adiabaticity during splitting. *Left* Measure of adiabaticity $A(t)$ (Eq. (3.33)) as a function of time for different ramp durations evenly spaced from 1 ms (*left*) to 57 ms (*right*). The *blue line* corresponds to the experimental value of 5 ms. The ramp are linear and the duration includes the whole splitting process between $\mathrm{RF_{Amp}} = 0.3$ and 0.65 (all ramps starting at $t = 0$), although A is only computed from the splitting point $\mathrm{RF^c_{Amp}} = 0.42$ on. The *black dashed line* $A = 1$ corresponds to the expected breakdown of adiabaticity. *Right* Evolution of number-(*top*) and phase- (*bottom*) squeezing factor as a function of $\mathrm{RF_{Amp}}$ (note that for a linear ramp, the time axis is proportional to the $\mathrm{RF_{Amp}}$ axis.). *Black lines* adiabatic prediction (number and phase squeezing factor in the ground state. The *black circles* correspond to the final trap $\mathrm{RF_{Amp}} = 0.65$). *Red lines* final squeezing values for the same ramp durations as in the *left panel*, assuming sudden freezing of the fluctuations when A reaches unity. The plots can be understood in this way: the state of the system first follows the *black curve*, until adiabaticity breaks down ($A \approx 1$) after which number and phase fluctuations are frozen. The *black points* with the error bars show the measured amount of number and phase squeezing and the corresponding uncertainty. Our model overestimates slightly the degree of number squeezing, and underestimates the phase spread (Color figure online)

at the splitting rate α to give an explicit expression for the degree of adiabaticity as a function of time

$$A_{\mathrm{lin}}(t) = \frac{5}{16\sqrt{2}} \left(\frac{\alpha}{\sigma_{\mathrm{RF}}}\right)^{5/2} \frac{t^{3/2}}{\omega_J(0)} \exp\left[\frac{1}{2}\left(\frac{\alpha t}{\sigma_{\mathrm{RF}}}\right)^{5/2}\right]. \tag{3.33}$$

Figure 3.17 shows how A varies for different splitting rates. Assuming that adiabaticity suddenly breaks down when $A(t) = 1$ (dashed line in left panel), this sets the level of number and phase fluctuations at the end of the splitting process. We find a rough agreement with the amount of number squeezing that we have measured, suggesting that for our 5 ms splitting ramp, adiabaticity breaks down after 4.2 ms,

at $\mathrm{RF}_{\mathrm{Amp}} = 0.6$. On the other hand, phase fluctuations are underestimated by our model, suggesting that other effects contribute to their broadening (see next section). However, to really assess the model, we would need to measure number and phase fluctuations for different ramp durations, which we have not yet done.

We can use this model to estimate how long it would take to achieve a given amount of number squeezing with a linear splitting ramp. By imposing that $A_{\mathrm{lin}}(t)$ is smaller than 1 at all times during the splitting, we find that the ramp duration diverges $\propto -\ln \xi_N/\xi_N^2$ when $\xi_N \to 0$. It means that it would need over 200 ms to achieve $\xi_N = 0.1$, suggesting that a linear splitting ramp is not the best protocol to achieve strong number squeezing, especially as other effects like atom losses and technical heating might interfere, as observed in Ref. [95].

Equation (3.33) could be used to infer an *Ansatz* for the optimal $I_{\mathrm{RF}}(t)$. In Ref. [103], the authors applied optimal control theory to a many-body, time-dependent description of a realistic condensate to propose tailored squeezing protocols much faster than adiabatic splitting. Simulating the many-body dynamics still remains a difficult task when trying to include finite temperature effects and the coupling to the motion in the two directions orthogonal to the splitting direction. Furthermore, it relies on a precise knowledge of the double-well potential. Implementing such protocols on our setup to achieve enhanced squeezing is currently under study.

3.4.5 Discussion

Altogether, we have seen that the transformation of the potential acts as a coherent beam-splitter for our Bose-Einstein condensates, creating a superposition of two spatial modes separated by $2\,\mu\mathrm{m}$, still retaining a high phase coherence ($\langle \cos\phi \rangle = 0.987 \pm 0.01$). While the deformation of the trap is almost adiabatic with respect to the transverse motion, it triggers a collective breathing excitation in the longitudinal direction.

The interplay between tunnel coupling and atomic interactions during the splitting generates strong number squeezing ($\xi_N = 0.41 \pm 0.04$), which together with the high phase coherence yields a spin-squeezing (or *useful squeezing*) factor $\xi_S = 0.41 \pm 0.04$. This implies a potential metrology gain of 7.8 ± 1 dB beyond the standard quantum limit. In other words, feeding this state into an ideal, noiseless Mach-Zehnder interferometer would allow measuring a phase shift with a sensitivity twice better than obtained with a coherent state. Figure 3.18 shows how our result compares to other measurements of spin-squeezed states of Bose-Einstein condensates reported in litterature.

We conjecture that the relatively high degree of spin-squeezing that we observed—one of the highest ever observed with external states of a BEC—is linked to the elongated geometry of our double well, which ensures that the system is initially in its transverse ground state. Although the energy difference between ground and first excited state shrinks considerably during splitting, we believe that the occupation

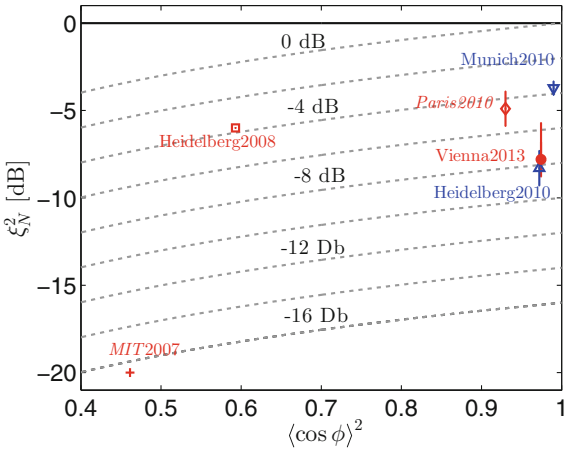

Fig. 3.18 Squeezing in Bose-Einstein condensates. Some measured number squeezing and phase coherence factors reported in literature (the uncertainty is displayed when available). For the results labeled in italic letters, one of the two quadrature was indirectly inferred. The continuous *black line* corresponds to $\xi_N = 1$, the *dashed lines* to constant values of the spin-squeezing factor $\xi_S \equiv \xi_N / \langle \cos\phi \rangle$. *Red* experiments with external states. MIT 2007: adiabatic splitting in a rf-dressed double well [11] (ξ_N was inferred from the phase diffusion rate); Heidelberg 2008: adiabatic splitting in an optical few-well potential [61]; Paris 2010: adiabatic splitting in a magnetic double well [95] (coherence computed from a theoretical model); Vienna 2013: our result. Blue: experiments with internal states. Munich 2010: control of interactions in state-dependent potentials [62]; Heidelberg 2010: interaction control with a Feshbach resonance [17] (Color figure online)

of the transverse states mimics an extremely low temperature, much lower than that associated to the occupation of the many accessible longitudinal modes, hence approaching the ideal zero-temperature limit.

We also observe that the product of the uncertainties on the conjugated variables n and ϕ is about two times larger than the minimum allowed by the Heisenberg uncertainty relation. Although the amount of number squeezing seems consistent with our simple model for adiabatic splitting, the phase fluctuations are stronger than expected. Note that while the measured number fluctuations can be corrected for detection noise, the intrinsic phase fluctuations are probably overestimated.

In any case, our zero-temperature model cannot explain deviation from the minimum uncertainty product (unless it is assumed that the system is not initially in the many-body ground state). In Ref. [105], Pitaevskii and Stringari evaluated the reduction of coherence due to both quantum and thermal fluctuations. In the classical regime, where both number and phase fluctuations are small, the coherence at thermal equilibrium at the temperature T reads

$$\alpha_{\mathrm{cl}} = \frac{\int_{-\pi}^{\pi} \cos\phi \, \exp\left(JN\cos\phi/k_B T\right) \mathrm{d}\phi}{\int_{-\pi}^{\pi} \exp\left(JN\cos\phi/k_B T\right) \mathrm{d}\phi}. \tag{3.34}$$

These results were successfully applied by R. Gati et al. to infer the temperature of the thermal phase fluctuations in a BJJ [59]. In their experiment, the phase coherence was measured after the BEC was slowly split by ramping up the tunnel barrier over hundreds of ms. This temperature showed fair agreement with that given by an independent thermometry method. Evaluated immediately after splitting, Eq. (3.34) yields in our case an effective temperature of the phase fluctuations $T_{\text{eff}} \sim 0.2$ nK, using the simulated value of the tunnel coupling in the split trap ($J = h \times 0.1$ Hz). This is two orders of magnitude below the initial temperature of the condensate, indicating that the system is strongly out of equilibrium. If the atoms are held in the symmetric $\text{RF}_{\text{Amp}} = 0.65$ double well, the phase coherence factor then relaxes within a few ms to a plateau value ∼0.8 ($T_{\text{eff}} \sim 2$ nK, see Fig. 3.26, right). As we will see in Sect. 3.5.2, the high value of the coherence factor for tens of ms can be attributed to the spurious tunnel coupling ($J/h \approx 0.1$ Hz). We also observe that the contrast of the interference patterns integrated along the direction remain also very high for tens of ms.

These observations seem to go along the lines of the investigations performed in our group on the relaxation of split 1D quasi-BECs to a prethermalized state [52, 63]. The authors showed that the spatial coherence properties of the relative phase of two quickly split 1D quasi BEC exhibited a seemingly thermal behaviour associated to an effective temperature determined by the relative number fluctuations after splitting. Indeed, for our parameters, which are very close to that of Ref. [52], the effective temperature in presence of number-squeezing is roughly given by

$$T_{\text{preth}} = \frac{\xi_N g_{1\text{D}} n_{1\text{D}}}{2k_B} \approx 6 \text{ nK}, \tag{3.35}$$

where $g_{1\text{D}} = 2\hbar a_s \omega_\perp$ is the 1D effective interaction constant and $n_{1\text{D}} = 35$ atoms/μm is the peak density of the initial unsplit BEC. The corresponding 1D phase correlation length [106]

$$\lambda_{\text{preth}} = \frac{2n_{1\text{D}}\hbar^2}{mk_B T_{\text{preth}}} \approx 60\,\mu\text{m}, \tag{3.36}$$

exceeds the length of the cloud, in agreement with the high contrast we observe after integration of individual interference patterns along the longitudinal direction (see Fig. 3.21).

For these reasons, we believe that at short times, it is legitimate to resort to a two-mode description ignoring the axial fluctuations of the relative phase. At long times ($t > 80$ ms), a reduction of contrast is observed, caused by axial phase fluctuations in the individual interference patterns, which will be discussed in Chap. 4. Taking the multimode nature of the quasi BECs into account when studying their squeezing properties is an extremely interesting task, that is beyond the scope of this thesis. However, we are confident that further experiments on our setup will contribute to the understanding of squeezing, and in particular clarify the role of finite temperature.

3.5 Phase Evolution

The second element needed to build an atom interferometer is a phase shifter, i.e. an element capable of imprinting a controlled phase shift to the quantum superposition. As our interferometer is symmetric, the phase shift is applied by deliberately introducing an energy difference between the two modes. By varying the time t_ϕ during which the two modes are subjected to this energy difference, we can adjust its relative phase ϕ. Additionally, we observe that the deterministic phase accumulation was accompanied by a dephasing which eventually causes the relative phase between the two halves of the BEC to become completely random.

In Sect. 3.5.1, we explain how a deterministic phase shift can be applied, and discuss the measured phase accumulation rate. In Sect. 3.5.2, we describe our observations of the evolution of the interference fringes after splitting in a symmetric and in a tilted double well and motivate why we the randomization of the phase in the tilted double wells can be attributed to interaction-induced, many-body phase diffusion. In Sect. 3.5.2, we investigate phase diffusion in absence and in presence of tunnel coupling. In Sect. 3.5.3, we compute the phase diffusion rate in two independent ways, and compare it to the results of our measurements.

3.5.1 Phase Accumulation

3.5.1.1 Phase Shifts in BEC Interferometers

In quantum mechanics, the phase picked up by an atom traveling along a certain trajectory in phase space is equal to the integral of its Lagrangian $\mathcal{L}$ along the path [107]. To compute the phase shift between the two arms of an interferometer, it is often sufficient to estimate the action integrals along the classical trajectories [12, 108]

$$\phi(\vec{r}, t_\phi) = \left[\int_0^{t_\phi} \frac{\mathcal{L}}{\hbar} \mathrm{d}t\right]_{\text{path 1}} - \left[\int_0^{t_\phi} \frac{\mathcal{L}}{\hbar} \mathrm{d}t\right]_{\text{path 2}}. \tag{3.37}$$

The differential phase in an interferometer may come from an energy difference between the two arms.[11] It can be the energy difference between two internal states, for example the hyperfine splitting in Ramsey interferometers [14], or a difference in kinetic or potential energy. The phase can be adjusted either by changing the energy difference or the time during which it is acting on the atoms.

Various effects have been used to apply controlled phase shifts in BEC interferometers. In Bloch oscillation interferometers such as the one presented in Ref. [40], the phase shift comes from an external force, for example gravity. In the guided Bragg

[11] In general, the differential phase is also position-dependent (Eq. (3.37)). It means for example that in a magnetically trapped Ramsey-interferometer, the accumulated phase varies at a rate proportional to the local difference in chemical potential [14].

interferometer of Ref. [15], a differential phase shift was applied either taking advantage of the Zeeman effect with a magnetic field gradient, or with an initial condensate velocity. The corresponding fringes were observed by scanning either the amplitude of the gradient, or the propagation time in the waveguide. In Ref. [44], inhomogeneous AC Stark shifts were applied by pulsing off the optical power generating the double-well potential. In Ref. [45], the evolution of the relative phase was controlled by deliberately tilting the double-well. The same technique was employed for example in Refs. [11, 47] as well as in the experiments presented in this thesis [1]. We will come back to the origin of the energy difference induced by this technique below. In the vibrational-state interferometer that we recently implemented [16], the phase evolution rate is essentially equal to the difference of chemical potential (including the single-particle motional energy) between the ground and the first excited eigenstates of the confining potential.

Interestingly, even when using a BEC with thousands of atoms, we always measure a one-atom phase shift (up to the corrections due to interactions). For example, if a differential gravitational potential energy is applied by lifting one half of the BEC with respect to the other by a height Δz, the phase will evolve at the rate $mg\Delta z/\hbar$, where $g = 9.81\,\mathrm{m/s^2}$ and m is the mass of one ^{87}Rb atom.

However, when an oscillating field is driving the BS transitions, there is an additional contribution from the interaction of the atom with the drive. In fact, as shown by Storey and Cohen-Tannoudji [108], in a symmetric $\pi/2 - \pi - \pi/2$ configuration such as the three-grating Bragg or Raman MZI used in gravimetry experiments [26], in absence of a perturbation, the two arms are expected to pick up the same phase, so that the differential phase comes only from the interaction with the laser beams. This allows scanning the interferometer phase shift by varying the phase of the recombination BS pulse with respect to that of the separation BS [6, 26]. This is also the case in Ramsey interferometers where the interference signal is obtained from the beating note between the coherent atomic superposition and the drive. In this case, the phase of the interference signal can be varied by changing the Ramsey time between the two BS pulses [14], the detuning of the drive with respect to the atomic transition [27] or the phase difference between the BS pulses [17].

3.5.1.2 The Phase Shifter

Once the condensate has been split in two, it starts accumulating a relative phase at a rate proportional to the difference in chemical potentials between the two halves (including the zero-point energy). Note that depending on the details of the splitting, the phase evolution can be driven by the difference in potential energy between the two minima of the double well (assuming for example the same number of atom in each well, as in this section), by the difference in chemical potential between two BECs with different atom number (in a symmetric double well, see Fig. 3.28) or, as in earlier experiments [45], by a combination of both.

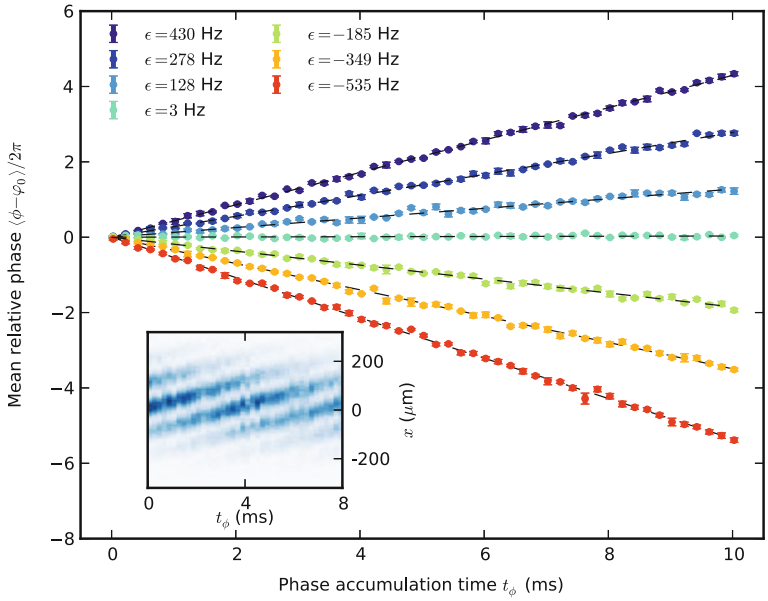

Fig. 3.19 Phase shifter. Linear evolution of the mean phase for various energy differences ϵ induced by tuning the angle α of the splitting axis with respect to the horizontal plane (each curve corresponds to one of 7 values of α evenly spaced between $-9°$ and $+12°$). Each point corresponds to the circular mean of the phase over a few realizations (error bars: one circular standard deviation). The values of ϵ shown in the legend are obtained from linear fits to the data (*black dashed lines*). Inset: "Carpet" obtained from integrating the interference patterns for $\epsilon/h = -349$ Hz along the longitudinal direction and concatenating them to show the time evolution

To apply a well-defined phase shift, we tilt the double well out of the horizontal plane in order to create a difference of potential energy ϵ. After a time t_ϕ spent in the tilted trap, the BEC accumulates a relative phase [12]

$$\phi \approx \left[\frac{1}{\hbar}\int V(x(t))\mathrm{d}t\right]_{\text{left path}} - \left[\frac{1}{\hbar}\int V(x(t))\mathrm{d}t\right]_{\text{right path}} \tag{3.38}$$

$$= \frac{\epsilon t_\phi}{\hbar} + \varphi_0. \tag{3.39}$$

Figure 3.19 shows the linear evolution of the mean phase for different tilt angles, yielding different phase evolution rates. For each measurement, we start with the coherent superposition obtained after splitting ($\langle n\rangle = 0$, $\langle\phi\rangle = 0$) and tilt the double well by an angle α between $-9°$ and $+12°$ by ramping linearly the current in each rf wire to its final value given by Eq. (2.30). This way, the well spacing is kept constant while the axis of the double well is tilted. The duration of the tilt ramp was set to 3 ms to ensure adiabaticity with respect to the transverse motion in the trap. Given a well spacing of 2 μm, the tilt velocity is much smaller than the velocity spread of each

individual BEC. Indeed, no vertical sloshing excitation was observed. After the phase has accumulated for a variable time t_ϕ, the tilt is reversed in another 3 ms. Note that the phase evolution starts already during the tilting ramp, which is responsible for the phase offset $\varphi_0(\alpha)$, independent of t_{IE}, which has been substracted in Fig. 3.19.

Eventually, the atoms are released and the phase is read out from the interference patterns in tof (see Sect. 3.2.1). The data of Fig. 3.19 proves that the phase evolution is linear for all angles and the high reproducibility of the mean phase for $t_\phi < 10$ ms allows to determine the phase evolution rate for each value of α with less than 2 Hz uncertainty. Note that similarly to Ref. [15], we can chose to adjust ϕ by changing either ϵ or t_ϕ.

3.5.1.3 Origin the Phase Accumulation Rate

From a linear fit to the values of $\epsilon(\alpha)$ obtained in Fig. 3.19, we can estimate the "slope" of the phase shifter

$$\left|\frac{\mathrm{d}\epsilon}{\mathrm{d}\alpha}\right|_{\mathrm{exp}} = h \times 44 \pm 2.9\,\mathrm{Hz}/\left[^\circ\right] \tag{3.40}$$

We expect the main contribution to ϵ to stem from the difference of gravitational potential energy due to the difference of height between the two wells. The gravitational potential energy gradient for one ^{87}Rb atom is $mg/h = 2.14$ Hz/nm. For small angles, using the well spacing $d = 2.1\,\mu$m given by the trap simulations, in agreement within 10 % with the value deduced from the measured fringe spacing (see Fig. 2.15), we expect

$$\left|\frac{\mathrm{d}\epsilon}{\mathrm{d}\alpha}\right|_{\mathrm{grav}} = mgd = h \times 75\ \mathrm{Hz}/\left[^\circ\right], \tag{3.41}$$

which is significantly higher than the experimental value.

In fact, as studied in Ref. [47], a double-well interferometer on an atom chip does not only measure the gravity gradient. Because of the small distance to the chip wires, introducing a height difference causes the two halves of the BEC to experience different rf fields. In Ref. [47], the difference in magnetic energy between the two wells, measured by rf spectroscopy, was found to be twice larger than the difference in gravitational potential energy.

Performing beyond-RWA simulations of our rf-dressed potential to include this effect, we found $|\mathrm{d}\epsilon/\mathrm{d}\alpha| = h \times 70.1$ Hz/ [°], still 60 % above the measured value. Furthermore, the correction due to the magnetic field difference in Ref. [47] was found to add up to the gravity gradient, yielding a stronger dependence of ϵ with the height difference, while we measure of weaker dependence than expected from gravity only.

The contribution to ϵ due to the slight difference in radial trap frequencies between the two wells, which modifies both the zero-point energy and the chemical potential difference [47], cannot be held responsible for this discrepancy, as it should not account to more than 2 % of the energy difference. The variation of the longitudinal trapping frequencies (for which the trap simulations can not be trusted due to potential corrugation, see Sect. 2.2.1.3) when the double well is tilted has not been measured. However it seems extremely unlikely that they would vary by the factor $\sim$2.4 needed to explain the discrepancy with the measured value of $|\mathrm{d}\epsilon/\mathrm{d}\alpha|$.

We currently don't have an explanation for the fact that we observe a slope $|\mathrm{d}\epsilon/\mathrm{d}\alpha|$ significantly lower than expected from the gravity gradient. Unfortunately, conversely to Refs. [46, 47], we are missing an imaging system parallel to the long axis of the trap, which would allow us to directly measure the splitting angle α, and hence infer the height difference between the wells. Furthermore, other systematic effects may contribute to the energy difference, such as uncontrolled inhomogeneous electric fields close to the chip.

3.5.2 Phase Diffusion

3.5.2.1 Evolution of the Phase and Contrast Distributions

We now turn to the evolution of the phase distribution. It can be conveniently displayed using the full distribution function (FDF) sketched in Fig. 3.20 [64]. Furthermore, it provides information on the intensity of the axial phase fluctuations along the BJJ, revealing 1D effects which we have ignored so far. It has been used in our group to evidence the multimode dynamics arising in the relative phase profile of coherently split 1D quasi BECs [64].

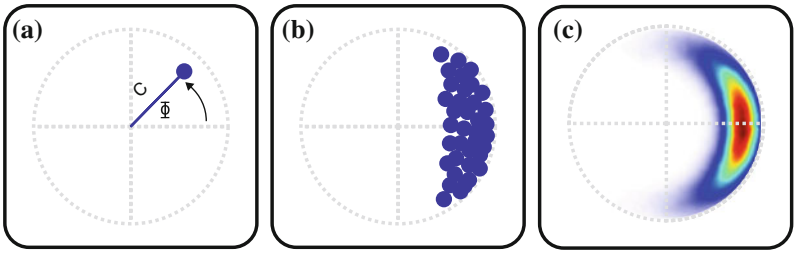

Fig. 3.20 Phase and contrast distribution. Adapted from Ref. [64]. The distribution of the phase and the contrast (full distribution function, FDF) of the matter-wave interference patterns can be displayed as a polar plot. For each individual realization, the phase ϕ and the contrast C are extracted from the longitudinally integrated interference fringes and plotted as a point in polar coordinates (**a**). The whole process is repeated up to 50 times and the scatter plot (**b**) is smoothed to produce a density plot (**c**)

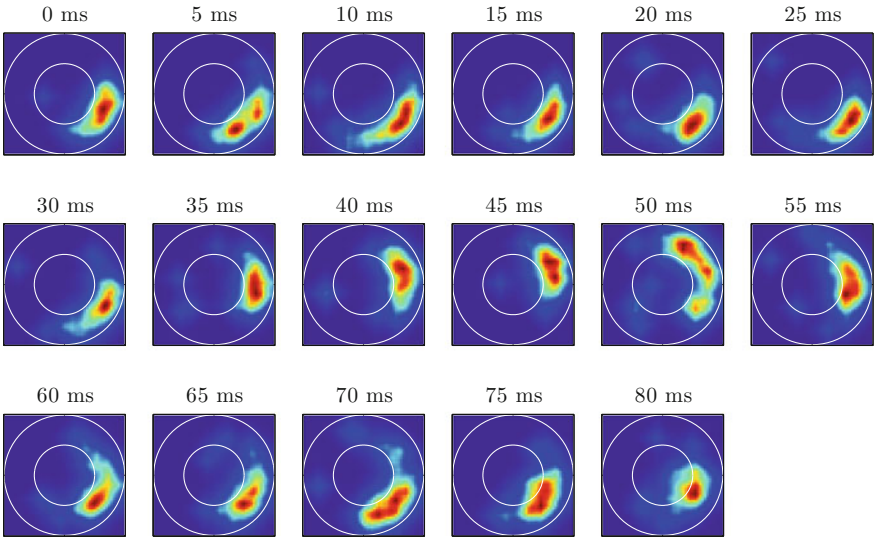

Fig. 3.21 Evolution of the FDF in the symmetric double well. Measured FDF of the contrast and the phase as a function of the phase accumulation time t_ϕ in the symmetric $\mathrm{RF}_{\mathrm{Amp}} = 0.65$ double well (estimated coupling strength: $J/h \approx 0.1$ Hz). Note that a time offset of 6 ms has been substracted to the total holding time in the symmetric double well to enable comparison with the data in Fig. 3.22, where tilting and leveling back the potential took 6 ms. The *two white circles* indicate 50 % and 100 % contrast. In the symmetric double well, the phase distribution remains peaked at all times ($\Delta\phi \approx 0.6$ rad), while its mean undergoes slow oscillations. The contrast of the interference patterns remains higher than 50 % up to $t_\phi \approx 80$ ms.

We resorted to this representation to monitor the evolution of the phase and contrast distribution in the symmetric (Fig. 3.21) and in the tilted (Fig. 3.22) $\mathrm{RF}_{\mathrm{Amp}} = 0.65$ double well ($\epsilon/h = 350$ Hz, orange curve in Fig. 3.19). Each FDF is the result of the analysis of about 50 interference pattern obtained in the same experimental conditions. Note that conversely to Ref. [64], we always integrated the fringes over the whole cloud length.[12]

After splitting into the symmetric $RF_{Amp} = 0.65$ double well, we observed a peaked phase distribution associated to a high coherence and a high fringe contrast for all individual realizations. The phase spread remained roughly constant (circ. standard deviation $\Delta\phi \approx 0.6$ rad) over more than 90 ms, while the mean phase underwent small amplitude oscillations at a frequency $f \approx 16$ Hz. The contrast of the interference fringes, which we found to be close to 85 % immediatly after splitting, slowly decreased to about 50 % after more than 80 ms holding time in the symmetric double well.

In the tilted $\mathrm{RF}_{\mathrm{Amp}} = 0.65$ double well, on the other hand, we observed that the deterministic, linear evolution of the mean phase at the rate $\epsilon/h = 350$ Hz was accompanied by a broadening of the phase distribution. After 30 ms, the phase

[12] i.e. $L \approx 100\,\mu$m, depending on the axial breathing, see Fig. 4.1.

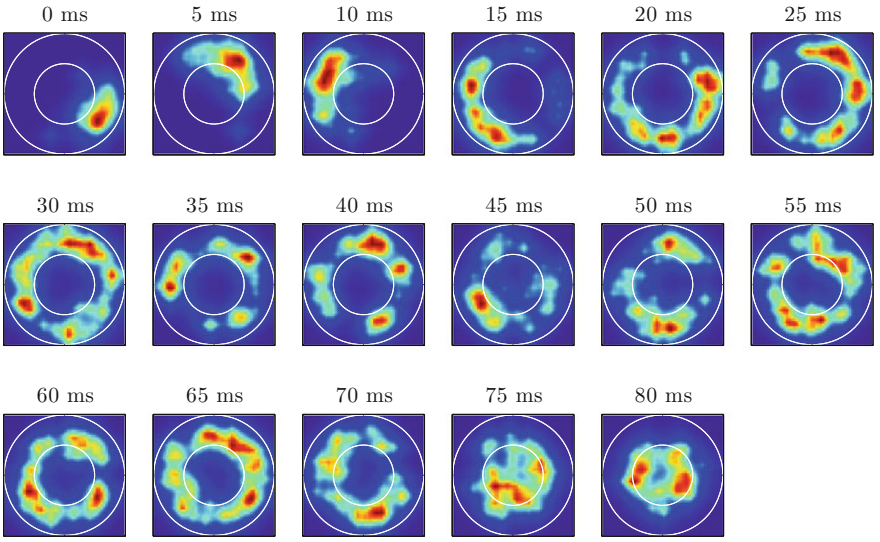

Fig. 3.22 Evolution of the FDF in the tilted double well. Measured FDF of the contrast and the phase as a function of the phase accumulation time t_ϕ in the tilted $\mathrm{RF}_{\mathrm{Amp}} = 0.65$ double well ($\epsilon/h = 350\,Hz$). At short times, the deterministic linear evolution of the phase at the rate ϵ/h can still be seen. The phase spread increases until the FDF is isotropic, indicating a random relative phase after $t_\phi \approx 30\,\mathrm{ms}$. The characteristic ring shap of the FDF is a signature of phase diffusion: although the phase is random, each interference pattern exhibits a high contrast. Only after $\sim$75 ms, the contrast of individual fringe patterns start to drop significantly

distribution was found to be essentially isotropic, implying that the phase coherence between the two halves of the BEC was completely lost. Strikingly, the loss of phase coherence did not imply a loss of contrast: even after 60 ms in the tilted double well, the BEC exhibited interference patterns with on average more than 60 % contrast (Fig. 3.23).

At longer times ($t_\phi \gtrsim 70\,\mathrm{ms}$), we observed a significant drop of contrast both in the symmetric and the tilted double wells. We will come back to the mechanisms that are responsible for the degradation of contrast in Chap. 4.

We observed a similar behaviour (phase randomization within 20–30 ms associated to a high contrast of the individual interference patterns) for all tilted double wells used in Fig. 3.19. The broadening of the phase distribution can be quantified by measuring the circular standard deviation of the phase $\Delta\phi$ (see Sect. 3.2.1.2) as a function of t_ϕ (see Fig. 3.24). At short times, we observed a linear increase of the phase spread. The dashed line in Fig. 3.24 corresponds to the average value for the circular standard deviation expected from $k = 50$ phases sampled from a uniform distribution, $\Delta\phi_{\mathrm{unif}} = \sqrt{\ln k}$, showing that the measured phase spread is compatible with a random distribution.

We attribute the randomization of the relative phase to atomic interactions. It is well-known that atom-atom interactions dramatically affect the evolution of the phase

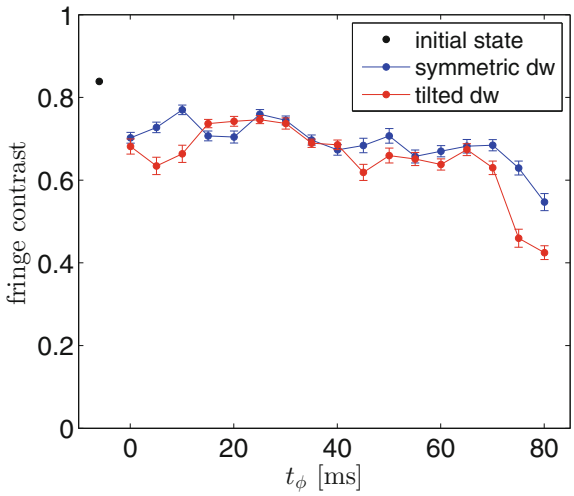

Fig. 3.23 Evolution of contrast during the phase accumulation stage. Mean fringe contrast of the tof interference patterns as a function of the holding time t_ϕ in the symmetric (*blue*) and tilted (*red*) $RF_{Amp} = 0.65$ double well. The black point at -6 ms displays the constrast measured immediatly at the end of the splitting ramp (see Sect. 3.4.3). The sudden drop of contrast at $t_\phi \geq 70$ ms is not fully understood yet. It is probably essentially caused by axial phase fluctuations, although the axial breathing mode and the fact that the number of atoms in the $m_F = 0$ state used for phase analyzes depends on t_ϕ (see Sect. 3.2.1) might play also a role

of a confined BEC. Currently, they represent a fundamental limitation for both the accuracy and the sensitivity of trapped BEC interferometers. An excellent discussion of the impact of interactions in Ramsey and Bragg interferometers can be found in the thesis of Altin [109].

Interactions affect the performance of BEC interferometers in essentially two ways:

- Mean-field interactions modify the energy of the two modes and give rise to a systematic shift limiting the accuracy of trapped atoms interferometers. Mean-field shifts are one of the main source of systematic errors in trapped atomic clocks [110]. In our vibrational-state interferometer [16], it was responsible for a shift of the phase accumulation rate of the order of 5 %. Interactions are also responsible for a degradation of the interferometric contrast comparable to an inhomogeneous broadening effect: in Ramsey interferometers, for example, the inhomogeneous mean-field energy causes the phase between the two modes to precess at a spatially-dependent rate [14]. This results in a loss of contrast when averaging over the whole BEC. Furthermore, the mean-field driven demixing dynamics in binary mixtures leads to a variation of the overlap between the states, and hence to a degradation of the contrast [9]. A similar effect was observed [15] and investigated [10] in guided Bragg interferometers. Importantly, mean-field shifts are deterministic and could be in principle accounted for. The "spatial dephasing" caused by mean-

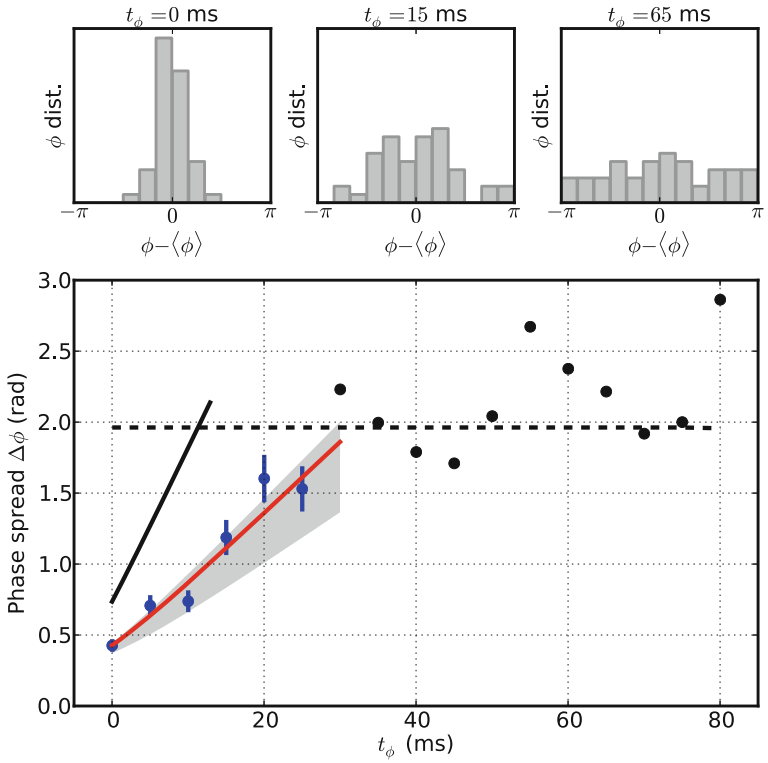

Fig. 3.24 Randomization of the phase. *Top* Phase distributions measured at three different phase accumulation times t_ϕ for $\epsilon/h = -349$ Hz (*orange curve* of Fig. 3.19). It exhibits phase diffusion: at short times $t_\phi \lesssim 30$ ms the mean phase is well defined (*blue points*); on the contrary, for longer times the phase distribution cannot be distinguished from a random distribution. *Bottom* Evolution of the circular standard deviation of the phase $\Delta\phi$. The *red line* is a fit to the *blue points* with the model of Eq. (3.57). *Shaded area* theoretical prediction without free parameter, taking into account the measured number squeezing (see (3.69)). *Black line* expected behaviour if the initial state were classical (i.e. not number-squeezed). Note that at $t_\phi = 0$ phase diffusion has already started (Color figure online)

field interactions is still compatible with a perfect contrast in each point in space, meaning that by not discarding the spatial dependence of the output signal in Ramsey or Bragg interferometers, one could retrieve all the information.

- In an interacting many-body quantum system, the fundamental *phase* uncertainty is known to increase in time as a result of the initial *number* uncertainty. This effect of interaction-induced phase diffusion will be detailed in the following sections. Importantly, it causes a randomization of the relative phase between the two arms of the interferometer and cannot be captured by a mean-field description, while still being compatible with a high contrast for each experimental realization. In the Bloch oscillations interferometer of Ref. [43], the dephasing effect due to the inhomogeneous mean-field shift was compensated by applying a external potential.

Because we observe that the contrast of individual realizations is preserved while the coherence is completely lost after averaging over identical realizations, we attribute the observed randomization of the phase to interaction-induced phase diffusion. The randomization of the phase between two superconductors after suppression of the Josephson coupling has been studied as early as 1994 [111]. In the context of atomic Bose-Einstein condensates, the question of how the phase of a single BEC with a fixed atom number is defined has been the subject of intense theoretical investigations, see for example Refs. [112–114]. It was shown in 1997 that the relative phase between the two halves of a split BEC should undergo a characteristic diffusion under the effect of interactions [66, 115]. The link between the rate at which the phase randomizes and the initial relative number uncertainty was highlighted in Refs. [104, 116], where it was conjectured that reduced number fluctuations would imply a lower phase diffusion rate.

Experimentally, the difficulty in studying phase diffusion comes from the fact that it is difficult to disentangle interaction-induced phase diffusion from the technical shot-to-shot fluctuations which are believed to have limited the coherence time of the first double-well experiments [44, 45]. In 2007, coherence times a factor of ten longer than expected from a coherent state with binomial number fluctuations were reported, and attributed to strong number squeezing in a Sodium BEC [11]. The link between phase diffusion and interactions was demonstrated in Bloch oscillations experiments, where the coherence time was massively extended by tuning the s-wave scattering by means a Feshbach resonance [41, 43]. The link between phase diffusion and number fluctuations was also studied in optical lattices, where extended coherence times were observed, in agreement with the inferred degree of number squeezing [117].

In Sect. 3.5.3, we will show that the measured diffusion rate is compatible with the rate expected from many-body phase diffusion. In Sect. 3.5.2.2, we describe the effect of phase diffusion and show how the evolution of the phase spread in absence of tunnel coupling can be computed. In Sect. 3.5.2.4, we include the effect of a weak spurious tunnel coupling and of a finite energy detuning.

3.5.2.2 Phase Diffusion in Absence of Tunnel Coupling

Interaction-induced phase diffusion is a consequence of the fact that, in a two-mode BEC with repulsive interactions, it costs more energy to have different numbers of atoms in each mode. Trivially, if the interaction energy in each mode is $E_{\mathrm{int,i}} = U/2 \times N_i^2$, where $i = L, R$, the total energy reads

$$E_{\mathrm{int}} = \frac{1}{2} U \left(N_L^2 + N_R^2 \right) = \frac{1}{8} U N^2 + U n^2, \tag{3.42}$$

($n \equiv (N_L - N_R)/2$) and is minimal for $N_L = N_R$.

Each Fock state with a well-defined n has a different energy. Hence, any state which is in a superposition of different Fock states will see its different components dephase, leading to a broadening of its phase distribution.

To describe the evolution of the phase distribution of the BEC after the end of the splitting, we follow the lines of Refs. [66, 104, 115]. We start from the Bose-Hubbard Hamiltonian (1.111) in absence of tunnel coupling

$$\hat{H}_{\mathrm{BH}} = U\hat{n}^2 + \epsilon\hat{n}. \tag{3.43}$$

with the interaction constant $U \equiv (U_L + U_R)/2$ and the detuning $\epsilon = (U_L - U_R)(N-1)/2 + \Delta \approx \Delta$. Note that here, we assume that there is no residual coupling in the split trap, which is not strictly true in our case. However, we will show in the following section that as soon as Δ is sufficiently large, the results of this section remain valid.

When $J = 0$, the Fock states are the eigenstates of the many-body Hamiltonian. We can decompose any initial state in this basis and compute its time evolution using Eq. (1.91). It reads

$$|\Psi(t)\rangle = \sum_{n=-N/2}^{N/2} c_n e^{-iE_n t/\hbar} |n\rangle . \tag{3.44}$$

where $c_n = \langle n|\ \Psi(t=0)\rangle$ and $E_n = Un^2 + \epsilon n$. Note that in the absence of tunneling, the number distribution cannot change (only the phases wind up). For simplicity, we assume that $p(n)$ is symmetric around zero (no net imbalance).

Because of interactions, the energy of the Fock state varies quadratically with n. Note that in Refs. [66, 104, 115], this quadratic dependence is obtained by expanding the energy of the Fock states up to the second order in n. Here, the quadratic dependence is already contained in the approximations leading to the two-mode Bose Hubbard Hamiltonian.

To compute the evolution of the phase distribution, we write the many-body wavefunction in the basis of the phase states (see Sect. 1.2.2.5), which corresponds to computing the discrete Fourier transform of Eq. (3.44). To obtain a simple analytical result, we take the continuous limit ($N \to \infty$, $c_n \to c(n)$) and replace the sums by integrals (Eq. (1.102)). The wavefunction in phase representation is given by the Fourier transform of the wavefunction in number representation

$$\tilde{c}(\phi, t) \equiv \frac{1}{\sqrt{2\pi}} \int_{-\infty}^{\infty} \underbrace{c(n) e^{-iUn^2 t/\hbar}}_{g(n)} e^{-i\epsilon n t/\hbar} e^{-i\phi n} \mathrm{d}n \tag{3.45}$$

$$= G\left(\phi - \epsilon t/\hbar\right) \tag{3.46}$$

where $G(\phi)$ is the Fourier transform of $g(n)$. We immediately identify the overall phase shift at the rate $\epsilon/\hbar$ driven by the energy difference (see also Sects. 1.2.4.3 and 1.2.5.2). Note that the linear detuning term is responsible for a shift of the whole phase distribution (and hence of its mean) but cannot broaden it nor squeeze it.

We rewrite the product in the Fourier transform Eq. (3.45) as a convolution product

$$\tilde{c}(\phi, t) = \frac{1}{\sqrt{4i\pi Ut/\hbar}} \int_{-\infty}^{\infty} \tilde{c}(\phi', t = 0) \exp\left[-\frac{\left(\phi - \epsilon t/\hbar - \phi'\right)^2}{4iUt/\hbar} \right] \mathrm{d}\phi' \tag{3.47}$$

to see that the interaction term is responsible for a Gaussian broadening of the initial phase probability distribution. This shows that interactions tend to broaden the phase distribution at a rate $\propto U$.

The mean-field model presented in Sect. 1.2.5 gives a good picture of phase diffusion, even if it has to be used carefully in the limit of zero coupling. Assuming an initially well-localized wave packet in phase representation (see Fig. 1.15), $J = 0$ means that the effective potential experienced by the wavefunction is flat. The kinetic energy term, which is proportional to U (see Eq. (1.197)), causes the spread of the wavefunction.

A Particular Case: Gaussian Ground State

We first treat the particular case of a system initially in a Gaussian, minimal-uncertainty state, such as the ground state of the bosonic Josephson junction at finite coupling strength. This would correspond for example to the output state of the splitting model of Sect. 3.4.4, where we assume that the BEC follows adiabatically the instantaneous ground state until adiabaticity breaks down. The initial half-number difference and phase distributions read

$$p(n) = \frac{1}{\sqrt{2\pi}\sigma_n} e^{-n^2/2\sigma_n^2} \tag{3.48}$$

$$p(\phi) = \frac{1}{\sqrt{2\pi}\sigma_\phi(0)} e^{-\phi^2/2\sigma_\phi^2(0)} \tag{3.49}$$

with $\sigma_n = \xi_N\sqrt{N}/2$ and $\sigma_n\sigma_\phi\,(0) = 1/2$. Inserting Eq. (3.49) in Eq. (3.47), we find that the phase distribution remains Gaussian with a time-dependent variance [66, 104]

$$\sigma_\phi^2(t) \equiv \left(\xi_N^2 N\right)^{-1} + R^2 t^2 \tag{3.50}$$

where the phase diffusion rate R is

$$R \equiv \xi_N \sqrt{N} \frac{U}{\hbar}. \tag{3.51}$$

R is proportional to both the interaction constant U and the initial number fluctuations. In particular, as pointed out in Ref. [104], the phase diffusion can be significantly slowed-down in presence of number squeezing ($\xi_N < 1$). At long times

($t^2 \gg \hbar^2/(\sigma_n^4 U^2)$), the phase spread grows linearly with time, which actually resembles more a dispersive than a diffusive behaviour, as pointed out in Ref. [115]. The coherence can also be computed by averaging over the phase distribution. It exhibits a typical Gaussian decay [114]

$$\langle \cos\phi \rangle (t) = \exp\left[-\sigma_\phi^2(t)/2\right] = \exp\left[-\sigma_\phi^2(0)/2\right] \exp\left[-t^2/2\tau_{\text{coh}}^2\right] \tag{3.52}$$

where the phase coherence time is defined as $\tau_{\text{coh}} \equiv R^{-1}$.

Extension to a Non-minimal-uncertainty Gaussian State

In practice, however, we do not start in a minimum-uncertainty state (we have measured $\sigma_n \sigma_\phi \approx 1.2 > 0.5$, see Sect. 3.4.3.3). We lift this assumption, still assuming Gaussian distributions for n and ϕ, and introduce the discrepancy $\beta \geq 0$ defined as

$$\beta \equiv \sqrt{4\sigma_n^2 \sigma_\phi^2(0) - 1}. \tag{3.53}$$

In this case, the variance of the phase distribution follows

$$\sigma_\phi^2(t) \equiv \sigma_\phi^2(0) + \frac{4U\beta t}{\hbar} + R^2 t^2. \tag{3.54}$$

Note that this does not affect the phase diffusion rate, which depends only on the initial number fluctuations. At long times, we recover the same behaviour as in Eq. (3.50). The term in factor of β is usually neglected (see Fig. 3.25), but can be significant if the initial state is far from a minimum-uncertainty state.

3.5.2.3 Full Many-Body Treatment: Collapses and Revivals

In the above section, we have resorted to the continuous approximation ($N \to \infty$) to obtain analytical results. However, the integrals computed in the continuous limit $N \to \infty$ only make sense when the phase spread is much smaller than 2π. Otherwise, the periodic nature of the phase cannot be neglected. Still, numerical computation of Eq. (3.44) for typical parameters shows good agreement with Eq. (3.54) up to times where the phase distribution could not be experimentally distinguished from a uniform random distribution (see Fig. 3.25, left panel).

The passage to the continuous limit conceals however one interesting phenomenon, namely that for a finite number of particles, the collapse of coherence should alternate with revivals, where a high value of the coherence factor should be observed [66, 111, 112, 114], similar to that observed in Ref. [118]. Revivals occur when the phases of all the Fock states in the superposition (3.44) resynchronize. For the quadratic Hamiltonian (3.43), this happens periodically every $T_{\text{revival}} = h/U$ (for

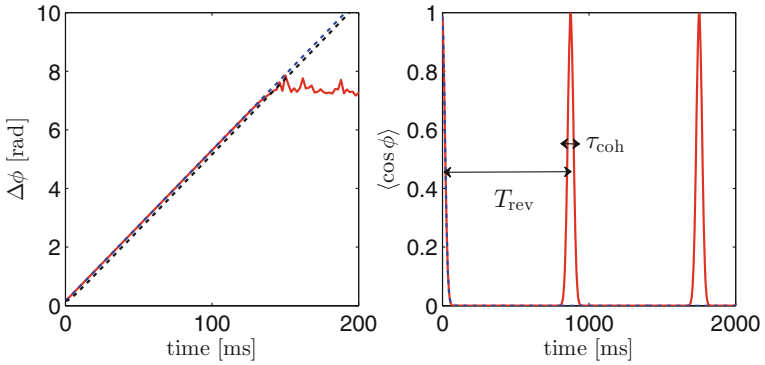

Fig. 3.25 Phase diffusion: numerical simulation. Circular standard deviation of the relative phase (*left*) and coherence factor (*right*) as a function of time after suppression of tunnel coupling ($J = 0$). The initial state was chosen such as to have the same number and phase fluctuations as the state characterized in Sect. 3.4.3. The interaction parameter $U = h \times 0.57$ Hz was adjusted to yield the same phase diffusion rate as observed experimentally. *Red* full numerical resolution of Eq. (3.44). *Dotted blue* analytical prediction (Eq. (3.54)). *Dotted black* same, omitting the term in factor of β. The analytical prediction for the phase spread is in good agreement with the numerical result up to times where $\Delta\phi \approx 2\pi$, after which the circular standard deviation ceases to be a relevant estimator of the phase spread. The effect of the linear term in Eq. (3.54) remains below ∼0.15 rad at all times, which is of the order of the experimental uncertainty. Conversely to the analytical model, the numerical simulation displays a revival of the coherence every $T_{\rm rev} \approx 0.9$ s (note the difference of time scales between the two panels). So far, though, no revival has been experimentally observed (Color figure online)

an initial state with a symmetric distribution of n, $T_{\rm revival} = h/2U$, see Fig. 3.25, right panel). So far, no revivals could be observed in our setup, possibly because of the effects of 1D dephasing, losses or technical heating over such a long timescale.

3.5.2.4 Phase Diffusion in Presence of (Weak) Tunnel Coupling

So far, we have considered phase diffusion in the limit where tunnel coupling is switched-off and the broadening of the phase distribution is governed by interactions only. In fact, we estimate from the simulations of the double-well potential that there should be a residual tunnel coupling in the $\mathrm{RF_{Amp}} = 0.65$ trap of the order of $J_{\rm split}/h \approx 0.1$ Hz (see Fig. 3.14). Indeed, when the condensate is held in the untilted double well ($\epsilon = 0$), no phase diffusion was observed (see Fig. 3.26, blue curve of left panel). Still, as soon as a tilt was applied to drive the phase accumulation, we observed phase diffusion and full randomization of the phase after ∼25 ms (red curve). Repeating the experiment for the different tilt angles of Fig. 3.19 yielded essentially the same diffusion rate.

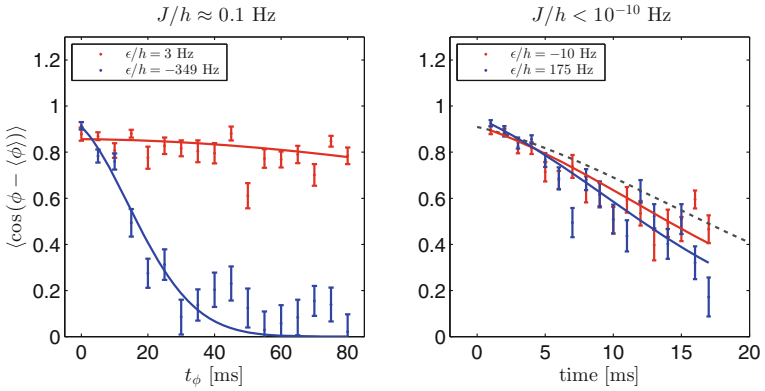

Fig. 3.26 Phase diffusion with and without tunnel coupling. Coherence factor as a function of the phase accumulation time in the $\mathrm{RF_{Amp}} = 0.65$ trap (*left*) and in the $\mathrm{RF_{Amp}} = 0.86$ trap (*right*), for which simulations of the double-well potentials yield respectively $J/h \approx 0.1$ Hz and $J/h \approx 4 \times 10^{-11}$ Hz. In presence of residual tunnel coupling (*left*), phase diffusion occurs only when the detuning ϵ is sufficiently large. When J is vanishingly small, phase diffusion occurs regardless of the detuning. Continuous lines: fit to the data, see Table 3.4. *Dotted gray line* in the *right panel* same as the *blue line* in the *left panel*, for comparison. The slightly faster phase diffusion in the $\mathrm{RF_{Amp}} = 0.86$ double well could be due to the higher transverse trap frequency, yielding a larger interaction energy

Symmetric Double Well

This behaviour can be understood looking at the mean-field model for the BJJ (Sect. 1.2.5), where the many-body wavefunction is identified to that of a single fictitious particle of mass $\propto 1/U$ in a cosine potential of depth $\propto JN$. It illustrates the fact that tunnel coupling tends to confine (or lock) the phase distribution, counteracting the effect of interactions. We can use the harmonic approximation (Eq. (1.197)) to derive a boundary between the phase-locking regime and phase-diffusion regime (here we assume a balanced double well, $\epsilon = 0$). Imposing that the depth $2JN$ of the cosine potential be larger than the zero-point energy in the harmonic approximation $\hbar\omega_J/2$, which roughly sets the condition for having at least one bound state, yields that no phase diffusion occurs as long as

$$J \ll J_c \equiv \frac{U}{2N} \tag{3.55}$$

This is the condition for entering the Fock regime (see Sect. 1.2.3.2). For our parameters, we estimate $J_c/h \approx 2 \times 10^{-4}$ Hz, which is compatible with the absence of phase diffusion in the $\mathrm{RF_{Amp}} = 0.65$ trap. Full numerical simulation of the two-mode Bose-Hubbard Hamiltonian confirm that phase diffusion is inhibited for $J/h \gg 10^{-3}$ Hz (see Fig. 3.27, left panel). We checked this by repeating the experiment in a more split trap ($\mathrm{RF_{Amp}} = 0.86$), for which simulations predict a negligible coupling, and indeed observed clear evidence of phase diffusion (see Fig. 3.26, right panel).

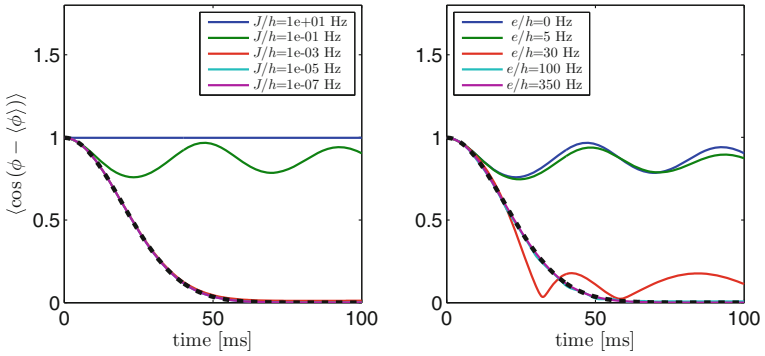

Fig. 3.27 Phase diffusion in presence of tunnel coupling. Coherence factor as a function of time for different values of the tunnel coupling J in a symmetric double well ($\epsilon = 0$) (*left*); and for different values of the detuning ϵ at $J/h = 0.1$ Hz (results of numerical resolution of the Bose-Hubbard Hamiltonian, $U = h \times 0.57$ Hz). *Dotted black line* analytical prediction in absence of coupling. The oscillations of coherence appearing in the *right panel* at *low* detuning correspond to a slow "breathing" mode of the many-body wavefunction at twice the Josephson frequency. It is due to the fact that the initial phase distribution is initially more narrow than the ground state at this coupling. Such a breathing is expected to occur at the moment where adiabaticity breaks down during the splitting but was not observed experimentally

It is interesting to note that although the ratio of interaction and tunnel coupling in the $\mathrm{RF_{Amp}} = 0.65$ trap strongly suppresses Josepshon oscillations (the self-trapping threshold $|z_c|$ is estimated to about 40 atoms, see (1.206)) and that the Josephson period should be of the order of 100 ms (2MM prediction), tunnel coupling is still strong enough to lock the relative phase and inhibits phase diffusion. Interestingly, the improved 2MM (see Sect. 1.2.5.4) predicts a period of 72 ms (in agreement with 1D transverse GPE simulations), which could match that of the observed low-amplitude oscillations of the mean phase, $f = 15.6 \pm 4$ Hz (see Fig. 3.21).[13]

It sheds light on a distinction between the Josephson and the Fock regime: in the Josephson regime ($1/N \ll U/2J \ll N$), the interactions are strong enough to modify or even strongly suppress tunneling, but conversely to the Fock regime, they are sufficient to maintain low phase fluctuations, allowing for a classical (or mean-field) description of the many-body wavefunction.

Tilted Double Well

However, since the currents in the wire are changed in a way to keep the spacing between the wells constant, the coupling energy is not expected to vary much when the trap is tilted. The observed phase diffusion, which seems to be compatible with an absence of coupling, is triggered by the energy detuning, similar to the way tunneling

[13] Note that other effects, such as the slow axial breathing and the different projection onto the Zeeman substates at switch off also affect the interference pattern on a comparable timescale.

can be frustrated in an optical lattice by applying a large energy gradient [117]. In Sect. 1.2.5.2, we have seen that ϵ acts as a drive for the mean phase. In the mean-field picture, it corresponds to a constant momentum applied to the fictitious particle. In a time-coordinate system evolving at the rate ϵ/h, the fictitious particle experiences a time-dependent cosine potential shifting at the velocity $-\epsilon/h$. When $|\epsilon|$ is sufficiently large, the wavefunction cannot adiabatically follow the drive and feels a time-averaged, flat potential, as in the zero-coupling limit. We can once again resort to the adiabaticity criterion (3.18) (this time, we use the shift term) to estimate that the detuning will overcome the effect of the tunnel coupling as soon as

$$\epsilon \gg \epsilon_c \approx \sqrt{2U\hbar\omega_J}. \tag{3.56}$$

In the $\mathrm{RF}_{\mathrm{Amp}} = 0.65$ trap, this implies that $\epsilon_c/h \gg 4$ Hz. This (a) confirms that even for the smallest tilts in Fig. 3.19, the tunnel coupling is too weak to prevent phase diffusion (b) the fact that we observe no phase diffusion in the horizontal double well indicates that it is balanced to better than $h \times 4$ Hz, which is compatible to the precision we have on the phase accumulation rate (2 Hz, see Sect. 3.5.1). The physical interpretation of this behaviour is that while tunnel coupling favors a relative phase close to zero with little spread (because it is energetically favorable), it cannot maintain $\phi \sim 0$ adiabatically in presence of a strong drive. Full numerical simulation of the two-mode Bose-Hubbard Hamiltonian at finite tunnel coupling strength $J/h = 0.1$ confirm that at short times ($t < 25$ ms), the evolution of $\Delta\phi$ in presence of a tilt cannot be distinguished from phase diffusion in absence of tunnel coupling. Interestingly, it implies that in order to cut the tunneling link between the BECs, it is sufficient to apply a detuning, without splitting the double well further apart.

3.5.3 Estimation of the Phase Diffusion Rate

To extract a phase diffusion rate from the data of Fig. 3.24, we compared the measured evolution of phase spread to that expected at short times from the theoretical prediction for a Gaussian state (Eq. (3.54)). We used a Rayleigh non-uniformity test [69] to distinguish the points compatible with a uniform phase distributions from the others. Only the points with a P-value below 5 %, indicating a probability below 5 % to be compatible with the distribution of $k = 47$ samples drawn from a uniform random distribution, were retained (blue points), similarly to what was done in Ref. [11].

The data of Fig. 3.24 was fitted with

$$\Delta\phi^2(t_\phi) = \Delta\phi_0^2 + R^2(t_\phi - t_i)^2, \tag{3.57}$$

yielding

Table 3.4 Phase coherence times

RF_{Amp}	J/h [Hz]	$\lvert\epsilon/h\rvert$ [Hz]	$\tau_{coh} = 1/R$ [ms]
0.65	0.1	3	195 ± 95
0.65	0.1	349	20 ± 3
0.86	$<10^{-10}$	10	17.4 ± 2.5
0.86	$<10^{-10}$	175	15.1 ± 2

Phase coherence times extracted from the phase diffusion model of Eq. (3.57), for two different dressing amplitudes (data of Fig. 3.26). The coupling J was estimated from simulations of the double well, the detuning was measured as in Sect. 3.5.1

$$R_{exp} = 51 \pm 4 \text{ mrad/ms}, \tag{3.58}$$

$$\Delta\phi_0 = 300 \pm 90 \text{ mrad} \tag{3.59}$$

(red line). $t_i = -6$ ms is a constant offset accounting for the 3 ms used before and after the phase accumulation stage to incline and level the double well, during which phase diffusion is also expected to occur. The uncertainties correspond to the 95 % confidence interval of the fit. Note that retaining the linear term in Eq. (3.54) does not change the fit result within the uncertainty, as expected from Fig. 3.25.

Alternatively, one can extract the phase coherence time $\tau_{GE} \equiv 1/R$ from the Gaussian decay of the coherence factor (Eq. (3.52)) with the fit model

$$\langle \cos(\phi - \langle\phi\rangle)\rangle(t_\phi) = \exp\left[-\Delta\phi_0^2/2\right] \exp\left[-(t - t_i)^2/2\tau_{coh}^2\right]. \tag{3.60}$$

This has the advantage that no points must be excluded for the fit. Table 3.4 summarizes the phase coherence times measured for different couplings and different detunings (see Fig. 3.26).

To give a quantitative prediction for the phase diffusion rate, we estimated R in two independent ways.

3.5.3.1 Ab initio Calculation

In absence of coupling, the phase diffusion rate is expected to be proportional to U, i.e. to the derivative of the chemical potential with respect to the atom number, evaluated for $N/2$ in the case of a symmetric splitting (see Sect. 1.2.2.2).

$$U = \left.\frac{\partial\mu}{\partial\mathcal{N}}\right|_{\mathcal{N}=N/2}. \tag{3.61}$$

In case of asymmetric splitting ($N_L \neq N_R$), $U_{L,R}$ is different in each well, and the partial derivative must be evaluated at the corresponding atom number (see Eq. 1.88).

However, on our setup, splitting is not adiabatic with respect to the longitudinal motion. This triggers a slow axial quadrupole mode and the condensates are not

at equilibrium during phase accumulation (see Sect. 3.4.1.3). More precisely, right after splitting, each condensate conserves the longitudinal profile of the initial BEC, while its suddenly sees its atom number divided by two (in the case of a symmetric splitting). It implies that immediately after the end of splitting, the effective chemical potential of each breathing condensate is different from that of a BEC at equilibrium in the same trap and with the same atom number.

Consequently, the chemical potential entering the term $\partial\mu_i/\partial\mathcal{N}$ is not the correct quantity describing the phase evolution. It must be replaced by an effective chemical potential

$$\mu_i^{\text{eff}} = \hbar\frac{\mathrm{d}\phi_i}{\mathrm{d}t}, \tag{3.62}$$

where $i = L, R$ and $\phi_i(t)$ is the time-dependent global phase of each breathing BEC. An expression for the time-dependent wavefunction is given by the scaling approach of Refs [91–93]. It shows that the axial wavefunction of each BEC subjected to breathing obeys

$$\varphi_i(z,t) = \frac{1}{\sqrt{b_i(t)}}\varphi_{\text{TF},i}\left(\frac{z}{b_i(t)}\right)\exp\left[-i\left(\frac{\mu_{1\text{D},i}}{\hbar}\tau_i(t) - \frac{m}{\hbar}\frac{\dot{b}_i(t)}{2b_i(t)}z^2\right)\right], \tag{3.63}$$

where $\varphi_{1\text{D},i}$ is the 1D Thomas-Fermi ground-state wavefunction in the new trap (see Eq. (1.56)), with the corresponding equilibrium chemical potential $\mu_{1\text{D},i}$ (Eq. (1.64)). The scaling parameter $b_i(t)$ follows Eq. (3.19) and the rescaled time τ_i is defined by

$$\tau_i(t) = \int_0^t \frac{du}{b_i(u)}. \tag{3.64}$$

Right after splitting ($t = 0$), the axial profile of each condensate is still equal to that of the initial unsplit BEC, but with a lower atom number. Each condensate starts breathing inwards, as shown on Fig. 3.13. Using the explicit expression for the 1D Thomas-Fermi radius (1.61), and taking into account the fact that the longitudinal frequency in the final trap ω_z' is slightly different from that of the initial trap ω_z, we find

$$b_i(0) = \left(\frac{\omega_z'}{\omega_z}\right)^{2/3}\left(\frac{N}{N_i}\right)^{1/3} \approx 1.04 \times \left(\frac{N}{N_i}\right)^{1/3} > 1, \tag{3.65}$$

$$\dot{b}_i(0) = 0. \tag{3.66}$$

At times short compared to the breathing period $T_\text{b} \approx 40$ ms, we can assume b constant and the phase of each condensates follows

$$\phi_i(t) \approx \frac{\mu_{1\text{D},i}}{\hbar}\frac{t}{b_i(0)} = \frac{1}{\hbar}\underbrace{g_{1\text{D}}n_i(0)}_{\mu_i^{\text{eff}}}t, \tag{3.67}$$

where g_{1D} is the 1D interaction constant in the new trap (we assume that transversely, the splitting is adiabatic) and $n_i(0)$ is the initial peak linear density of each (out-of-equilibrium) BEC.

In case of a sudden splitting, the longitudinal profile of each cloud first remains unaffected so that $n_i(0) = n(0)N_i/N$, where $n(0)$ is the peak linear density of the unsplit cloud. Because of this *linear* dependence of μ_i^{eff} with the number of atoms N_i in the condensate,

$$\frac{\partial \mu^{\text{eff}}}{\partial \mathcal{N}} = \frac{g_{1D}}{N} n(0). \tag{3.68}$$

From the estimated peak linear density in the initial BEC $n(0) = 36$ atoms/μm and the transverse trap frequencies in each individual well, we get $U_{\text{eff}}/h = 0.52\,\text{Hz}$. Note that this value differs significantly from that estimated from the the equilibrium chemical potential of the initial unsplit BEC ($U/h = 0.33\,\text{Hz}$) or the equilibrium chemical potential in each single well ($U/h = 0.40\,\text{Hz}$).

Using the measured squeezing factor $\xi_N = 0.41$, the expected phase diffusion rate is

$$R_{\text{th}} = 46 \pm 4\ \text{mrad/ms}, \tag{3.69}$$

or equivalently $\tau_{\text{coh}} = 22 \pm 2$ ms. The uncertainty on R_{th} is computed by error propagation from the experimental uncertainty on each parameter. This theoretical prediction with no free parameter, represented as a gray shaded area in Fig. 3.24, is in fair agreement with the experimental value, suggesting that the axial breathing cannot be ignored.

3.5.3.2 Chemical Potential Measurement

To further confirm our understanding of phase diffusion, we performed an independent measurement of $\partial \mu^{\text{eff}}/\partial \mathcal{N}$. This was done by measuring the rate of phase accumulation driven by a difference of chemical potential between the two condensates. For that, we split the BEC with an angle in order to prepare a well-controlled population imbalance (see Fig. 3.12). The double well was then leveled ($\Delta = 0$) and we observed a linear phase evolution with a rate dependent on $\langle z \rangle$.

In a symmetric double well ($\Delta = 0$), the energy difference which drives the phase accumulation stems from the difference of interaction energy[14] $U\,(N_L - N_R)$ (see Eq. (1.208)). Assuming that both wells are identical,

$$\langle \phi \rangle\,(t) = \frac{1}{\hbar} U N \langle z \rangle\, t, \tag{3.70}$$

[14]Strictly speaking, the phase accumulation rate is proportional to the difference of $\partial\mu/\partial\mathcal{N}$ multiplied by the corresponding atom number. For a Hamiltonian such as that of the Bose-Hubbard mode, which is quadratic in n, this is equivalent to the difference of chemical potential.

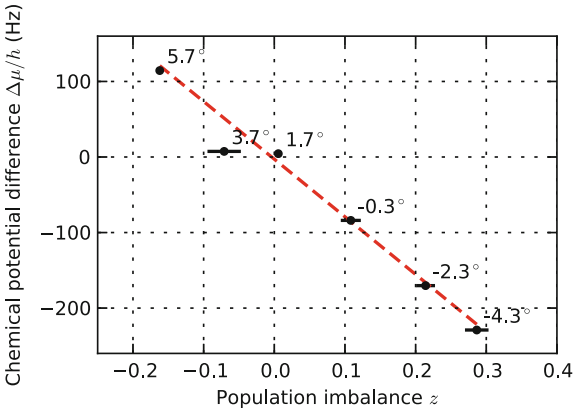

Fig. 3.28 Direct measurement of $\Delta\mu(z)$ when the condensate is split to yield a population imbalance. The numbers labelling the points are the angles (in °) used during splitting to obtain the measured imbalance. The obtained population imbalance is responsible for $\Delta\mu$ measured in the leveled double well. The *dashed line* is a linear fit to the data from which $gn(0)$ is extracted according to Eq. (3.71). The horizontal error bars are ± 1 standard error of the mean. The vertical error bars representing ± 1 standard error of the fitted energy difference are smaller than the points

where $\langle z \rangle$ is the average population imbalance.

Here also, we have to take into account the fact that the condensates are not at equilibrium. For $t \ll T_\mathrm{b}$, Eq. (3.67) yields

$$\langle \phi \rangle(t) = \frac{1}{\hbar} g_{1\mathrm{D}} n(0) \langle z \rangle t. \tag{3.71}$$

The phase accumulation rate is simply proportional to $\partial\mu^{\mathrm{eff}}/\partial\mathcal{N}$. Repeating this measurement for 6 different values of the imbalance $\langle z \rangle$, we indeed observed that the phase accumulation rate depends linearly on the population imbalance and extracted the slope $g_{1\mathrm{D}} n(0)/h = 763 \pm 53$ Hz (see Fig. 3.28). This yields a third value of the phase diffusion rate

$$R_\mu = 57 \pm 5 \text{ mrad/ms}, \tag{3.72}$$

($\tau_{\mathrm{coh}} = 17.5 \pm 2$ ms), in agreement with both previous values.

3.5.4 Conclusion on the Phase Evolution

In this section. we have shown how to apply a reproducible phase shift to our condensate by tilting the double well. This triggers a deterministic linear evolution of the mean phase with a rate that we can measure with a precision of the order of 2 Hz.

If ϵ were only equal to the difference of gravitational potential energy, this sensitivity would allow detecting the energy gained by one ^{87}Rb atom lifted 1 nm. However, we cannot explain quantitatively this rate from the known sources of phase drive. We speculate that the $\sim$60 % discrepancy between the expected and the measured values of the phase accumulation rate comes from a an unknown behaviour of the tilted trap. For this reason, performing a precision measurement of gravity with a double-well interferometer on chip seems challenging.

We observe a randomization of the relative phase within a few tens of ms as soon as the two wells are detuned, even in presence of tunnel coupling. The high interferometric contrast observed in single realizations long after the coherence has been lost indicates a phase diffusion process. Both the theoretical value of the interaction-induced dephasing rate and the value inferred from measurement of the interaction-driven phase accumulation are in agreement with the observed diffusion rate, strongly suggesting that atom-atom interactions are responsible for the decay of phase coherence. Importantly, the fact that the BECs are out-of-equilibrium after the end of the splitting has to be taken into account.

The measured phase diffusion rate is in agreement with the measured fluctuations of the relative atom number in our two-mode BEC. Through the use of a number-squeezed state, we report a coherence time $\tau_{\mathrm{coh}} = 20 \pm 3$ ms, twice longer than expected with a coherent, uncorrelated state ($\tau_{\mathrm{coh}} \approx 9$ ms). Extended coherence times have already been observed and attributed to number squeezing [11, 117], but without directly measuring the number fluctuations. To the best of our knowledge, our measurement constitutes the first direct evidence of the link between number uncertainty and phase diffusion. It calls for the improvement of methods to produce controlled number squeezing, in order to systematically verify the way how phase diffusion varies with the amount of number squeezing. The development of these methods is currently in progress on our experiment.

Moreover, this result shows that the interrogation time of our interferometer is currently limited by atomic interactions, and not by technical noise. The use of number-squeezed states is a first way by which to extend the coherence time. The control of atomic interactions, for example by the use of a Feshbach resonance, seems a more promising option. By strongly reducing the s-wave scattering length in a ^{39}K BEC, coherence times up to $\sim$1 s, limited by technical noise, were demonstrated [41]. Similarly, both inhomogeneous mean-field shifts and interaction-induced phase diffusion could be reversed by interaction control together with the application of a spin-echo-like technique, enabling the observation of a revival of the interferometric contrast [43]. The high degree of control of interactions offered by Feshbach resonances motivate the strive for high-precision BEC interferometers, such as the ones which are currently being built in Canberra [39] or Florence.[15]

[15] https://sites.google.com/a/lens.unifi.it/quantum-interferometry/.

3.6 Two Phase-Sensitive Condensate Recombiners

The last element needed to close the interferometric sequence is a phase-sensitive recombiner (see Fig. 3.2). In an optical Mach-Zehnder interferometer, this operation is realized by means of a recombination beam splitter, such as a half-silvered mirror or a fiber coupler. Its function is to transform the phase difference between the two paths of the interferometer into a measurable signal: usually an intensity difference between the two output ports.

Conceptually, this operation is exactly symmetric to the separation beam splitter. Indeed, Bragg or Ramsey interferometers use essentially identical[16] rf, microwave or laser pulses to split and recombine the matter waves. In contrast, most trapped BEC interferometers rely on the tof recombination scheme detailed in Sect. 3.2.1. The fact that tof expansion greatly reduces the interactions when the condensates overlap is generally put forward as an advantage of this method.

Different techniques have been suggested to read out the phase between trapped BECs. In Ref. [56], the phase-dependent heating at the merging of two condensates has been used to infer their relative phase. Recently, we have developed a scheme to read-out the phase from a trapped BEC prepared in a superposition of vibrational states by monitoring the evolution of its momentum distribution [16].

Here we have explored new methods to recombine trapped BECs in a way to map their relative phase into a population imbalance between the two wells. One motivation to seek for such a scheme has been mentioned in Sect. 3.2.1.4: while the sensitivity of our phase readout from the spatial interference fringes seems incompatible with measurements beyond the SQL, our fluorescence imaging already enables atom counting with a precision better than the shot noise. More generally, it has been shown that even though phase estimation based on a fit to the tof interference pattern can in principle reach sub-shot-noise sensitivity($\Delta\phi < 1/\sqrt{N}$) [119], it is fundamentally bounded by $N^{2/3}$ and hence cannot reach the Heisenberg scaling of the sensitivity [120].

A related motivation is the development of methods to manipulate coherently the state of an external BJJ. We have seen in Sect. 1.2.4.3 that in the collective spin representation, the coherent manipulation of the many-body wavefunction requires rotations around the axes of the Bloch sphere. Such techniques have been already implemented with high performance in internal BJJ, making use of rf and microwave pulses. While the energy detuning applied during the phase accumulation stage (see Sect. 3.5.1) acts as a rotation around the (z)-axis, tools to perform rotations around the (x) and (y) axis efficiently are still to be developed.

Several interferometric schemes based on the splitting and recombination of trapped atoms have been proposed. In Ref. [121] a "conveyor belt" was implemented on an atom chip and used to merge two clouds of thermal atoms. This experiment motivated the proposal for a trapped-atom interferometer using a time-varying

[16]Up to the relative phase of the two BS pulses, which can be tuned to vary the interferometric phase.

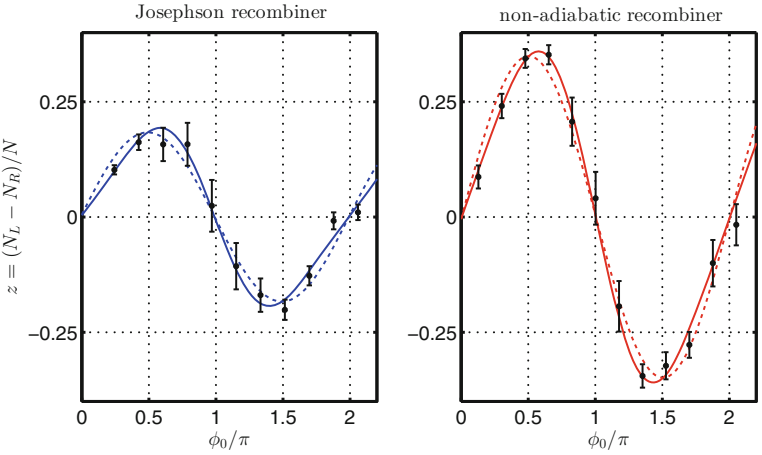

Fig. 3.29 Josephson and non-adiabatic recombiner. Normalized population imbalance z of the output state of the *Josephson* (*left*) and *non-adiabatic* (*right*) recombiner, as a function of the phase ϕ_0 of the input state. Each black dot corresponds to the ensemble average over ∼18 independent experimental realizations (error bars: standard error of the mean). The phase of the input state is varied by scanning the phase accumulation time over ∼3 ms (phase accumulation rate: $\epsilon/h \approx$ 350 Hz). *Continuous lines* fit to the data with a two-harmonic model (see text). *Dashed line* Lowest harmonic of the fit (sine)

magnetic potential [122]. A similar multimode interferometer consisting in two Y-shaped beam splitter was proposed in 2002 [85].

Several authors have suggested to make use of the controlled tunneling of atoms in a double well potential in order to read out the phase either directly from the mean population imbalance [102, 123] or from its fluctuations [124]. Although it was discussed that the effect of interactions during the recombination procedure would degrade the performance of the beam splitter [119, 125], it has been pointed out that controlled interactions could in contrary allow for phase estimation beyond the standard quantum limit. Even more, J. Grond et al. showed that the Heisenberg scaling of the phase sensitivity could be reached in a fully trapped double-well interferometer [123].

On our experiment, we explored two different approaches to perform a phase-sensitive recombination, i.e. to transform a state with a given phase ϕ_0 and no population imbalance into another state, whose imbalance is a function of ϕ_0 (see Fig. 3.29). The first method (Sect. 3.6.1) consists in using Josephson oscillations to achieve controlled phase-dependent tunneling. The second approach (Sect. 3.6.2) relies on a fast transformation of the potential to make use of the double well as a semi-reflective barrier. The population imbalance of the output state is the result of the interference between the reflected and the transmitted parts of the matter wave. For each case, we will explain the principle of the recombiner, present its implementation and discuss some of its limitation. This section will finish by a comparison of the two schemes.

The inverse recombiner

Following Refs. [85, 122], the most straightforward recombining beam splitter for our Mach-Zehnder interferometric scheme is to time-reverse the splitting Sect. 3.4.1, i.e. to ramp down the tunnel barrier and to merge the two condensates into a single one. Provided the transformation of the potential can be performed adiabatically with respect to the transverse motion, the state of the condensate prior recombination should be mapped onto a superposition of the ground and first excited state of the single-well potential [122]. The population of these two states, as well as their relative phase, could be inferred from monitoring the evolution of the wavefunction during a holding time after the end of the merging, as was already done in our experiment to analyze superpositions of vibrational states [16, 76, 126]. The value of the relative phase prior merging could also be inferred from the position of the center-of-mass of the merged cloud.

However, the merging of two interacting Bose-Einstein condensates is expected to result in a phase-dependent heating, due to the decay of excitations which are created at the phase discontinuity [127]. When $\phi_0 = \pi$, the merged condensate is even expected to contain a dark soliton. It has been pointed out that enhanced phase sensitivity could be achieved by observing the dynamics of the soliton [128]. By monitoring the phase-dependent reduction of the condensate fraction, Jo et. al. could obtain an interferometric signal with up to $\sim$20 % contrast [56]. Our first attempts to merge the condensates indeed produced highly excited clouds. We could even observe indications of the decay of transverse excitations into longitudinal modes, probably following the same mechanism as in Ref. [76].

3.6.1 Josephson Recombiner

3.6.1.1 Principle

The idea of using Josephson oscillations as a way to coherently transform a state with no imbalance and a given relative phase into a state whose imbalance is a function of the phase has been studied in various publications [102, 123, 125]. A Josephson beam-splitter is conceptually very similar to a $\pi/2$ Rabi pulse between two internal states coupled by a radio-frequency field, as used for example in Ramsey interferometry [4]. It is also not without similarity with fiber couplers used in laser optics.

Let us assume that initially, the BEC is in a coherent superposition of left and right mode with vanishing average imbalance ($\langle z \rangle = 0$) and a mean relative phase ϕ_0. This corresponds for example to the state of the BEC after the phase accumulation stage. If the tunnel coupling energy J is suddenly set to a finite value,[17] by lowering the potential barrier, the phase difference triggers an oscillating tunnel current of atoms

[17] We assume here that initially, J=0, although in practice there is a slight residual coupling even before recombination.

between the two condensates (see Sect. 1.2.5.3). Neglecting interactions, we find by solving Eqs. (1.198) and (1.199) for $\Lambda = 0$ and $\epsilon = 0$ that z undergoes sinusoidal Rabi oscillations, the amplitude of which is equal to the sine of the initial phase[18]

$$z(t) = \sin\phi_0 \ \sin\left(2Jt/\hbar\right). \tag{3.73}$$

After a quarter of a Rabi oscillation ($T_{\rm BS} = h/8J$), the final population imbalance is simply equal to the sine of the initial phase. In particular, when $\phi_0 = \pi/2$, the maximal value $z\left(T_{\rm BS}\right) = 1$ is reached. The evolution of z can then eventually be frozen by ramping up the barrier again ($J \to 0$).

In the collective spin representation (see Sect. 1.2.4), the beam-splitter operation precisely corresponds to a rotation of angle $\pi/2$ around the x-axis of the Bloch sphere (see Fig. 1.12). In absence of interactions, Eq. (1.152)) reads

$$|\psi(T_{\rm BS})\rangle = \exp\left(i\frac{2J}{\hbar}T_{\rm BS}\hat{S}_x\right)|\psi(0)\rangle\,, \tag{3.74}$$

where the coupling J is applied during the beam-splitter time $T_{\rm BS}$.

In practice, the tunnel coupling is dynamically varied by ramping up and down the rf dressing intensity. For a non-interacting system, the condition for a $\pi/2$ pulse becomes

$$\frac{1}{\hbar}\int_0^{T_{\rm BS}} 2J(t)\mathrm{d}t = \frac{\pi}{2}, \tag{3.75}$$

namely that the area of the pulse should be equal to $\pi/2$.

3.6.1.2 Implementation

We implemented the Josephson beam-splitter by ramping down the dressing intensity in 3 ms from its initial value $\mathrm{RF_{Amp}} = 0.65$ ($J/h \approx 0.1$ Hz) to a lower value $\mathrm{RF_{Amp}^{BS}}$, corresponding to a more coupled trap (see Figs. 3.14 and 3.35). The duration of the recombination ramp was chosen as to avoid excitations of transverse modes of the BEC. The condensates were then held for an adjustable time $t_{\rm BS}$ in the coupled trap, before the barrier was raised again to separate the atoms for counting as described in Sect. 3.2.2.1. The beam-splitting procedure is illustrated in Fig. 3.30.

To find the optimal recombiner parameters, i.e. maximize the contrast of the read out, we prepared a state with $\langle\phi_0\rangle = \pi/2$ at the input of the recombiner and repeated the operation for different values of $\mathrm{RF_{Amp}^{JBS}}$. For each value, we scanned the beam-splitter time $t_{\rm BS}$, looking at the extrema of the Josephson oscillations. Figure 3.31 shows Josephson oscillations recorded in the $\mathrm{RF_Amp} = 0.55$ trap, for

[18] Note that $\phi(t)$, on the other hand, has a non trivial time-dependence. For instance, when $\phi_0 = \pi/2$, $\phi(t)$ flips between $\pm\pi/2$ every half-period (square oscillations).

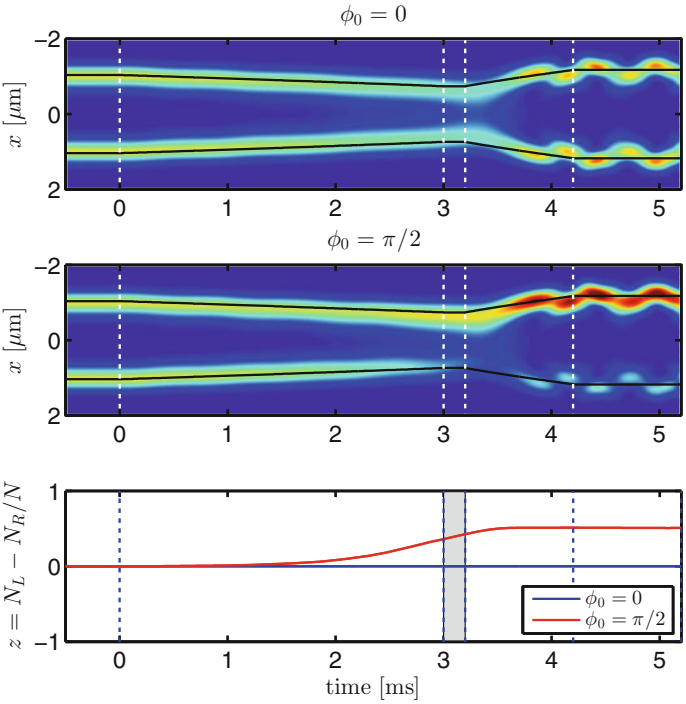

Fig. 3.30 Simulation of the Josephson recombiner. Evolution of the transverse density profile during the beam-splitter operation ($t_{\mathrm{BS}} = 0.225$ ms), for an initial state with $z = 0$, $\phi_0 = 0$ (*top*) and $z = 0$, $\phi_0 = \pi/2$ (*middle*), obtained by solving numerically the 1D GPE in the transverse potential. The continuous *black lines* indicate the position of the potential minima at each time. The vertical *dotted lines* show the duration of the recombination ramp, the beam-splitter time t_{BS} and the separation ramp ($t = 0$ corresponds to the beginning of the recombination ramp). While for $\phi_0 = 0$, the density profile is symmetric at all times, an imbalance builds up when $\phi_0 = \pi/2$. Note the transverse excitations for $t > 4$ ms caused by the separation ramp. *Bottom* Evolution of the normalized population imbalance during the beam-splitter operation (*gray area* beam-splitter time t_{BS}). Atoms already start tunneling through the potential barrier during the 3 ms recombination ramp, explaining why the maximal final imbalance is obtained for a very small value of t_{BS}

which we obtained the highest amplitude $\langle z_m \rangle \approx 0.2$ at $t_{\mathrm{BS}} = 0.225$ ms. From the measured frequency of the Josephson oscillation, we estimate $J/h \approx 40$ Hz and $\Lambda \approx 7$. Repeating the whole procedure for different values of the initial phase, we observed a sine-like dependence of the final imbalance, as displayed in Fig. 3.29, left panel.

The contrast of the recombiner is given by the amplitude of $z(\phi_0)$. Note that because of phase diffusion, $\langle z_m \rangle$ is not the right quantity to infer the recombiner contrast, as we will see in Sect. 3.7.2: the measured final imbalance is the result of the averaging over different initial phases, which has the effect of decreasing the contrast. However, correcting for this effect, we still find a contrast of the order of 20 % (see Sect. 3.7.2.1).

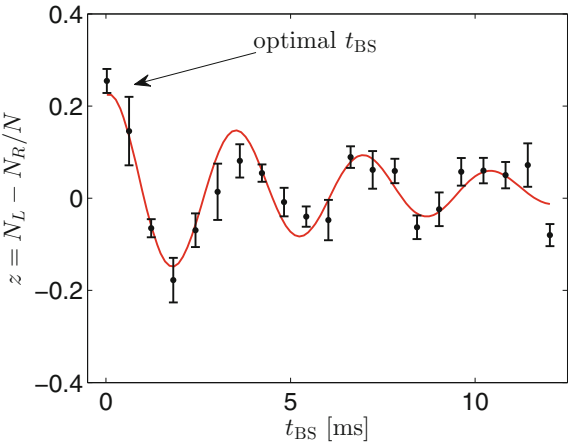

Fig. 3.31 Optimization of the Josephson recombiner. Final population imbalance z as a function of the beam splitter time t_{BS} in the $\mathrm{RF}_{\mathrm{Amp}}$ double well, showing damped Josephson oscillations triggered by the initial phase difference $\phi_0 \approx \pi/2$ (no initial population imbalance). *Black* ensemble average over up to 5 single individual realizations (*gray dots*). *Red* fit with a sine multiplied by a Gaussian damping, yielding a rms decay time of 14 ± 7 ms. The arrow indicates the maximum amplitude $z = 0.23$ obtained for the optimal beam-splitter time $t_{\mathrm{BS}} = 0.225$ ms, which was used for the recombiner sequence. Note that even for $t_{\mathrm{BS}} = 0$, atoms have already tunneled through the barrier during the 3 ms recombination ramp

The fact that the final imbalance differs from zero even when $t_{\mathrm{BS}} = 0$ shows that atoms have already started to tunnel before the end of the recombination ramp. Indeed, simulations show that most of the tunneling occurs while the barrier is beeing lowered (see Fig. 3.30). We also observed a strong damping of the Josephson oscillations over $\sim$10 ms (see Chap. 4), which sets a drastic limit to the duration of the recombiner sequence.

3.6.1.3 Limitations of the Josephson Recombiner

Maximum Contrast

Interactions modify the functioning of the Josephson recombiner. First, in presence of interactions, the period of (low-amplitude) Josephson oscillations, $T = h/\left(2J\sqrt{1+\Lambda}\right)$ (see Eq. (1.132)), is shorter than that of the Rabi oscillations $T = h/2J$. Secondly, the maximum imbalance that can be achieved starting from a zero-imbalance initial state is set by the self-trapping threshold and reads (see Eq. 3.76)

$$|z_c| = 2\frac{\sqrt{\Lambda - 1}}{\Lambda}. \tag{3.76}$$

For $\mathrm{RF_{Amp}} = 0.55$, we find $|z_c| \approx 0.7$ while for $\mathrm{RF_{Amp}} = 0.6$, $|z_c|$ is already lower than 0.2 (see Fig. 3.41). This shows that in order to achieve a high contrast, the recombination must be performed in a strongly coupled double well. Ideally, this would impose lowering the dressing down to a trap where $\Lambda < 2$ and entering the Rabi regime. In our double well, however, this would imply ramping the dressing amplitude down to a potential where the barrier is lower than the ground state energy, which effectively means merging the two condensates.

Adiabaticity

Moreover, our two-mode description of the Josephson recombiner relies on the assumption that at each time, the wavefunction can be written as a superposition of the two modes of the double well, as introduced in Sect. 1.2.1. When the transverse motion is fast with respect to the transverse trap frequency ($\omega_x/2\pi \sim 1$ kHz), this assumption breaks down. It means that in order to reach low values of Λ while still remaining adiabatic at all times, the recombination must be carried out slowly, probably over tenths of ms. This however seems challenging, given the strong damping observed over a few ms.

Anharmonicity

Interactions are also responsible for a non-linearity of the response of the recombiner (see Fig. 3.29, left panel). In absence of interactions, the final imbalance is at all times proportional to the sine of the initial phase (see Eq. (3.73)). For an interacting system, however, the simulations of the recombiner show that $z(\phi_0)$ is anharmonic, with a steeper slope around $\phi_0 = \pi$ (see Fig. 3.32, left panel).[19]

We can understand the shape of $z(\phi_0)$ by looking at the phase portrait of the BJJ in presence of interactions (Fig. 3.32, right panel). It suggests that, conversely to the non-interacting case, the best contrast is obtained by following the separatrix (black line), i.e. for $\phi_0 = \pi$. However, ($z = 0$, $\phi_0 = \pi$) is a hyperbolic fixed point, meaning that the system cannot evolve from this point. For ϕ_0 close to, but different from π, the trajectories are close to the separatrix but the period of the oscillations of z diverges as $-\ln|\phi_0 - \pi|$ [129] (see Fig. 3.42).

The final imbalance $z(\phi_0)$ is a periodic function of ϕ_0. Accounting for the symmetry $z(-\phi_0) = -z(\phi_0)$, we can express it as a Fourier series

$$z(\phi_0) = \sum_{n=1}^{M} a_n \sin(n\phi_0)\,. \tag{3.77}$$

[19] The central symmetry around $\phi = \pi$ comes from the fact that the whole BJJ equations are invariant under the transformation $z \to -z, \phi_0 \to \phi_0 = \phi_0 + \pi$, which is simply equivalent to swapping the left and the right mode.

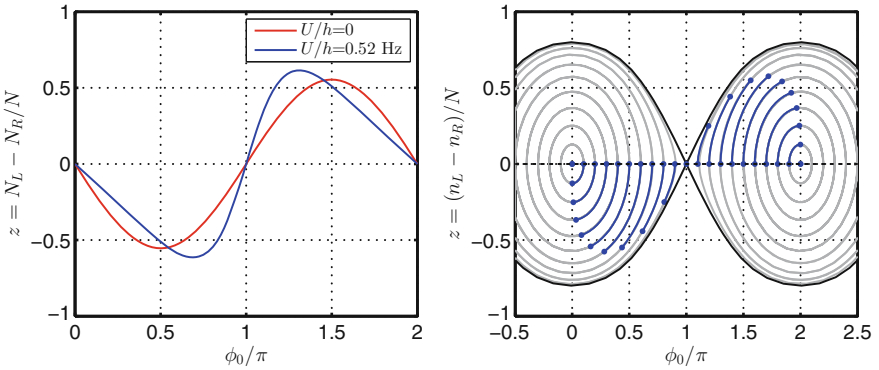

Fig. 3.32 Effect of interactions. *Left* Final population imbalance z as function of the phase ϕ_0 of the state at the input of the Josephson recombiner, in absence (*red*) and in presence (*blue*) of interactions (full 1D GPE simulation of the recombiner sequence). Interactions are responsible for the anharmonicity of the blue curve. Note the steep slope close to $\phi_0 = \pi$. *Right* Classical phase portrait of the BJJ for $\Lambda = 10$ (*gray lines*). The *blue points* on the $z = 0$ axis correspond to input states of the recombiner with different initial phases. The *blue lines* represent the trajectory each state travels in phase space during a fixed time equal to $\pi/2\omega_J$, i.e. a quarter of a Josephson oscillation. Note that ω_J represents only the period of the small amplitude Josephson oscillations. As the initial state gets closer from the hyperbolic fixed point ($\phi_0 = \pi, z = 0$), the oscillations become increasingly slow and approach asymptotically the separatrix (*black line*) (Color figure online)

Note that since it relies only on the periodicity and symmetry of $z(\phi_0)$, this decomposition is very general and can describe the signal of any phase-sensitive recombiner. The anharmonicity of the data in Fig. 3.29, left panel, is already reasonably accounted for by retaining the two first harmonics ($M = 2$, blue line). However, as we will see in Sect. 3.7.2.1, it is necessary to characterize the phase distribution of the input state of the recombiner to infer the amplitude of the harmonics of the recombiner response. Although ϕ is a 2π-periodic variable, it is scanned in practice by varying the phase accumulation time. The mere fact that the time-evolution of the BEC is not linear indicates that the final imbalance is not likely to be a periodic function of time.

Anharmonicity also implies that the value of the phase maximizing the imbalance depends on the beam-splitter duration. Strictly speaking, this invalidates the procedure that we used to find the optimal parameters by keeping the initial phase equal to $\pi/2$. It is thus not straightforward to find the parameters maximizing the contrast of the Josephson recombiner. For a given value of $\mathrm{RF}_{\mathrm{Amp}}^{\mathrm{JBS}}$, both t_{BS} and ϕ_0 must be varied to find the best working point. The simulations displayed in Fig. 3.42 show that in the $\mathrm{RF}_{\mathrm{Amp}} = 0.55$ double well, up to 80 % contrast can be achieved, while for a more split trap ($\mathrm{RF}_{\mathrm{Amp}} = 0.6$), the oscillations of z do not exceed 25 %.

The discrepancy between the highest values of the contrast we could observe (of the order of 20 %) and the theoretical mean-field predictions shows that effects beyond the zero-temperature, 1D dynamics are limiting the contrast, as suggested by the strong damping of the Josephson oscillation we observed. These effects, in particular the coupling between the different spatial directions, are currently being investigated by Bruno Juliá-Díaz and Artur Polls at the University of Barcelona.

3.6.2 Non-Adiabatic Recombiner

Because it requires adiabaticity with respect to the transverse motion of the condensate, the Josephson recombiner cannot simultaneously meet the constraints of high contrast and fast operation. A slow transformation of the potential, however, does not allow for a high contrast, because of the fast damping observed on a few ms timescale.

Instead, we decided to lift the adiabaticity constraint and to seek for a fast beam-splitter operation. Rather than slowly ramping down the rf dressing to tunnel-couple the two halves of the condensate, we tried to abruptly launch them on the potential barrier. As we will see, this mimics the operation of a half-silvered mirror in optics: a wave packet impinging on the beam splitter is split between a reflected and a transmitted wave. The intensity at each output port is the result of the interference between reflected and transmitted waves, and hence depends on the initial phase difference.

3.6.2.1 Implementation

Instead of slowly ramping down the rf dressing amplitude, we abruptly[20] decreased it to a lower value $\mathrm{RF}_{\mathrm{Amp}}^{\mathrm{FBS}}$. This had the effect of simultaneously reducing the height of the potential barrier and the distance between the two wells (see Fig. 3.35). The clouds were accelerated towards the barrier and after an adjustable time t_{BS}, the barrier was raised again to separate the atoms for counting. Figure 3.33 shows simulations of the complex, phase-dependent dynamics of the wavefunction during the recombination.

Here also, we prepared a state with vanishing imbalance and a phase close to $\pi/2$ and scanned both the time t_{BS} and the dressing amplitude $\mathrm{RF}_{\mathrm{Amp}}^{\mathrm{FBS}}$ to find the optimal working point for the recombiner. We recorded the highest final imbalance $z \approx 0.42$ for $\mathrm{RF}_{\mathrm{Amp}}^{\mathrm{FBS}} = 0.55$ and $t_{\mathrm{BS}} = 2.25$ ms (see Fig. 3.34). It is interesting to note that the optimum was found for the same value of the dressing amplitude as for the Josephson recombiner. Simulations indicate a spacing of 1.5 μm and a barrier height $E_{\mathrm{b}}/h \approx 1$ kHz in this potential (see Fig. 3.35). Repeating the procedure for different values of the initial phase, we also observed a sine-like dependence of the output imbalance (see Fig. 3.29, right panel).

3.6.2.2 Propagation of Two Non-interacting Wave Packets in a Symmetric Potential

To gain some insight into the working principle of the non-adiabatic recombiner, it is useful to first consider the propagation of two non-interacting wave packets with

[20] Within 0.25 μs, which is much lower than the inverse transverse trap frequency.

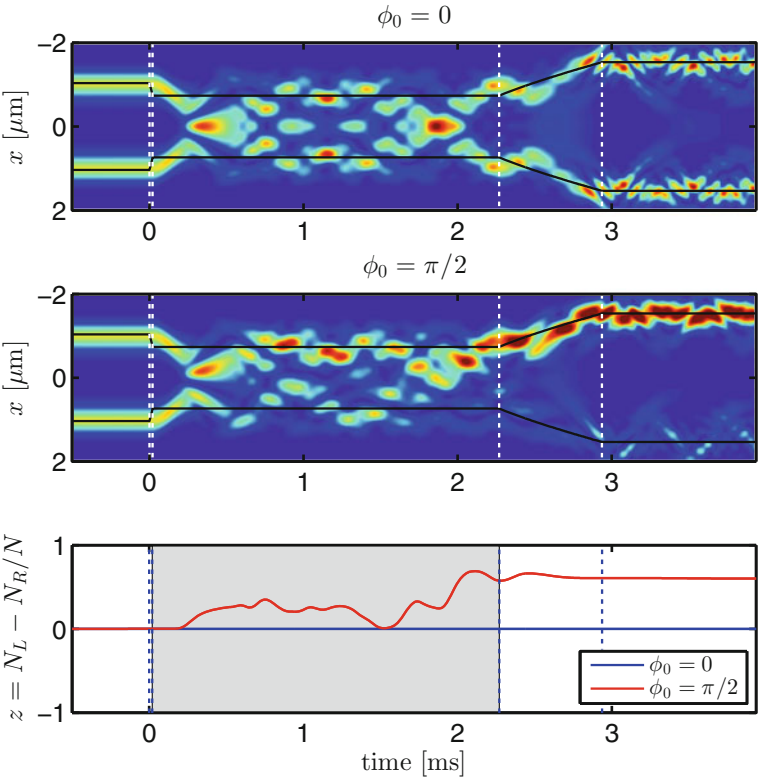

Fig. 3.33 Simulation of the non-adiabatic recombiner. Evolution of the transverse density profile during the beam-splitter operation ($t_{\mathrm{BS}} = 2.25$ ms), for an initial state with $z = 0$, $\phi_0 = 0$ (*top*) and $z = 0$, $\phi_0 = \pi/2$ (*middle*), obtained by solving numerically the 1D GPE in the transverse potential. The continuous black lines indicate the position of the potential minima at each time. The vertical dotted lines show the duration of the recombination ramp, the beam-splitter time t_{BS} and the separation ramp ($t = 0$ corresponds to the beginning of the recombination ramp). While for $\phi_0 = 0$, the density profile is symmetric at all times, an imbalance builds up when $\phi_0 = \pi/2$. Note that conversely to the Josephson recombiner, the transverse profile exhibits a complex structure due to the multiple reflections and transmissions in the double-well potential. *Bottom* Evolution of the normalized population imbalance during the beam-splitter operation (*gray area* beam-splitter time t_{BS})

a given relative phase ϕ_0. We assume a 1D symmetric potential $V(-x) = V(x)$ and the wavefunction initially to read

$$\psi(x, t = 0) = \frac{1}{\sqrt{2}}\left[\psi_L(x) + e^{i\phi_0}\psi_R(x)\right], \tag{3.78}$$

where $\psi_L(-x) = \psi_R(x)$. This implies in particular that the two wave packets have opposite momenta $\langle\hat{p}\rangle_L = -\langle\hat{p}\rangle_R$, for example both heading towards $x = 0$.

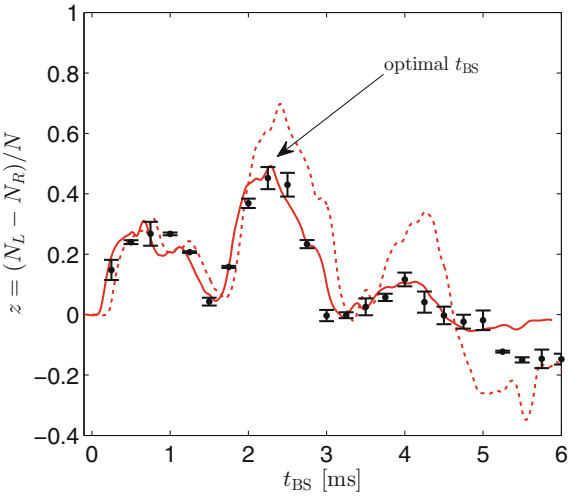

Fig. 3.34 Optimization of the non-adiabatic recombiner. Measured final population imbalance z as a function of the beam splitter duration $t_{\rm BS}$. The input state was prepared to have $\langle z\rangle = 0$ and $\langle\phi_0\rangle = \pi/2$. Each black dot is an ensemble average over a few realizations. The uneven shape of $z(t_{\rm BS})$ reflects the complex dynamics of the wave packet in the $\mathrm{RF_{Amp}} = 0.55$ double-well potential. The *arrow* indicates the optimal beam-splitter time $t_{\rm BS} = 2.25$ ms, for which the maximum imbalance $\langle z\rangle \approx 0.42$ was observed. *Dashed red line* result of a 3D Gross-Pitaevskii simulation of the BEC dynamics in the recombiner (without the separation ramp). *Plain red line* result of the same simulation, multiplied by a Gaussian damping term and time-shifted to fit the experimental points (rms time σ: 2.7 ms, time shift: 0.12 ms) to heuristically account for the observed relaxation mechanisms and the evolution of the condensate during the separation. The 3D GPE simulations were performed by Bruno Juliá-Díaz at the University of Barcelona (preliminary) (Color figure online)

Equation 3.78 describes for example the initial configuration in the recombiner, right after the dressing amplitude has been abruptly decreased (see Fig. 3.35).

If we assume no interaction, the evolution of the wave packets is governed by the linear Schrödinger equation. The superposition principle and the parity of the potential allow to write at all times

$$\psi(x,t) = \frac{1}{\sqrt{2}}\left[\psi_L(x,t) + e^{i\phi_0}\psi_R(x,t)\right], \tag{3.79}$$

where $\psi_R(x,t) = \psi_L(-x,t)$. The time-dependent population imbalance, which we define as $z(t) \equiv \int_{-\infty}^{0} |\psi|^2\,\mathrm{d}x - \int_{0}^{\infty} |\psi|^2\,\mathrm{d}x$ hence reads

$$z(t) = C(t)\sin\phi_0, \tag{3.80}$$

$$\text{where } C(t) = 2\int_0^\infty \mathrm{Im}\left[\psi_R^*(x,t)\psi_L(x,t)\right]\mathrm{d}x, \tag{3.81}$$

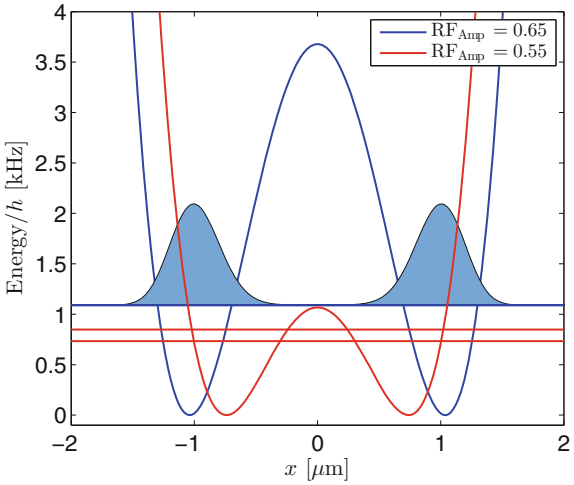

Fig. 3.35 Initial and final double-well potentials. Cut along the splitting direction of the double-well potential prior recombination ($\mathrm{RF_{Amp}} = 0.65$, *blue*) and that used for the non-adiabatic recombiner ($\mathrm{RF_{Amp}} = 0.55$, *red*). The horizontal lines correspond to the chemical potential of the ground and first excited state in each potential (for $\mathrm{RF_{Amp}} = 0.65$, the spacing between the levels is smaller than the width of the line). The density distributions of left and right modes of the $\mathrm{RF_{Amp}} = 0.65$ double well are also represented. When the dressing intensity is abruptly lowered to 0.55, it confers to the atoms a potential energy equal to the height of the barrier (Color figure online)

Im [] denoting the imaginary part. At each time, the population imbalance is proportional to the sine of the initial phase ϕ_0 of the superposition. The contrast $C(t)$ is, for each time, a constant number independent of ϕ_0, and the Cauchy-Schwartz inequality ensures that $|C(t)| \leq 1$. It is interesting to note that this simple result relies only on the symmetry of the potential, that of the initial wavefunction, and the linearity of the Schrödinger equation, without other assumptions on the shape of V [12].

Altogether, the propagation in a symmetric potential for a fixed time t transforms an initial state which has equal populations on both sides of the barrier and a relative phase ϕ_0, into a state whose population imbalance is proportional to the sine of the phase ϕ_0. For $\phi_0 = 0$ and $\phi_0 = \pi$, the wavefunction is even (respectively odd) at all times and no imbalance can appear. Conversely, when $\phi_0 = \pm\pi/2$, the imbalance is maximal $|z| = |C(t)|$.

The contrast $C(t)$ depends on the overlap between $\psi_L(x,t)$ and $\psi_R(x,t)$. It is useful to look at a few particular cases to understand how it can be maximized.

Flat Potential

The simplest situation is that of a flat potential $V(x) = 0$. This describes for example the tof recombiner of Sect. 3.2.1, just after the potential has been switched off. In this case, it is reasonable to neglect interactions during expansion. Evaluating the contrast

with (3.81), we find that, at all times and regardless of the shape of the modes, parity imposes that $C(t) = 0$.

The absence of imbalance does not mean however that the wave packet is symmetric at all times. We have seen in Sect. 3.2.1.2 that ϕ_0 can be deduced from the position of the interference fringes. It has even been shown that the phase could be inferred from the position of the center of mass of the interference pattern with sub-shot noise sensitivity [74].

Square Potential Barrier

The previous result suggests that a potential barrier is needed for an imbalance to build up. A simple textbook case is that of a square potential barrier (see for example Ref. [130]). A wave packet impinging on the barrier is split between a transmitted and a reflected wave. For a plane matter wave of momentum $\hbar k$ impinging on a potential barrier of height V_0 and size d, the the transmission coefficient reads

$$T = \frac{4\epsilon\,(\epsilon - 1)}{4\epsilon\,(\epsilon - 1) + \sin^2\left[\sqrt{(\epsilon - 1)}d/L\right]} \quad \text{if } E > V_0 \tag{3.82}$$

$$T = \frac{4\epsilon\,(1 - \epsilon)}{4\epsilon\,(\epsilon - 1) + \sinh^2\left[\sqrt{(1 - \epsilon)}d/L\right]} \quad \text{if } E < V_0 \tag{3.83}$$

where $\epsilon = V_0/(\hbar^2 k^2/2m)$ is the kinetic energy of the plane wave in units of the barrier height and $L(V_0) = \hbar/\sqrt{2mV_0}$ is the tunneling length associated to the energy V_0. L corresponds to the extension of a wave packet of kinetic energy V_0, and is a typical measure of the penetration depth of an evanescent matter wave into a potential barrier of height V_0 at low energy [130]. For $V_0/h = 1$ kHz, $L = 1.5\,\mu$m gives the typical length scale of a tunneling barrier.

Figure 3.36, left panel, shows how the transmission probability T depends on the energy and the barrier. Two regimes must be distinguished:

- $E > V_0$ corresponds to a situation where classically, the particles would pass over the barrier. Quantum mechanically, the wave packet is partly transmitted and partly reflected. The transmission probability oscillates between $[1 + 4\epsilon\,(\epsilon - 1)]^{-1}$ (dashed line) and 1. Transmission resonances occur whenever the energy of the incoming wave corresponds to the existence of a standing wave in the barrier. To build a 50:50 beam-splitter, one must achieve $T = 0.5$. The lower bound for T imposes the (necessary) condition

$$E \leq \frac{1 + \sqrt{2}}{2} V_0. \tag{3.84}$$

  In other words: a 50:50 beam-splitter can only be achieved in the classical regime ($E > V_0$) if the energy is of the order of the barrier height ($V_0 \leq E \lesssim 1.2 \times V_0$).

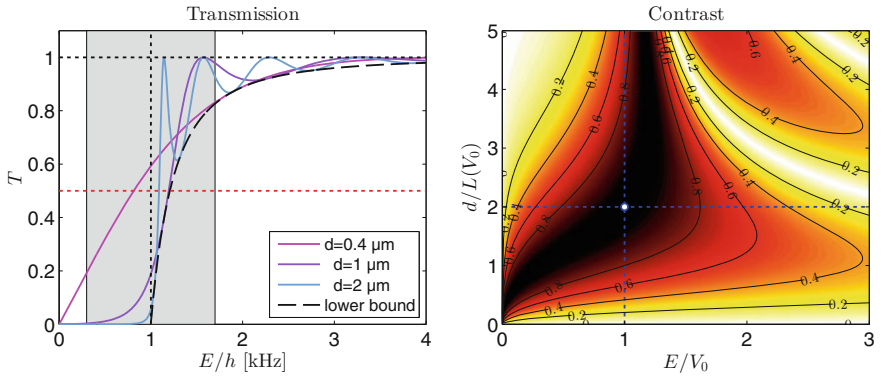

Fig. 3.36 Transmission and contrast of the square beam splitter. *Left* Transmission probability for a plane wave of energy E impinging on a heightheigth $V_0/h = 4$ kHz and width $d = 0.4,\ 1$ or 2 μm. Note the oscillations of T associated with the transmission resonances for $E > V_0$. *Dashed black line* lower bound for T in the classical regime ($E > V_0$). *Gray shaded area* uncertainty on the kinetic energy of the initial state in the double well $\Delta E = \pm\hbar\omega/2$. The *red dotted line* corresponds to the transmission of a semi-reflective mirror $T = 0.5$. *Right* Contrast of a square beam splitter when two plane matter waves of opposite momentum and equal intensities are impinging on it. High contrast can be achieved in the tunneling regime ($E < V_0$) provided the barrier is sufficiently narrow and in the classical regime when $E \approx V_0$. At higher energy, secondary maxima can be observed when a transmission resonance is reached. 100 % contrast is obtained for $E = V_0$ and $d = 2L$ (*white point*) (Color figure online)

- $E < V_0$ corresponds to a situation where the atoms can only tunnel through the barrier. The transmission probability is a monotonically decreasing function of E. $T = 0.5$ can only be achieved as long as

$$d < 2L(V_0). \tag{3.85}$$

  This second condition simply means that in the tunneling regime, the transmission drops when the barrier is much larger than the penetration depth.

Still, $\langle E \rangle \approx V_0$ is not sufficient to achieve a high contrast. The mode-matching condition of Eq. (3.81) shows that in order for C to be large, there must be a good overlap between the reflected and the transmitted wave on each side of the barrier (see Fig. 3.37).

In the case of a square barrier, we can derive an explicit expression for the contrast from the model of Ref. [130]. Assuming that two plane waves of equal intensity and opposite momentum are impinging on the square barrier, the contrast reads

$$C = \frac{4\sqrt{\epsilon\,(\epsilon-1)}\,\sin\left[\sqrt{(\epsilon-1)}d/L\right]}{4\epsilon\,(\epsilon-1)+\sin^2\left[\sqrt{(\epsilon-1)}d/L\right]} \quad \text{if } E > V_0,$$
$$C = \frac{4\sqrt{\epsilon\,(1-\epsilon)}\,\sinh\left[\sqrt{(1-\epsilon)}d/L\right]}{4\epsilon\,(1-\epsilon)+\sinh^2\left[\sqrt{(1-\epsilon)}d/L\right]} \quad \text{if } E < V_0. \tag{3.86}$$

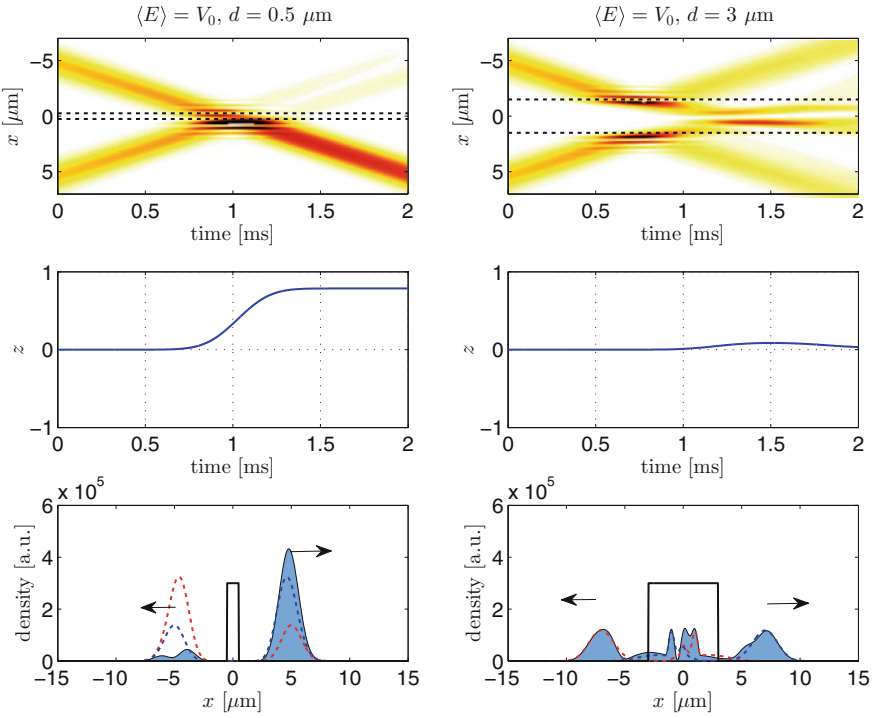

Fig. 3.37 Beam-splitting with a square potential barrier. Simulation of the dynamics of two non-interacting Gaussian wave packets with a phase difference of $\pi/2$ impinging on a square potential barrier for two different barrier widths (*left* $d = 0.5\,\mu$m, *right* $d = 3\,\mu$m). In both case, the height of the barrier is equal to the mean kinetic energy of each wave packet. *Top* Density profile as a function of time. The *dotted lines* denote the edges of the barrier. *Middle* Population imbalance as a function of time. *Bottom* The final wavefunction (filled shapes with outgoing *arrows*) are the result of the constructive or destructive interference between the reflected and transmitted waves originating from the *left* (*blue*) and *right* (*red*) incoming wave packet. When $d = 0.5\,\mu$m, the overlap is good and the final imbalance is significant. When $d = 3\,\mu$m, there is little overlap between the reflected and the transmitted wave and the contrast is low (Color figure online)

The result is displayed in Fig. 3.36, right panel. As expected, the maximal contrast $C = 1$ is achieved when

$$E = V_0, \tag{3.87}$$

$$\text{and} \quad d = 2L(V_0) = \sqrt{\frac{2\hbar^2}{mV_0}}. \tag{3.88}$$

When the kinetic energy is larger than the barrier height, the contrast is approximately equal to V_0/E. In the tunneling regime ($E < V_0$), high contrast can be achieved, provided the barrier is made narrow enough. For a given energy E of the incoming

waves, taking the limit $d \to 0$ imposes that V_0 must diverge like $1/d$ to ensure a contrast of unity. This corresponds to the limit of an ideal δ potential, or, in optics, to an infinitely thin half-silvered mirror.

In practice however, the wave packets are not plane waves, they have instead a finite momentum spread which is non-negligible compared to V_0 (gray shaded area in Fig. 3.35). It means that the atoms tunnel through the barrier as much as they cross it classically. The potential barrier in our double wells also has a finite extension, which is always comparable to the width of wave packets (see Fig. 3.35).

Furthermore, in our rf dressed double wells, the well spacing and the barrier height are not independent[21]: V_0 increases roughly like d^4. From simulations of the double wells, we find that it should be possible to fulfill $d < 2L$ up to $\mathrm{RF}_{\mathrm{Amp}} = 0.6$. Interestingly, the best contrast was precisely achieved in the double well $\mathrm{RF}_{\mathrm{Amp}} = 0.55$, for which simulations predict that the barrier height is equal to the potential energy of the clouds (see Fig. 3.35).

3.6.2.3 Dynamics of an Interacting Condensate in the Non-adiabatic Recombiner

1D GPE Simulations

To understand the complex dynamics of the BEC in the double well during the recombination stage, we simulate it by solving the 1D GPE in the $\mathrm{RF}_{\mathrm{Amp}} = 0.55$ potential (see Fig. 3.38). It exhibits a complex density pattern arising from the multiple reflections and transmissions of the matter wave on the potential barrier, the outer edges of the trap as well as from the interference between the condensates. Solving the classical equations of motion for a point-like particle initially at the same position as the center of mass of one of the BEC shows anharmonic oscillations in each single well at the period $T_{\mathrm{anh}} \approx 1.2$ ms ($\nu_{\mathrm{anh}} \approx 800$ Hz, note that the oscillating pattern in the GPE simulations has a higher frequency than the classical oscillation).

For an initial phase of $\pi/2$, imbalance seems to build up after an integer number of center-of-mass oscillations. The final imbalance can be maximized by separating the clouds when they are at a classical turning point, i.e. when the distance between the clouds is maximal. Indeed, the evolution of the final imbalance shows a sequence of bumps and dips spaced by roughly 1 ms. How many center-of-mass oscillations are necessary to reach the maximum imbalance is not obvious from the GPE simulations, but in practice, the structure we observed experimentally (see Fig. 3.34) suggests that already after a few ms, unknown relaxation mechanisms completely damp the coherent evolution.

[21] At least, they cannot be tuned independently with only one control parameter (the dressing amplitude). It has not yet been checked whether adding a new degree of freedom, such as the RF dressing detuning, could allow tuning d and V_0 independently.

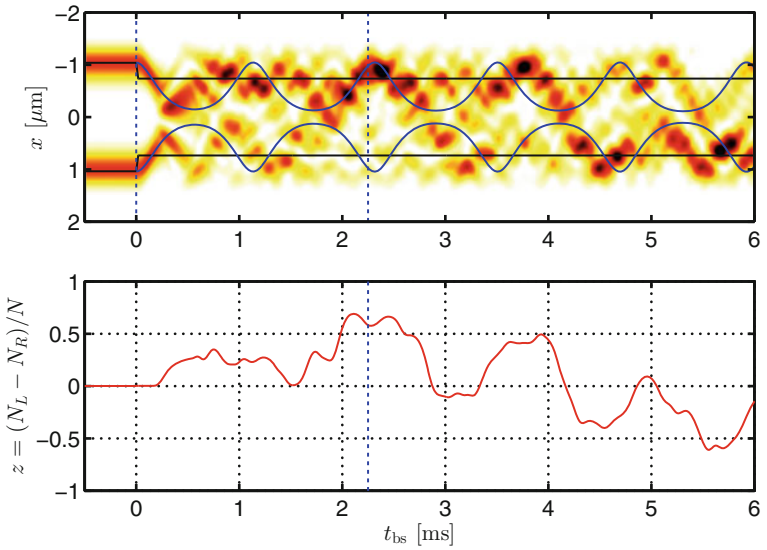

Fig. 3.38 Dynamics of the BEC in the recombiner. Transverse density profile of the BEC in the recombiner (*top*, 1D GPE simulation. $\phi_0 = \pi/2$) and corresponding population imbalance (*bottom*). At $t = 0$, the splitting is abruptly reduced. An oscillating feature emerges in the complex dynamics of the density pattern. It roughly corresponds to the center-of-mass oscillations of the atoms in each well. At regular intervals, imbalance builds up. *Vertical dashed line* time at which the barrier is raised in the normal recombining procedure in order to separate the atoms for counting ($t_{\rm BS} = 2.25$ ms). It corresponds to the turning point of the second oscillation period

Comparison to Experiment

To validate the simulations of the BEC dynamics in the recombiner, we monitored the evolution of the wavefunction for seven different initial phases prepared using the phase shifter (see Sect. 3.5.1). For each phase, we abruptly reduced the splitting as explained before and let the condensates evolve for a variable time $t_{\rm BS}$. Eventually, instead of ramping up the barrier to separate the clouds, we switched off the potential and imaged the atoms after tof. Due to the high transverse confinement, the transverse density distribution after 46 ms expansion is almost homothetic to the momentum distribution of the atoms in the trap. This gives us access to the momentum distribution at any time during the recombiner sequence (Fig. 3.39).

Figure 3.40 shows the comparison between the measured transverse density profiles in expansion (top) and the result of the GPE simulations (the computed momentum distributions were rescaled by a factor t/m, where $t = 46$ ms is the tof and m is the mass of one ^{87}Rb atom, to be compared to the experimental data). Each experimental profile is the result of the average over 3 to 5 experimental realizations. The results of the simulations were convoluted with a 10 μm rms Gaussian function to account for the finite imaging resolution.

For all phases, the simulations reproduce the coarse features of the measured profiles. The beating patterns we observed are a direct proof of the coherence of the

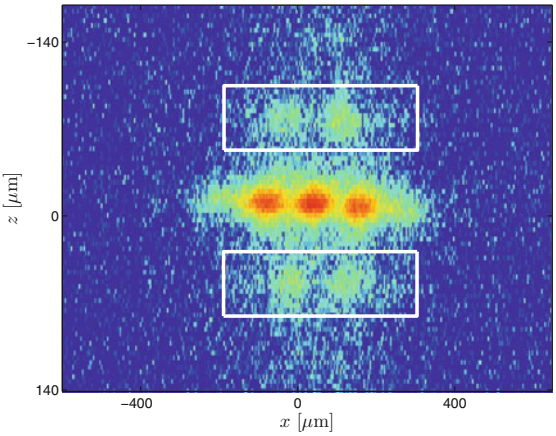

Fig. 3.39 Hints of longitudinal excitations appearing after the fast recombination. Fluorescence picture after expansion of a BEC having evolved in the non-adiabatic recombiner for ∼4 ms. Symmetric pattern appear in the longitudinal (along (z)) density profile, showing hints of the excitation of high-energy momentum modes (*white boxes*). The spacing between these symmetric features and the *center* of the main cloud indicates a kinetic energy in longitudinal direction comparable to the transverse energy scale. The relaxation of the transverse excitations created during the fast recombination into longitudinal modes might be a reason for the fast decay of the recombiner contrast. Note that a logarithmic colormap has been chosen to enhance the visibility of the longitudinal features

evolution in the recombiner. The contrast of the experimental data is systematically lower than in the simulations, probably indicating beyond mean-field effects. At long times ($t_{\mathrm{BS}} \gtrsim 2$ ms), we observe a blurring of the density pattern, resembling the decay of coherence we observed in the evolution of a superposition of vibrational states [16]. We conjecture that this blurring is due to the same relaxation mechanism as the one responsible for the damping of the Josephson oscillations (see Fig. 3.31) and the one suspected from the evolution of z in the non-adiabatic recombiner (Fig. 3.34).

Interestingly, for the longest times ($t_{\mathrm{BS}} \gtrsim 5$ ms), we observed features in the longitudinal momentum distribution reminiscent of the highly excited axial modes we studied in Ref. [76] (Fig. 3.39). It suggests that the damping is connected to the decay of the transverse excitations into longitudinal modes. Such damping mechanisms are currently being investigated.

3.6.3 Comparison of the Two Recombiners

We have implemented two different schemes to achieve the phase-sensitive recombination of a trapped Bose-Einstein condensate. Both rely on a controlled modification of the confining potential. In the first case, it aims at being adiabatic with respect to the transverse motion of the wavefunction while enabling controlled tunneling between the two wells, in a similar fashion as a fiber coupler in laser optics. In the

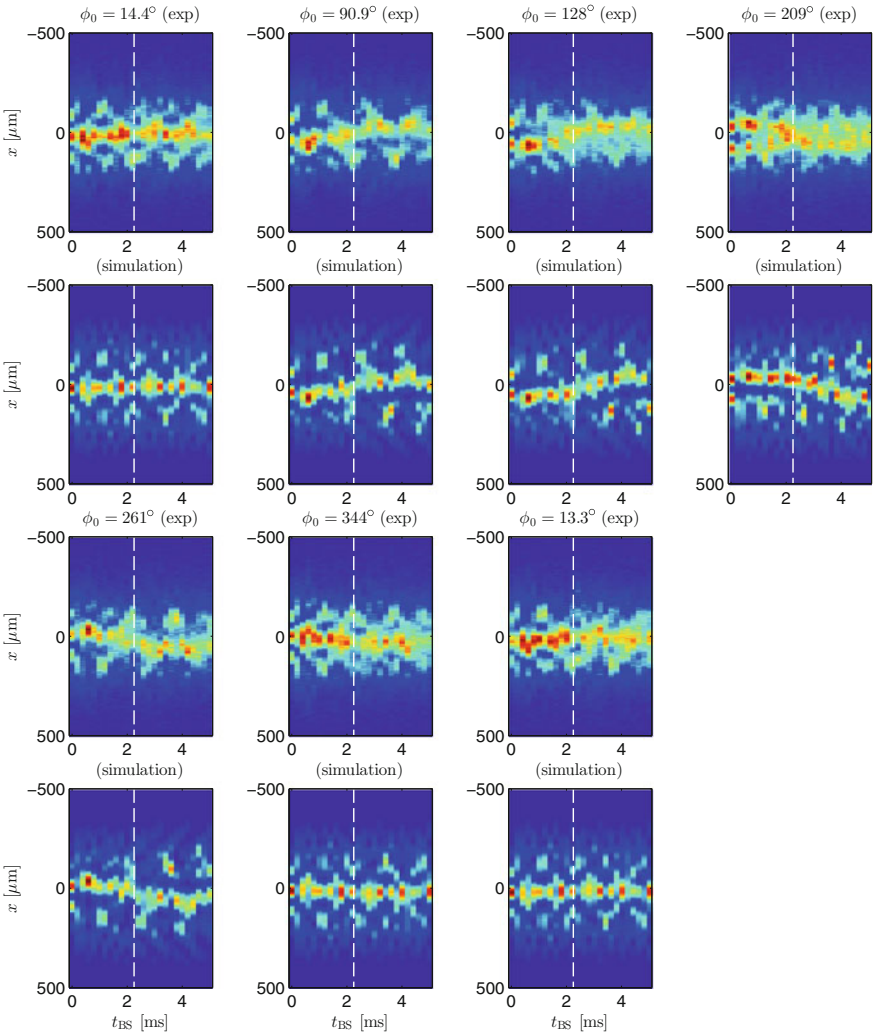

Fig. 3.40 Dynamics of the condensates in the recombiner monitored in tof. Time-evolution of the density profile in expansion ($t = 46$ ms tof) during the non-adiabatic recombination, for seven different initial phases. *Top* experimental profiles, averaged over 3–5 independent realizations. *Bottom* Simulated momentum distributions (1D GPE), rescaled by t/m and convolved with a 10 μm rms Gaussian function to account for finite imaging resolution. The *vertical dashed line* at $t_{BS} = 2.25\,\mu$m indicates the time at which the barrier is normally ramped up to separate and count the atoms. At short times, the 1D transverse mean-field simulations correctly reproduce the observed patterns. After a few ms, the measured profiles appear blurred, conversely to the simulated ones

second case, the manipulation of the potential was deliberately non-adiabatic, in order to launch the atoms onto the semi-reflective potential barrier, as in an optical half-silvered mirror.

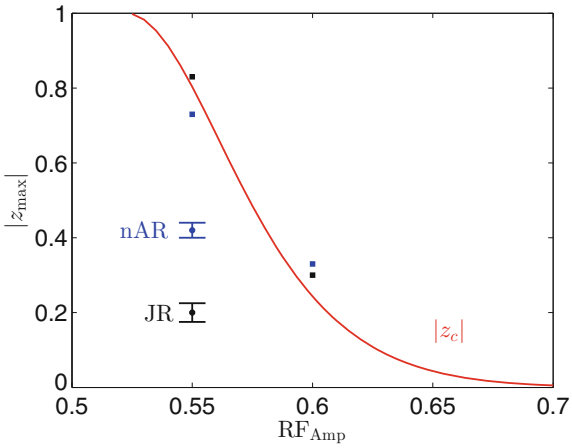

Fig. 3.41 Contrast of the BEC recombiners Maximum achievable imbalance at the output of the recombiner as a function of the dressing amplitude (*black* Josephson recombiner, *blue* non-adiabatic recombiner, see next section). *Squares* best result of the 1D GPE simulations (see Fig. 3.42). *Circles* experimentally measured contrast. *Red line* critical imbalance (self-trapping threshold) predicted by the 2MM (Color figure online)

The difficulty in disentangling the timescales associated to the tunneling dynamics from that of the motion of the wavefunction sheds light on the link between tunneling, or superfluid oscillations, and the motion of the wavefunction in a tunable bosonic Josephson junction in a double well, as already pointed out in Ref. [131].

Both recombiners are affected by atomic interactions. Interactions are responsible for the anharmonicity of the response $z(\phi)$ of the recombiners. In Sect. 3.7.2, we will show that the anharmonicity of $z(\phi_0)$, defined as the ratio of the amplitude of the two first harmonics $\eta \equiv |a_2/a_1|$, is twice larger for the Josephson recombiner ($\eta \approx 0.26$) than for the non-adiabatic recombiner ($\eta \approx 0.12$). This behaviour is only partially captured by our 1D GPE simulations which predict $\eta = 0.28$ (Josephson) and $\eta = 0.23$ (non-adiabatic) respectively.[22] One possible explanation for the fact that the non-adiabatic recombiner seems to be less affected by interactions is that the wavefunction is stretched during the non-adiabatic motion, implying a lower mean-field energy.

The anharmonic shape of the recombiner response shows a steeper slope around $\phi_0 = \pi$. It is not clear yet whether this feature might yield enhanced interferometric sensitivity to small deviations from $\phi_0 = \pi$, or whether the loss of amplitude of $z(\phi_0)$ caused by interactions dominates. Exploiting interactions to improve the sensitivity close to $\phi_0 = \pi$ has been proposed in Ref. [128].

It is difficult to make any general statement about the best contrast achievable with each scheme, because it depends on the details of the control sequence as well as on the role of interactions. We believe that the contrast—defined as the maximal amplitude of $z(\phi)$—of the Josephson recombiner is ultimately limited by the onset of self-trapping (see Fig. 3.41), which suggests that we should work in the Rabi regime. However, this condition is difficult to meet in our double wells, as it requires going down to a very weak splitting, which in turn implies slow ramps.

[22] We found that the simulated recombiner response $z(\phi_0)$ was better described by three harmonic. In this case, the anharmonicity was defined $\eta = (|a_2| + |a_3|)/a_1$.

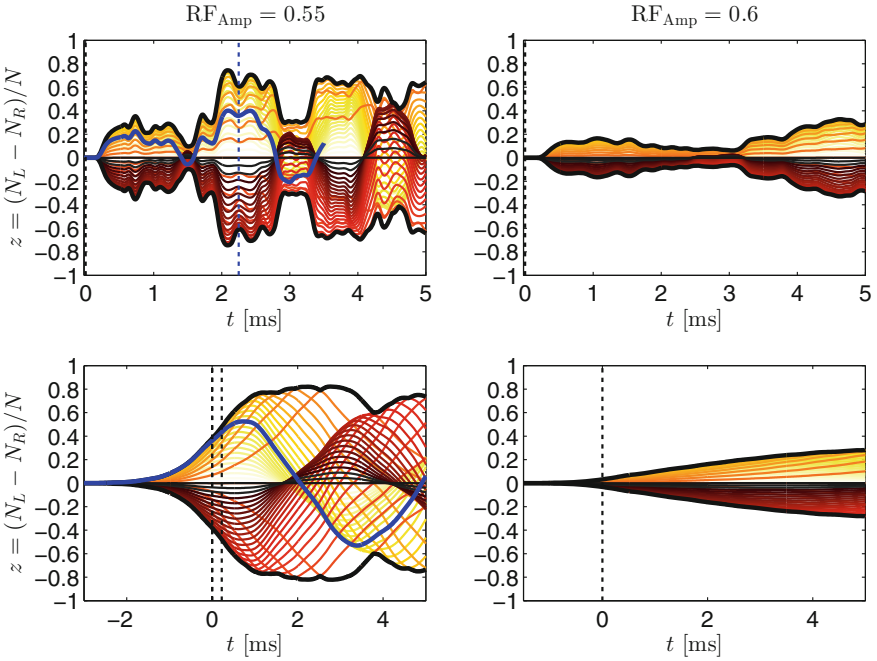

Fig. 3.42 Comparison of the two recombiners. Evolution of the population imbalance for 50 different initial phases ϕ_0 during the non-adiabatic recombiner sequence (*top*) and the Josephson recombiner sequence (*bottom*) in two different double wells (*left* $\mathrm{RF}_{\mathrm{Amp}} = 0.55$, for which we obtained the best result; *right* less coupled $\mathrm{RF}_{\mathrm{Amp}} = 0.6$ double well). Note that the final separation was not simulated. The origin of the time axis corresponds to the end of the recombination ramp (*vertical dashed line*). The values of ϕ_0 are evenly spaced between 0 (*pale yellow*) and 2π (*dark red*). The *thick black lines*, corresponding to the time-dependent maximum of $|z|$ over all phases, indicates the recombiner contrast. The Josephson recombiner enables up to 85 % contrast for $\mathrm{RF}_{\mathrm{Amp}} = 0.55$, and up to 20 % for $\mathrm{RF}_{\mathrm{Amp}} = 0.6$. Note how, in the Josephson recombiner, $z(t)$ oscillates at a rate which is all the more slow than ϕ_0 is close to π, explaining the anharmonicity of the response $z(\phi_0)$. With the non-adiabatic recombiner, up to 75 % contrast are reached for $\mathrm{RF}_{\mathrm{Amp}} = 0.55$, and up to 30 % for $\mathrm{RF}_{\mathrm{Amp}} = 0.6$. The *vertical blue dashed line* at $t = 2.25$ ms shows the duration for which the best contrast of 42 % was observed. In any case, it shows that for each beam-splitter duration, the value ϕ_0 maximizing the final imbalance is different, underlining the difficulty of optimizing the recombination procedure (Color figure online)

This constraint has been lifted in the non-adiabatic recombiner. Here, it is not clear what ultimately limits the contrast, but the finite position and momentum spread of the wave packets, which have to be compared to the size and the energy of the barrier, are believed to hinder this scheme to approach the performance of an ideal, infinitely thin δ-potential barrier.

In any case, it seems that the most stringent limitation to the contrast comes from relaxation mechanisms which are not captured by our simple 1D mean-field models. In principle, our 1D GPE simulations indicate similar performances for both schemes, with contrasts up to 75–80 % (see Fig. 3.42), much higher than what we observed:

$C \approx 20\,\%$ (Josephson recombiner) and $C \approx 42\,\%$ (non-adiabatic recombiner) (see Sect. 3.7.2.1). Our data indicate that both schemes are subjected to a strong damping of $z(t_{\mathrm{BS}})$ over a time scale of a few ms. We suspect these effects to arise from the coupling to the other spatial directions as well as effects beyond mean-field. Understanding these relaxation mechanisms is a necessary step to succeed in the robust implementation of such recombination schemes.

Alternatively, it also suggests that a fast recombiner operation is necessary. The slightly lower total duration of the non-adiabatic procedure (3.3 ms) compared to the adiabatic procedure (4.3 ms) might be a hint why it achieves a better performance. Further reducing the duration of the recombination could be achieved by means of optimal-control of the motion of the BEC [16].

3.7 Interferometer Signal

After having characterized independently each stage of the interferometric sequence, we combined them as depicted in Fig. 3.2 and recorded the output signal using either the Josephson recombiner or the non-adiabatic recombiner.[23] In Sect. 3.7.1, we describe the measured interference fringes, which we then compare to a theoretical model (Sect. 3.7.2). In particular, we show in Sect. 3.7.2.1 how to use the interferometric signal to infer the contrast of each recombiner. Eventually, we evaluate the sensitivity of our interferometer and discuss the observed decay of coherence (Sect. 3.7.3).

3.7.1 Mach-Zehnder Fringes

After having adjusted the phase shifter tilt to $\epsilon/h \approx 350$ Hz, we recorded the normalized imbalance $z = (N_L - N_R)/(N_L + N_R)$ at the output of the recombiner, as a function of the phase accumulation time t_ϕ. This is similar to scanning the phase shift of an optical interferometer by varying the difference of lengths between both arms. For each value of t_ϕ, we repeated the whole sequence up to 18 times (with each of the two recombiners) in order to accumulate more statistics. Given our experimental cycle time of 37 s, a complete fringe set such as that of Fig. 3.43 involves about 20 hours of data taking. Achieving the according degree of stability of the experiment has been the result of many improvements carried on over the last years.

The imbalance for each of the $\sim 2 \times 2000$ individual realizations is displayed as a grey dot on Fig. 3.43 (Josephson recombiner) and Fig. 3.44 (non-adiabatic recombiner). As expected, a periodic fringe structure is observed, similar to the modulation of intensity difference between both output ports of an optical Mach-Zehnder

[23] In the following, we will refer to them as "*trapped* recombiners", in contrast to the time-of-flight recombiner.

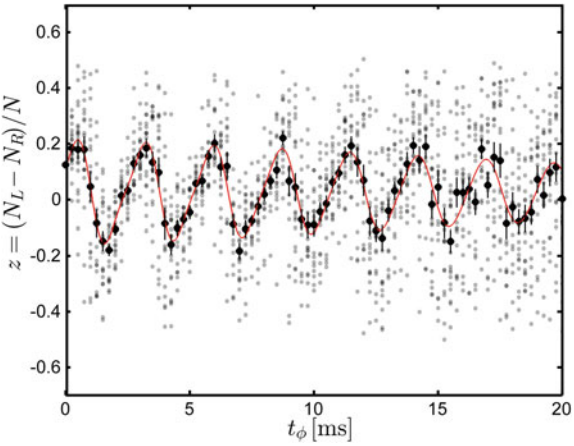

Fig. 3.43 Mach-Zehnder interferometric fringes obtained with the Josephson recombiner. Normalized population imbalance z as a function of the phase accumulation time t_ϕ obtained using the Josephson recombiner. It exhibits interference fringes which are anharmonic under the effect of interactions in the recombiner and a damping caused by phase diffusion. *Grey dots* imbalance of individual experimental realizations. *Black dots* ensemble average $\langle z \rangle$ at each phase accumulation time (the error bars denote $\pm$ one standard error of the mean). *Red* fit with the theoretical model (Color figure online)

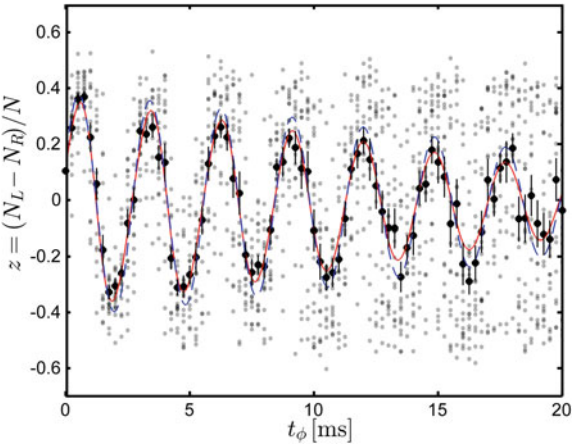

Fig. 3.44 Mach-Zehnder interferometric fringes obtained with the non-adiabatic recombiner. Normalized population imbalance z as a function of the phase accumulation time t_ϕ obtained using the non-adiabatic recombiner (note that the scale is the same as in Fig. 3.43 for both axes). The contrast of the fringes is higher and the anharmonicity is less obvious than with the Josephson recombiner. *Grey dots* imbalance of individual experimental realizations. *Black dots* ensemble average $\langle z \rangle$ at each phase accumulation time (the error bars denote $\pm$ one standard error of the mean). *Red* fit with the theoretical model of Eq. (3.93). *Dashed blue* fit with the same model, using values of the parameters measured independently or self-consistently extracted from the data, with only c and ϕ_0 as free parameters (Color figure online)

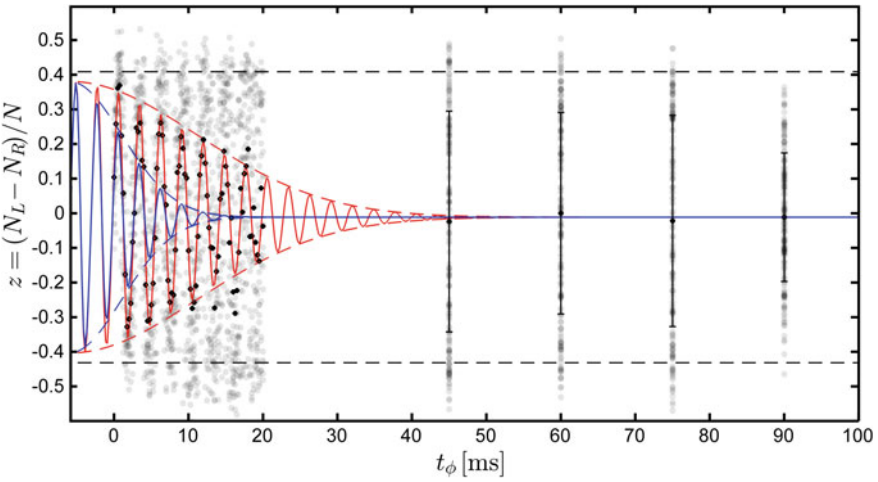

Fig. 3.45 Dephasing and the onset of relaxation of the Mach-Zehnder fringes. Normalized population imbalance z as a function of the phase accumulation time t_ϕ obtained with the non-adiabatic recombiner (same data as Fig. 3.44 at short times). The spread of the *grey dots* (imbalance of individual realizations) shows that while z is completely random after ∼40 ms under the effect of phase diffusion, high contrast can still be obtained on individual realizations after up to $t_{\rm QE} \approx 70$ ms. At $t_\phi = 90$ ms, we see first hints of a drop of contrast, probably due to relaxation mechanisms. *Black points* ensemble average for a given phase accumulation time. For $t_\phi \geq 45$ ms, the error bars indicate $\pm$ one standard deviation. *Red* fit with the model for phase diffusion (*dahsed red* envelope showing the Gaussian decay of coherence). *Blue* prediction for $\langle z \rangle$ in absence of squeezing. *Dashed black line* $\pm$ contrast of the recombiner $C \approx 0.42$, extracted from the full distribution of z. Note that the time axis starts at $t_i = -6$ ms

interferometer. As the phase accumulation time is scanned, the structure gets increasingly blurred, while its envelope remains essentially constant ($z \approx \pm 0.45$) for both recombiners.

Computing for each phase accumulation time the ensemble average $\langle z \rangle$ (t_ϕ) and the standard deviation Δz, we observe that the mean imbalance undergoes damped oscillations over a timescale of approximately 20 ms, while the fluctuations of z increase. After ∼40 ms (see Fig. 3.45), the average imbalance is essentially equal to zero, while $\Delta z \approx 0.3$ (for the non-adiabatic recombiner) and an imbalance larger than 0.4 is observed on more than 5 % of the individual realizations.

This interferometric signal is a direct illustration of the dynamics of the relative phase between the two halves of the condensate: while the deterministic phase accumulation is responsible for the oscillations of $\langle z \rangle$ at the frequency ϵ/h, phase diffusion causes the spread of z to increase, until the phase is completely random, yielding a random output imbalance with vanishing average.

To be more quantitative, we make use of the results of the previous sections to derive a model of the interferometric signal.

3.7.2 Model for the Interferometric Signal

We have seen in Sect. 3.5 that the distribution of the relative phase is subjected to a linear drive (phase accumulation) at rate ϵ together with a linear dispersion caused by interactions, meaning that the phase spread grows linearly in time at the phase diffusion rate $R = \tau_{\mathrm{coh}}^{-1}$. We assume that at all times, the phase distribution is Gaussian with time-dependent mean and variance given by (see Eqs. (3.39) and (3.57))

$$\langle\phi\rangle\left(t_\phi\right) = \phi_0 + \epsilon\left(t_\phi - t_i\right)/\hbar, \tag{3.89}$$

$$\Delta\phi^2\left(t_\phi\right) = \Delta\phi_0^2 + R^2(t_\phi - t_i)^2. \tag{3.90}$$

The offset time t_i accounts for the fact that phase diffusion and phase accumulation already start during the time needed to tilt and level the double well (see Sect. 3.5.3).

We model the action of the recombiner, taking into account the effect of interactions, by writing the output imbalance as the Fourier series (see Eq. (3.77))

$$z(\phi) = \sum_{n=1}^{M} a_n \sin(n\phi) = a_1 \sin(\phi) + a_2 \sin(2\phi) + \cdots, \tag{3.91}$$

where M is the number of harmonics. After integration over the Gaussian phase distribution, we find that the average imbalance at the output of the recombiner reads

$$\langle z\rangle\left(t_\phi\right) = \sum_{n=1}^{M} a_n e^{-n^2\Delta\phi_0^2/2}\, e^{-n^2\left(t_\phi - t_i\right)^2/2\tau_{\mathrm{coh}}^2} \sin\left[n\left(\epsilon\left(t_\phi - t_i\right)/\hbar + \phi_0\right)\right]. \tag{3.92}$$

The mean interferometric signal $\langle z\rangle(t_\phi)$ is a sum of harmonics. The contribution of each harmonic to the total signal consists of a sine term oscillating at a multiple of the phase accumulation rate ϵ/h (Mach-Zehnder fringes) and a Gaussian damping associated to the rms time τ_{coh}/n. Note that in this context, the word *fringe* refers to the oscillations of $\langle z\rangle$ as a function of the phase accumulation time and not to the interference pattern which appears in the density profile after tof recombination in each single realization (see for example Fig. 3.3).

For a weak non-linearity, we expect the weight of the harmonics to rapidly decrease with n. Moreover, the contribution of the nth harmonic drops within the time τ_{coh}/n. We checked by fitting the fringes with up to 5 harmonics that only the contribution of the two lowest harmonics is statistically significant within our measurement uncertainty.

The Gaussian damping of the Mach-Zehnder interference fringes is a direct illustration of the Gaussian decay of the coherence factor due to phase diffusion (see Eq. (3.52)). It is the consequence of ensemble averaging over rising fluctuations of the phase when t_ϕ is increased. It must be distinguished from the damping of the Josephson oscillations observed by scanning the evolution time t_{BS} in the recombiner for a constant input phase (see Fig. 3.31), although both effects might be linked.

Table 3.5 Parameters of the model for the interferometric signal

	Josephson BS	Non-adiabatic BS	Indep. meas.
A_1	0.18 ± 0.02	0.38 ± 0.02	
A_2	-0.04 ± 0.02	-0.05 ± 0.03	
ϕ_0	-0.32 ± 0.19 rad	-0.16 ± 0.16 rad	
c	0.03 ± 0.01	-0.01 ± 0.01	
τ_{coh}	25 ± 7 ms	17.1 ± 2.2 ms	20 ± 3 ms
ϵ	363 ± 3 Hz	349 ± 2 Hz	349 ± 2 Hz
$\Delta\phi_0$	—		160 ± 20 mrad
a_1	0.18 ± 0.02	0.39 ± 0.03	
a_2	-0.05 ± 0.02	-0.05 ± 0.03	
$\eta = \lvert a_1/a_2 \rvert$	0.26 ± 0.13	0.12 ± 0.09	

Values of the parameters fitted to the interferometric signal obtained with the Josephson recombiner (left column) or the non-adiabatic recombiner (central column) with the model of Eq. (3.92). The third column recapitulates the values of the coherence time, energy difference and initial phase spread measured with the tof recombination method. The uncertainties indicate either the 95 % confidence of the fit or 2 σ

The prefactor $a_n e^{-n^2\Delta\phi_0^2/2} e^{-n^2\left(t_\phi - t_i\right)^2/2\tau_{\text{coh}}^2}$ represents the amplitude of each harmonic in the Mach-Zehnder signal. Compared to the "bare" visibility a_n, which is intrinsic to the recombiner, the amplitude of the fringes after ensemble averaging is reduced by (a) the fluctuations of the phase already present at $t = t_i$ (b) the increase in phase spread due to phase diffusion. For this reason, we always slightly underestimate the contrast of the recombiner when we look only at the mean output imbalance $\langle z \rangle$ for input states which—necessarily—have a finite phase uncertainty. We will show in next section how the "true" contrast of the recombiner can be inferred from the statistical distribution of z.

Table 3.5 summarizes the result of fitting the two-harmonic model

$$\begin{aligned}\langle z \rangle \left(t_\phi\right) = {} & A_1 e^{-\left(t_\phi - t_i\right)^2/2\tau_{\text{coh}}^2} \sin\left[\epsilon\left(t_\phi - t_i\right)/\hbar + \phi_0\right] \\ & + A_2 e^{-2\left(t_\phi - t_i\right)^2/\tau_{\text{coh}}^2} \sin\left[2\epsilon\left(t_\phi - t_i\right)/\hbar + 2\phi_0\right] + c \end{aligned} \tag{3.93}$$

to the interferometric signal obtained with either the Josephson recombiner or the non-adiabatic recombiner. In both cases, the time offset t_i was set to -6 ms. The parameters $a_{1,2}$ and $\Delta\phi_0^2$ in Eq. (3.92) are collinear and were merged into the two fit parameters

$$A_n = a_n e^{-n^2\Delta\phi_0^2/2}, \tag{3.94}$$

($n = 1, 2$). c is a constant offset accounting for imperfect balancing of the double well.

We found that the values for ϵ and τ_{coh} obtained from the fit to the Mach-Zehnder fringes were consistent with that measured independently using the tof recombiner.[24] The amplitudes $a_{1,2}$, which we suppose to be intrinsic to the recombiner, could be inferred from the initial phase spread measured independently with the tof recombiner (see Sect. 3.4.3.2). They were found to be very close to $A_{1,2}$ because of the high initial coherence. The fits confirmed that the Josephson recombiner ($\eta = |a_2/a_1| \approx 0.26$) is more strongly anharmonic than the non-adiabatic recombiner ($\eta \approx 0.12$).

We found that the damping of the Mach-Zehnder interference fringes was correctly described by a Gaussian decay[25] and that the corresponding coherence time was consistent with that extracted from the phase diffusion data in tof (see Sect. 3.5.3).

For consistency, we re-fitted the data obtained with the non-adiabatic recombiner with the model of Eq. (3.93), using the values of ϵ and τ_{coh} measured with the tof recombiner. We also fixed the value of A_1 using the initial phase spread $\Delta\phi_0$ measured with the tof recombiner and the contrast $C = 0.42$ extracted from the distribution of imbalance (see next section), and set A_2 to zero, leaving only c and ϕ_0 as free fit parameters. The good agreement of the model with the measurement confirms that the data taken with the non-adiabatic recombiner is consistent with that based on the tof recombiner.

Figure 3.45 displays data obtained with the non-adiabatic recombiner over longer phase accumulation times (up to 90 ms). It shows that while dephasing is responsible for the complete scrambling of the fringes within 40 ms, the noise envelope only starts to shrink after ∼90 ms. This decay is consistent with the onset of the loss of contrast observed on individual interference patterns with the tof recombiner (see Fig. 3.23).

As mentionned in Sect. 3.5.3, the fact that we measured a phase diffusion rate compatible with the measured amount of number squeezing shows that the use of a number-squeezed state in our interferometer more than doubles its interrogation time. The blue curve in Fig. 3.45 shows the signal expected in the absence of number squeezing. In this case, coherence would be already lost after ∼15 ms.

3.7.2.1 How to Extract the Recombiner Contrast from the Number Distribution

Model

The difficulty in estimating the contrast of the trapped recombiners stems from the fact that we must disentangle the reduction of fringe visibility caused by phase diffusion from that intrinsically present due to the finite contrast of the recombiners.

[24] We attribute the discrepancy between the value of ϵ measured with the Josephson recombiner and that measured with the two other methods to the fact that this measurement was carried out about one week later and that ϵ had not been readjusted in the meanwhile.

[25] In fact, to discriminate between a Gaussian damping model and, for example, an exponential decay, we would need to measure $\langle z \rangle$ at very short times, which is not possible due to the finite tilting and levelling time of the double well.

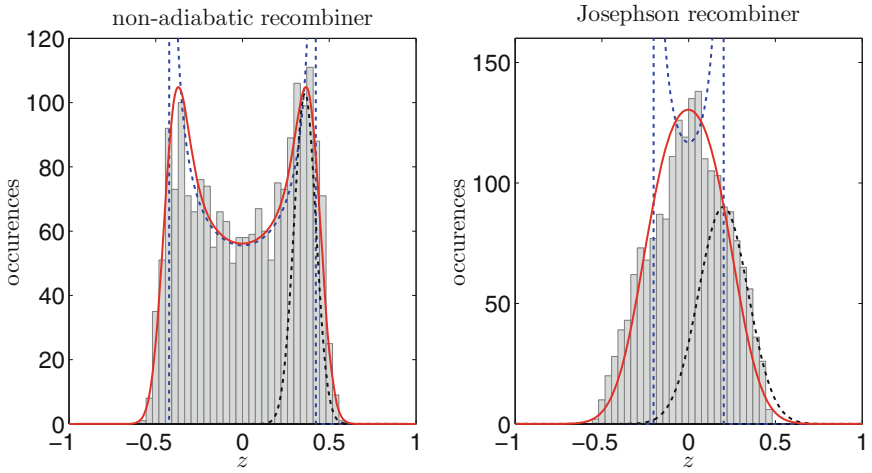

Fig. 3.46 Distribution of the population imbalance. Histogram of the single-run population imbalance z obtained at all times with the non-adiabatic (*left*) and the Josephson recombiner (*grey dots* of Figs. 3.43 and 3.45, excepted $t_\phi > 80$ ms). The histogram of the non-adiabatic recombiner data exhibits the characteristic double structure expected from sampling the sine of a uniformly distributed phase, while that of the Josephson recombiner data is single-peaked. The contrast and the amplitude noise of the recombiners are estimated from convolving the probability distribution function given in Eq. (3.96) (*dotted blue*) with a Gaussian noise (*dotted black*). The *red line* shows the resulting distribution fitted to the data

The ensemble-averaged imbalance $\langle z \rangle(t_\phi)$ alone does not allow inferring precisely the contrast of the recombiners.

Instead, we can estimate it from the full distribution of z by resorting to a method used in atom interferometry [132] to disentangle phase and amplitude noise (see in particular the comprehensive discussion on the robustness of the method in Ref. [133]). We observe that even at long phase accumulation times, high imbalance can be achieved in single realizations, and that up to $\sim$70 ms, the noise envelope is almost constant. We make the assumption that during the phase accumulation stage, ϕ uniformly samples the interval $[0, 2\pi]$ under the combined effect of deterministic phase accumulation and phase diffusion. It means that by "histogrammizing" the outcome of all individual realizations, binning over all times,[26] we can reconstruct the probability distribution function of the output imbalance z corresponding to a uniform input phase.

Figure 3.46 shows the corresponding histograms obtained with the non-adiabatic recombiner (left) and the Josephson recombiner (right). The variance of the distribution of z is connected to the contrast of the recombiners. By integrating Eq. (3.91) over a uniformly distributed phase, we get

[26] Restricting ourselves to the data at $t_\phi > 40$ ms, where the phase is completely random, yields essentially the same distribution. We decided to integrate over all times to accumulate more statistics.

$$\Delta z^2 = \frac{1}{2}\sum_{n=1}^{M} a_n^2. \tag{3.95}$$

Neglecting the anharmonicity of the recombiner ($a_n = 0$ for $n > 1$), we simply obtain $C_{\text{var}} \approx a_1 = 0.43$ for the non-adiabatic recombiner and 0.31 for the Josephson recombiner. However, this is assuming no noise on z (*amplitude noise*), in which case the output imbalance is expected to be distributed according to

$$\begin{aligned} p(z) &= \frac{1}{\pi}\frac{1}{\sqrt{z^2 - C^2}} \quad \text{if } |z| < C, \\ &= 0 \quad \text{elsewhere}, \end{aligned} \tag{3.96}$$

(pale blue dotted lines in Fig. 3.46). $p(z)$ has a characteristic double-peaked shape due to the fact that the probability density of z diverges at the two turning points $z = \pm C$. In practice, these sharp peaks are broadened by amplitude noise coming for example from technical noise of the recombiner as well as detection noise. We assumed that the noise is independent of the value of z and took it into account by convolving p with a normally distributed Gaussian noise of constant variance σ_d^2 (dashed black curve) to fit the two histograms in Fig. 3.46 (red curves).

Non-adiabatic Recombiner

The distribution of z from the non-adiabatic recombiner is well described by our model, yielding $C = 0.42$ and $\sigma_d = 0.07$.

The convolution with a Gaussian noise independent from z is a simplistic model for the amplitude noise. In fact, feeding an interaction-free, noiseless beam-splitter of finite contrast C with a N-atom coherent state of phase ϕ, should yield an output distribution of z with mean $\langle z \rangle(\phi) = C \sin\phi$ and variance

$$\Delta z^2(\phi) = \frac{1 - C^2\cos^2\phi}{N}. \tag{3.97}$$

$\Delta z^2(\phi)$ simply represents the beam-splitter shot noise at a given finite atom number and reflection/transmission ratio. Even in absence of technical noise, the variance of z depends on $\langle z \rangle$. At the points of steepest slope ($\phi = 0$ or π), we find that $\Delta z^2 = 1/N$ regardless of the contrast, while at the turning points ($\phi = \pm\pi/2$), $\Delta z^2 = (1 - C^2)/N$. With $C = 0.42$ and $N = 1200$ atoms, the beam-splitter shot noise varies between $\Delta z = 0.29$ rad ($\phi = 0$) and $\Delta z = 0.22$ rad ($\phi = \pi/2$). The shot noise is much smaller than the noise extracted by the fit,[27] which seems to

[27] Uncorrelated errors add up quadratically.

imply that we are currently limited by technical noise in the beam-splitter operation and read out. Since we know that our imaging system is sensitive enough to detect sub-shot noise fluctuations, we assume that the extra noise comes mostly from the violent manipulation of the cloud during the recombiner procedure.

Josephson Recombiner

The distribution of z for the Josephson recombiner on the other hand does not exhibit a double-peaked structure, which makes it difficult to fit with our model. Imposing $C \approx 0.2$, we find rough agreement with the measured distribution for $\sigma_d = 0.15$, but the result of the fit is not robust with respect to the initial guess for C. We attribute the failure of our fit model to (a) the low contrast of the Josephson recombiner fringes, (b) their higher anharmonicity. We also compared the measured distribution to artificial distributions of z generated by sampling the anharmonic recombiner function (Eq. (3.91)) with a uniform random phase and adding a random Gaussian noise to the result. We found a strong correlation between a_1 and σ_d, indicating that it is difficult to distinguish between a low recombiner contrast and a high amplitude noise. Yet, the comparison to the experimental data indicates that $C \approx a_1 \lesssim 0.2$ and $\sigma_d \gtrsim 0.15$.

Why the non-adiabatic recombiner yields a higher visibility than the Josephson recombiner is still to be understood. We find it surprising that apparently, the reduced contrast of the Josephson recombiner goes together with a stronger amplitude noise, so that the envelope of the fringes in Figs. 3.43 and 3.44 are of similar amplitude ($z \approx \pm 0.45$). These issues, as well as a full characterization of the two recombiners, are currently beeing theoretically investigated in collaboration with Bruno Juliá-Díaz and Artur Polls at the University of Barcelona.

3.7.3 Discussion of the Interferometric Signal

3.7.3.1 Sensitivity of the BEC Interferometer

Sensitivity to Small Phase Shifts

One figure of merit to evaluate the performance of the interferometer is its ability to detect small phase shifts. It is common to resort to the first-order sensitivity to phase shifts introduced in Eq. (1.169):

$$\delta\phi = \frac{\Delta z}{|\partial\langle z\rangle/\partial\phi|_{\phi=\phi_0}}. \tag{3.98}$$

It is determined by the noise on the measured imbalance (be it projection noise, technical noise...) and the slope of the average interferometric signal at the working

point ϕ_0. For a coherent state, the best sensitivity of a phase measurement is limited by the standard quantum limit $\Delta\phi_{\mathrm{SQL}} = 1/\sqrt{N}$. For $N = 1200$ atoms, $\Delta\phi_{\mathrm{SQL}} = 0.03$ rad.

We can estimate the maximal sensitivity intrinsically allowed by the trapped BEC recombiners, independently on the state of the BEC in the interferometer, by evaluating Eq. (3.98) using the amplitude noise and the contrast fitted from the distribution of z at all times (see Fig. 3.46)

$$\delta\phi \approx \sigma_d / C. \tag{3.99}$$

It yields $\delta\phi \approx 0.18$ rad (non-adiabatic recombiner) and $\delta\phi \gtrsim 0.75$ rad (Josephson recombiner). The poor performance of the Josephson recombiner is due to both a high amplitude noise and a low contrast.

In practice however, both amplitude and phase noise must be taken into account. Because of interactions, the slope of the averaged fringes is steeper for $\phi_0 = \pi$ than for $\phi_0 = 0$ (see Fig. 3.29). We interpolate the measured fluctuations of z to estimate Δz at the time of the first zero-crossing and compute the derivative of $z(\phi_0)$ using the model of Eq. (3.91) to find that with the non-adiabatic recombiner, $\delta\phi = 0.56$ rad, while with the Josephson recombiner, $\delta\phi = 0.98$ rad.

Sensitivity on the Determination of the Energy Difference

Besides the sensitivity to absolute phase shifts, it is also meaningful to ask ourselves what is the smallest measurable phase shift relatively to the total accumulated phase, or equivalently: what is the smallest detectable change of the phase accumulation rate ϵ? The value of ϵ is inferred from the evolution of z as a function of t_ϕ, and depends therefore on the available interrogation time. The uncertainty on an estimation of $\epsilon/\hbar$ scales like $1/\tau_{\mathrm{coh}}$. From the expression of the phase diffusion rate, the uncertainty on ϵ therefore scales like

$$\Delta\epsilon \propto \xi_N \sqrt{N} U. \tag{3.100}$$

This result underlines the simple fact that increasing the interrogation time of the interferometer enhances proportionally the precision at which the energy difference between the two paths can be read out. For example, the 95 % confidence interval on the estimation of ϵ/h from the fit to the data of Fig. 3.45 is ± 2 Hz, consistent to the results of the fits from the tof recombination data (Fig. 3.19). It also shows that the use of a number-squeezed state allows enhancing the interrogation time of the trapped BEC interferometer beyond what would be possible with a classical coherent state.

Comparison with the Time-of-flight Recombiner

We can compare our estimations of the intrinsic sensitivity of the two trapped BEC recombiners to the estimated sensitivity of the tof recombination for a coherent state with $N = 1200$ atoms, $\Delta\phi \approx 0.08$ rad (see Sect. 3.2.1.4). The intrinsic noise of the non-adiabatic recombiner is still currently about twice larger than that of the tof recombiner. This is partly due to the moderate contrast of the trapped recombiners: were its contrast increased to 100 %, the sensitivity of the non-adiabatic recombiner would be comparable to that of the tof recombiner.

It must also be underlined that phase estimation based on atom counting is more robust than phase extraction from interference patterns. First, it does not require high imaging resolution; second, using a recombiner to convert the relative phase into a population imbalance allows the use of the precise atom counting techniques already available [61, 79, 80].

A more fundamental distinction between both methods is their potential sensitivity limits. Even though phase estimation based on a fit to the tof interference pattern can reach sub-shot-noise sensitivity [119] ($\Delta\phi < 1/\sqrt{N}$), it is fundamentally bounded by $N^{2/3}$ [120]. This lower bound holds for any entangled state used in the interferometer. This result underlines that the Heisenberg scaling of the phase sensitivity $\Delta\phi = 1/N$ will not be accessible to atom interferometers using this phase estimation strategy. On the contrary, theoretical studies suggest that trapped BEC schemes can reach the Heisenberg scaling of the phase sensitivity [102, 123].

Towards Scalable Quantum-Enhanced Interferometers?

Although we could demonstrate an extension of the interrogation time by the use of a number-squeezed state, our interferometer is far from being shot noise limited. The best sensitivity on the phase estimation is achieved using the tof recombiner. The measured phase spread right after splitting yielded $\Delta\phi = 0.16$ rad, more than 5 time above the SQL. Using a coherent state, though, it should be possible to measure a phase noise twice as large as the SQL.

Because the state of the BEC in the interferometer is number-squeezed and not phase-squeezed, our Mach-Zehnder scheme is currently not optimized to yield the best sensitivity. Although the two trapped BEC recombiners that we implemented constitute a further step in the controlled manipulation of the state of a BEC in a double well, a generic tool to perform efficiently rotations around the (x)-axis of the Bloch sphere is still missing.

Since 2010, quantum-enhanced measurements, as well as the generation of spin-squeezed states that could potentially yield a sensitivity gain beyond the SQL, have been recently reported in internal-state Ramsey BEC interferometers [8, 17, 62]. In every case, the BEC contained a few thousands of atoms (approx. 2300 atoms in Ref. [17]). While quantum enhancement is an asset for measurements where a high spatial resolution is required, because the number of atoms in a small volume must be kept small to avoid collisional losses [8], it is still an open question whether the

schemes currently under investigation are scalable up to atom numbers where sub shot-noise measurements become competitive with current shot-noise limited atom interferometers. A promising step in this direction has been achieved in 2010 with the demonstration of a shot-noise limited Ramsey interferometer with $N \gtrsim 10^4$ freely propagating atoms extracted from a BEC.

3.7.3.2 Decoherence of the Quantum Superposition

The evolution of the interferometric signal with the phase accumulation time seems to reveal the existence of two timescales resembling the T_1 and T_2 times commonly referred to in Nuclear Magnetic Resonance (NMR) spectroscopy [134]: the first timescale (T_2 time), of the order of $\tau_{\mathrm{coh}} \approx 20$ ms, is due to an interaction-induced *dephasing* effect. Currently, this timescale is limiting the interrogation time of our interferometer. In principle, one could think of reversing this dephasing through a spin echo-like procedure [135], for example by performing a π-Rabi pulse to swap the occupation number of the two wells. One could also think of switching either the sign of interactions through a Feshbach resonance, or modulating the tunnel coupling to implement a negative effective coupling [136].

On a longer timescale (T_1 time), of the order of hundreds of ms, even the contrast of individual realizations is lost, suggesting that *relaxation* mechanisms are at work. Conversely to the dephasing mechanism, they imply a redistribution of energy from the degrees of freedom relevant to the 2-mode dynamics to other modes, possibly in the other spatial directions, as will be discussed in Chap. 4.

References

1. T. Berrada, S. van Frank, R. Bücker, T. Schumm, J.-F. Schaff, J. Schmiedmayer, Integrated Mach-Zehnder interferometer for Bose-Einstein condensates. Nat. Commun. **4**, 2077 (2013)
2. A.D. Cronin, D.E. Pritchard, Optics and interferometry with atoms and molecules. Rev. Mod. Phys. **81**(3), 1051–1129 (2009)
3. C.S. Adams, M. Sigel, J. Mlynek, Atom optics. Phys. Rep. **240**(3), 143–210 (1994)
4. N.F. Ramsey, Experiments with separated oscillatory fields and hydrogen masers. Science **248**(4963), 16–129 (1990)
5. W. Ketterle, When atoms behave as waves: bose-einstein condensation and the atom laser (2001)
6. Y. Torii, Y. Suzuki, M. Kozuma, T. Sugiura, Lu Takahiro Kuga, E.Hagley Deng, Mach-Zehnder Bragg interferometer for a Bose-Einstein condensate. Phys. Rev. A **61**(4), 041602 (2000)
7. I. Carusotto, L. Pitaevskii, S. Stringari, G. Modugno, M. Inguscio, Sensitive measurement of forces at the micron scale using bloch oscillations of ultracold atoms. Phys. Rev. Lett. **95**(9), 093202 (2005)
8. C.F. Ockeloen, R. Schmied, M.F. Riedel, P. Treutlein, Quantum metrology with a scanning probe atom interferometer. Phys. Rev. Lett. **111**(14), 143001 (2013)
9. R. Anderson, C. Ticknor, A. Sidorov, B. Hall, Spatially inhomogeneous phase evolution of a two-component Bose-Einstein condensate. Phys. Rev. A **80**(2), 023603 (2009)
10. M. Horikoshi, K.I. Nakagawa, Dephasing due to atom atom interaction in a waveguide interferometer using a Bose-Einstein condensate. Phys. Rev. A **74**(3), 031602 (2006)

11. G.B. Jo, Y. Shin, S. Will, T. Pasquini, M. Saba, W. Ketterle, D. Pritchard, M. Vengalattore, M. Prentiss, Long phase coherence time and number squeezing of two Bose-Einstein condensates on an atom chip. Phys. Rev. Lett. **98**(3), 030407 (2007)
12. J.F. Schaff, T. Langen, J. Schmiedmayer, Interferometry with atoms, in *Proceedings of the International School of Physics "Enrico Fermi"* (2014)
13. M.R. Andrews, Observation of interference between two Bose condensates. Science **275**(5300), 637–641 (1997)
14. D.S. Hall, M.R. Matthews, C.E. Wieman, E.A. Cornell, Measurements of relative phase in two-component Bose-Einstein condensates. Phys. Rev. Lett. **81**(8), 1543–1546 (1998)
15. Y. Wang, D. Anderson, V. Bright, E. Cornell, Q. Diot, T. Kishimoto, M. Prentiss, R. Saravanan, S. Stephen, W. Saijun, Atom Michelson Interferometer on a Chip Using a Bose-Einstein Condensate. Phys. Rev. Lett. **94**(9), 090405 (2005)
16. S. van Frank, A. Negretti, T. Berrada, R. Bücker, S. Montangero, J.-F. Schaff, T. Schumm, T. Calarco, J. Schmiedmayer, Interferometry with non-classical motional states of a Bose-Einstein condensate. p. 7 (2014)
17. C. Gross, Spin squeezing and non-linear atom interferometry with Bose-Einstein condensates, Ph.D. thesis, Ruperto-Carola University of Heidelberg, 2010
18. P.A. Altin, G. McDonald, D. Döring, J.E. Debs, T.H. Barter, J.D. Close, N.P. Robins, S.A. Haine, T.M. Hanna, R.P. Anderson, Optically trapped atom interferometry using the clock transition of large 87 Rb Bose-Einstein condensates. New J. Phys. **13**(6), 065020 (2011)
19. M. Egorov, R.P. Anderson, V. Ivannikov, B. Opanchuk, P. Drummond, B.V. Hall, A.I. Sidorov, Long-lived periodic revivals of coherence in an interacting Bose-Einstein condensate. Phys. Rev. A **84**(2), 021605 (2011)
20. F. Minardi, C. Fort, P. Maddaloni, M. Modugno, M. Inguscio, Time-domain atom interferometry across the threshold for Bose-Einstein condensation. Phys. Rev. Lett. **87**(17), 170401 (2001)
21. J. Petrovic, I. Herrera, P. Lombardi, F. Schäfer, F.S. Cataliotti, A multi-state interferometer on an atom chip. New J. Phys. **15**(4), 043002 (2013)
22. I. Bloch, T. Hänsch, T. Esslinger, Atom laser with a cw output coupler. Phys. Rev. Lett. **82**(15), 3008–3011 (1999)
23. F. Chevy, K. Madison, V. Bretin, J. Dalibard, Interferometric detection of a single vortex in a dilute Bose-Einstein condensate. Phys. Rev. A **64**(3), 031601 (2001)
24. S. Machluf, Y. Japha, R. Folman, Coherent Stern-Gerlach momentum splitting on an atom chip. Nat. Commun. **4**, 2424 (2013)
25. P. Böhi, M.F. Riedel, J. Hoffrogge, J. Reichel, T.W. Hänsch, P. Treutlein, Coherent manipulation of Bose Einstein condensates with state-dependent microwave potentials on an atom chip. Nat. Phys. **5**(8), 592–597 (2009)
26. M. Kasevich, S. Chu, Atomic interferometry using stimulated Raman transitions. Phys. Rev. Lett. **67**(2), 181–184 (1991)
27. D. Döring, G. McDonald, J.E. Debs, C. Figl, P.A. Altin, H.-A. Bachor, N.P. Robins, J.D. Close, Quantum-projection-noise-limited interferometry with coherent atoms in a Ramsey-type setup. Phys. Rev. A **81**(4), 043633 (2010)
28. E. Hagley, L. Deng, M. Kozuma, M. Trippenbach, Y. Band, M. Edwards, M. Doery, P. Julienne, K. Helmerson, S. Rolston, W. Phillips, Measurement of the coherence of a Bose-Einstein condensate. Phys. Rev. Lett. **83**(16), 3112–3115 (1999)
29. J. Simsarian, J. Denschlag, M. Edwards, C. Clark, L. Deng, E. Hagley, K. Helmerson, S. Rolston, W. Phillips, Imaging the phase of an evolving Bose-Einstein condensate wave function. Phys. Rev. Lett. **85**(10), 2040–2043 (2000)
30. J. Denschlag, Generating solitons by phase engineering of a Bose-Einstein condensate. Science **287**(5450), 97–101 (2000)
31. E. Rasel, M. Oberthaler, H. Batelaan, J. Schmiedmayer, A. Zeilinger, Atom wave interferometry with diffraction gratings of light. Phys. Rev. Lett. **75**(14), 2633–2637 (1995)
32. D. Giltner, R. McGowan, S. Lee, Atom interferometer based on bragg scattering from standing light waves. Phys. Rev. Lett. **75**(14), 2638–2641 (1995)

33. J.E. Debs, P.A. Altin, T.H. Barter, D. Döring, G.R. Dennis, G. McDonald, R.P. Anderson, J.D. Close, N.P. Robins, Cold-atom gravimetry with a Bose-Einstein condensate. Phys. Rev. A **84**(3), 033610 (2011)
34. G.D. McDonald, H. Keal, P.A. Altin, J.E. Debs, S. Bennetts, C.C.N. Kuhn, K.S. Hardman, M.T. Johnsson, J.D. Close, N.P. Robins, Optically guided linear Mach-Zehnder atom interferometer. Phys. Rev. A **87**(1), 013632 (2013)
35. H. Müntinga, H. Ahlers, M. Krutzik, A. Wenzlawski, S. Arnold, D. Becker, K. Bongs, H. Dittus, H. Duncker, N. Gaaloul, C. Gherasim, E. Giese, C. Grzeschik, T.W. Hänsch, O. Hellmig, W. Herr, S. Herrmann, E. Kajari, S. Kleinert, C. Lämmerzahl, W. Lewoczko-Adamczyk, J. Malcolm, N. Meyer, R. Nolte, A. Peters, M. Popp, J. Reichel, A. Roura, J. Rudolph, M. Schiemangk, M. Schneider, S.T. Seidel, K. Sengstock, V. Tamma, T. Valenzuela, A. Vogel, R. Walser, T. Wendrich, P. Windpassinger, W. Zeller, T. van Zoest, W. Ertmer, W.P. Schleich, E.M. Rasel, Interferometry with Bose-Einstein condensates in microgravity. Phys. Rev. Lett. **110**(9), 093602 (2013)
36. S. Gupta, K. Dieckmann, Z. Hadzibabic, D. Pritchard, Contrast interferometry using Bose-Einstein condensates to measure h/m and α. Phys. Rev. Lett. **89**(14), 140401 (2002)
37. O. Garcia, B. Deissler, K. Hughes, J. Reeves, C. Sackett, Bose-Einstein-condensate interferometer with macroscopic arm separation. Phys. Rev. A **74**(3), 031601 (2006)
38. D. Hellweg, L. Cacciapuoti, M. Kottke, T. Schulte, K. Sengstock, W. Ertmer, J. Arlt, Measurement of the spatial correlation function of phase fluctuating Bose-Einstein condensates. Phys. Rev. Lett. **91**(1), 010406 (2003)
39. C.C.N. Kuhn, G.D. McDonald, K.S. Hardman, S. Bennetts, P.J. Everitt, P.A. Altin, J.E. Debs, J.D. Close, N.P. Robins, A Bose-condensed, simultaneous dual species Mach-Zehnder atom interferometer. p. 7 (2014)
40. B.P. Anderson, Macroscopic quantum interference from atomic tunnel arrays. Science **282**(5394), 1686–1689 (1998)
41. M. Fattori, C. D'Errico, G. Roati, M. Zaccanti, M. Jona-Lasinio, M. Modugno, M. Inguscio, G. Modugno, Atom interferometry with a weakly interacting Bose-Einstein condensate. Phys. Rev. Lett. **100**(8), 080405 (2008)
42. D. Gallego, S. Hofferberth, T. Schumm, P. Krüger, J. Schmiedmayer, Optical lattice on an atom chip. Opt. Lett. **34**(22), 3463–3465 (2009)
43. M. Gustavsson, E. Haller, M.J. Mark, J.G. Danzl, R. Hart, A.J. Daley, H.-C. Nägerl, Interference of interacting matter waves. New J. Phys. **12**(6), 065029 (2010)
44. Y. Shin, M. Saba, T. Pasquini, W. Ketterle, D. Pritchard, A. Leanhardt, Atom interferometry with Bose-Einstein condensates in a double-well potential. Phys. Rev. Lett. **92**(5), 050405 (2004)
45. T. Schumm, S. Hofferberth, L.M. Andersson, S. Wildermuth, S. Groth, I. Bar-Joseph, J. Schmiedmayer, P. Krüger, Matter-wave interferometry in a double well on an atom chip. Nat. Phys. **1**(1), 57–62 (2005)
46. S. Hofferberth, I. Lesanovsky, B. Fischer, J. Verdu, J. Schmiedmayer, Radiofrequency-dressed-state potentials for neutral atoms. Nat. Phys. **2**(10), 710–716 (2006)
47. F. Baumgärtner, R.J. Sewell, S. Eriksson, I. Llorente-Garcia, J. Dingjan, J.P. Cotter, E.A. Hinds, Measuring energy differences by BEC interferometry on a chip. Phys. Rev. Lett. **105**(24), 243003 (2010)
48. G.-B. Jo, J.-H. Choi, C.A. Christensen, Y.-R. Lee, T.A. Pasquini, W. Ketterle, D.E. Pritchard, Matter-wave interferometry with phase fluctuating Bose-Einstein condensates. Phys. Rev. Lett. **99**(24), 240406 (2007)
49. S. Hofferberth, I. Lesanovsky, B. Fischer, T. Schumm, J. Schmiedmayer, Non-equilibrium coherence dynamics in one-dimensional Bose gases. Nature **449**(7160), 32–47 (2007)
50. S. Hofferberth, I. Lesanovsky, T. Schumm, A. Imambekov, V. Gritsev, E. Demler, J. Schmiedmayer, Probing quantum and thermal noise in an interacting many-body system. Nat. Phys. **4489** (2008)
51. T. Betz, S. Manz, R. Bücker, T. Berrada, C. Koller, G. Kazakov, I. Mazets, H.-P. Stimming, A. Perrin, T. Schumm, J. Schmiedmayer, Two-point phase correlations of a one-dimensional bosonic Josephson junction. Phys. Rev. Lett. **106**(2), 020407 (2011)

52. M. Gring, M. Kuhnert, T. Langen, T. Kitagawa, B. Rauer, M. Schreitl, I. Mazets, D. Adu Smith, E. Demler, J. Schmiedmayer, Relaxation and prethermalization in an isolated quantum system. Science **337**(6100), 131–822 (2012)
53. T. Stöferle, H. Moritz, C. Schori, M. Köhl, T. Esslinger, Transition from a strongly interacting 1D superfluid to a mott insulator. Phys. Rev. Lett. **92**(13), 130403 (2004)
54. Z. Hadzibabic, P. Krüger, M. Cheneau, B. Battelier, J. Dalibard, Berezinskii-Kosterlitz-Thouless crossover in a trapped atomic gas. Nature **441**(7097), 111–821 (2006)
55. M. Albiez, R. Gati, J. Foelling, S. Hunsmann, M. Cristiani, M.K. Oberthaler, Direct observation of tunneling and nonlinear self-trapping in a single bosonic Josephson junction. Phys. Rev. Lett. **95**(1), 010402 (2005)
56. G.-B. Jo, J.-H. Choi, C.A. Christensen, T.A. Pasquini, Y.-R. Lee, W. Ketterle, D.E. Pritchard, Phase-sensitive recombination of two Bose-Einstein condensates on an atom chip. Phys. Rev. Lett. **98**(18), 180401 (2007)
57. A. Günther, S. Kraft, C. Zimmermann, J. Fortágh, Atom interferometer based on phase coherent splitting of Bose-Einstein condensates with an integrated magnetic grating. Phys. Rev. Lett. **98**(14), 140403 (2007)
58. M. Matthews, B. Anderson, P. Haljan, D. Hall, C. Wieman, E. Cornell, Vortices in a Bose-Einstein condensate. Phys. Rev. Lett. **83**(13), 2498–2501 (1999)
59. R. Gati, B. Hemmerling, J. Fölling, M. Albiez, M. Oberthaler, Noise thermometry with two weakly coupled Bose-Einstein condensates. Phys. Rev. Lett. **96**(13), 130404 (2006)
60. M. Fattori, G. Roati, B. Deissler, C. D'Errico, M. Zaccanti, M. Jona-Lasinio, L. Santos, M. Inguscio, G. Modugno, Magnetic dipolar interaction in a Bose-Einstein condensate atomic interferometer. Phys. Rev. Lett. **101**(19), 190405 (2008)
61. J. Estève, C. Gross, A. Weller, S. Giovanazzi, M.K. Oberthaler, Squeezing and entanglement in a Bose-Einstein condensate. Nature **455**(7217), 1216–1219 (2008)
62. M.F. Riedel, P. Böhi, Y. Li, T.W. Hänsch, A. Sinatra, P. Treutlein, Atom-chip-based generation of entanglement for quantum metrology. Nature **464**(7292), 70–113 (2010)
63. D. Adu Smith, M. Gring, T. Langen, M. Kuhnert, B. Rauer, R. Geiger, T. Kitagawa, I. Mazets, E. Demler, J. Schmiedmayer, Prethermalization revealed by the relaxation dynamics of full distribution functions. New J. Phys. **15**(7), 075011 (2013)
64. M. Kuhnert, R. Geiger, T. Langen, M. Gring, B. Rauer, T. Kitagawa, E. Demler, D. Adu Smith, J. Schmiedmayer, Multimode dynamics and emergence of a characteristic length scale in a one-dimensional quantum system. Phys. Rev. Lett. **110**(9), 090405 (2013)
65. T. Langen, R. Geiger, M. Kuhnert, B. Rauer, J. Schmiedmayer, Local emergence of thermal correlations in an isolated quantum many-body system. Nat. Phys. **9**(10), 640–643 (2013)
66. Y. Castin, J. Dalibard, Relative phase of two Bose-Einstein condensates. Phys. Rev. A **55**(6), 4330–4337 (1997)
67. T. Schum, Bose-Einstein condensates in magnetic double well potentials, Ph.D. thesis, Université Paris 11, 2005
68. J.C. Camparo, R.P. Frueholz, A dressed atom interpretation of adiabatic rapid passage. J. Phys. B At. Mol. Phys. **17**(20), 4169–4178 (1984)
69. N.I. Fisher, *Statistical Analysis of Circular Data* (Cambridge University Press, Cambridge, 1995)
70. T. Betz, Phase correlations of coupled one-dimensional Bose gases, Ph.D. thesis, Vienna University of Technology, 2011
71. H. Batelaan, S. Bernet, M.K. Oberthaler, E. Rasel, J. Schmiedmayer, A. Zeilinger, Classical and quantum atom fringes. In *Atom Interferometry*, (Academic Press, 1997) pp. 112–112
72. J. Chwedeńczuk, F. Piazza, A. Smerzi, Phase estimation with interfering Bose-Einstein-condensed atomic clouds. Phys. Rev. A **82**(5), 051601 (2010)
73. C.W. Helstrom, *Quantum Detection and Estimation Theory* (Academic Press, New York, 1976)
74. J. Chwedeńczuk, F. Piazza, A. Smerzi, Phase estimation from atom position measurements. New J. Phys. **13**(6), 065023 (2011)

75. C. Buggle, Collective and collisional properties of the rubidium quantum gas, Ph.D. thesis, University of Amsterdam, 2005
76. R. Bücker, J. Grond, S. Manz, T. Berrada, T. Betz, C. Koller, U. Hohenester, T. Schumm, A. Perrin, J. Schmiedmayer, Twin-atom beams. Nat. Phys. **7**(8), 608–611 (2011)
77. R. Bücker, Twin-atom beam generation in a one-dimensional Bose gas, Ph.D. thesis, Vienna University of Technology, 2013
78. R. Bücker, Fluorescence imaging of ultracold atoms, Diploma thesis, Heidelberg, 2008
79. R. Bücker, A. Perrin, S. Manz, T. Betz, C.H. Koller, T. Plisson, J. Rottmann, T. Schumm, J. Schmiedmayer, Single-particle-sensitive imaging of freely propagating ultracold atoms. New J. Phys. **11**(10), 24 (2009)
80. B. Lücke, M. Scherer, J. Kruse, L. Pezzé, F. Deuretzbacher, P. Hyllus, O. Topic, J. Peise, W. Ertmer, J. Arlt, L. Santos, A. Smerzi, C. Klempt, Twin matter waves for interferometry beyond the classical limit. Science **334**(6057), 63–77 (2011)
81. H.-P. Stimming, N. Mauser, J. Schmiedmayer, I. Mazets, Fluctuations and stochastic processes in one-dimensional many-body quantum systems. Phys. Rev. Lett. **105**(1), 18–21 (2010)
82. V.N. Popov, On the theory of the superfluidity of two- and one-dimensional bose systems. Theor. Math. Phys. **11**(3), 565–573 (1972)
83. D. Petrov, G. Shlyapnikov, J. Walraven, Regimes of quantum degeneracy in trapped 1D gases. Phys. Rev. Lett. **85**(18), 3745–3749 (2000)
84. A. Günther, S. Kraft, M. Kemmler, D. Koelle, R. Kleiner, C. Zimmermann, J. Fortágh, Diffraction of a Bose-Einstein condensate from a magnetic lattice on a microchip. Phys. Rev. Lett. **95**(17), 170405 (2005)
85. E. Andersson, T. Calarco, R. Folman, M. Andersson, B. Hessmo, J. Schmiedmayer, Multimode interferometer for guided matter waves. Phys. Rev. Lett. **88**(10), 100401 (2002)
86. J. van Es, S. Whitlock, T. Fernholz, A. van Amerongen, N. van Druten, Longitudinal character of atom-chip-based rf-dressed potentials. Phys. Rev. A **77**(6), 063623 (2008)
87. B. Hall, S. Whitlock, R. Anderson, P. Hannaford, A. Sidorov, Condensate splitting in an asymmetric double well for atom chip based sensors. Phys. Rev. Lett. **98**(3), 030402 (2007)
88. D. Cassettari, B. Hessmo, R. Folman, T. Maier, J. Schmiedmayer, Beam splitter for guided atoms. Phys. Rev. Lett. **85**(26), 5483–5487 (2000)
89. C. Brif, R. Chakrabarti, H. Rabitz, Control of quantum phenomena: past, present and future. New J. Phys. **12**(7), 075008 (2010)
90. D. Comparat, General conditions for quantum adiabatic evolution. Phys. Rev. A **80**(1), 012106 (2009)
91. Y. Castin, R. Dum, Bose-Einstein condensates in time dependent traps. Phys. Rev. Lett. **77**(27), 5315–5319 (1996)
92. Y. Kagan, E. Surkov, G. Shlyapnikov, Evolution of a Bose-condensed gas under variations of the confining potential. Phys. Rev. A **54**(3), R1753–R1756 (1996)
93. Y. Kagan, E.L. Surkov, G.V. Shlyapnikov, Evolution of a Bose gas in anisotropic time-dependent traps. Phys. Rev. A **55**(1), R18–R21 (1997)
94. C. Orzel, A.K. Tuchman, M.L. Fenselau, M. Yasuda, M.A. Kasevich, Squeezed states in a Bose-Einstein condensate. Science **291**(5512), 23–869 (2001)
95. K. Maussang, G.E. Marti, T. Schneider, P. Treutlein, Y. Li, A. Sinatra, R. Long, J. Estève, J. Reichel, Enhanced and reduced atom number fluctuations in a BEC splitter. Phys. Rev. Lett. **105**(8), 080403 (2010)
96. C. Gross, H. Strobel, E. Nicklas, T. Zibold, N. Bar-Gill, G. Kurizki, M.K. Oberthaler, Atomic homodyne detection of continuous-variable entangled twin-atom states. Nature **480**(7376), 219–223 (2011)
97. M. Jääskeläinen, W. Zhang, P. Meystre, Limits to phase resolution in matter-wave interferometry. Phys. Rev. A **70**(6), 063612 (2004)
98. M. Kitagawa, M. Ueda, Squeezed spin states. Phys. Rev. A **47**(6), 5138–5143 (1993)
99. B. Lücke, J. Peise, G. Vitagliano, J. Arlt, L. Santos, G. Tóth, C. Klempt, Detecting multiparticle entanglement of dicke states. Phys. Rev. Lett. **112**(15), 155304 (2014)

100. F. Haas, J. Volz, R. Gehr, J. Reichel, J. Estève, Entangled states of more than 40 atoms in an optical fiber cavity. Science **344**(6180), 180–183 (2014)
101. J. Javanainen, M. Ivanov, Splitting a trap containing a Bose-Einstein condensate: atom number fluctuations. Phys. Rev. A **60**(3), 2351–2359 (1999)
102. L. Pezzé, L. Collins, A. Smerzi, G. Berman, A. Bishop, Sub-shot-noise phase sensitivity with a Bose-Einstein condensate Mach-Zehnder interferometer. Phys. Rev. A **72**(4), 043612 (2005)
103. J. Grond, G. von Winckel, J. Schmiedmayer, U. Hohenester, Optimal control of number squeezing in trapped Bose-Einstein condensates. Phys. Rev. A **80**(5), 053625 (2009)
104. A. Leggett, F. Sols, Comment on phase and phase diffusion of a split Bose-Einstein condensate. Phys. Rev. Lett. **81**(6), 1344–1344 (1998)
105. L. Pitaevskii, S. Stringari, Thermal vs quantum decoherence in double well trapped Bose-Einstein condensates. Phys. Rev. Lett. **87**(18), 180402 (2001)
106. C. Mora, Y. Castin, Extension of Bogoliubov theory to quasicondensates. Phys. Rev. A **67**(5), 053615 (2003)
107. R. Feynman, A. Hibbs, *Quantum Mechanics and Path Integrals* (McGraw-Hill, New York, 1965)
108. P. Storey, C. Cohen-Tannoudji, The Feynman path integral approach to atomic interferometry: a tutorial. J. Phys. II France **4**(11), 1999–2027 (1994)
109. P.A. Altin, The role of interactions in atom interferometry with Bose-condensed atoms, Ph.D. thesis, Australian National University, 2012
110. D. Harber, H. Lewandowski, J. McGuirk, E. Cornell, Effect of cold collisions on spin coherence and resonance shifts in a magnetically trapped ultracold gas. Phys. Rev. A **66**(5), 053616 (2002)
111. F. Sols, Randomization of the phase after suppression of the Josephson coupling. Phys. B Condens. Matter **194–196**, 1389–1390 (1994)
112. E. Wright, D. Walls, J. Garrison, Collapses and revivals of Bose-Einstein condensates formed in small atomic samples. Phys. Rev. Lett. **77**(11), 2158–2161 (1996)
113. M. Lewenstein, L. You, Quantum phase diffusion of a Bose-Einstein condensate. Phys. Rev. Lett. **77**(17), 3489–3493 (1996)
114. A. Leggett, Bose-Einstein condensation in the alkali gases: some fundamental concepts. Rev. Mod. Phys. **73**(2), 307–356 (2001)
115. J. Javanainen, M. Wilkens, Phase and phase diffusion of a split Bose-Einstein condensate. Phys. Rev. Lett. **78**(25), 4675–4678 (1997)
116. J. Javanainen, M. Wilkens, Javanainen and wilkens reply. Phys. Rev. Lett. **81**(6), 1345–1345 (1998)
117. W. Li, A. Tuchman, H.-C. Chien, M. Kasevich, Extended coherence time with atom-number squeezed states. Phys. Rev. Lett. **98**(4), 040402 (2007)
118. M. Greiner, O. Mandel, T.W. Hänsch, I. Bloch, Collapse and revival of the matter wave field of a Bose-Einstein condensate. Nature **419**(6902), 5–41 (2002)
119. J. Grond, U. Hohenester, I. Mazets, J. Schmiedmayer, Atom interferometry with trapped Bose Einstein condensates: impact of atom atom interactions. New J. Phys. **12**(6), 065036 (2010)
120. J. Chwedeńczuk, P. Hyllus, F. Piazza, A. Smerzi, Sub-shot-noise interferometry from measurements of the one-body density. New J. Phys. **14**(9), 093001 (2012)
121. W. Hänsel, J. Reichel, P. Hommelhoff, T. Hänsch, Magnetic conveyor belt for transporting and merging trapped atom clouds. Phys. Rev. Lett. **86**(4), 608–611 (2001)
122. W. Hänsel, J. Reichel, P. Hommelhoff, T. Hänsch, Trapped-atom interferometer in a magnetic microtrap. Phys. Rev. A **64**(6), 063607 (2001)
123. J. Grond, U. Hohenester, J. Schmiedmayer, A. Smerzi, Mach-Zehnder interferometry with interacting trapped Bose-Einstein condensates. Phys. Rev. A **84**(2), 023619 (2011)
124. J. Dunningham, K. Burnett, Sub-shot-noise-limited measurements with Bose-Einstein condensates. Phys. Rev. A **70**(3), 033601 (2004)
125. L. Pezzé, A. Smerzi, G. Berman, A. Bishop, L. Collins, Nonlinear beam splitter in Bose-Einstein-condensate interferometers. Phys. Rev. A **74**(3), 033610 (2006)

126. R. Bücker, T. Berrada, S. van Frank, J.-F. Schaff, T. Schumm, J. Schmiedmayer, G. Jäger, J. Grond, U. Hohenester, Vibrational state inversion of a Bose-Einstein condensate: optimal control and state tomography (2012). December, arXiv:1212.4173
127. I. Zapata, F. Sols, A. Leggett, Phase dynamics after connection of two separate Bose-Einstein condensates. Phys. Rev. A **67**(2), 021603 (2003)
128. A. Negretti, C. Henkel, Enhanced phase sensitivity and soliton formation in an integrated BEC interferometer. J. Phys. B **37**, L385 (2004)
129. S. Raghavan, A. Smerzi, S. Fantoni, S. Shenoy, Coherent oscillations between two weakly coupled Bose-Einstein condensates: josephson effects, Pi oscillations, and macroscopic quantum self-trapping. Phys. Rev. A **59**(1), 620–633 (1999)
130. C. Cohen-Tannoudji, B. Diu, F. Laloë, Stationary states of a particle in one-dimensional square potentials. Quantum Mech. **I**, 67–89 (1977)
131. L. LeBlanc, A. Bardon, J. McKeever, M. Extavour, D. Jervis, J. Thywissen, F. Piazza, A. Smerzi. Dynamics of a Tunable Superfluid Junction, Phys. Rev. Lett. **106**(2) (2011)
132. R. Geiger, V. Ménoret, G. Stern, N. Zahzam, P. Cheinet, B. Battelier, A. Villing, F. Moron, M. Lours, Y. Bidel, A. Bresson, A. Landragin, P. Bouyer, Detecting inertial effects with airborne matter-wave interferometry. Nat. Commun. **2**, 474 (2011)
133. R. Geiger, Senseur inertiel à ondes de matière aéroporté, Ph.D. thesis, Université Paris Sud XI, 2011
134. M.A. Nielsen, I.L. Chuang, Examples of quantum noise and quantum operations, *Quantum Computation and Quantum Information* (Cambridge University Press, Cambridge, 2000), pp. 380–395
135. E. Hahn, Spin Echoes. Phys. Rev. **80**(4), 580–594 (1950)
136. A. Eckardt, C. Weiss, M. Holthaus, Superfluid-insulator transition in a periodically driven optical lattice. Phys. Rev. Lett. **95**(26), 260404 (2005)

Chapter 4
Outlook: Bosonic Josephson Junctions Beyond the Two-Mode Approximation

Throughout this thesis manuscript, we have analyzed our experimental observations of the dynamics of a BEC in a double-well potential resorting to a two-mode description of the BJJ. We believe that the 2MM is an appropriate description at short times in our elongated double-well geometry. Furthermore, the good agreement of the data with the 2MM predictions, for example to infer the amount of squeezing in our BEC, or the phase diffusion rate, shows how surprisingly well it describes our system.

Nevertheless, the 2MM is not expected to capture the complexity of a real-world BJJ, realized with a finite temperature BEC in an elongated, three-dimensional double-well potential. In this outlook, we present some observations that cannot be explained within the standard two-mode model and argue that a more elaborate picture is needed to model the rich physics of a BEC in an elongated double-well potential.

The two-mode formalism that we have presented in Chap. 1 relies on the two-site Bose Hubbard Hamiltonian, giving insight into the interplay between tunnel coupling and on-site interactions in the double well. It allows restricting the many-body dynamics of the BEC to a finite-dimensional Hilbert space, enabling exact calculations. The 2MM has proven to be extremely powerful to compute the fluctuations of the macroscopic observables (number and phase) and describe non-classical many-body states (in particular squeezed states) as well as the many-body phase diffusion. The associated collective-spin picture appears to be a generic framework for atom interferometry. The mean-field version of the two-mode model describes the non-linear dynamics of the BJJ, including Josephson oscillations and macroscopic quantum self-trapping.

However, many features of a real-world BJJ cannot be captured by this simplified model. We have shown in Sect. 1.2.5.4 that the standard 2MM was not always able to give reliable quantitative predictions for the Josephson oscillation frequency or the self-trapping threshold, nor could it explain the moderate contrast of our trapped BEC recombiners. On several occasions, we resorted to mean-field descriptions beyond the

T. Berrada, *Interferometry with Interacting Bose-Einstein Condensates in a Double-Well Potential*, Springer Theses,
DOI 10.1007/978-3-319-27233-7_4

standard 2MM, including the improved two-mode model presented in Sect. 1.2.5.4 and the one-dimensional Gross-Pitaevskii equation in the transverse direction.

It is crucial to extend the existing theoretical models to take into account the complexity of a real-life BJJ and explain effects beyond two mode that we are already able to observe. In the following, we present some experimental observations that cannot be explained within the two-mode picture and discuss what processes might be at work, highlighting the rich physics in our elongated BJJs.

4.1 Observations Beyond the Two-Mode Picture

Emergence of 1D Axial Phase Fluctuations

In Sect. 3.5.2, we observed that the "global" relative phase of the BECs (after integration along the longitudinal direction) underwent a fast randomization process although individual interference patterns exhibited a high contrast long after the phase coherence was lost, suggesting that a phase-diffusion process was at work. High fringe contrast was recorded for tens of ms after splitting in a symmetric (Fig. 3.21) as well as in a tilted double well (Fig. 3.22). At longer times, though, a significant drop of contrast was observed in single images (see Fig. 3.23), which seems consistent with the loss of contrast of the Mach-Zehnder number fringes (see Fig. 3.45). We attribute this decay of contrast to the emergence of fluctuations of the local relative phase along the long axis of the double well, as can be seen in Fig. 4.1, where individual interference patterns obtained for various holding times in the tilted $\mathrm{RF}_{\mathrm{Amp}} = 0.65$ trap are displayed. The loss of the spatial coherence of the relative phase in split 1D quasi BECs has been intensely studied in our group [1, 2]. The observation of wavy interference fringes is a clear sign that many axial modes contribute to the dynamics of the relative phase.

Damping of the Josephson Oscillations

We have studied the oscillations of the population imbalance in symmetric double wells with different tunnel coupling strengths. The BEC was initially prepared either with a finite phase difference or with a finite population imbalance. The phase difference was adjusted by splitting a BEC symmetrically and then applying a detuning for a given time, as explained in Sect. 3.5.1.2. The number imbalance was prepared by first splitting the BEC asymmetrically (i.e. with a finite tilt angle, see Fig. 3.12) and then leveling back the double well.[1] In both cases, the manipulation of the potential was near-to-adiabatic with respect to the transverse dynamics, although strict adiabaticity cannot be ensured.

The number or phase difference triggered oscillations of the population imbalance symmetric around zero, as first observed in 2005 with a BEC in a single optical double well [3]. As expected, we observed that the frequency of the oscillations of $z(t)$ decreases with increasing splitting of the double well (see Fig. 4.2). We could only

[1] Note that in this case, the evolution in the tilted double well may also cause a phase difference.

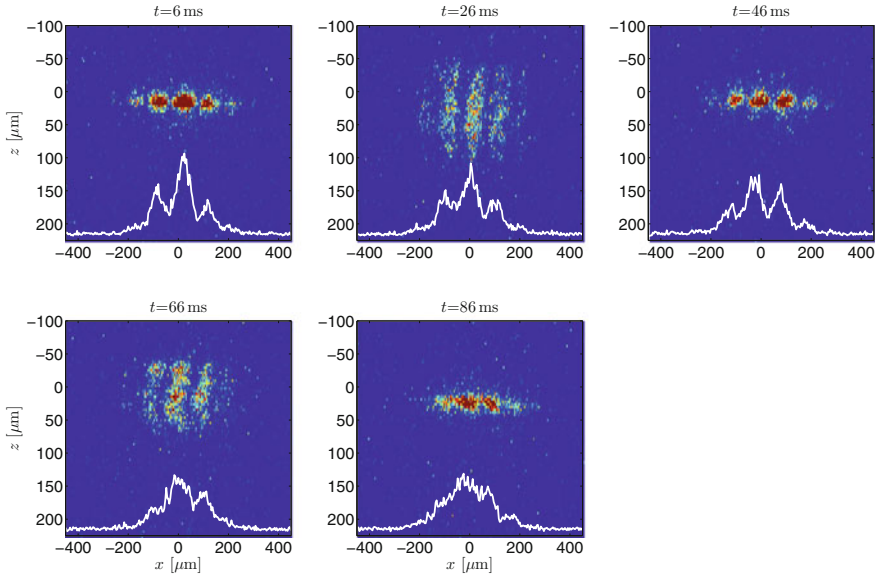

Fig. 4.1 Evolution of the axial relative phase after splitting. Fluorescence images of individual interference patterns in tof for different holding times in the tilted $\mathrm{RF_{Amp}} = 0.65$ potential ($\epsilon/h = 350\,\mathrm{Hz}$, $J/h \approx 0.1\,\mathrm{Hz}$). The holding times are computed from the end of the 5 ms splitting ramp. A strong axial breathing can be observed, caused by the fact that the atom number drops by a factor of two in each condensate after splitting in a much shorter time than the axial dynamics (see Sect. 3.4.1.3). First, the contrast remains high for tens of ms, although the global phase is random ∼30 ms after the end of splitting. At longer times, axial phase fluctuations (wavy fringes) are believed to scramble the axial relative phase, causing a loss of contrast of the integrated interference patterns in every individual realizations (*white lines*)

record such oscillations in strongly coupled double wells, where the barrier height was of the order of the chemical potential.[2] In Ref. [4], the authors monitored the continuous transition between hydrodynamic superfluid oscillations and Josephson oscillations in a strongly coupled double well through the emergence of a second frequency component.[3]

Comparing the oscillation frequencies measured for different values of the rf dressing amplitude to theoretical predictions computed using the simulated double-well potentials, we found fair agreement with the results of the two-mode model computations, particularly when using its refined version [5] (see Fig. 1.19). The even better agreement obtained by simulating the whole 3D mean-field dynamics builds a strong case for our knowledge of the double well potential (the 3D GPE simulations were performed by B. Juliá-Díaz in Barcelona).

[2] In the least coupled double well where we observed Josephson oscillations, we estimate that the barrier height was 1.5 larger than the chemical potential of the first excited state (including zero-point energy), corresponding to $\Lambda \approx 12$.

[3] Note that we did not see any obvious second frequency component in our data for strong coupling.

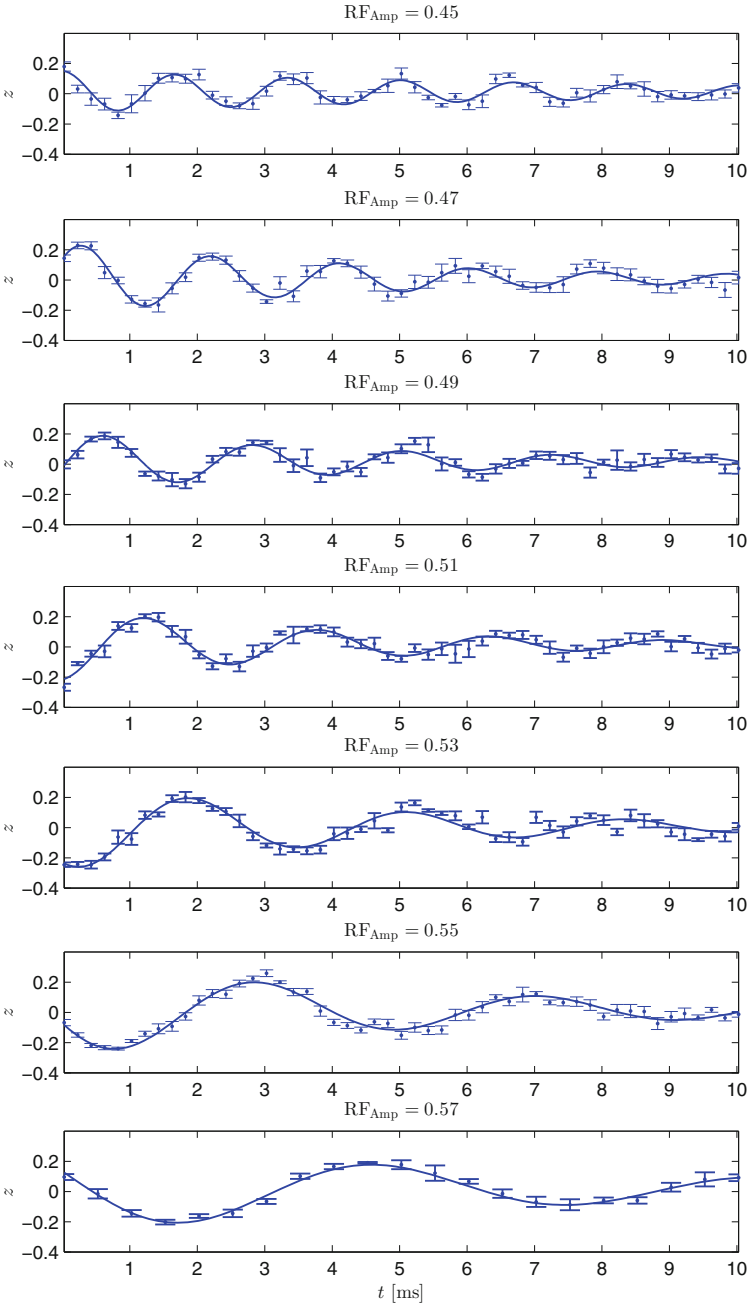
$\mathrm{RF}_{\mathrm{Amp}} = 0.45$
$\mathrm{RF}_{\mathrm{Amp}} = 0.47$
$\mathrm{RF}_{\mathrm{Amp}} = 0.49$
$\mathrm{RF}_{\mathrm{Amp}} = 0.51$
$\mathrm{RF}_{\mathrm{Amp}} = 0.53$
$\mathrm{RF}_{\mathrm{Amp}} = 0.55$
$\mathrm{RF}_{\mathrm{Amp}} = 0.57$
z
t [ms]

◀ **Fig. 4.2** Damped Josephson oscillations. Time evolution of the normalized population imbalance $z = (N_L - N_R)/N$ in different double wells. Conversely to the data displayed in Fig. 3.31, the Josephson oscillations were triggered by preparing a finite initial population imbalance: the BEC was first split asymmetrically into the $\mathrm{RF_{Amp}} = 0.65$ trap to prepare $z(0) \approx 0.2$. The rf dressing was then lowered in 5 ms to an adjustable value, and raised again after a variable time t to separate the atoms for counting. As expected, the Josephson oscillations become slower for decreasing tunnel coupling strength. *Continuous line* fit with an exponentially damped sine, yielding $1/e$ damping times comprised between 4 and 8 ms. The *error bars* (standard error of the mean) do not indicate a randomization of z at long times. A similar behaviour was observed for the phase of the integrated tof of interference patterns

Additionally, we systematically observed a damping of the oscillations of the population imbalance over a few periods. Fitting $z(t)$ with an exponentially damped sine yielded decay times of the order of 4–9 ms with an uncertainty of a few ms. Looking at the tof interference patterns obtained in the same conditions (without separating the atoms for counting), we also saw that the oscillations of $\phi(t)$ decayed to zero over a few periods. A similar behaviour was reported in two other experiments where Josephson oscillations were observed between a single pair of condensates [3, 4]. The decay observed in Ref. [3] was attributed to a shot-to-shot dephasing caused by the technical fluctuations of the initial state, as well as heating. Importantly, we observed that both $z(t)$ and $\phi(t)$ were damped to zero in all individual realizations at long time, while the contrast of tof interference patterns also decayed.

Decay of the Macroscopic Quantum Self-trapping

In another series of experiments, we studied the transition between Josephson oscillations and macroscopic quantum self-trapping. In a double well with finite tunnel coupling, the population imbalance may become "self-trapped" above a certain threshold under the effect of interactions (see Sect. 1.2.5.3). MQST was observed for the first time in 2005 in an optical double-well potential, together with the first Josephson oscillations [3]. In 2007, MQST was monitored with a BEC in a magnetic trap split with an optical potential barrier using non-destructive phase contrast imaging [6].

By varying the initial splitting angle before leveling back the trap, we prepared BECs with different population imbalances (up to $z(0) = 1$, where all the atoms are in the same well) in a given symmetric double-well potential. Figure 4.3 shows the evolution of $z(t)$ in the $\mathrm{RF_{Amp}} = 0.54$ double well, for which simulation predict $J \approx 60$ Hz. While at low initial imbalance, $z(t)$ underwent symmetric Josephson oscillations, we observed that for the strongest initial imbalances, z monotonously decayed to zero. A Gaussian fit to the curve with the highest initial imbalance yielded a $1/e^2$ time of 10.8 ± 1 ms. The corresponding tof interference patterns exhibited a strong loss of contrast with increasing initial imbalance. A fast decay of the population imbalance was also reported in Refs. [3, 6]. In Ref. [6], a faster decay of MQST was observed when increasing the non-condensed fraction.

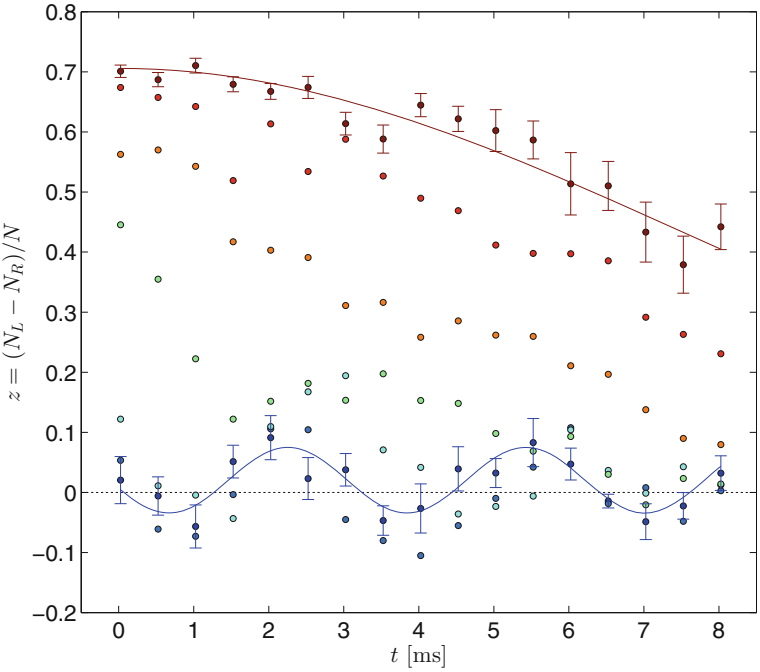

Fig. 4.3 Transition between Josephson oscillations and macroscopic quantum self-trapping. Normalized population imbalance as a function of time in the symmetric $\mathrm{RF}_{\mathrm{Amp}} = 0.54$ double well ($J \approx 60\,\mathrm{Hz}$). Different initial population imbalances were prepared by splitting the initial condensate asymmetrically at different angles, before leveling back the double well (here again, the evolution in the tilted double well may cause a different initial phase for the different imbalances). Josephson oscillations are clearly seen for the lowest initial imbalances (*blue line* fit with a sine to the curve with the lowest initial imbalance, yielding the frequency $f = 315 \pm 22\,\mathrm{Hz}$), while for the strongest initial imbalances, $z(t)$ monotonously decays to zero. *Dark red line* fit with a Gaussian decay to the curve with the highest initial imbalance, yielding a $1/e^2$ time $\tau = 10.8 \pm 1\,\mathrm{ms}$. The *error bars* indicate ± 1 std. err. of the mean (they have been omitted from the other curves for clarity). Interestingly, the shot-to-shot fluctuations of z grow in time for the data with the highest initial imbalance, conversely to that exhibiting Josephson oscillations

4.2 Discussion

None of the effects presented above can be explained within the two-mode model. The mean-field version of the 2MM (even in its refined form [5]), expected to be valid for sufficiently large number of atoms, predicts a periodic evolution of the system (see Fig. 1.16). While the coupled equations (1.198) and (1.199) for the conjugate variables n and ϕ contain non-linear dynamics such as bifurcations or anharmonic oscillations, they cannot explain the damping of the Josephson oscillations and the decay of MQST. The many-body version of the 2MM contains dephasing effects, such as phase diffusion, and could explain a damping of the expectation value of the

imbalance (see for example Ref. [7]). However, our data does not seem to indicate that the fluctuations of z increase in time. Incidentally, this observation also rules out the effect of technical shot-to-shot fluctuations of the initial state. Moreover, the observation of axial phase fluctuations, and the corresponding loss of contrast of the integrated interference patterns indicates a multimode dynamics, necessarily absent from the 2MM, which assumes static orbitals and absorbs the spatial dynamics into time-independent coefficients.

These observations call for more elaborate models to describe our BJJ. In the last section of this outlook, we discuss mechanisms that could explain the observed deviations from the two-mode dynamics and propose avenues for the study of beyond two-mode effects that we already see, or could readily observe with our setup.

Transverse Modes

The decay of the Josephson and MQST dynamics could in principle arise from excitations in the transverse plane. Indeed, the timescale of the damping of the tunneling dynamics (5–10 ms) is not fully incompatible with that of the transverse motion ($\sim$0.5 ms). In Sect. 3.6, we already resorted to 1D GPE simulations in the direction of splitting to describe the evolution of the wave function in the recombiners. In the non-adiabatic recombiner, in particular, the complex evolution of the wave function involved several transverse excited states (see Fig. 3.35). Yet, our 1D transverse GPE simulations of the Josephson oscillations did not indicate any damping (see Fig. 4.4). We conjecture that this is due to the fact that the high transverse energy scale ensures that only a few discrete transverse modes are populated. Even 1D GPE simulations of the non-adiabatic recombiner did not suggest a "damping" of $z(t)$ (see Fig. 3.38), in agreement with the fact that only a few transverse states are energetically

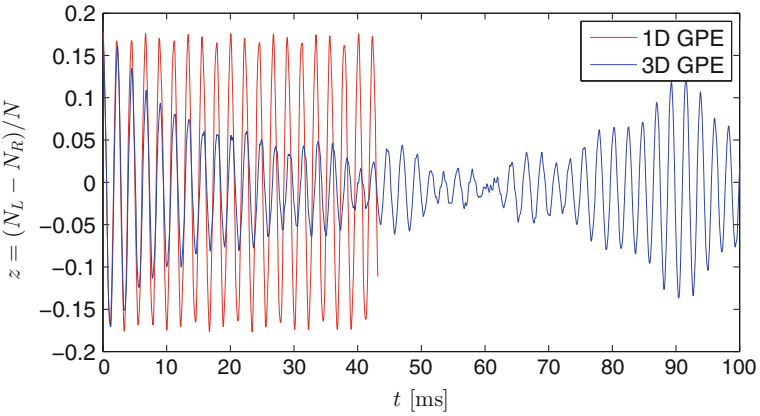

Fig. 4.4 Mean-field simulation of the Josephson oscillations. *Red* numerical resolution of the 1D GPE in the transverse double-well potential. *Blue* numerical resolution of the 3D GPE in the (3D) double-well potential, performed by B. Juliá-Díaz at the university of Barcelona. While the 1D GPE simulation does not show hints of damping, the 3D GPE simulation exhibits a damping over many periods followed by revivals (Color figure online)

accessible (see Fig. 3.35). We believe that this is a consequence of our elongated trapping geometry, which ensures that the wave function is close to the transverse ground state.

So far, we resorted only to mean-field simulations of the transverse dynamics. Interestingly, new methods are now available to compute the many-boson Schrödinger equation in one (transverse) dimension, enabling access to the fluctuations and the correlations between the transverse modes [8–11]. Although we think that we are not affected by the many-body dephasing studied in Ref. [10], owing to our relatively high atom number, such methods are very powerful for example to study the generation of non-classical states in a double well [12, 13].

Longitudinal Modes

The wavy interference patterns displayed in Fig. 4.1 indicate unambiguously the appearance of longitudinal fluctuations in the relative phase profile between the condensates after splitting. It seems likely that longitudinal excitations also come into play when the BECs are recoupled. We suspect that the decay of the Josephson oscillations and of the MQST are associated to the coupling between the tunneling dynamics and longitudinal modes: the essentially transverse tunneling dynamics may act as a drive from which energy would be "pumped" into axial excitations.

Due to the huge difference of energy scales (our typical aspect ratios are of the order of 100), many longitudinal modes are energetically accessible. In fact, the longitudinal modes almost appear as a continuum, making multimode many-body simulations extremely strenuous. Preliminary 3D GPE simulations of the BEC in the double-well potential suggest a redistribution of the energy from the transverse tunneling dynamics to the axial momentum modes (see Fig. 4.4). The 3D mean-field, zero-temperature model seem nonetheless to underestimate the damping rate, and predicts revivals that we did not observe so far.

We believe that much insight into our physical system could be gained by modeling our elongated BJJ by a pair of coupled, truly 1D condensates [14, 15]. This would imply discarding the transverse spatial dynamics, which seems fair as long as the temperature, the interaction energy and the coupling strength are much smaller than the transverse confinement energy [14]. Such a formalism has already been applied in our group to describe the axial phase fluctuations of a BJJ at thermal equilibrium [16] as well as the non-equilibrium dynamics following the sudden splitting of a 1D quasi BEC [1, 2]. In absence of coupling between symmetric and antisymmetric modes, the dephasing between the asymmetric axial momentum modes was shown to cause a rapid loss of coherence and a relaxation to a state with thermal-like properties [2, 17–19]. Interestingly, the effective temperature of such a prethermalized state was shown to depend on the initial number fluctuations, regardless of the initial temperature. We believe that our strong number squeezing is responsible for the high contrast observed over tens of ms after splitting (see discussion in Sect. 3.4.5). Our ability to prepare and detect number squeezing allow us studying prethermalization. In particular, it would be extremely interesting to probe the squeezing and the coherence properties of axial excitations, for example by means of condensate focusing [20–22].

At longer times, the 1D BJJ is expected to thermalize under the effect of the coupling of the symmetric and antisymmetric longitudinal modes [23]. The transition from the prethermalized to the thermalized state is currently under investigation in our group. It might shed some light into the role of the finite temperature of the initial unsplit BEC in the relaxation of the relative phase.

So far, we have not applied this 1D formalism to describe the tunneling dynamics of coupled elongated BECs. It was shown that in a pair of coupled 1D systems, modulational instabilities would cause the uniform Josephson oscillation mode to decay into axial excitations [15]. Revivals were also predicted in Ref. [15], arguably resembling that displayed by the 3D GPE simulations (see Fig. 4.4). The same mechanism was invoked to show that in 1D, the MQST mode should decay into correlated pairs of elementary axial excitations [24], and to predict the appearance of localized defects in the relative phase profile of coupled 1D quasi BECs [25].

A pair of coupled elongated BECs is a complex quantum system. It is an exciting playground to control and directly probe the rich interplay between tunnel coupling, interactions, 1D physics and many-body dynamics. We believe that our observations of effects beyond the two-mode picture will contribute to the understanding of the dynamics of coupled BECs and stimulate the development of more elaborate theoretical models.

References

1. S. Hofferberth, I. Lesanovsky, B. Fischer, T. Schumm, J. Schmiedmayer, Non-equilibrium coherence dynamics in one-dimensional Bose gases. Nature **449**(7160), 324–327 (2007)
2. M. Gring, M. Kuhnert, T. Langen, T. Kitagawa, B. Rauer, M. Schreitl, I. Mazets, D.A. Smith, E. Demler, J. Schmiedmayer, Relaxation and prethermalization in an isolated quantum system. Science **337**(6100), 1318–1322 (2012)
3. M. Albiez, R. Gati, J. Foelling, S. Hunsmann, M. Cristiani, M.K. Oberthaler, Direct observation of tunneling and nonlinear self-trapping in a single Bosonic Josephson junction. Phys. Rev. Lett. **95**(1) (2005)
4. L. LeBlanc, A. Bardon, J. McKeever, M. Extavour, D. Jervis, J. Thywissen, F. Piazza, A. Smerzi, Dynamics of a tunable superfluid junction. Phys. Rev. Lett. **106**(2) (2011)
5. D. Ananikian, T. Bergeman, Gross-Pitaevskii equation for Bose particles in a double-well potential: two-mode models and beyond. Phys. Rev. A **73**(1), 013604 (2006)
6. S. Levy, E. Lahoud, I. Shomroni, J. Steinhauer, The a.c. and d.c. Josephson effects in a Bose-Einstein condensate. Nature **449**(7162), 579–583 (2007)
7. G.J. Milburn, J. Corney, E.M. Wright, D.F. Walls, Quantum dynamics of an atomic Bose-Einstein condensate in a double-well potential. Phys. Rev. A **55**(6), 4318–4324 (1997)
8. Ofir Alon, Alexej Streltsov, Lorenz Cederbaum, Multiconfigurational time-dependent Hartree method for bosons: many-body dynamics of bosonic systems. Phys. Rev. A **77**(3), 033613 (2008)
9. Alexej Streltsov, Ofir Alon, Lorenz Cederbaum, Role of excited states in the splitting of a trapped interacting Bose-Einstein condensate by a time-dependent barrier. Phys. Rev. Lett. **99**(3), 030402 (2007)
10. K. Sakmann, A.I. Streltsov, O.E. Alon, L.S. Cederbaum, Exact quantum dynamics of a Bosonic Josephson junction. Phys. Rev. Lett. **103**(22) (2009)

11. K. Sakmann, A. Streltsov, O. Alon, L. Cederbaum, Quantum dynamics of attractive versus repulsive bosonic Josephson junctions: Bose-Hubbard and full-Hamiltonian results. Phys. Rev. A **82**(1) (2010)
12. Julian Grond, Gregory von Winckel, Jörg Schmiedmayer, Ulrich Hohenester, Optimal control of number squeezing in trapped Bose-Einstein condensates. Phys. Rev. A **80**(5), 053625 (2009)
13. Julian Grond, Jörg Schmiedmayer, Ulrich Hohenester, Optimizing number squeezing when splitting a mesoscopic condensate. Phys. Rev. A **79**(2), 021603 (2009)
14. N. Whitlock, I. Bouchoule, Relative phase fluctuations of two coupled one-dimensional condensates. Phys. Rev. A **68**(5), 053609 (2003)
15. I. Bouchoule, Modulational instabilities in Josephson oscillations of elongated coupled condensates. Eur. Phys. J. D **35**(1), 147–154 (2005)
16. T. Betz, S. Manz, R. Bücker, T. Berrada, Ch. Koller, G. Kazakov, I. Mazets, H.-P. Stimming, A. Perrin, T. Schumm, J. Schmiedmayer, Two-point phase correlations of a one-dimensional Bosonic Josephson junction. Phys. Rev. Lett. **106**(2) (2011)
17. D.A. Smith, M. Gring, T. Langen, M. Kuhnert, B. Rauer, R. Geiger, T. Kitagawa, I. Mazets, E. Demler, J. Schmiedmayer, Prethermalization revealed by the relaxation dynamics of full distribution functions. New J. Phys. **15**(7), 075011 (2013)
18. M. Kuhnert, R. Geiger, T. Langen, M. Gring, B. Rauer, T. Kitagawa, E. Demler, D.A. Smith, J. Schmiedmayer, Multimode Dynamics and Emergence of a Characteristic Length Scale in a One-Dimensional Quantum System. Physical Review Letters **110**(9), 090405 (2013)
19. T. Langen, R. Geiger, M. Kuhnert, B. Rauer, J. Schmiedmayer, Local emergence of thermal correlations in an isolated quantum many-body system. Nat. Phys. **9**(10), 640–643 (2013)
20. I. Shvarchuck, Ch. Buggle, D. Petrov, K. Dieckmann, M. Zielonkowski, M. Kemmann, T. Tiecke, W. von Klitzing, G. Shlyapnikov, J. Walraven, Bose-Einstein condensation into nonequilibrium states studied by condensate focusing. Phys. Rev. Lett. **89**(27), 270404 (2002)
21. M.J. Davis, P.B. Blakie, A.H. van Amerongen, N.J. van Druten, K.V. Kheruntsyan, Yang-Yang thermometry and momentum distribution of a trapped one-dimensional Bose gas. Phys. Rev. A **85**(3), 031604 (2012)
22. Thibaut Jacqmin, Bess Fang, Tarik Berrada, Tommaso Roscilde, Isabelle Bouchoule, Momentum distribution of one-dimensional Bose gases at the quasicondensation crossover: theoretical and experimental investigation. Phys. Rev. A **86**(4), 043626 (2012)
23. H.-P. Stimming, N.J. Mauser, J. Schmiedmayer, I.E. Mazets, Dephasing in coherently split quasicondensates. Phys. Rev. A **83**(2), 023618 (2011)
24. Rafael Hipolito, Anatoli Polkovnikov, Breakdown of macroscopic quantum self-trapping in coupled mesoscopic one-dimensional Bose gases. Phys. Rev. A **81**(1), 013621 (2010)
25. C. Neuenhahn, A. Polkovnikov, F. Marquardt, Localized phase structures growing out of quantum fluctuations in a quench of tunnel-coupled atomic condensates. Phys. Rev. Lett. **109**(8) (2012)

Appendix A
One-Dimensional Gross-Pitaevskii Simulations in the Transverse Potential

A.1 Effective Interaction Constant for the Transverse GPE Simulations

Because of our elongated geometries (see Sect. 1.1.3.3) and also because the dynamics of the BEC in the double wells occurs essentially in the direction of splitting, it is often sufficient to resort to 1D simulations in the transverse horizontal direction. The 1D Gross-Pitaevskii equation in the (x)-direction reads

$$i\hbar\frac{\partial\psi}{\partial t} = -\frac{\hbar^2}{2m}\frac{\partial^2\psi}{\partial^2 x} + V_\perp(x)\psi + g_\perp N|\psi|^2\psi \tag{A.1}$$

where $\psi(x)$ denotes the transverse wave function and $g_\perp$ is the effective transverse interaction constant. We want to derive an analytical expression for $g_\perp$ at short times right after splitting.

We begin by assuming that the wave function is separable, and that the initial unsplit cloud is described by a 1D Thomas-Fermi profile $\varphi_0(z)$ for N atoms at equilibrium in the initial (close-to) harmonic trap (frequencies $\omega^{(0)}_{x,y,z}$). The splitting process, which occurs within ms, can be seen as non-adiabatic with respect to the slow axial dynamics. We therefore that immediately after splitting, the axial profile remains unchanged. In the transverse direction, on the other hand, we assume that the wave function is close to the non-interacting transverse ground state. In particular, we assume that in the vertical transverse direction, the potential after splitting is harmonic with the frequency ω_y and that the wave function $\phi(y)$ in (y)-direction is in the non-interacting Gaussian ground state.

Under these assumptions, the effective transverse interaction constant reads

$$g_\perp \equiv g_{3\mathrm{D}} \int |\varphi_0(z)|^4 \,\mathrm{d}z \int |\phi(y)|^4 \,\mathrm{d}y \tag{A.2}$$

T. Berrada, *Interferometry with Interacting Bose-Einstein Condensates in a Double-Well Potential*, Springer Theses,
DOI 10.1007/978-3-319-27233-7

$$= \underbrace{\frac{2}{5}3^{2/3}}_{\approx 2.09}\sqrt{2\pi}\hbar\left(\frac{a_s^2 a_x^{(0)}\omega_z^{(0)}\omega_y}{N}\sqrt{\frac{\omega_y}{\omega_y^{(0)}}}\right)^{1/3} \tag{A.3}$$

For usual parameters, $g_\perp/h = 0.30\,\mathrm{Hz}\,\mu\mathrm{m}$ (to be compared for example to the axial 1D effective interaction constant $g_{1\mathrm{D}} = 2\hbar\omega_\perp = h \times 17\,\mathrm{Hz}\,\mu\mathrm{m}$. It means that in the transverse direction, where kinetic energy dominates, the effect of non-linearity is rather weak.

A.2 Parameter Estimation of the BJJ

The parameters of the BJJ, such as displayed in Fig. 3.14, are calculated by computing the left and right mode wave functions in the one-dimensional transverse potential obtained from the rf-dressing simulations beyond the RWA. More precisely:

- The ground and the first excited state wavefunctions $\phi_g(x)$ and $\phi_e(x)$ of the 1D GPE equation in the transverse potential are computed using the effective interaction constant introduced above. We resorted to an imaginary-time evolution using the standard split-operator method (with a symmetrized time step, ensuring that the local error at each time step is of order $\mathcal{O}(\Delta t^3)$ and the global error on the final result is of order $\mathcal{O}(\Delta t^2)$ [1].
- The left and right mode wavefunctions are defined as linear combinations of ϕ_g and ϕ_e:

$$\phi_L(x) = \frac{\phi_g + \phi_e}{\sqrt{2}} \tag{A.4}$$

$$\phi_R(x) = \frac{\phi_g - \phi_e}{\sqrt{2}} \tag{A.5}$$

- The parameters of the BJJ in the standard two-mode model (tunnel coupling and on-site interaction energies) are numerically computed using the integrals

$$J = -\int\left(\frac{\hbar^2}{2m}\nabla\phi_L\nabla\phi_R + \phi_L V\phi_R\right)\mathrm{d}x, \tag{A.6}$$

$$U_{L,R} = g_\perp\int|\phi_{L,R}|^4\mathrm{d}x. \tag{A.7}$$

  To compute the spatial derivatives, we make use of the fact that the ∇ operator is diagonal in momentum representation and compute the Fourier transforms of $\phi_{L,R}$.
- The parameters of the improved two-mode model (see Ref. [2]) can also be numerically computed using ϕ_g and ϕ_e.

Great care has to be given to the choice of the space and time steps. Typical values are $\Delta x = 5\,\mathrm{nm}$ (to be compared to the radial harmonic oscillator length $\sim 250\,\mathrm{nm}$) and $\Delta t = 5\,\mu\mathrm{s}$ (to be compared to the typical transverse oscillation period $\sim 0.5\,\mathrm{ms}$).

The same propagation method can be used to compute the GPE dynamics in the 1D potential. It can be adapted to the case of a time-dependent potential, for example to simulate the splitting and recombination ramps.

Appendix B
List of Symbols

The numerical values specific to Rubidium 87 are given for the $F = 1, m_F = -1$ hyperfine level of the ground state ($5^2S_{1/2}$).

Physical constants

$\hbar$	Reduced Planck constant: 1.05×10^{-34} m^2 kg s^{-1}
k_B	Boltzmann constant: 1.38×10^{-23} m^2 kg s^{-2} K^{-1}
a_0	Bohr radius: 5.29×10^{-11} m
μ_B	Bohr magneton: 9.27×10^{-24} J T^{-1}
μ_0	Vacuum permeability: $4\pi \times 10^{-7}$ V s A^{-1} m^{-1}

The ideal Bose gas

n_0	Ground state uniform density
$\vec{l}$	Quantum numbers $\vec{k} = \frac{2\pi}{L}\left(l_x\hat{x} + l_y\hat{y} + l_z\hat{z}\right)$
$\epsilon_{\vec{l}}$	Kinetic energy of plane (matter-)wave
β	Inverse temperature in units of k_B
Λ_T	Thermal de Brolie wavelength
T_c	Critical temperature for Bose-Einstein condensation

The weakly interacting Bose gas

m	Mass of one boson: 1.44×10^{-25} kg
a_s	s-wave scattering length: 5.32×10^{-9} m
$a_l^\dagger$, a_l	Bosonic creation and annihilation operator in the mode $\|l\rangle$.
$\hat{\Psi}^\dagger$, $\hat{\Psi}$	Bosonic field operators.
$V(\vec{r})$	External potential
$g_{3D} = 4\pi\hbar^2 a_s/m$	3D interaction constant: 5.14×10^{-51} J m^3

T. Berrada, *Interferometry with Interacting Bose-Einstein Condensates in a Double-Well Potential*, Springer Theses,
DOI 10.1007/978-3-319-27233-7

Elongated condensates

$a_\perp, a_\parallel$	Harmonic oscillator length in the transverse (longitudinal) direction
$\chi = N a_s a_\perp / a_\parallel{}^2$	χ-parameter (ratio of interaction energy over radial kinetic energy)
$g_{1D} = 2\hbar\omega_\perp a_s$	Effective 1D interaction constant
R_{TF1D}	1D Thomas-Fermi radius
μ_{TF1D}	1D Thomas-Fermi chemical potential

Two-mode Bose-Hubbard model

N	Total atom number
$N_{L,R}$	Number of atoms in the left (right) mode
$\phi_L(\vec{r})$	Spatial wave function for the left (right) mode
$a^\dagger_{L,R}, a_{L,R}$	Bosonic creation and annihilation operator
Energies	
J	Tunnel coupling energy
$U_{L,R}$	On-site interaction energy constant in the left (right) mode
$U = (U_L + U_R)/2$	Averaged on-site interaction energy constant
$\Delta = E^0_L - E^0_R$	Difference of zero-point energies between the modes
$\epsilon = (U_L - U_R)(N-1)/2 + \Delta$	Full energy detuning

Dimensionless parameters: ratio of tunneling and interaction energy	
$\Lambda = UN/2J$	MQST threshold: $\Lambda > 2$
$\gamma = U/2J$	Rabi: $\gamma \ll 1/N$, Josephson: $1/N \ll \gamma \ll N$, Fock: $\gamma \ll N$
$\eta = NJ/2U$	Phase diffusion threshold: $\eta \ll 1/4$
Macroscopic observables	
$n = (N_L - N_R)/2$	Half-number imbalance
$z = (N_L - N_R)/N$	Normalized population imbalance
$\phi = (\phi_L - \phi_R)/2$	Half-number imbalance
$\phi = (\phi_L - \phi_R)/2$	Half-number imbalance
$\langle\cos(\phi - \langle\phi\rangle)\rangle$	Coherence factor
Squeezing factors	
$\xi_N = \Delta(N_L - N_R)/\sqrt{N}$	Number-squeezing factor
$\xi_\phi = \Delta(\phi) \cdot \sqrt{N}$	Phase-squeezing factor
$\xi_S = \xi_N / \langle\cos\phi\rangle$	(Coherent, or useful) spin-squeezing factor

Magnetic trapping and rf-dressed potentials

g_F	Landé factor: 2.00
$\kappa = \lvert g_F \rvert \mu_B$	Linear Zeeman shift: $h \times 0.7$ MHz/G
V_{TB}	Trap bottom
$\omega_{x,y,z}$	Angular trap frequencies
Ω_s	Static field magnetic energy (over $hbar$)
Ω_{RF}	Radio-frequency field Rabi angular frequency
ω	rf frequency
$\delta = \omega - \Omega_s$	rf detuning
α	Tilt angle
RF_{Amp}	rf dressing intensity (in each wire) in unit of $I_0^{max} = 79.5$ mA pp
RF_{Amp}^c	Critical splitting intensity (appearance of second minimum)

Imaging

$\Gamma = 2\pi \times 6.07$ MHz	Natural line width
$\sigma_0 = 2.91 \times 10^{-9}$ cm^2	Absorption cross section
$I_{sat} = 1.67$mW cm^{-2}	Saturation intensity
$\alpha = \sigma_0/\sigma_{eff}$	Absorption cross section correction factor
$\bar{p}, \sigma_p$	Number of detected photons per atom, (mean, std. dev)
$\bar{b}, \sigma_b$	Number of background photons per pixel (mean, std. dev.)

Sensitivity limits

$\Delta\phi_{SQL} = 1/\sqrt{N}$	Standard quantum limit (or shot noise limit, quantum proj. noise)
$\Delta\phi_H = 1/N$	Heisenberg limit
$\Delta\phi_d$	Phase noise on tof phase estimation for coh. states
$\xi_{N,d}$	Minimum detectable number squeezing

Miscellaneous

Phase diffusion	
R	Phase diffusion rate
$\tau_{coh} = 1/R$	Phase coherence time
Timings	
t_ϕ	Phase accumulation time
t_{BS}	Duration of the beam-splitter operation

Curriculum Vitae

Dr. Tarik Berrada
Theresiengasse 26/8, 1180 Vienna (Austria)
born on 30/07/1985 in Brive-la-Gaillarde (France)
French/Moroccan nationalities
+43 (0)650 32 42 053
dr.tarik.berrada@gmail.com
Researcher ID: H-3960-2014

Professional Experience

2014–2015 **Analyst**, Metalogic GmbH, Munich Development of statistical short-term prediction methods for the energy market.

2014–2015 **Postdoctoral researcher**, Vienna University of Technology (J. Schmiedmayer's group) Experimental and theoretical research on the physics of ultracold atomic quantum gases.

Studies

2009–2014 **Ph.D. in physics**, Vienna University of Technology (J. Schmiedmayer's group)
Austrian-French research project in quantum physics between TU Vienna and Institut d'Optique, Palaiseau, France.
Development of new techniques for quantum noise reduction in high precision interferometric measurements with ultracold atoms.

12/05/2014 Ph.D. defence: Mach-Zehnder interferometry with interacting Bose-Einstein condensates in a double-well potential, passed with distinction (sehr gut).

2008–2009 **Research assistant**, University of Vienna (M. Arndt's group)

T. Berrada, *Interferometry with Interacting Bose-Einstein Condensates in a Double-Well Potential*, Springer Theses,
DOI 10.1007/978-3-319-27233-7

2005–2008 **Master of engineering**, Télécom ParisTech, Paris Double degree with: **Master of Science** in quantum physics at Université Paris Sud XI, Orsay.
2003–2005 **Preparatory class**, Lycée Saint Louis, Paris

Scholarships:

2011–2013 Fellowship of the Vienna Doctoral Program on Complex Quantum Systems (CoQuS)
2007–2008 French studies scholarship
Other: **2012** **Organizer of the annual summer school** on Complex Quantum Systems, Vienna

Languages

French: Native speaker
English: Fluent
German: Bilingual, lived in Austria for more than 10 years
Arabic: Fair oral skills

List of Publications

Publications Resulting from the Ph.D. thesis:

2014 **Interferometry with non-classical motional states of a Bose-Einstein condensate**, S. van Frank, A. Negreti, T. Berrada, R. Bücker, S. Montangero, J.-F. Schaff, T. Schumm, T. Callarco & J. Schmiedmayer, Nat. Commun. 5, 4009 (2014)

2013 **Integrated Mach-Zehnder interferometer for Bose-Einstein condensates**, T. Berrada, S. van Frank, R. Bücker, T. Schumm, J.-F. Schaff & J. Schmiedmayer, Nat. Commun. 4, 2077 (2013)

Vibrational state inversion of a Bose-Einstein condensate: optimal control and state tomography, R. Bücker, T. Berrada, S. van Frank, J.-F. Schaff, T. Schumm, J. Schmiedmayer, G. Jäger, J. Grond & U. Hohenester, J. Phys. B 46, 104012 (2013)

2012 **Momentum distribution of one-dimensional Bose gases at the quasicondensation crossover: Theoretical and experimental investigation**, T. Jacqmin, B. Fang, T. Berrada, T. Roscilde & I. Bouchoule, Phys. Rev. A 86, 043626 (2012)

Dynamics of parametric matter-wave amplification, R. Bücker, U. Hohenester, T. Berrada, S. van Frank, A. Perrin, S. Manz, T. Betz, J. Grond, T. Schumm, and J. Schmiedmayer, Phys. Rev. A 86, 013638 (2012)

2011 **Sub-Poissonian Fluctuations in a 1D Bose Gas: From the Quantum Quasicondensate to the Strongly Interacting Regime**, T. Jacqmin, J. Armijo, T. Berrada, K. Kheruntsyan & I. Bouchoule, Phys. Rev. L **106**, 230405 (2011)

Twin-atom beams, R. Bücker, J. Grond, S. Manz, T. Berrada, T. Betz, C. Koller, U. Hohenester, T. Schumm, A. Perrin & J. Schmiedmayer, Nature Physics 7, 608–611 (2011)

Two-Point Phase Correlations of a One-Dimensional Bosonic Josephson Junction, T. Betz, S. Manz, R. Bücker, T. Berrada, C. Koller, G. Kazakov, I. Mazets, H. Stimming, A. Perrin, T. Schumm & J. Schmiedmayer, Phys. Rev. L 106, 020407 (2011)

Publications Resulting from the Master thesis:

2010 **Influence of conformational molecular dynamics on matter wave interferometry**, M. Gring, S. Gerlich, S. Eibenberger, S. Nimmrichter, T. Berrada, M. Arndt, H. Ulbricht, K. Hornberger, M. Müri, M. Mayor, M. Bröckmann & N. Doltsinis, Phys. Rev. A 81, 031604(R) (2010)